

DTIC FILE COPY

2

GL-TR-89-0315

GRAVITY GRADIOMETER SURVEY SYSTEM (GGSS)  
POST-MISSION DATA PROCESSING NUMERICAL RESULTS

AD-A230 833

Dr. Sam C. Bose  
Glenn E. Thobe

APPLIED SCIENCE ANALYTICS, INC.  
7049 Owensmouth Avenue  
Canoga Park, CA 91303

November 1989

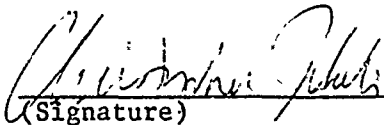
Final Report  
June 1986 - June 1989

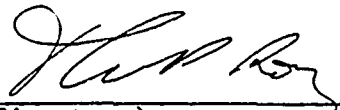
DTIC  
ELECTE  
JAN 11 1991  
S B D

Approved for public release; distribution unlimited

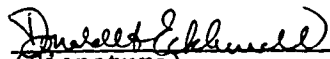
Prepared for:  
GEOPHYSICS LABORATORY  
AIR FORCE SYSTEMS COMMAND  
United States Air Force  
Hanscom AFB, Massachusetts 01731-5000

"This technical report has been reviewed and is approved for publication"

  
(Signature)  
CHRISTOPHER JEKELI  
Contract Manager

  
(Signature)  
THOMAS ROONEY  
Branch Chief

FOR THE COMMANDER

  
(Signature)  
DONALD H. ECKHARDT  
Division Director

This report has been reviewed by the ESD Public Affairs Office (PA) and is releasable to the National Technical Information Service (NTIS).

Qualified requestors may obtain additional copies from the Defense Technical Information Center. All others should apply to the National Technical Information Service.

If your address has changed, or if you wish to be removed from the mailing list, or if the addressee is no longer employed by your organization, please notify GL/IMA, Hanscom AFB, MA 01731. This will assist us in maintaining a current mailing list.

Do not return copies of this report unless contractual obligations or notices on a specific document requires that it be returned.

# REPORT DOCUMENTATION PAGE

Form Approved  
OMB No. 0704-0188

Public reporting burden for this collection of information is estimated to average 1 hour per response, including the time for reviewing instructions, searching existing data sources, gathering and maintaining the data needed, and completing and reviewing the collection of information. Send comments regarding this burden estimate or any other aspect of this collection of information, including suggestions for reducing this burden, to Washington Headquarters Services, Directorate for Information Operations and Reports, 1215 Jefferson Davis Highway, Suite 1204, Arlington, VA 22202-4302, and to the Office of Management and Budget, Paperwork Reduction Project (0704-0188), Washington, DC 20503.

<b>1. AGENCY USE ONLY (Leave blank)</b>		<b>2. REPORT DATE</b> November 1989	<b>3. REPORT TYPE AND DATES COVERED</b> FINAL REPORT(June 1986-June 1989)	
<b>4. TITLE AND SUBTITLE</b> Gravity Gradiometer Survey System (GGSS) Post-Mission Data Processing Numerical Results			<b>5. FUNDING NUMBERS</b> PE: 60370 P 3204 T 3204DM WU 3204DMA: Contract F19628-86-C-0075	
<b>6. AUTHOR(S)</b> Sam C. Bose Glenn E. Thobe				
<b>7. PERFORMING ORGANIZATION NAME(S) AND ADDRESS(ES)</b> Applied Science Analytics, Inc 7049 Owensmouth Avenue Canoga Park, CA 91303			<b>8. PERFORMING ORGANIZATION REPORT NUMBER</b>	
<b>9. SPONSORING/MONITORING AGENCY NAME(S) AND ADDRESS(ES)</b> Geophysics Laboratory Hanscom AFB, Massachusetts 01731-5000  Contract Manager: Christopher Jekeli/LWG			<b>10. SPONSORING/MONITORING AGENCY REPORT NUMBER</b>  GL-TR-89-0315	
<b>11. SUPPLEMENTARY NOTES</b>				
<b>12a. DISTRIBUTION/AVAILABILITY STATEMENT</b>  Approved for public release; distribution unlimited			<b>12b. DISTRIBUTION CODE</b>	
<b>13. ABSTRACT (Maximum 200 words)</b> Software implementation and numerical results of a Karhunen-Loève estimator of local surface gravity fields from measurements of airborne gravity gradient fields are presented. The software was validated using simulated synthetic data from a single dipole gravitational field. Numerical experiments were performed on simulated measurements based on multiple layers of random dipoles, selected in such a way as to produce gravity fields which are statistically similar to those observed in a certain region of Texas. Error analyses were based on qualitative comparison of the plots and on quantitative comparison of indicators computed from the minima and maxima of the plotted gravity vector fields. Results indicate that the method is a viable estimation technique suitable for small computers. Several technical advances were made including 1) an arrangement of equations which minimizes computer storage of arrays and permits (field) measurements to be made sequentially; 2) the application of fast sine and cosine transforms to speed computation dramatically.				
<b>14. SUBJECT TERMS</b> Gravity gradient measurements, gravity field estimation, Dipole fields, Karhunen-Loève estimator, Toeplitz matrix, Large sample grids, Fast sine and cosine transforms			<b>15. NUMBER OF PAGES</b> 160	
			<b>16. PRICE CODE</b>	
<b>17. SECURITY CLASSIFICATION OF REPORT</b> Unclassified	<b>18. SECURITY CLASSIFICATION OF THIS PAGE</b> Unclassified	<b>19. SECURITY CLASSIFICATION OF ABSTRACT</b> Unclassified	<b>20. LIMITATION OF ABSTRACT</b> SAR	

# Contents

<b>1 INTRODUCTION</b>	<b>1</b>
1.1 Purpose and Scope . . . . .	1
1.2 Problem Statement . . . . .	1
1.3 Overview of Report . . . . .	1
<b>2 TECHNICAL APPROACH</b>	<b>2</b>
2.1 Algorithm Overview . . . . .	2
2.2 Software Overview . . . . .	2
2.3 Single Channel Measurements on a Single Grid . . . . .	4
2.4 Full Tensor Measurement on a Single Grid . . . . .	5
2.5 Full Tensor Measurement on a Dual Grid . . . . .	5
2.6 Error Analysis . . . . .	8
<b>3 SOFTWARE VALIDATION</b>	<b>9</b>
3.1 Dipole Simulation . . . . .	9
3.2 Dipole Math Model . . . . .	9
3.3 Simulation Results . . . . .	10
3.3.1 Gradient Measurements . . . . .	10
3.3.2 Gravity Truth . . . . .	11
3.3.3 Single Channel . . . . .	11
3.3.4 Full Tensor . . . . .	11
3.4 Error Analysis . . . . .	11
<b>4 NSWC DATA</b>	<b>13</b>
4.1 Data Tape . . . . .	13
4.2 Grid—Index Mapping . . . . .	13
4.3 Cropping of the Data Region . . . . .	13
4.4 Data Preprocessing—Transformation . . . . .	14
4.5 Gradient Measurements . . . . .	15
4.5.1 File 1 . . . . .	15
4.5.2 File 2 . . . . .	15
4.6 Gravity Truth, File 3 . . . . .	15
<b>5 TEST RESULTS—NSWC DATA</b>	<b>16</b>
5.1 Single Channel, File 1 . . . . .	16
5.2 Full Tensor, File 1 . . . . .	16
5.3 Single Channel, File 2 . . . . .	17
5.4 Full Tensor, File 2 . . . . .	17
5.5 Full Tensor, Combined Files . . . . .	18
5.5.1 Intersection Method . . . . .	18



For	
&I	<input checked="" type="checkbox"/>
ed	<input type="checkbox"/>
tion	<input type="checkbox"/>
ion/	
Availability Codes	
Dist.	Avail and/or Special
A-1	

5.5.2	Union Method . . . . .	18
<b>6</b>	<b>ANALYSIS OF RESULTS</b>	<b>19</b>
6.1	Directional Instability . . . . .	19
6.2	Gain and Bias . . . . .	19
6.3	Boundary and Edge Effects . . . . .	20
<b>7</b>	<b>SUMMARY, CONCLUSIONS, RECOMMENDATIONS</b>	<b>23</b>
7.1	Summary . . . . .	23
7.2	Conclusions . . . . .	23
7.3	Recommendations . . . . .	24
<b>A</b>	<b>Algorithm Summary</b>	<b>25</b>
A.1	Local Region . . . . .	25
A.2	Sensor Signal Model . . . . .	25
A.3	Measurement Model . . . . .	25
A.4	Measurement Grid . . . . .	26
A.5	Measurement Matrices . . . . .	26
A.6	Transformed Measurements . . . . .	27
A.7	Karhunen-Loève Coefficient Estimates . . . . .	28
A.8	Interpolation Grid . . . . .	29
A.9	Signal Estimates . . . . .	29
<b>B</b>	<b>Software Implementation</b>	<b>31</b>
B.1	Estimator Module . . . . .	31
B.2	Synthesizer Module . . . . .	32
B.3	Matrix Formulation . . . . .	32
<b>C</b>	<b>Bibliography</b>	<b>34</b>
<b>D</b>	<b>Plots</b>	<b>35</b>

## List of Tables

1	Single Dipole Gain and Bias. . . . .	12
2	Sampling Grids . . . . .	14
3	File 1 Gain and Bias. . . . .	16
4	File 2 Gain and Bias. . . . .	17
5	Files 1 & 2 (intersection method) Gain and Bias. . . . .	18
6	Files 1 & 2 (union method) Gain and Bias. . . . .	18
7	Signal dependent functions . . . . .	31

## List of Figures

1	Software Modules . . . . .	3
2	Rectangular Grid: File 1, S-N Tracks . . . . .	4
3	Rectangular Grid: File 2, W-E Tracks . . . . .	4
4	Dual Grid: Files 1 & 2 Overlapped . . . . .	6
5	Densified Dual Grid . . . . .	6
6	K-L Coefficient Grid: File 1, S-N Tracks . . . . .	6
7	K-L Coefficient Grid: File 2, W-E Tracks . . . . .	7
8	K-L Coefficient Grid: Combined Files 1 & 2, Union Method . . . . .	7
9	K-L Coefficient Grid: Combined Files 1 & 2, Intersection Method . . . . .	7
10	True $T_x$ , Single Dipole. . . . .	36
11	True $T_y$ , Single Dipole. . . . .	37
12	True $T_z$ , Single Dipole. . . . .	38
13	Measured $T_{xx}$ , Single Dipole. . . . .	39
14	Measured $T_{yy}$ , Single Dipole. . . . .	40
15	Measured $T_{zz}$ , Single Dipole. . . . .	41
16	Measured $T_{xy}$ , Single Dipole. . . . .	42
17	Measured $T_{yz}$ , Single Dipole. . . . .	43
18	Measured $T_{xz}$ , Single Dipole. . . . .	44
19	$\hat{\alpha}$ given $T_{xx}$ , Single Dipole. . . . .	45
20	$\hat{T}_x$ given $T_{xx}$ , Single Dipole. . . . .	46
21	$\hat{T}_y$ given $T_{xx}$ , Single Dipole. . . . .	47
22	$\hat{T}_z$ given $T_{xx}$ , Single Dipole. . . . .	48
23	$\hat{\alpha}$ given $T_{yy}$ , Single Dipole. . . . .	49
24	$\hat{T}_x$ given $T_{yy}$ , Single Dipole. . . . .	50
25	$\hat{T}_y$ given $T_{yy}$ , Single Dipole. . . . .	51
26	$\hat{T}_z$ given $T_{yy}$ , Single Dipole. . . . .	52
27	$\hat{\alpha}$ given $T_{zz}$ , Single Dipole. . . . .	53
28	$\hat{T}_x$ given $T_{zz}$ , Single Dipole. . . . .	54
29	$\hat{T}_y$ given $T_{zz}$ , Single Dipole. . . . .	55
30	$\hat{T}_z$ given $T_{zz}$ , Single Dipole. . . . .	56
31	$\hat{\alpha}$ given $T_{xy}$ , Single Dipole. . . . .	57
32	$\hat{T}_x$ given $T_{xy}$ , Single Dipole. . . . .	58
33	$\hat{T}_y$ given $T_{xy}$ , Single Dipole. . . . .	59
34	$\hat{T}_z$ given $T_{xy}$ , Single Dipole. . . . .	60
35	$\hat{\alpha}$ given $T_{yz}$ , Single Dipole. . . . .	61
36	$\hat{T}_x$ given $T_{yz}$ , Single Dipole. . . . .	62
37	$\hat{T}_y$ given $T_{yz}$ , Single Dipole. . . . .	63
38	$\hat{T}_z$ given $T_{yz}$ , Single Dipole. . . . .	64
39	$\hat{\alpha}$ given $T_{xz}$ , Single Dipole. . . . .	65

40	$\hat{T}_x$ given $T_{xx}$ , Single Dipole. . . . .	66
41	$\hat{T}_y$ given $T_{xx}$ , Single Dipole. . . . .	67
42	$\hat{T}_z$ given $T_{xx}$ , Single Dipole. . . . .	68
43	$\hat{\alpha}$ given full tensor gradient, Single Dipole. . . . .	69
44	$\hat{T}_x$ given full tensor gradient, Single Dipole. . . . .	70
45	$\hat{T}_y$ given full tensor gradient, Single Dipole. . . . .	71
46	$\hat{T}_z$ given full tensor gradient, Single Dipole. . . . .	72
47	Measured $T_{xx}$ , File 1. . . . .	73
48	Measured $T_{yy}$ , File 1. . . . .	74
49	Measured $T_{zz}$ , File 1. . . . .	75
50	Measured $T_{xy}$ , File 1. . . . .	76
51	Measured $T_{yz}$ , File 1. . . . .	77
52	Measured $T_{xz}$ , File 1. . . . .	78
53	$\hat{\alpha}$ given $T_{xx}$ , File 1. . . . .	79
54	$\hat{T}_x$ given $T_{xx}$ , File 1. . . . .	80
55	$\hat{T}_y$ given $T_{xx}$ , File 1. . . . .	81
56	$\hat{T}_z$ given $T_{xx}$ , File 1. . . . .	82
57	$\hat{\alpha}$ given $T_{yy}$ , File 1. . . . .	83
58	$\hat{T}_x$ given $T_{yy}$ , File 1. . . . .	84
59	$\hat{T}_y$ given $T_{yy}$ , File 1. . . . .	85
60	$\hat{T}_z$ given $T_{yy}$ , File 1. . . . .	86
61	$\hat{\alpha}$ given $T_{zz}$ , File 1. . . . .	87
62	$\hat{T}_x$ given $T_{zz}$ , File 1. . . . .	88
63	$\hat{T}_y$ given $T_{zz}$ , File 1. . . . .	89
64	$\hat{T}_z$ given $T_{zz}$ , File 1. . . . .	90
65	$\hat{\alpha}$ given $T_{xy}$ , File 1. . . . .	91
66	$\hat{T}_x$ given $T_{xy}$ , File 1. . . . .	92
67	$\hat{T}_y$ given $T_{xy}$ , File 1. . . . .	93
68	$\hat{T}_z$ given $T_{xy}$ , File 1. . . . .	94
69	$\hat{\alpha}$ given $T_{yz}$ , File 1. . . . .	95
70	$\hat{T}_x$ given $T_{yz}$ , File 1. . . . .	96
71	$\hat{T}_y$ given $T_{yz}$ , File 1. . . . .	97
72	$\hat{T}_z$ given $T_{yz}$ , File 1. . . . .	98
73	$\hat{\alpha}$ given $T_{xz}$ , File 1. . . . .	99
74	$\hat{T}_x$ given $T_{xz}$ , File 1. . . . .	100
75	$\hat{T}_y$ given $T_{xz}$ , File 1. . . . .	101
76	$\hat{T}_z$ given $T_{xz}$ , File 1. . . . .	102
77	$\hat{\alpha}$ given full tensor gradient, File 1. . . . .	103
78	$\hat{T}_x$ given full tensor gradient, File 1. . . . .	104
79	$\hat{T}_y$ given full tensor gradient, File 1. . . . .	105
80	$\hat{T}_z$ given full tensor gradient, File 1. . . . .	106

81	Measured $T_{xx}$ , File 2. . . . .	107
82	Measured $T_{yy}$ , File 2. . . . .	108
83	Measured $T_{zz}$ , File 2. . . . .	109
84	Measured $T_{xy}$ , File 2. . . . .	110
85	Measured $T_{yz}$ , File 2. . . . .	111
86	Measured $T_{xz}$ , File 2. . . . .	112
87	$\hat{\alpha}$ given $T_{xx}$ , File 2. . . . .	113
88	$\hat{T}_x$ given $T_{xx}$ , File 2. . . . .	114
89	$\hat{T}_y$ given $T_{xx}$ , File 2. . . . .	115
90	$\hat{T}_z$ given $T_{xx}$ , File 2. . . . .	116
91	$\hat{\alpha}$ given $T_{yy}$ , File 2. . . . .	117
92	$\hat{T}_x$ given $T_{yy}$ , File 2. . . . .	118
93	$\hat{T}_y$ given $T_{yy}$ , File 2. . . . .	119
94	$\hat{T}_z$ given $T_{yy}$ , File 2. . . . .	120
95	$\hat{\alpha}$ given $T_{zz}$ , File 2. . . . .	121
96	$\hat{T}_x$ given $T_{zz}$ , File 2. . . . .	122
97	$\hat{T}_y$ given $T_{zz}$ , File 2. . . . .	123
98	$\hat{T}_z$ given $T_{zz}$ , File 2. . . . .	124
99	$\hat{\alpha}$ given $T_{xy}$ , File 2. . . . .	125
100	$\hat{T}_x$ given $T_{xy}$ , File 2. . . . .	126
101	$\hat{T}_y$ given $T_{xy}$ , File 2. . . . .	127
102	$\hat{T}_z$ given $T_{xy}$ , File 2. . . . .	128
103	$\hat{\alpha}$ given $T_{yz}$ , File 2. . . . .	129
104	$\hat{T}_x$ given $T_{yz}$ , File 2. . . . .	130
105	$\hat{T}_y$ given $T_{yz}$ , File 2. . . . .	131
106	$\hat{T}_z$ given $T_{yz}$ , File 2. . . . .	132
107	$\hat{\alpha}$ given $T_{xz}$ , File 2. . . . .	133
108	$\hat{T}_x$ given $T_{xz}$ , File 2. . . . .	134
109	$\hat{T}_y$ given $T_{xz}$ , File 2. . . . .	135
110	$\hat{T}_z$ given $T_{xz}$ , File 2. . . . .	136
111	$\hat{\alpha}$ given full tensor gradient, File 2. . . . .	137
112	$\hat{T}_x$ given full tensor gradient, File 2. . . . .	138
113	$\hat{T}_y$ given full tensor gradient, File 2. . . . .	139
114	$\hat{T}_z$ given full tensor gradient, File 2. . . . .	140
115	$\hat{\alpha}$ given full tensor gradient, Files 1 & 2, intersection method. . . . .	141
116	$\hat{T}_x$ given full tensor gradient, Files 1 & 2, intersection method. . . . .	142
117	$\hat{T}_y$ given full tensor gradient, Files 1 & 2, intersection method. . . . .	143
118	$\hat{T}_z$ given full tensor gradient, Files 1 & 2, intersection method. . . . .	144
119	$\hat{\alpha}$ given full tensor gradient, Files 1 & 2, union method. . . . .	145
120	$\hat{T}_x$ given full tensor gradient, Files 1 & 2, union method. . . . .	146
121	$\hat{T}_y$ given full tensor gradient, Files 1 & 2, union method. . . . .	147

122	$\hat{T}_z$ given full tensor gradient, Files 1 & 2, union method. . . . .	148
123	Truth value of $T_x$ , File 3 . . . . .	149
124	Truth value of $T_y$ , File 3 . . . . .	150
125	Truth value of $T_z$ , File 3 . . . . .	151

# 1 INTRODUCTION

## 1.1 Purpose and Scope

The purpose of this report is to document the software implementation of a Karhunen-Loève estimator of local surface gravity fields from measurements of airborne gravity gradient fields, and to present and discuss the results of associated numerical experiments. Extensive derivations and theoretical justifications are avoided. For these the reader is referred to Bose [2] of which a brief extract covering the principal equations is presented in Appendix A.

Here we place special emphasis on the validation of the software using synthetic data from a single dipole gravitational field, which we simulated ourselves. The main body of experiments were performed on simulated measurements produced at the Naval Surface Weapons Center (NSWC) based on multiple layers of random dipoles.

## 1.2 Problem Statement

Given a measurement of the gravity gradient field collected on a regular grid at an altitude  $h$  above the earth's surface, estimate the gravity vector field at altitude 0. Design and implement in software an estimator based on the Karhunen-Loève algorithm. Validate the software using controlled data and test it on foreign data supplied by the NSWC. Perform an error analysis on the results.

## 1.3 Overview of Report

Chapter 2 briefly discusses the technical approach including an overview of the algorithm, software design, various sets of measurements, and finally error analysis. The theory and results of validating the software using known single dipole simulations are presented in Chapter 3. Naval Surface Weapons Center (NSWC) data and related pre-processing are discussed in Chapter 4. Results of testing the Karhunen-Loève estimator for various sets of measurements are presented in Chapter 5. Observations made from analysing the results are discussed in Chapter 6. A summary of the research performed, significant conclusions drawn and recommendations for future research are outlined in Chapter 7.

## 2 TECHNICAL APPROACH

### 2.1 Algorithm Overview

The modeling approach taken here is to exploit the marriage of physical geodesy and random process theory. Laplace's equation is solved with the unknown mass distribution below the surface of the earth modelled as a two-dimensional white noise layer representing the vertical derivative of the disturbance potential to any pre-specified order. This results in a series solution of the disturbance potential wherein the unknown coefficients of the expansion are forced to be uncorrelated by invoking the Karhunen-Loève condition. It can be shown that the disturbance potential covariance obtained from this model is both non-stationary and non-isotropic.

The six (6) gravity gradient measurements are represented in terms of the Karhunen-Loève series expansion of the disturbance potential resulting in six basis functions. These basis functions are shown to be orthogonal. A linear mean square estimator utilizing all the gravity gradient measurements simultaneously is obtained in continuous domain by solving an integral equation involving the estimator gains which are represented by the same orthogonal basis functions. The discrete implementation of the estimator is facilitated by exploiting the orthogonality or near-orthogonality of the transformation matrices so that inverting these matrices becomes computationally trivial. It turns out that the near-orthogonal cosine matrix must be of even order for its inverse to exist, a minor restriction. The gravity disturbance vector is obtained in a two-dimensional grid which can be denser than the measurement grid and also at any altitude, including the surface of the earth. Thus, interpolation and downward continuation are performed automatically. Details of the mathematical development of the algorithm are discussed in Bose [2]. A summary extraction of the relevant equations necessary for software development are outlined in Appendix A.

### 2.2 Software Overview

A modular software package was constructed to realize the estimation algorithm and facilitate numerical experiments, see Figure 1. The estimation process is split into two parts: in module KLE (Karhunen-Loève Estimator) the measured gravity gradient fields are processed to produce the K-L (Karhunen-Loève) coefficients  $\hat{\alpha}_k$  of the estimated potential field; in module SYN (synthesizer) the coefficients are used to synthesize the gravity vector field from the now known coefficients. Incidentally, the SYN module can be used to simulate random gravitational fields by feeding it coefficients from a suitably distributed pseudo-random variable. These two modules are constructed so that, in principle at least, any combination of derivatives of the potential may be used as the observation, and any combination may be estimated: this includes the potential  $T$ , the gravity vector  $\vec{T}$ , and the gradient tensor  $\vec{\vec{T}}$  or any subset of their components. For computational speed, fast sine

and cosine transforms (FST and FCT) are used to compute the discrete sine and cosine transforms (DST and DCT) in both the KLE and SYN modules. Note that the sine matrix of our algorithm is identical to the standard DST, whereas our cosine matrix differs from the standard DCT in that it lacks the first and last rows and columns corresponding to the region boundaries. This fact does not prevent the use of the FST and FCT to obtain the speed advantage of the fast transforms. In order to fully realize this speed advantage, the number of samples transformed plus one must be an (odd) product of small primes.

In addition, there are modules which prepare the measurements for processing and which generate plotting files from any of the measured or computed fields. Yet another module was created to merge the K-L coefficients from west-east and north-south tracks to form K-L coefficients representing the best estimate from all of the data, i.e. the S-N and W-E grids together. A module was designed to generate single dipole gravitational fields including the gravity vector and gradients; the controlled data produced by this module were used to exercise and validate the estimation software during its development.

These modules are coded in portable Fortran 77 and are invoked by VAX (tm) DCL command procedures to do production runs. Internally, all the programs compute using physically consistent SI/MKS units. Inputs and outputs may be expressed in units convenient for the user, e.g. mgal or Eotvos. Any conversions between internal and external units are performed when the data are input or output.

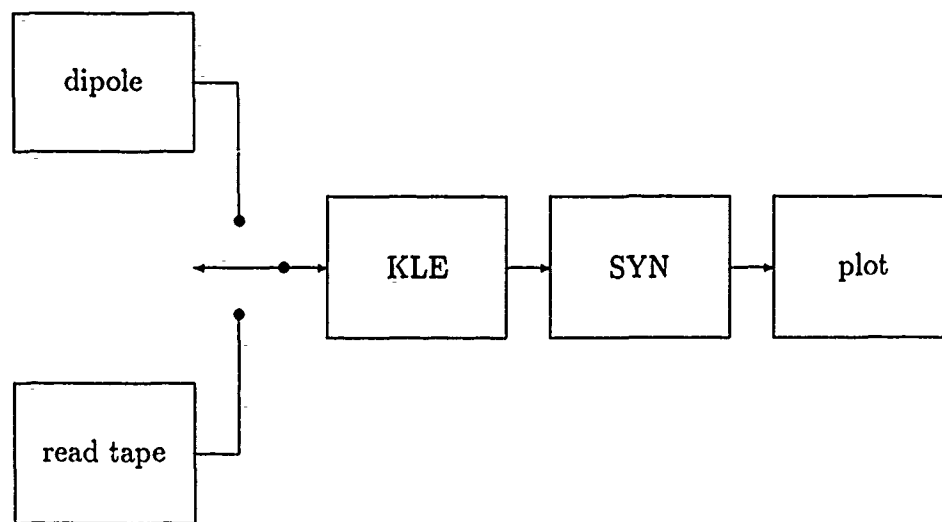


Figure 1: Software Modules

### 2.3 Single Channel Measurements on a Single Grid

Experiments were performed consisting of estimating the gravity vector from each gravity gradient component. The measurement data were presented on a rectangular grid. File 1 measurements are taken every 1 km on south-north (S-N) tracks which are 5 km apart. File 2 measurements were taken on west-east (W-E) tracks with the same spacings.

Figures 2 and 3 illustrate rectangular grids with S-N and W-E tracks, respectively. The sample points used in the estimation are represented by the dots. The border, which is not processed, is represented by the enclosing box. The width and height of the box are the half periods  $A$  and  $B$  of the Fourier series representation of the fields. The numbers of interior sample points horizontally and vertically are given by  $K$  and  $L$ . The numbers of samples in the illustrations are not those of the actual data processed.

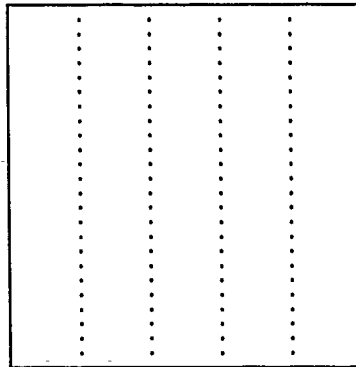


Figure 2: Rectangular Grid: File 1, S-N Tracks

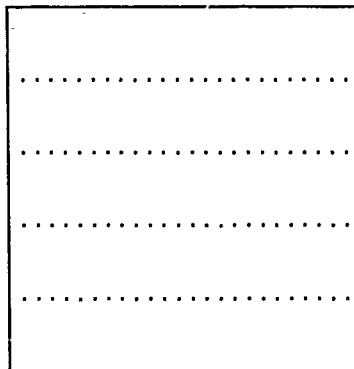


Figure 3: Rectangular Grid: File 2, W-E Tracks

## 2.4 Full Tensor Measurement on a Single Grid

After successful estimation of the gravity vector from single gravity gradient components, the full gravity gradient tensor was used as a measurement and an estimate successfully produced. The six components measured were  $T_{xx}$ ,  $T_{yy}$ ,  $T_{zz}$ ,  $T_{xy}$ ,  $T_{yz}$ , and  $T_{xz}$ . Strictly speaking, any one of the first three of these may be considered redundant in view of Laplace's equation, but all were still included and all six measurement noises were considered independent. For simplicity, all of the six measurement noise variances were taken to be equal to unity. This experiment was performed with both file 1 and file 2 data, i.e. the same measurements which were used singly in the previous set of experiments.

## 2.5 Full Tensor Measurement on a Dual Grid

Files 1 and 2 contain measurements of the same fields over the same survey region, but one has south-north tracks and the other has east-west tracks. Samples are taken 1 km apart and the tracks are 5 km apart. Thus the sampling densities differ in each horizontal direction. We would like to use both sets of measurements together in obtaining our estimates, but the basic estimation process requires an orthogonal sampling grid, which the union of the two grids is not. Figure 4 illustrates the irregular grid obtained by overlapping the S-N and W-E tracks of figures 2 and 3.

A direct approach to extending the method so that the survey data from both files could be used is to superimpose the two grids and fill in the missing points, i.e. the interiors of the squares between the tracks, by interpolation. The new, densified grid would then have samples separated by 1 km in both directions. Unfortunately, the sample count of the new grid, illustrated by Figure 5, would thus be much larger than either of the two original grids.

A much simpler method has been devised whereby the K-L coefficients are estimated on each of the two grids separately and then combined to form a single K-L coefficient field from which the estimated gravity vector is computed. The two fields are rectangular and overlap. For the overlapping portion, the mean of the two fields is used. For non overlapping portions of the two fields, whichever field is present is used to form the combined field. Otherwise, zero is used. This is called the *union method* because all of the two coefficient fields were used, i.e. the (square) convex hull of their union. A variation of this method was also employed, called the *intersection method* because only the overlap, i.e. the (square) intersection of the two coefficient fields was used to reconstruct the gravity vector field estimates. The K-L coefficient field grids are illustrated in Figures 6 and 7. The two combination methods, the *union* and *intersection*, are illustrated in Figures 8 and 9.

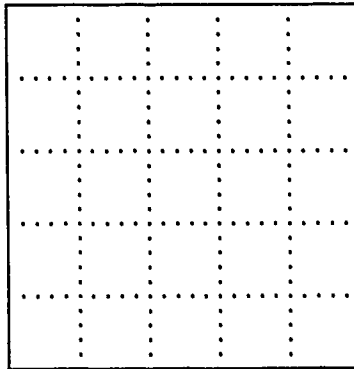


Figure 4: Dual Grid: Files 1 & 2 Overlapped

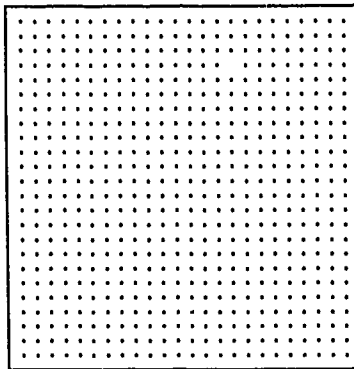


Figure 5: Densified Dual Grid

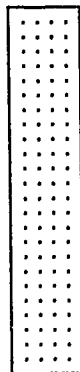


Figure 6: K-L Coefficient Grid: File 1, S-N Tracks

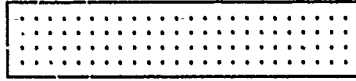


Figure 7: K-L Coefficient Grid: File 2, W-E Tracks

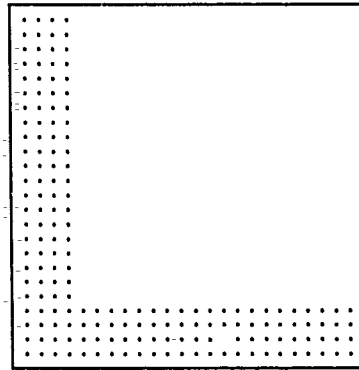


Figure 8: K-L Coefficient Grid: Combined Files 1 & 2, Union Method



Figure 9: K-L Coefficient Grid: Combined Files 1 & 2, Intersection Method

## 2.6 Error Analysis

The primary error analysis tool employed is the three dimensional plot of gravity vector estimates and truth values, which can be compared visually. A error analysis based on the plots was undertaken, in which the minima and maxima of the estimate and truth fields were employed to compute some simple indicators. Both the plots and the indicators appear in this report.

The minimum and maximum values over the plotted region of the estimates  $\hat{T}_x$ ,  $\hat{T}_y$ ,  $\hat{T}_z$ , and the truth values  $T_x$ ,  $T_y$ , and  $T_z$  were taken from the graphs and fed into an *awk* [1] program. The following indicators were computed and tabulated for each estimate:

$$\text{gain}_i \equiv \frac{\max \hat{T}_i - \min \hat{T}_i}{\max T_i - \min T_i} \quad (1)$$

$$\text{bias}_i \equiv \frac{\max \hat{T}_i - \max T_i + \min \hat{T}_i - \min T_i}{2} \quad (2)$$

$$\text{relativebias}_i \equiv \frac{\text{bias}_i}{\max T_i - \min T_i} \quad (3)$$

where  $i = x, y, z$ .

## 3 SOFTWARE VALIDATION

### 3.1 Dipole Simulation

The estimator software was tested with deterministic controlled data generated by a simulation of the gravity field due to a single gravity dipole. Whether or not such dipoles exist in nature is, of course, entirely immaterial; they were selected because of their theoretical simplicity, the ease of computing them, and the ease of interpreting the results. Formulas for a dipole potential and its first and second gradients were derived from elementary physics and differential calculus. The gravity gradient field was computed at altitude and the gravity vector field was computed at ground level for comparison. A  $104 \times 104$  sample grid with 1 km was used. The choice of 104 was dictated by the fact that 1) it is even, which makes the cosine matrices Equations (97) and (99) invertible and their inverses expressible in terms of the fast cosine transform, and 2)  $104 + 1 = 105 = 3 \cdot 5 \cdot 7$  is highly composite, a property which makes the fast sine and cosine transforms computationally more efficient. Row spacing is 1 km in both directions. The dipole is horizontal, centered in the region, and oriented antiparallel to the  $x = y$  line, i.e. parallel to the vector  $(x, y, z) = (-1, -1, 0)$ , at a depth of  $105/8$  km. The gravity gradient was computed at a height of 2 km, and the gravity vector was computed at a height at 0 km.

### 3.2 Dipole Math Model

The gravitational potential  $T$  due to a point mass  $m$  is given by

$$T = mr^{-1} \quad (4)$$

where  $r$  is the distance from the mass point to the observation point. Suppose we have two point masses  $+m$  and  $-m$  at distances of  $r_+$  and  $r_-$ , respectively, from the observation point. Then the potential at the observation point is

$$T = m(r_+^{-1} - r_-^{-1}) \quad (5)$$

If the masses are separated by the vector  $\vec{\delta}$ , then linearizing the inverse distance, this becomes

$$T \approx m\vec{\delta} \cdot \frac{\partial}{\partial \vec{r}} r^{-1} \quad (6)$$

where  $r \approx r_+ \approx r_-$  is the norm of the vector  $\vec{r}$  from the midpoint between the two masses to the observation point. Defining the mass dipole

$$\vec{\mu} = m\vec{\delta} \quad (7)$$

and letting the distance  $\|\vec{\delta}\| \rightarrow 0$  while preserving the product in equation (7), equation (6) becomes exact:

$$T = \vec{\mu} \cdot \frac{\partial}{\partial \vec{r}} r^{-1} \quad (8)$$

To synthesize the dipole field, we need equations for the potential  $T$ , the gravity vector  $\vec{\nabla}T$  and the gravity gradient tensor  $\vec{\nabla}\vec{\nabla}T$ . Switching to component notation, direct differentiation yields:

$$T = \sum_k \mu_k \partial_k r^{-1} \quad (9)$$

$$T_i = \partial_i T = \sum_k \mu_k \partial_{ki} r^{-1} \quad (10)$$

$$T_{lm} = \partial_{lm} T = \sum_k \mu_k \partial_{klm} r^{-1} \quad (11)$$

Note that  $\partial_{kl\dots}$  is shorthand notation for the partial derivative operator with respect to the vector components  $r_k, r_l, \dots$ . Also, all indices range over the set  $\{x, y, z\}$ . The partial differentiation of powers of  $r$  is facilitated by the formula

$$\partial_k r^n = n r^{n-2} r_k \quad (12)$$

The partial derivatives are

$$\partial_k r^{-1} = -r^{-3} r_k \quad (13)$$

$$\partial_{ki} r^{-1} = 3r^{-5} r_k r_i - r^{-3} \delta_{ki} \quad (14)$$

$$\partial_{klm} r^{-1} = -15r^{-7} r_k r_l r_m + 3r^{-5} (r_k \delta_{lm} + r_l \delta_{mk} + r_m \delta_{kl}) \quad (15)$$

where  $\delta_{ki}$  is the Kronecker delta. In the dipole simulation program, where correctness takes precedence over speed, the partials given by equations (13)–(15) are computed and substituted into equations (9)–(11) yielding the gravity potential, gravity vector, and gravity gradient tensor.

For completeness of presentation, we note that the substitution can be performed symbolically and simplified to obtain the following formulas for the potential and its derivatives:

$$T = -r^{-3} \sum_k \mu_k r_k \quad (16)$$

$$T_i = r^{-3} [3r^{-2} (\sum_k \mu_k r_k) r_i - \mu_i] \quad (17)$$

$$T_{lm} = 3r^{-5} [(\sum_k \mu_k r_k) (-5r^{-2} r_l r_m + \delta_{lm}) + r_l \mu_m + r_m \mu_l] \quad (18)$$

These equations are slightly more general, as well as more compact, than equations (2.1-4)–(2.1-13) of White [4], which are restricted to vertically oriented dipoles. By setting  $\mu_x = \mu_y = 0$  in equations (16)–(18), the White equations may be derived, which were supposedly used to produce the NSWC data described in this report.

### 3.3 Simulation Results

#### 3.3.1 Gradient Measurements

The simulated gravity gradient measurements are plotted in Figures 13–18.

### 3.3.2 Gravity Truth

The simulated true gravity vector components are plotted in Figures 10-12.

### 3.3.3 Single Channel

The estimated gravity vector components, based on measured single components of the gravity gradient, are plotted in Figures 19-42. Also plotted are the K-L coefficient fields  $\hat{\alpha}$ .

### 3.3.4 Full Tensor

The estimated gravity vector components, based on the measured full gravity gradient tensor, are plotted in Figures 43-46. Also plotted is the K-L coefficient field  $\hat{\alpha}$ .

## 3.4 Error Analysis

Visual comparison of the plots shows excellent agreement between the truth values of the gravity vector and the estimates. Edge effects can be seen clearly in the estimate plots. Table 1 shows the results of a simple error analysis based on just the maxima and minima of the true and estimated fields. In this and subsequent tables, the first three rows in the table represent the truth values themselves, hence the unity gain and zero bias. In subsequent tables, missing row entries correspond to estimates which exhibited directional instability (discussed later in the report) so that the minimum and maximum values are not meaningful.

Table 1: Single Dipole Gain and Bias.

meas	est	min	max	gain	bias	relbias
$T_x$	$T_x$	-9.37e-14	3.11e-13	1	0	0
$T_y$	$T_y$	-9.37e-14	3.11e-13	1	0	0
$T_z$	$T_z$	-3.79e-13	3.79e-13	1	0	0
$T_{xx}$	$T_x$	-9.76e-14	3.07e-13	0.998	4.31e-15	0.0106
$T_{xx}$	$T_y$	-1.05e-13	2.92e-13	0.98	1.49e-14	0.0369
$T_{xx}$	$T_z$	-3.66e-13	3.66e-13	0.965	0	0
$T_{yy}$	$T_x$	-1.05e-13	2.92e-13	0.98	1.49e-14	0.0369
$T_{yy}$	$T_y$	-9.76e-14	3.07e-13	0.998	4.31e-15	0.0106
$T_{yy}$	$T_z$	-3.66e-13	3.66e-13	0.965	0	0
$T_{zz}$	$T_x$	-9.73e-14	3.08e-13	1	3.65e-15	0.00902
$T_{zz}$	$T_y$	-9.73e-14	3.08e-13	1	3.65e-15	0.00902
$T_{zz}$	$T_z$	-3.79e-13	3.79e-13	0.999	0	0
$T_{xy}$	$T_x$	-9.73e-14	3.06e-13	0.996	4.37e-15	0.0108
$T_{xy}$	$T_y$	-9.73e-14	3.06e-13	0.996	4.38e-15	0.0108
$T_{xy}$	$T_z$	-3.84e-13	3.84e-13	1.01	-6e-18	-7.91e-06
$T_{yz}$	$T_x$	-9.7e-14	3.07e-13	0.998	3.65e-15	0.009
$T_{yz}$	$T_y$	-1.08e-13	3.09e-13	1.03	8.21e-15	0.0203
$T_{yz}$	$T_z$	-3.86e-13	3.86e-13	1.02	-8e-18	-1.05e-05
$T_{zx}$	$T_x$	-1.08e-13	3.09e-13	1.03	8.22e-15	0.0203
$T_{zx}$	$T_y$	-9.7e-14	3.07e-13	0.998	3.64e-15	0.00899
$T_{zx}$	$T_z$	-3.86e-13	3.86e-13	1.02	-6e-18	-7.91e-06
full	$T_x$	-9.69e-14	3.08e-13	1	3.18e-15	0.00785
full	$T_y$	-9.69e-14	3.08e-13	1	3.18e-15	0.00785
full	$T_z$	-3.78e-13	3.78e-13	0.996	-2.01e-18	-2.64e-06

## 4 NSWC DATA

### 4.1 Data Tape

The algorithm was tested on foreign data obtained from the Naval Surface Weapons Center (NSWC) [3]. The data were synthesized from a multilayer vertical dipole array. The magnitude of the dipoles was randomly selected in such a way as to produce gravity fields which are statistically similar to those observed in a certain region of Texas. Details of the model are found in White [4].

The simulation data were supplied on a magnetic tape which we refer to as "tape 1". There are three files of data on this tape: the first two contain simulated gravity gradient measurements such as would be obtained by a survey aircraft. The third contains the gravity force vector at zero altitude. File 1 data are presented as south-to-north (S-N) tracks, file 2 data are presented as west-to-east (W-E) tracks, and file 3 data are presented at the intersections of the S-N and W-E tracks. The sampling density is greater along track than across track.

### 4.2 Grid—Index Mapping

Each file was divided into records, each record constituting a sample point. The  $x$  (east) and  $y$  (north) coordinates for the point were given and then either the six components of the gravity gradient tensor (files 1 and 2) or the three components of the gravity disturbance vector (file 3).

The range of  $x$  and  $y$  was  $-250$  km to  $+250$  km. In the direction of the tracks, the sampling interval was 1 km and in the perpendicular direction it was 5 km. This makes the full arrays  $501 \times 101$  points (file 1),  $101 \times 501$  points (file 2) and  $101 \times 101$  points (file 3).

Each tape file was read into the computer and processed. Each physical quantity represented was placed in a matrix whose elements represented the sampling nodes in the grid. The value of the coordinate  $x$  or  $y$  was mapped linearly as appropriate so that the lowest index value of 1 represented the lowest coordinate value, and the highest index value represented the highest coordinate value. The matrices were then output sequentially; this permitted the estimation software to be structured so that one measurement field at a time could be processed. This sequential processing of the measurements greatly reduces the amount of storage needed to perform estimation from multi-component (vector and tensor) measurements.

### 4.3 Cropping of the Data Region

The number of samples in each direction recorded on the tape was selected without regard to the requirements of any particular estimation algorithm. Because the cosine matrix equations (58)–(59) must have an even number of rows and columns in order to be invertible, we require an even number of samples. Furthermore, in order to use fast sine and

cosine transforms efficiently, the number of samples in each direction should be one less than a highly composite<sup>1</sup> (odd) number. Of the 101 available points in the cross-track direction, we therefore used  $98 = 3^2 \cdot 11 - 1$  corresponding to the range  $-240, -235, \dots, +245$  km. Of the 501 available points in the along track direction, we used  $494 = 3^2 \cdot 5 \cdot 11 - 1$  corresponding to the range  $-246, -245, \dots, +247$  km. Table 2 summarizes the grid information. The symbols  $\Delta x$ , and  $\Delta y$  denote the sampling intervals along each axis (east and north),  $K$  and  $L$  denote the numbers of samples, and  $A = (K + 1)\Delta x$  and  $B = (L + 1)\Delta y$  denote the region dimensions.

#### 4.4 Data Preprocessing—Transformation

The data were presented in north-east-down (NED) coordinates. They were originally believed to have been in east-north-up (ENU) coordinates. Because our analysis and software were based on ENU (really any right-handed frame with the  $z$  axis pointing upward) we applied a transformation from NED to ENU to all the data. The equations for this transformation are:

$$x', y', z' = y, x, -z \quad (19)$$

$$T'_x, T'_y, T'_z = T_y, T_x, -T_z \quad (20)$$

$$T'_{xx}, T'_{yy}, T'_{zz} = T_{yy}, T_{xx}, T_{zz} \quad (21)$$

$$T'_{xy}, T'_{yz}, T'_{xz} = T_{xy}, -T_{xz}, -T_{yz} \quad (22)$$

where unprimed coordinates are in the old NED frame and the primed coordinates are in the new ENU frame. Here also  $T$  is the disturbing potential and the  $x$ ,  $y$ , and  $z$  subscripts denote partial differentiation.

Incidentally, the transformation works equally well in reverse.

---

<sup>1</sup>The product of small primes.

Table 2: Sampling Grids

file no.	$\Delta x$ (km)	$\Delta y$ (km)	$A$ (km)	$B$ (km)	$K$	$L$
1	1	5	495	495	494	98
2	5	1	495	495	98	494
3	5	5	495	495	98	98

## **4.5 Gradient Measurements**

### **4.5.1 File 1**

The simulated gravity gradient measurements along S-N tracks, recorded on tape 1, file 1, are plotted in Figures 47-52.

### **4.5.2 File 2**

The simulated gravity gradient measurements along W-E tracks, recorded on tape 1, file 2, are plotted in Figures 81-86.

## **4.6 Gravity Truth, File 3**

The simulated true gravity vector components, recorded on tape 1, file 3, are plotted in Figures 123-125.

## 5 TEST RESULTS—NSWC DATA

### 5.1 Single Channel, File 1

The estimated gravity vector components, based on measured single components of the gravity gradient (tape 1, file 1) measured on S-N tracks, are plotted in Figures 53-76. Also plotted are the K-L coefficient fields  $\hat{\alpha}$ . Table 3 shows the gain and bias indicators for this series of estimates.

### 5.2 Full Tensor, File 1

The estimated gravity vector components, based on the measured full gravity gradient tensor (tape 1, file 1) measured on S-N tracks, are plotted in Figures 77-80. Also plotted is the K-L coefficient field  $\hat{\alpha}$ . Table 3 shows the gain and bias indicators for this series of estimates.

Table 3: File 1 Gain and Bias.

meas	est	min	max	gain	bias	relbias
$T_x$	$T_x$	-38.2	45	1	0	0
$T_y$	$T_y$	-24.5	59.6	1	0	0
$T_z$	$T_z$	-53.4	64.3	1	0	0
$T_{xx}$	$T_x$	-45.1	52.4	1.17	-0.229	-0.00276
$T_{yy}$	$T_x$	-37	32.3	0.833	5.76	0.0692
$T_{yy}$	$T_y$	-44.3	35.9	0.953	21.7	0.258
$T_{yy}$	$T_z$	-66.4	53.7	1.02	11.8	0.1
$T_{zz}$	$T_x$	-41.4	40.9	0.989	3.69	0.0444
$T_{zz}$	$T_y$	-47.3	34.9	0.976	23.8	0.283
$T_{zz}$	$T_z$	-59.8	59.6	1.02	5.56	0.0473
$T_{xy}$	$T_x$	-40.5	40.2	0.971	3.57	0.043
$T_{yz}$	$T_x$	-41.8	40.8	0.993	3.92	0.0472
$T_{yz}$	$T_y$	-47.3	35.5	0.984	23.4	0.279
$T_{yz}$	$T_z$	-77.1	65.5	1.21	11.3	0.0959
$T_{xz}$	$T_x$	-41.2	46.5	1.05	0.776	0.00933
full	$T_x$	-40.3	41.4	0.983	2.89	0.0348
full	$T_y$	-47	31.9	0.938	25.1	0.298
full	$T_z$	-56.9	59.4	0.989	4.16	0.0354

### 5.3 Single Channel, File 2

The estimated gravity vector components, based on measured single components of the gravity gradient (tape 1, file 2) measured on W-E tracks, are plotted in Figures 87-110. Also plotted are the K-L coefficient fields  $\hat{\alpha}$ . Table 4 shows the gain and bias indicators for this series of estimates.

### 5.4 Full Tensor, File 2

The estimated gravity vector components, based on the measured full gravity gradient tensor (tape 1, file 2) measured on W-E tracks, are plotted in Figures 111-114. Also plotted is the K-L coefficient field  $\hat{\alpha}$ . Table 4 shows the gain and bias indicators for this series of estimates.

Table 4: File 2 Gain and Bias.

meas	est	min	max	gain	bias	relbias
$T_x$	$T_x$	-38.2	45	1	0	0
$T_y$	$T_y$	-24.5	59.6	1	0	0
$T_z$	$T_z$	-53.4	64.3	1	0	0
$T_{xx}$	$T_x$	-40	42.5	0.991	2.18	0.0262
$T_{xx}$	$T_y$	-4.7	29.8	0.861	24	0.286
$T_{xx}$	$T_z$	-52.5	62.4	0.977	0.495	0.00421
$T_{yy}$	$T_y$	-52.4	34.8	1.04	26.4	0.314
$T_{zz}$	$T_x$	-39.3	39.6	0.949	3.26	0.0392
$T_{zz}$	$T_y$	-46.6	32.8	0.943	24.4	0.291
$T_{zz}$	$T_z$	-58.7	57.9	0.991	5.85	0.0497
$T_{xy}$	$T_y$	-50	37.9	1.04	23.7	0.281
$T_{yz}$	$T_y$	-47.6	36.2	0.996	23.2	0.276
$T_{xz}$	$T_x$	-40.1	43.1	1	1.91	0.023
$T_{xz}$	$T_y$	-47.6	40.2	1.04	21.3	0.253
$T_{xz}$	$T_z$	-52.8	72	1.06	-4.14	-0.0352
full	$T_x$	-39.4	41.4	0.972	2.44	0.0294
full	$T_y$	-46	31.2	0.917	24.9	0.296
full	$T_z$	-55.4	59.3	0.975	3.54	0.0301

## 5.5 Full Tensor, Combined Files

### 5.5.1 Intersection Method

The estimated gravity vector components and K-L coefficients, based on using the *intersection method*, on the measured full gravity gradient tensor from both S-N tracks (tape 1, file 1) and W-E tracks (tape 1, file 2), are plotted in Figures 115-118. Table 5 shows the gain and bias indicators for this series of estimates.

Table 5: Files 1 & 2 (intersection method) Gain and Bias.

meas	est	min	max	gain	bias	relbias
$T_x$	$T_x$	-38.2	45	1	0	0
$T_y$	$T_y$	-24.5	59.6	1	0	0
$T_z$	$T_z$	-53.4	64.3	1	0	0
full	$T_x$	-39.1	40.3	0.955	2.86	0.0344
full	$T_y$	-45.2	31.2	0.908	24.6	0.292
full	$T_z$	-55.1	59.5	0.974	3.27	0.0278

### 5.5.2 Union Method

The estimated gravity vector components and K-L coefficients, based on using the *union method*, on the measured full gravity gradient tensor measured on both S-N tracks (tape 1, file 1) and W-E tracks (tape 1, file 2), are plotted in Figures 119-122. Table 6 shows the gain and bias indicators for this series of estimates.

Table 6: Files 1 & 2 (union method) Gain and Bias.

meas	est	min	max	gain	bias	relbias
$T_x$	$T_x$	-38.2	45	1	0	0
$T_y$	$T_y$	-24.5	59.6	1	0	0
$T_z$	$T_z$	-53.4	64.3	1	0	0
full	$T_x$	-40.5	41.1	0.982	3.13	0.0376
full	$T_y$	-46.4	31.1	0.921	25.2	0.299
full	$T_z$	-57.6	60	1	4.26	0.0362

## 6 ANALYSIS OF RESULTS

### 6.1 Directional Instability

An interesting phenomenon which occurred with some *single channel* measurement estimates is directional instability, i.e. the appearance of a surface which is smooth when scanned along one horizontal axis but which oscillates wildly when scanned in the direction of the other horizontal axis. The occurrence of these instabilities has been noted from the graphs and tabulated for file 1 (S-N tracks) and file 2 (W-E tracks) single channel estimates. We observe that only the gravity vector component which can be consistently estimated is the horizontal one at right angles to the tracks, that is in the sparsely sampled direction. Only half the remaining combinations yield smooth, reasonable estimates. The other half (six combinations for each file) are unstable in the direction parallel to the tracks, i.e. the direction on the higher sampling density. For file 1 we can state the rule that an estimate will be unstable in the y (dense) direction if and only if the measurement is an x partial derivative and the estimated quantity is not. For file 2 the same rule applies if only we exchange the x and y in the rule for file 1. Thus a gravity component in either the densely sampled or vertical direction can not be obtained from a gradient component in the sparsely sampled direction.

More investigation is required to determine whether the problem of directional instability for single channel measurements with unequal sampling intervals in the two horizontal directions, is fundamental or can be overcome. In any case they do not pose a serious problem so long as *full tensor measurements, which do not exhibit directional instability*, are available. Even if the full tensor is not available, the method is general enough to accommodate any subset of the six (five independent) gradient tensor components, which presumably would be sufficient to overcome the instability.

### 6.2 Gain and Bias

In examining the tabulated estimator gain and bias errors, we observe that single axis gains ranged from a decrease of 17% to an increase of 21% for file 1 and from a decrease of 14% to an increase of 6% for file 2. Relative biases vary from -3% to +30% for file 1 and from -4% to +31% for file 2. Gain and bias errors based on full tensor gradient measurements show much less spread, however, than the single axis errors: the gains range from 6% less than unity (file 2) to 1% less than unity (file 1). Relative biases range from +3% to +30% (both files). Interestingly, estimates of  $T_y$  show a consistent relative bias of approximately 30%. Results are similar for the combined estimates using both the intersection and union methods, although the latter seems slightly better on gain and the former slightly better on relative bias.

The slight attenuation typical of most of the estimates is fairly easily explained by noting that the estimator is a low pass filter. This is because the estimator knows that the

measurement noise is a wide band signal. By filtering out the higher spatial frequencies, the estimator will dull the sharp peaks which more than likely include the minima and maxima, resulting in a smaller peak-to-peak magnitude and hence a less than unity gain by our definition.

### 6.3 Boundary and Edge Effects

Likely error sources are boundary and edge effects. By the former we mean errors resulting from assuming boundary conditions which do not in fact obtain. Boundary effects which are in evidence only near the edges of the region are known as edge effects. The potential model of a pure sine Fourier series in  $x$  and  $y$  given by

$$T(x, y, z) = \sum_{k=1}^{\infty} \sum_{l=1}^{\infty} \alpha_{kl} \sin(a_k x) \sin(b_l y) \exp(-c_{kl} z) \quad (23)$$

where

$$a_k = k\pi/A, \quad b_l = l\pi/B, \quad c_{kl} = \sqrt{a_k^2 + b_l^2} \quad (24)$$

implies certain boundary conditions: 1)  $T$  is periodic with period  $(2A, 2B)$ , i.e.

$$T(x, y, z) = T(x + 2A, y, z) = T(x, y + 2B, z) \quad (25)$$

and 2)  $T$  is odd symmetric in  $x$  and  $y$ , i.e.

$$T(x, y, z) = -T(-x, y, z) = -T(x, -y, z) \quad (26)$$

These follow directly from the properties of the sine function and are readily verifiable from the representation of  $T(x, y, z)$  given by equation (23). A corollary to these conditions is that  $T$  is odd symmetric about any of the survey region boundaries:

$$T(A + x, y, z) = -T(A - x, y, z), \quad T(x, B + y, z) = -T(x, B - y, z) \quad (27)$$

It follows that the mass distribution which induces  $T$  must satisfy the same conditions as the potential, i.e. each mass particle or feature will have a two-dimensional infinite series of reflective and periodic images of itself, some of which are sign reversed.

To the extent that the real mass distribution meets these conditions, the estimator will produce correct results. Generally, however, the mass distribution will not meet these symmetry and periodicity conditions. In such cases, good estimates may still be possible away from the boundaries. The sources of error may be masses outside the region, which are necessarily not modeled, and the reflective and periodic images located outside the region which are unavoidably and erroneously modeled. Since the potential due to a mass particle declines with distance from the observer, estimates can be expected to be good near the surface and away from the edges, provided there are not unduly significant mass distributions near or beyond the edges or at great depth compared to  $A$  and  $B$ .

Let us remark that the symmetry condition can be done away with by switching to a potential representation which includes the cosine-cosine as well a mixed sine and cosine terms of the Fourier series

$$\begin{aligned}
 T(x, y, z) = [ & \hspace{15em} (28) \\
 & \sum_{k=1}^{\infty} \sum_{l=1}^{\infty} \alpha_{kl}^{ss} \sin(a_k x) \sin(b_l y) \\
 & + \sum_{k=1}^{\infty} \sum_{l=0}^{\infty} \alpha_{kl}^{sc} \sin(a_k x) \cos(b_l y) \\
 & + \sum_{k=0}^{\infty} \sum_{l=1}^{\infty} \alpha_{kl}^{cs} \cos(a_k x) \sin(b_l y) \\
 & + \sum_{k=0}^{\infty} \sum_{l=0}^{\infty} \alpha_{kl}^{cc} \cos(a_k x) \cos(b_l y) \\
 & ] \exp(-c_{kl} z)
 \end{aligned}$$

or the equivalent complex Fourier series. This alternative approach requires data to be expanded to a full period, i.e. a rectangle of dimensions  $2A \times 2B$ . It has the advantage of being able to handle non-zero potentials on the boundary.

An alternative approach to dealing with non-zero boundary potentials is to fit a simple harmonic field to the region boundaries and then apply the existing estimation algorithm to estimating the residual field, which will necessarily meet the zero boundary value condition. The final field estimate is the sum of the simple field which fits the boundaries and the estimated residual field. Such a fit must be done using measurements of the gravity gradient on the region boundary. Currently these measurements are not utilized in our algorithm. A model for the boundary-fitting harmonic field is obtained from the full Fourier series equation (28) by restricting the range of the cosine summation indices to a maximum of 1.

$$\begin{aligned}
 T(x, y, z) = [ & \hspace{15em} (29) \\
 & \sum_{k=1}^{\infty} \sum_{l=1}^{\infty} \alpha_{kl}^{ss} \sin(a_k x) \sin(b_l y) \\
 & + \sum_{k=1}^{\infty} \sum_{l=0}^1 \alpha_{kl}^{sc} \sin(a_k x) \cos(b_l y) \\
 & + \sum_{k=0}^1 \sum_{l=1}^{\infty} \alpha_{kl}^{cs} \cos(a_k x) \sin(b_l y) \\
 & + \sum_{k=0}^1 \sum_{l=0}^1 \alpha_{kl}^{cc} \cos(a_k x) \cos(b_l y) \\
 & ] \exp(-c_{kl} z)
 \end{aligned}$$

The details of estimating the boundary coefficients are beyond the scope of the present research. The purpose of introducing them here is to demonstrate a model for the errors

incurred when the boundary values of the potential, being observed through the gradients, are non-zero.

The Fourier coefficients in equation (29) are obtained sequentially. The  $\alpha_{kl}^{cc}$  are determined first so that the four cosine-cosine terms produce a harmonic field which fits the corners of the potential. The residual field is computed by subtracting the cosine-cosine terms from the total field  $T(x, y, z)$  leaving a harmonic field with zero potential on the four corners. Then each set of mixed coefficients is computed to fit the interiors of one parallel set of sides. A new residual field is computed which has homogenous boundary conditions and is thus representable in terms of sine-sine terms only. But we have already solved the problem of estimating the sine-sine coefficients by the Karhunen-Loève method. The details of this multistep estimation process based on equation (29) are beyond the scope of this research. Note, however, that besides providing a means of extending the K-L method to handle non-homogenous problems, it gives one a model for determining what types of errors may be present when the homogenous K-L method is applied to non-homogenous data as was done in this study.

By visualizing several of these boundary harmonics, the reader can imagine what types of errors may be present. Some examples:

- constant in both  $x$  and  $y$  directions
- cosine in  $x$ , constant in  $y$
- cosine in  $x$  and  $y$
- arbitrary  $C_2$  curve in  $x$  vanishing at the endpoints, constant in  $y$
- arbitrary  $C_2$  curve in  $y$  vanishing at the endpoints, constant in  $x$

By this analysis we demonstrate a rather large family of harmonic surfaces from which to select one which corrects for the boundary values.

## 7 SUMMARY, CONCLUSIONS, RECOMMENDATIONS

### 7.1 Summary

The Karhunen-Loève algorithm was implemented, validated on controlled data, and tested on foreign data. Successful recovery of the unknown gravity field was accomplished in most cases, the only exceptions being certain single-component measurement cases where the sampling interval is different in the two horizontal directions. Plots of the measured gravity gradients and of the true and estimated gravity vectors have been presented. A capability to simulate dipole fields was developed and applied to produce controlled data based on a single horizontal gravity dipole; the single dipole data were used for software validation.

Error analyses were based on qualitative comparison of the plots and on quantitative comparison of indicators computed from the minima and maxima of the plotted gravity vector fields. Since a method designed for homogeneous potential fields, i.e. zero-valued on the rectangular survey region boundaries, was being applied to data derived from a non-homogenous potential, the estimate regions were cropped on the hypothesis that boundary and edge effect errors would be mostly restricted to near the rectangle boundaries. This hypothesis was at least partially justified by the results. Ways to extend the method to deal properly with the non-homogenous boundary conditions were suggested.

In the process of implementing the K-L algorithm in software, several technical advances were made. These include 1) an arrangement of equations which minimizes computer storage of arrays and permits (field) measurements to be made sequentially; 2) the application of fast sine and cosine transforms to speed computation dramatically, especially for large sample grids.

### 7.2 Conclusions

We conclude that the Karhunen-Loève method of gravity estimation from gravity gradient measurements as implemented for this study is a viable estimation technique. The present experiments did not attempt to account for non-homogenous boundary values, which limited the region of acceptable estimates to center of the measurement region, i.e. away from the boundaries. It is believed that better performance over the whole region will be attained when the method is enhanced in the ways recommended. Still the method worked well within its present limitations. Because of its excellent results, computational economy, and suitability for small computers, its eventual wide adoption is suggested.

### 7.3 Recommendations

The principal recommendation for further work is that the method be extended to account for non-homogeneous boundary conditions. Two approaches have been pointed out: first, adding a sufficient number of cosine and mixed sine-cosine harmonics to the disturbing potential model and estimating the additional coefficients from the boundary data alone; and alternatively, by adding the full complement of cosine and mixed sine-cosine terms and expanding the data region to a full period in the  $x$  and  $y$  directions. A variation on the latter method would be to use a complex Fourier series instead of the real sine-cosine series to represent the potential. Additional tests with simulated measurement noise are recommended.

We note that the algorithm is not limited to simply obtaining estimates of the gravity vector from measurements of the gradient. With minimal modification to the software, combinations of measurements of the potential derivatives of any or different orders can be processed and likewise derivatives of any order can be estimated.

The mathematical model for the method tested here can be extended in potentially useful ways. For example, instead of representing the source of the disturbing potential by a *single* white noise layer, multiple layers should be considered. These would be placed at various depths as in the model used to produce the NSWG data.

## A Algorithm Summary

### A.1 Local Region

A local region of interest is represented as such, where  $x$  and  $y$  coordinates are on the surface of the earth and the  $z$  coordinate is vertical above the surface of the earth. The local region of interest is specified by the spatial domain  $D$  given as

$$D(x, y) = \{x, y; 0 \leq x \leq A, 0 \leq y \leq B\} \quad (30)$$

where

$A$  - length of the survey region

$B$  - width of the survey region

The survey measurements are taken at an altitude  $H$  above the surface of the earth.

### A.2 Sensor Signal Model

The gradiometer sensor signal  $S(x, y, z)$  has six (6) components: three (3) inline signals and three crossline signals. The six (6) signals of the gradiometer are given below

$$S_1(x, y, z) = \frac{\partial^2 T}{\partial x^2} \quad (31)$$

$$S_2(x, y, z) = \frac{\partial^2 T}{\partial y^2} \quad (32)$$

$$S_3(x, y, z) = \frac{\partial^2 T}{\partial z^2} \quad (33)$$

$$S_4(x, y, z) = \frac{\partial^2 T}{\partial x \partial y} \quad (34)$$

$$S_5(x, y, z) = \frac{\partial^2 T}{\partial y \partial z} \quad (35)$$

$$S_6(x, y, z) = \frac{\partial^2 T}{\partial z \partial x} \quad (36)$$

### A.3 Measurement Model

The measurement  $Z(x, y)$  at  $z = H$  of the gradiometer signal  $S(x, y)$  is contaminated with an additive noise  $V(x, y)$  such that

$$Z(x, y) = S(x, y) + V(x, y) \quad (37)$$

The autocorrelation function of the additive noise is assumed to be a diagonal matrix such that

$$R_{VV}(x_1, y_1; x_2, y_2) = \{V(x_1, y_1)V^T(x_2, y_2)\} \quad (38)$$

$$= \begin{bmatrix} \sigma_1^2 & 0 & 0 & 0 & 0 & 0 \\ 0 & \sigma_2^2 & 0 & 0 & 0 & 0 \\ 0 & 0 & \sigma_3^2 & 0 & 0 & 0 \\ 0 & 0 & 0 & \sigma_4^2 & 0 & 0 \\ 0 & 0 & 0 & 0 & \sigma_5^2 & 0 \\ 0 & 0 & 0 & 0 & 0 & \sigma_6^2 \end{bmatrix} \delta(x_1 - x_2)\delta(y_1 - y_2) \quad (39)$$

The vector signal  $S(x, y)$  and measurement noise  $V(x, y)$  are assumed to be uncorrelated, i.e.

$$E \{S(x_1, y_1)V^T(x_2, y_2)\} = \{V(x_1, y_1)S^T(x_2, y_2)\} = 0 \quad (40)$$

#### A.4 Measurement Grid

In order to obtain the vector signal estimates for all the spatial points of interest a definition of the two-dimensional grid is necessary. For the present development the two-dimensional grid of data points is defined to be equally spaced in each direction with  $K$  data points in the  $x$  - direction and  $L$  data points in the  $y$  - direction. With  $\Delta x$  and  $\Delta y$  the grid spacing in the  $x$  and  $y$  directions respectively the spatial domain  $D$  is given as

$$(K + 1)\Delta x = A \quad 1 \leq k \leq K \quad (41)$$

$$(L + 1)\Delta y = B \quad 1 \leq l \leq L \quad (42)$$

#### A.5 Measurement Matrices

$$[Z_1]_{K \times L} = \begin{bmatrix} Z_1(x_1, y_1) & Z_1(x_1, y_2) & \cdots & Z_1(x_1, y_L) \\ Z_1(x_2, y_1) & & & \vdots \\ \vdots & & & \vdots \\ Z_1(x_K, y_1) & \cdots & \cdots & Z_1(x_K, y_L) \end{bmatrix} \quad (43)$$

$$[Z_2]_{K \times L} = \begin{bmatrix} Z_2(x_1, y_1) & Z_2(x_1, y_2) & \cdots & Z_2(x_1, y_L) \\ Z_2(x_2, y_1) & & & \vdots \\ \vdots & & & \vdots \\ Z_2(x_K, y_1) & \cdots & \cdots & Z_2(x_K, y_L) \end{bmatrix} \quad (44)$$

$$[Z_3]_{K \times L} = \begin{bmatrix} Z_3(x_1, y_1) & Z_3(x_1, y_2) & \cdots & Z_3(x_1, y_L) \\ Z_3(x_2, y_1) & & & \vdots \\ \vdots & & & \vdots \\ Z_3(x_K, y_1) & \cdots & \cdots & Z_3(x_K, y_L) \end{bmatrix} \quad (45)$$

$$[Z_4]_{K \times L} = \begin{bmatrix} Z_4(x_1, y_1) & Z_4(x_1, y_2) & \cdots & Z_4(x_1, y_L) \\ Z_4(x_2, y_1) & & & \vdots \\ \vdots & & & \vdots \\ Z_4(x_K, y_1) & \cdots & \cdots & Z_4(x_K, y_L) \end{bmatrix} \quad (46)$$

$$[Z_5]_{K \times L} = \begin{bmatrix} Z_5(x_1, y_1) & Z_5(x_1, y_2) & \cdots & Z_5(x_1, y_L) \\ Z_5(x_2, y_1) & & & \vdots \\ \vdots & & & \vdots \\ Z_5(x_K, y_1) & \cdots & \cdots & Z_5(x_K, y_L) \end{bmatrix} \quad (47)$$

$$[Z_6]_{K \times L} = \begin{bmatrix} Z_6(x_1, y_1) & Z_6(x_1, y_2) & \cdots & Z_6(x_1, y_L) \\ Z_6(x_2, y_1) & & & \vdots \\ \vdots & & & \vdots \\ Z_6(x_K, y_1) & \cdots & \cdots & Z_6(x_K, y_L) \end{bmatrix} \quad (48)$$

## A.6 Transformed Measurements

$$[\tilde{Z}_1]_{K \times L} = \frac{AB}{(K+1)(L+1)} \begin{matrix} [S\Delta X]^T [Z_1] [S\Delta Y] \\ K \times K \quad K \times L \quad L \times L \end{matrix} \quad (49)$$

$$[\tilde{Z}_2]_{K \times L} = \frac{AB}{(K+1)(L+1)} \begin{matrix} [S\Delta X]^T [Z_2] [S\Delta Y] \\ K \times K \quad K \times L \quad L \times L \end{matrix} \quad (50)$$

$$[\tilde{Z}_3]_{K \times L} = \frac{AB}{(K+1)(L+1)} \begin{matrix} [S\Delta X]^T [Z_3] [S\Delta Y] \\ K \times K \quad K \times L \quad L \times L \end{matrix} \quad (51)$$

$$[\tilde{Z}_4]_{K \times L} = \frac{AB}{(K+1)(L+1)} \begin{matrix} [I + 2C][C\Delta X]^T [Z_4] [C\Delta Y][I + 2C] \\ K \times K \quad K \times K \quad K \times L \quad L \times L \quad L \times L \end{matrix} \quad (52)$$

$$[\tilde{Z}_5]_{K \times L} = \frac{AB}{(K+1)(L+1)} \begin{matrix} [S\Delta X]^T [Z_5] [C\Delta Y][I + 2C] \\ K \times K \quad K \times L \quad L \times L \quad L \times L \end{matrix} \quad (53)$$

$$[\tilde{Z}_6]_{K \times L} = \frac{AB}{(K+1)(L+1)} \begin{matrix} [I + 2C][C\Delta X]^T [Z_6] [S\Delta Y] \\ K \times K \quad K \times K \quad K \times L \quad L \times L \end{matrix} \quad (54)$$

where  $K$  and  $L$  are even,  $[I]$  is the  $K \times K$  or  $L \times L$  identity matrix, and  $[C]$  is a  $K \times K$  or  $L \times L$  Toeplitz Circulant matrix of alternating one's (1) and zeroes (0), a  $4 \times 4$  example of which is

$$[C] = \begin{bmatrix} 1 & 0 & 1 & 0 \\ 0 & 1 & 0 & 1 \\ 1 & 0 & 1 & 0 \\ 0 & 1 & 0 & 1 \end{bmatrix} \quad (55)$$

The transformation matrices are given by

$$[S\Delta X(i, j)] = \sin \pi(i \times j) \frac{\Delta X}{A} \quad \begin{array}{l} 1 \leq i \leq K \\ 1 \leq j \leq K \end{array} \quad (56)$$

$$[S\Delta Y(i, j)]^T = \sin \pi(i \times j) \frac{\Delta Y}{B} \quad \begin{array}{l} 1 \leq i \leq L \\ 1 \leq j \leq L \end{array} \quad (57)$$

$$[C\Delta X(i, j)] = \cos \pi(i \times j) \frac{\Delta X}{A} \quad \begin{array}{l} 1 \leq i \leq K \\ 1 \leq j \leq K \end{array} \quad (58)$$

$$[C\Delta Y(i, j)]^T = \cos \pi(i \times j) \frac{\Delta Y}{B} \quad \begin{array}{l} 1 \leq i \leq L \\ 1 \leq j \leq L \end{array} \quad (59)$$

## A.7 Karhunen-Loève Coefficient Estimates

$$\begin{aligned} [\hat{\alpha}_{mn}]_{K \times L} = & \beta_{mn1} \otimes \tilde{Z}_1(m, n) \otimes \gamma_{mn1} + \beta_{mn2} \otimes \tilde{Z}_2(m, n) \otimes \gamma_{mn2} \\ & + \beta_{mn3} \otimes \tilde{Z}_3(m, n) \otimes \gamma_{mn3} + \beta_{mn4} \otimes \tilde{Z}_4(m, n) \otimes \gamma_{mn4} \\ & + \beta_{mn5} \otimes \tilde{Z}_5(m, n) \otimes \gamma_{mn5} + \beta_{mn6} \otimes \tilde{Z}_6(m, n) \otimes \gamma_{mn6} \end{aligned} \quad (60)$$

where  $\otimes$  is point-by-point matrix multiplication and not row-by-column matrix multiplication and,

$$\beta_{mni} = \frac{\lambda_{mn} \prod_{j=1, j \neq i}^6 \sigma_j^2}{\prod_{j=1}^6 \sigma_j^2 + \frac{AB}{4} \lambda_{mn} \left( \sum_{j=1}^6 \gamma_{mnj}^2 \prod_{k=1, k \neq j}^6 \sigma_k^2 \right)} \quad (61)$$

and

$$\lambda_{mn} = \frac{\sigma_0^2}{c_{mn}^{2k_0}} \quad (62)$$

and

$$\gamma_{mn1} = \frac{-2}{\sqrt{AB}} a_m^2 e^{-c_{mn}|H+D|} \quad (63)$$

$$\gamma_{mn2} = \frac{-2}{\sqrt{AB}} b_n^2 e^{-c_{mn}|H+D|} \quad (64)$$

$$\gamma_{mn3} = \frac{2}{\sqrt{AB}} c_{mn}^2 e^{-c_{mn}|H+D|} \quad (65)$$

$$\gamma_{mn4} = \frac{2}{\sqrt{AB}} a_m b_n e^{-c_{mn}|H+D|} \quad (66)$$

$$\gamma_{mn5} = \frac{-2 \operatorname{sgn}(H+D)}{\sqrt{AB}} b_n c_{mn} e^{-c_{mn}|H+D|} \quad (67)$$

$$\gamma_{mn6} = \frac{-2 \operatorname{sgn}(H+D)}{\sqrt{AB}} a_m c_{mn} e^{-c_{mn}|H+D|} \quad (68)$$

## A.8 Interpolation Grid

The signal estimates are available at any altitude  $h$ . The estimates of the Karhunen-Loève coefficients  $\hat{\alpha}_{mn}$ , are on the measurement grid  $K \times L$ . For the signal estimates, a finer interpolated grid can be used that is defined by

$$(P+1)\Sigma X = A \quad \Sigma X \leq \Delta X \quad (69)$$

$$(Q+1)\Sigma Y = B \quad \Sigma Y \leq \Delta Y \quad (70)$$

## A.9 Signal Estimates

Disturbance Potential Estimate:

$$\begin{matrix} [\hat{T}] = [S\Sigma X]([\hat{\alpha}_{mn}] \otimes [\theta_{mn1}])[S\Sigma Y]^T \\ P \times Q \quad P \times K \quad K \times L \quad K \times L \quad L \times Q \end{matrix} \quad (71)$$

Gravity Vector Estimates:

$$\begin{matrix} \left[ \frac{\partial \hat{T}}{\partial x} \right] = [C\Sigma X]([\hat{\alpha}_{mn}] \otimes [\theta_{mn2}])[S\Sigma Y]^T \\ P \times Q \quad P \times K \quad K \times L \quad K \times L \quad L \times Q \end{matrix} \quad (72)$$

$$\begin{matrix} \left[ \frac{\partial \hat{T}}{\partial y} \right] = [S\Sigma X]([\hat{\alpha}_{mn}] \otimes [\theta_{mn3}])[C\Sigma Y]^T \\ P \times Q \quad P \times K \quad K \times L \quad K \times L \quad L \times Q \end{matrix} \quad (73)$$

$$\begin{matrix} \left[ \frac{\partial \hat{T}}{\partial z} \right] = [S\Sigma X]([\hat{\alpha}_{mn}] \otimes [\theta_{mn4}])[S\Sigma Y]^T \\ P \times Q \quad P \times K \quad K \times L \quad K \times L \quad L \times Q \end{matrix} \quad (74)$$

Gravity Gradient Estimates:

$$\begin{matrix} \left[ \frac{\partial^2 \hat{T}}{\partial x^2} \right] = [S\Sigma X]([\hat{\alpha}_{mn}] \otimes [\theta_{mn5}])[S\Sigma Y]^T \\ P \times Q \quad P \times K \quad K \times L \quad K \times L \quad L \times Q \end{matrix} \quad (75)$$

$$\begin{matrix} \left[ \frac{\partial^2 \hat{T}}{\partial y^2} \right] = [S\Sigma X]([\hat{\alpha}_{mn}] \otimes [\theta_{mn6}])[S\Sigma Y]^T \\ P \times Q \quad P \times K \quad K \times L \quad K \times L \quad L \times Q \end{matrix} \quad (76)$$

$$\begin{matrix} \left[ \frac{\partial^2 \hat{T}}{\partial z^2} \right] = [S\Sigma X]([\hat{\alpha}_{mn}] \otimes [\theta_{mn7}])[S\Sigma Y]^T \\ P \times Q \quad P \times K \quad K \times L \quad K \times L \quad L \times Q \end{matrix} \quad (77)$$

$$\begin{matrix} \left[ \frac{\partial^2 \hat{T}}{\partial x \partial y} \right] = [C\Sigma X]([\hat{\alpha}_{mn}] \otimes [\theta_{mn8}])[C\Sigma Y]^T \\ P \times Q \quad P \times K \quad K \times L \quad K \times L \quad L \times Q \end{matrix} \quad (78)$$

$$\left[ \frac{\widehat{\partial^2 T}}{\partial y \partial z} \right] = \underset{P \times Q}{[S \Sigma X]} \left( \underset{P \times K}{[\widehat{\alpha}_{mn}] \otimes \underset{K \times L}{[\theta_{mn9}]} \right) \underset{L \times Q}{[C \Sigma Y]}^T \quad (79)$$

$$\left[ \frac{\widehat{\partial^2 T}}{\partial z \partial x} \right] = \underset{P \times Q}{[C \Sigma X]} \left( \underset{P \times K}{[\widehat{\alpha}_{mn}] \otimes \underset{K \times L}{[\theta_{mn10}]} \right) \underset{L \times Q}{[S \Sigma Y]}^T \quad (80)$$

where  $\otimes$  has been defined earlier as point-by-point matrix multiplication and

$$[S \Sigma X(i, j)] = \sin \pi(i \times j) \frac{\Sigma X}{A} \quad \begin{array}{l} 1 \leq i \leq P \\ 1 \leq j \leq K \end{array} \quad (81)$$

$$[S \Sigma Y(i, j)]^T = \sin \pi(i \times j) \frac{\Sigma Y}{B} \quad \begin{array}{l} 1 \leq i \leq L \\ 1 \leq j \leq Q \end{array} \quad (82)$$

$$[C \Sigma X(i, j)] = \cos \pi(i \times j) \frac{\Sigma X}{A} \quad \begin{array}{l} 1 \leq i \leq P \\ 1 \leq j \leq K \end{array} \quad (83)$$

$$[C \Sigma Y(i, j)]^T = \cos \pi(i \times j) \frac{\Sigma Y}{B} \quad \begin{array}{l} 1 \leq i \leq L \\ 1 \leq j \leq Q \end{array} \quad (84)$$

and,

$$\theta_{mn1} = \frac{2}{\sqrt{AB}} e^{-c_{mn}|h+D|} \quad (85)$$

$$\theta_{mn2} = \frac{2}{\sqrt{AB}} a_m e^{-c_{mn}|h+D|} \quad (86)$$

$$\theta_{mn3} = \frac{2}{\sqrt{AB}} b_n e^{-c_{mn}|h+D|} \quad (87)$$

$$\theta_{mn4} = \frac{-2 \operatorname{sgn}(h+D)}{\sqrt{AB}} c_{mn} e^{-c_{mn}|h+D|} \quad (88)$$

$$\theta_{mn5} = \frac{-2}{\sqrt{AB}} a_m^2 e^{-c_{mn}|h+D|} \quad (89)$$

$$\theta_{mn6} = \frac{-2}{\sqrt{AB}} b_n^2 e^{-c_{mn}|h+D|} \quad (90)$$

$$\theta_{mn7} = \frac{2}{\sqrt{AB}} c_{mn}^2 e^{-c_{mn}|h+D|} \quad (91)$$

$$\theta_{mn8} = \frac{2}{\sqrt{AB}} a_m b_n e^{-c_{mn}|h+D|} \quad (92)$$

$$\theta_{mn9} = \frac{-2 \operatorname{sgn}(h+D)}{\sqrt{AB}} b_n c_{mn} e^{-c_{mn}|h+D|} \quad (93)$$

$$\theta_{mn10} = \frac{-2 \operatorname{sgn}(h+D)}{\sqrt{AB}} a_m c_{mn} e^{-c_{mn}|h+D|} \quad (94)$$

$$(95)$$

## B Software Implementation

### B.1 Estimator Module

The two software modules KLE (Karhunen-Loève estimator) and SYN (synthesizer) form the two stages of the estimation process. The estimator equations of the previous section have been modified in form only, not in substance, and adapted for programming.

In the first stage of the estimator, KLE, the  $i$ th measurement field is sampled on the rectangular grid. It is transformed on the left and right by the sine and/or cosine matrix given by

$$2 \sin \frac{\pi kl}{K+1}, \quad k, l = 1, \dots, K \quad (96)$$

or

$$2 \cos \frac{\pi kl}{K+1}, \quad k, l = 1, \dots, K \quad (97)$$

or

$$2 \sin \frac{\pi kl}{L+1}, \quad k, l = 1, \dots, L \quad (98)$$

or

$$2 \cos \frac{\pi kl}{L+1}, \quad k, l = 1, \dots, L \quad (99)$$

depending upon the matrix type as given in table 7 and the number of grid samples in the

Table 7: Signal dependent functions

$i$ th signal	$\gamma_{kli}$	left	right
$T$	2	sine	sine
$T_x$	$2a_k$	cosine	sine
$T_y$	$2b_l$	sine	cosine
$T_z$	$-2c_{kl}$	sine	sine
$T_{xx}$	$-2a_k^2$	sine	sine
$T_{yy}$	$-2b_l^2$	sine	sine
$T_{zz}$	$2c_{kl}^2$	sine	sine
$T_{xy}$	$2a_k b_l$	cosine	cosine
$T_{yz}$	$-2b_l c_{kl}$	sine	cosine
$T_{xz}$	$-2a_k c_{kl}$	cosine	sine

interior of the survey region,  $K$  in the  $x$  direction and  $L$  in the  $y$  direction. The multiplier of 2 is for compatibility with the FST and FCT functions in the Swarztrauber FFT software

package FFTPACK. If the table entry is "cosine", then the cosine transform is followed by an application of the matrix

$$\delta_{ij} + 2|i - j + 1|_2, \quad i, j = 1, \dots, K \quad (100)$$

or

$$\delta_{ij} + 2|i - j + 1|_2, \quad i, j = 1, \dots, L \quad (101)$$

Note that  $|k|_2$  denotes  $k$  modulo 2, i.e. 1 for  $k$  odd and 0 for  $k$  even and  $\delta$  is the Kronecker delta. The transformed  $i$ th measurement field is denoted by  $z_{kli}$ .

The following equations combine the transformed measurement fields to yield the K-L coefficients  $\alpha_{kl}$ .

$$c_{kl} = \sqrt{a_k^2 + b_l^2}, \quad a_k = \pi k/A, \quad b_l = \pi l/B \quad (102)$$

$$t_{kl} = \exp(-c_{kl} \cdot (h + D)) \sqrt{AB} \quad (103)$$

$$\lambda_{kl} = \sigma_0^2 / c_{kl}^{2k_0} \quad (104)$$

$$\beta_{kli} = \frac{\lambda_{kl} \cdot (t_{kl} \gamma_{kli})}{\sigma_i^2 \left[ 1 + \frac{AB}{4} \lambda_{kl} \sum_j (t_{kl} \gamma_{klj})^2 / \sigma_j^2 \right]} \quad (105)$$

$$\alpha_{kl} = \frac{AB/4}{(K+1)(L+1)} \sum_i \beta_{kli} z_{kli} \quad (106)$$

The main computational loop in the program increments the index  $i$  so that measurements are processed sequentially. Only the selected measurements are processed. The K-L coefficient field  $\alpha_{kl}$  is stored in a disk file.

## B.2 Synthesizer Module

The SYN module reads the K-L coefficient field  $\alpha_{kl}$ , recomputes  $t_{kl}$  and  $\gamma_{kli}$  and computes the field

$$z'_{kli} = t_{kl} \gamma_{kli} \alpha_{kl} / 4 \quad (107)$$

where now  $i$  represents the quantity to be estimated. The  $z'_{kli}$  matrix for the given  $i$  is then multiplied on the left and right by the appropriate sine and/or cosine matrix to produce the estimate of the  $i$ th signal.

## B.3 Matrix Formulation

It is useful to look at the computational process in high level matrix notation. In fact, the computations can be summarized in just two equations:

$$\hat{A} = \sum_i B_i \odot \{L'_i Z_i R'_i\} \quad (108)$$

and

$$\hat{Y}_i = L_i \{ \hat{A} \odot \Gamma_i \} R_i \quad (109)$$

In equation (108) the  $i$ th measurement field is transformed on the left and the right by  $L'_i$  and  $R'_i$  which are the sine or cosine matrix of Equations (96)-(99) multiplied by the matrix of Equations (100)-(101). This puts the measurement field into the K-L domain where it is multiplied by the weighting matrix  $B_i$ . The elements of  $B_i$ , which may be inferred from Equation (106) and its predecessors, are given by

$$[B_i]_{kl} = \frac{AB/4}{(K+1)(L+1)} \beta_{kli} \quad (110)$$

The " $\odot$ " product is simply the element by element product given by

$$A \odot B = C \Leftrightarrow a_{kl} b_{kl} \equiv c_{kl} \quad (111)$$

The summation over the measurement index  $i$  yields the field of K-L coefficients. In Equation (109) we obtain an estimate of the  $i$ th signal field. The K-L coefficient matrix is multiplied element by element by another weighting matrix  $\Gamma_i$ , which may be inferred from Equation (107) and its predecessors. Specifically, the elements of  $\Gamma_i$  are given by

$$[\Gamma_i]_{kl} = \frac{t_{kl} \gamma_{kli}}{4} \quad (112)$$

The result is left and right multiplied by  $L_i$  and  $R_i$ , respectively, each of which is either the sine or cosine matrix of Equations (96)-(99).

*It is the power of the Karhunen-Loève method that the estimation equations can be cast in such a simple form as Equations (108) and (109), in particular the fact that the elements of the K-L coefficient matrix are uncorrelated.*

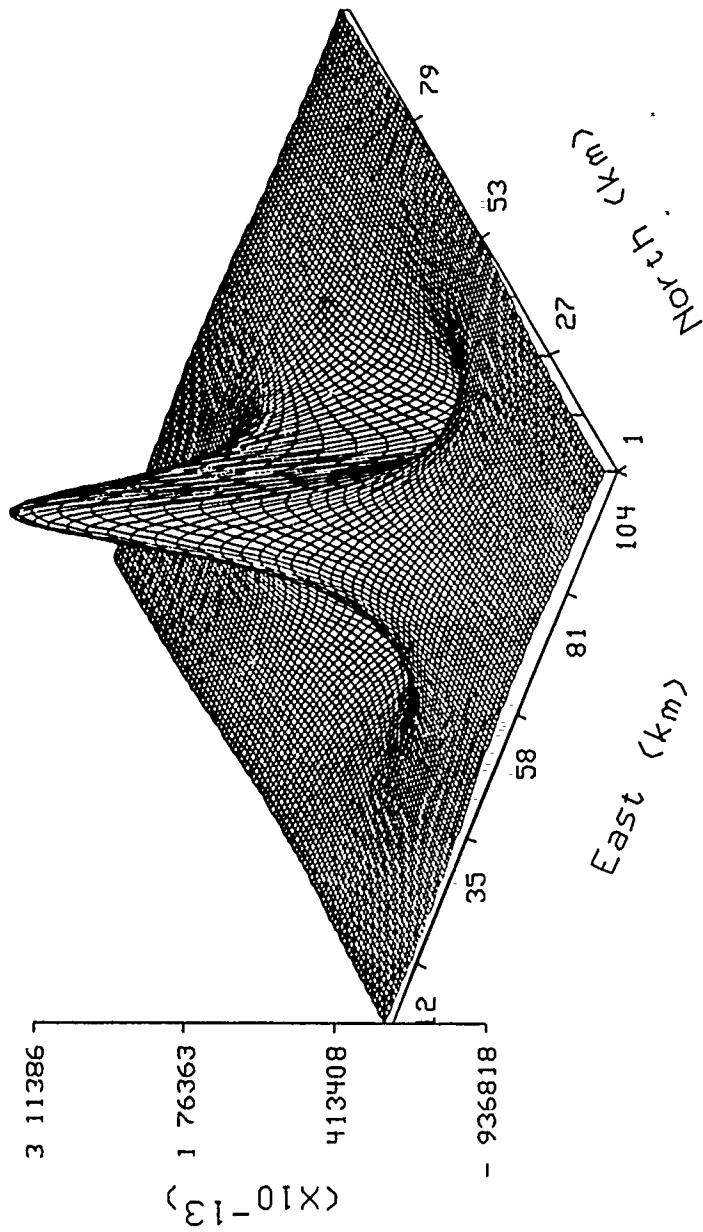
## C Bibliography

### References

- [1] Aho, A.V., B.W. Kernighan, and P.J. Weinberger, The AWK Programming Language, AT&T, 1988.
- [2] Bose, S.C., Gravity Gradiometer Survey System (GGSS) Post-Mission Data Processing, AFGL-TR-88-0008, ADA200739, August 1987.
- [3] NSWC, Informal description of content and format of the magnetic tape containing gravity gradient data and gravity truth, Naval Surface Weapons Center, 15 Feb. 1985.
- [4] White, J.V., A statistical gravity model for northern Texas, TASC TIM No. 4423-5, 19 Nov. 1984.

## D Plots

$T_x$  (m/sec/sec)

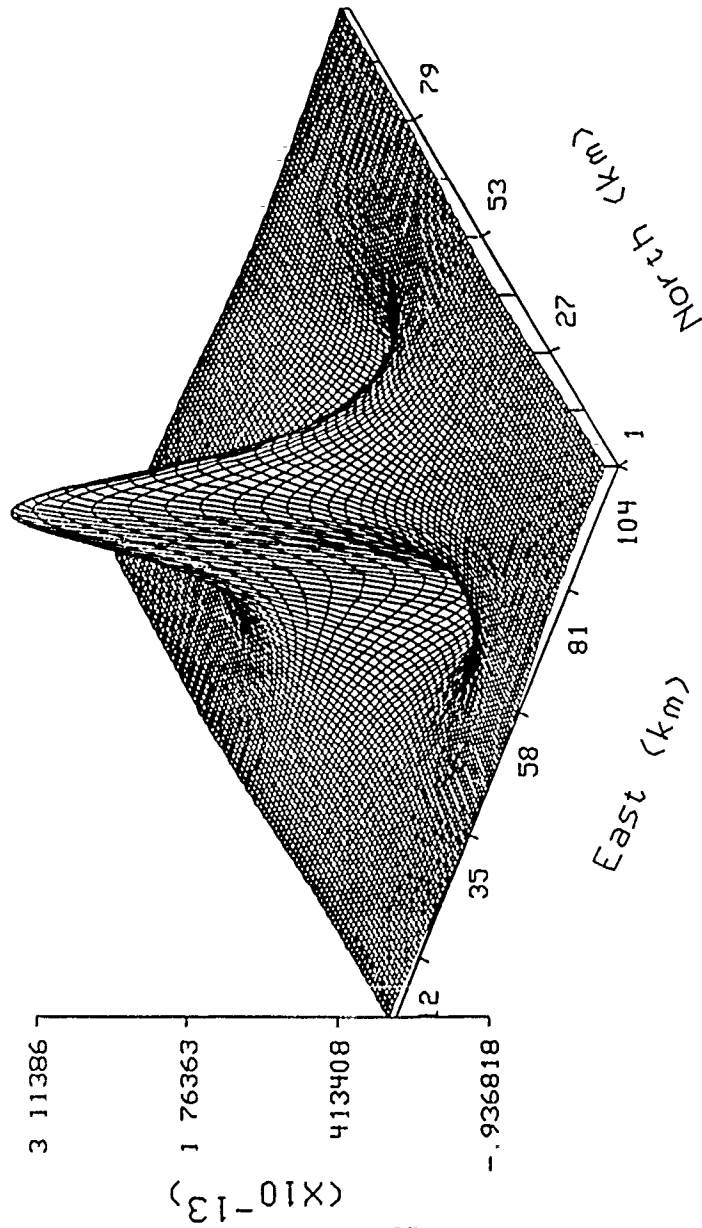


36

Single Dipole, truth at  $h=0$

Figure 10: True  $T_x$ , Single Dipole

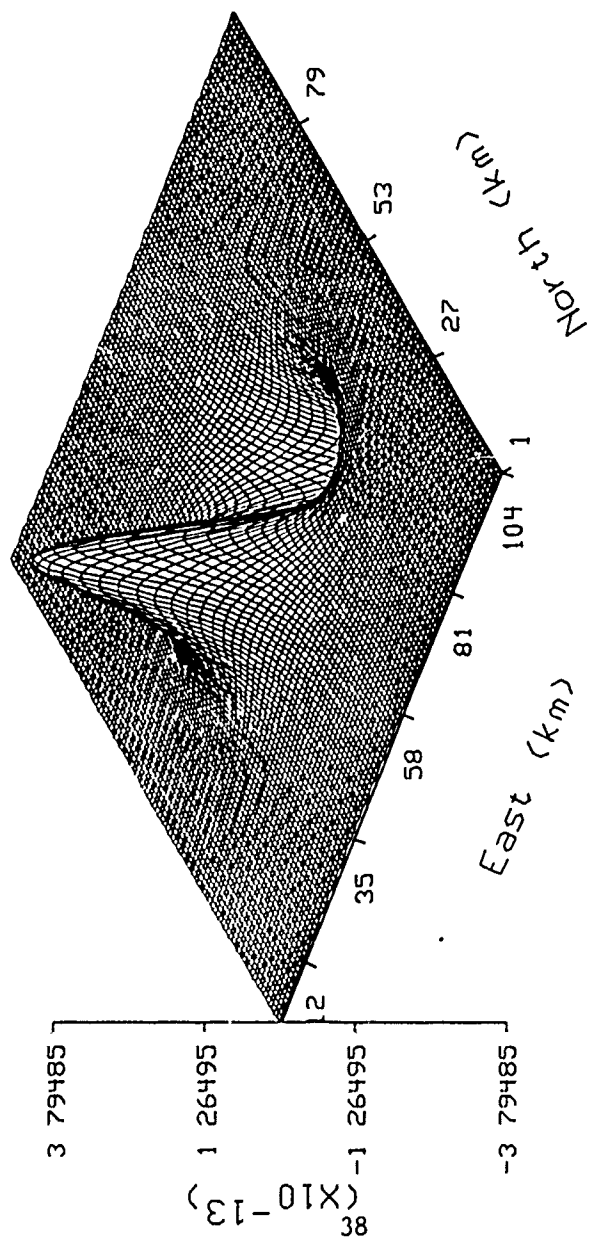
$T_y$  (m/sec/sec)



Single Dipole, truth at  $h=0$

Figure 11: True  $T_y$ , Single Dipole

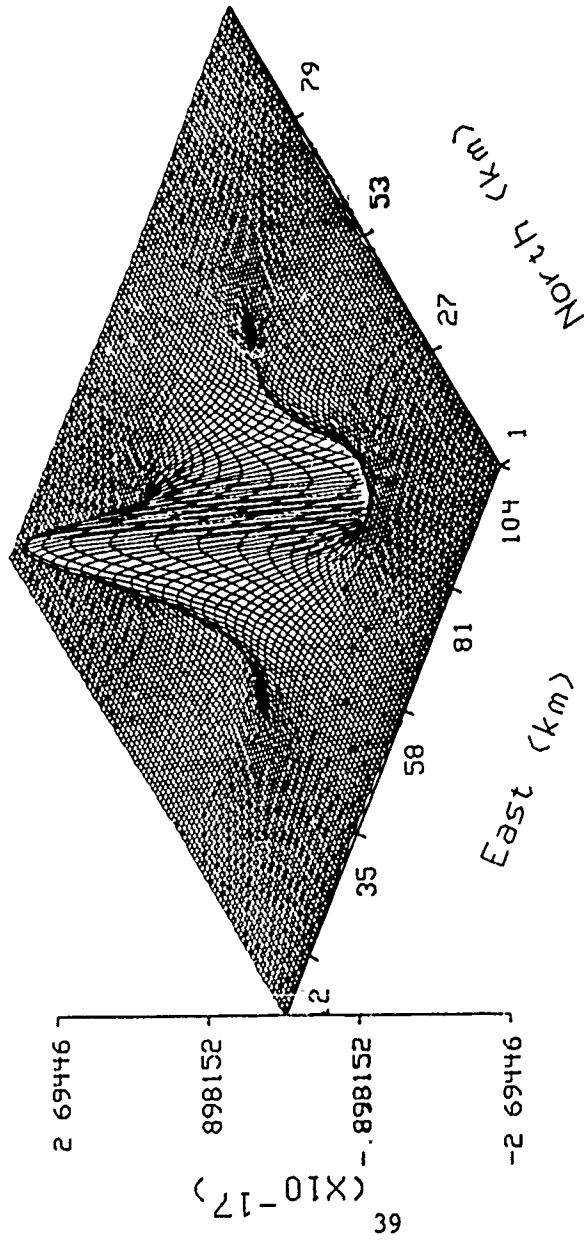
$T_z$  (m/sec/sec)



Single Dipole, truth at  $h=0$

Figure 12: True  $T_z$ , Single Dipole

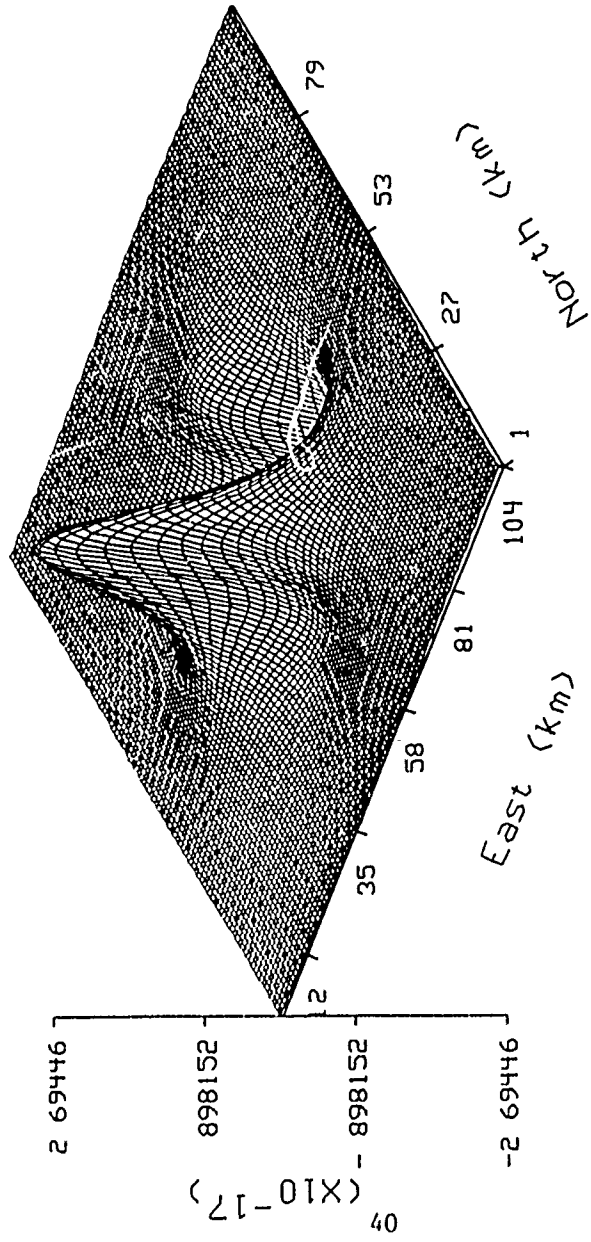
$T_{xx}$  (1/sec/sec)



Single Dipole, meas at  $h=2\text{km}$

Figure 13: Measured  $T_{xx}$ , Single Dipole

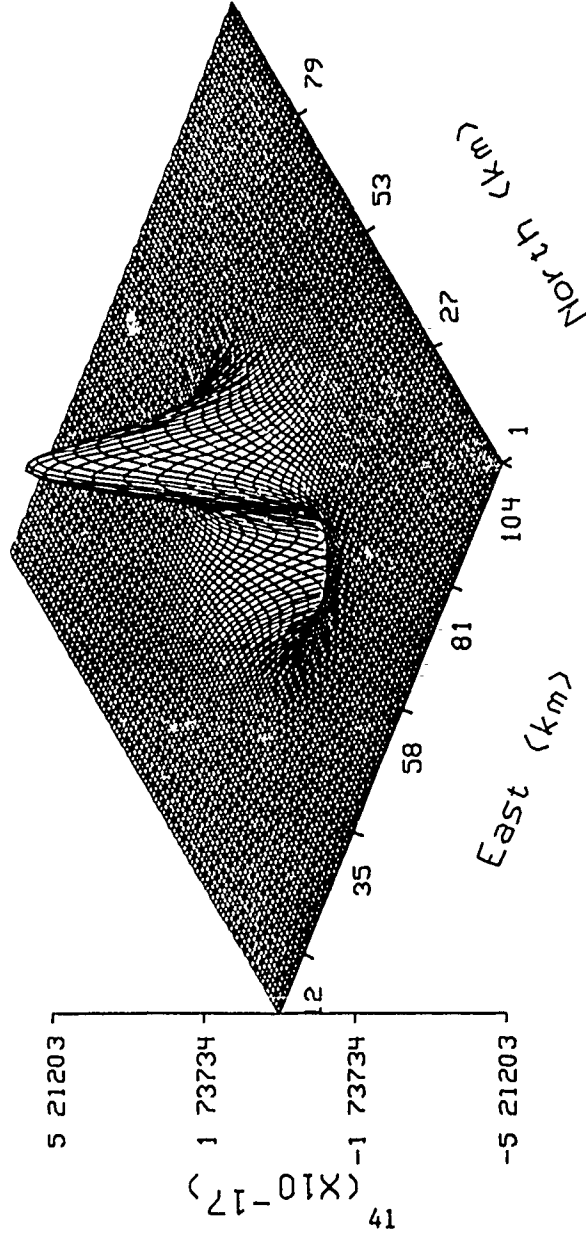
$T_{yy}$  (1/sec/sec)



Single Dipole, meas at  $h=2\text{km}$

Figure 14: Measured  $T_{yy}$ , Single Dipole

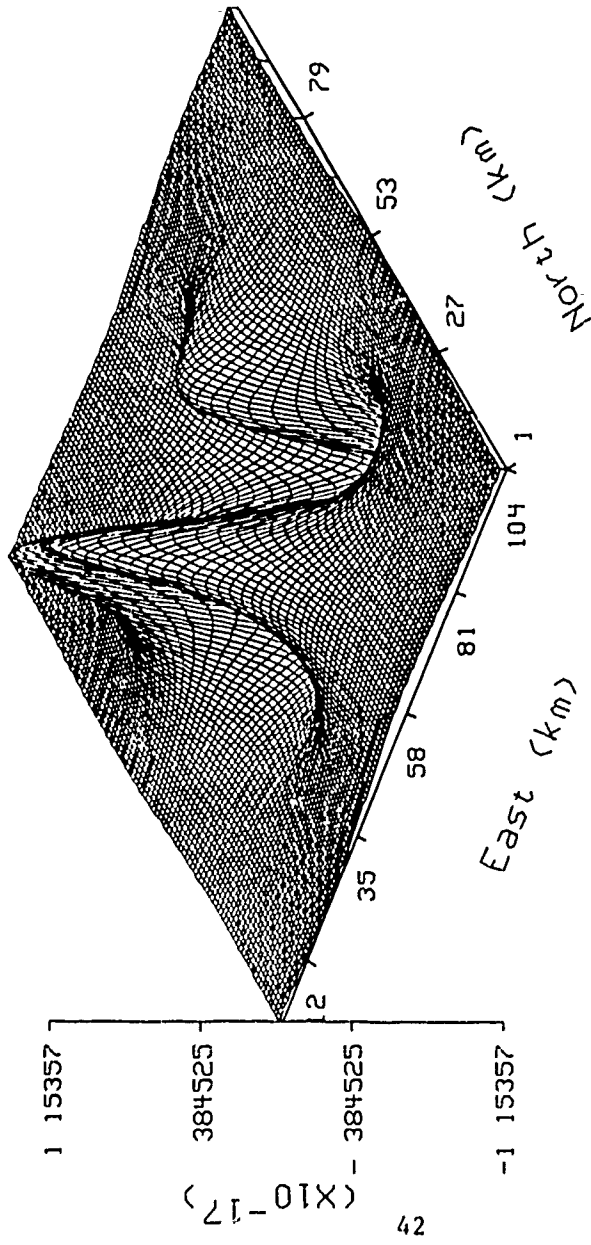
$T_{zz}$  (1/sec/sec)



Single Dipole, meas at  $h=2\text{km}$

Figure 15: Measured  $T_{zz}$ , Single Dipole

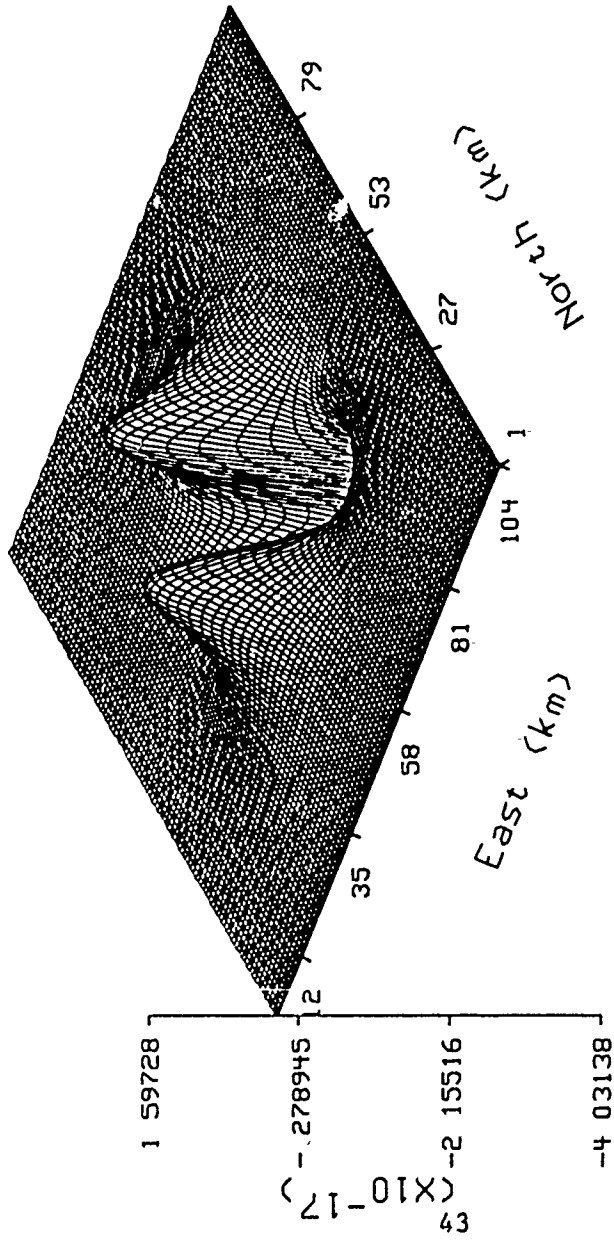
$T_{xy}$  (1/sec/sec)



Single Dipole, meas at  $h=2\text{km}$

Figure 16: Measured  $T_{xy}$ , Single Dipole

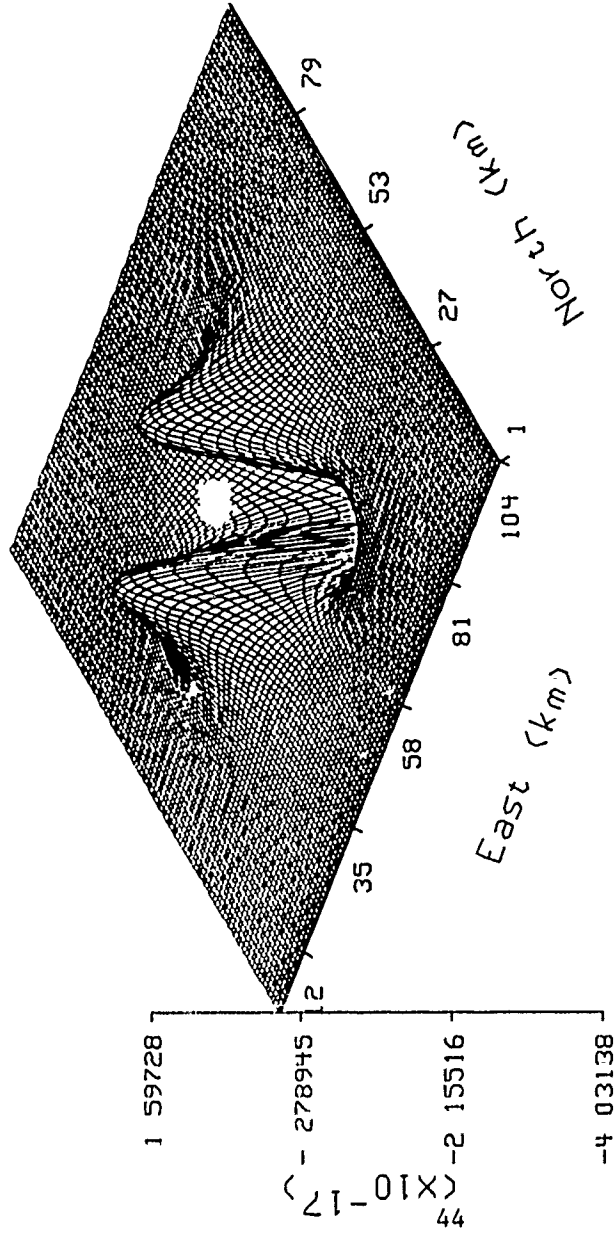
$T_{yz}$  (1/sec/sec)



Single Dipole, meas at  $h=2\text{km}$

Figure 17: Measured  $T_{yz}$ , Single Dipole

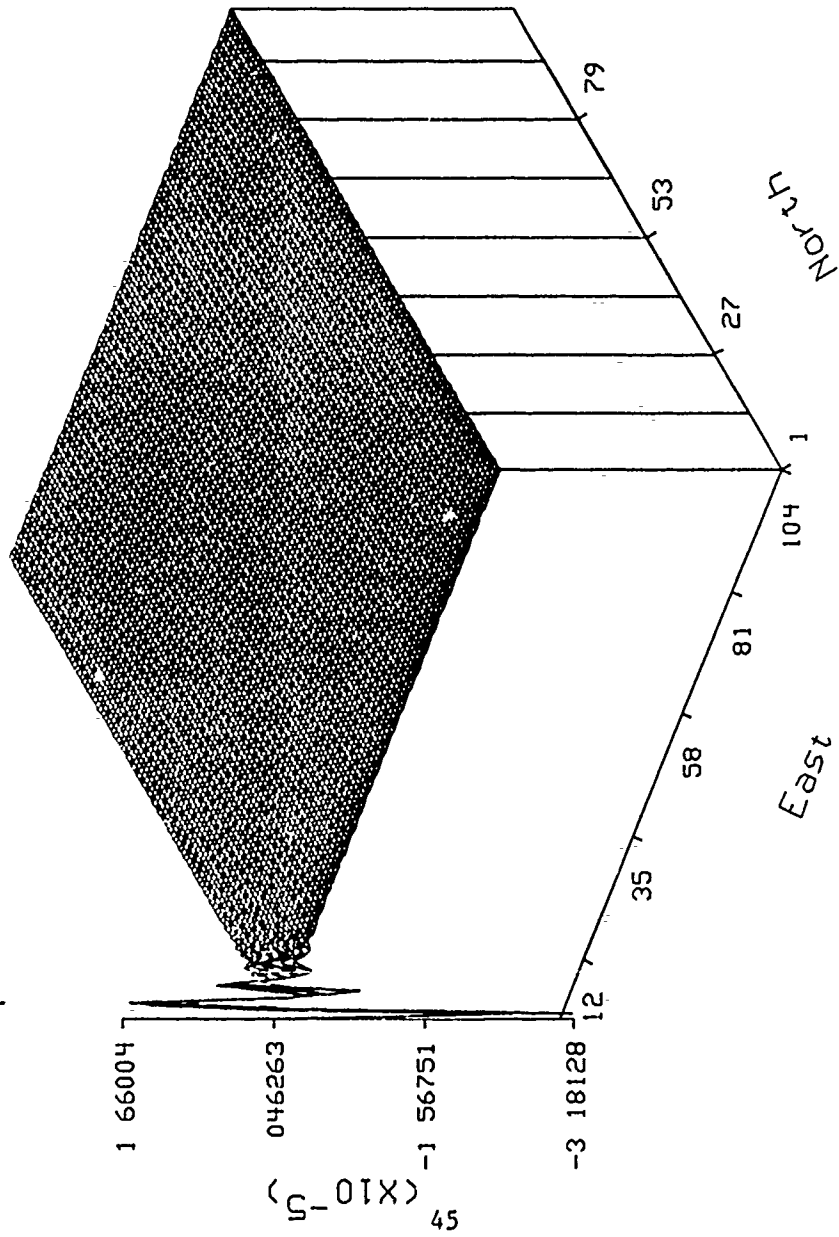
$T_{xz}$  (1/sec/sec)



Single Dipole, meas at  $h=2$ km

Figure 18: Measured  $T_{xz}$ , Single Dipole

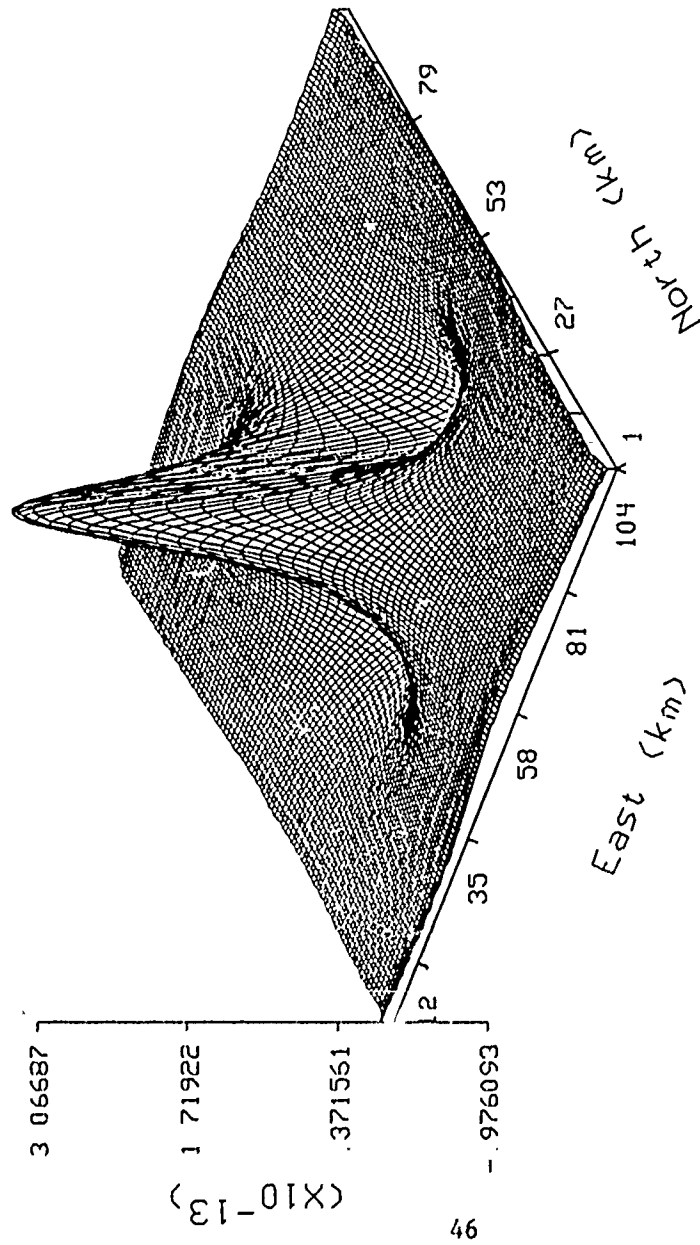
alpha hat



Single Dipole, meas  $T_{xx}$ , at  $h=2\text{km}$

Figure 19:  $\hat{\alpha}$  given  $T_{xx}$ , Single Dipole

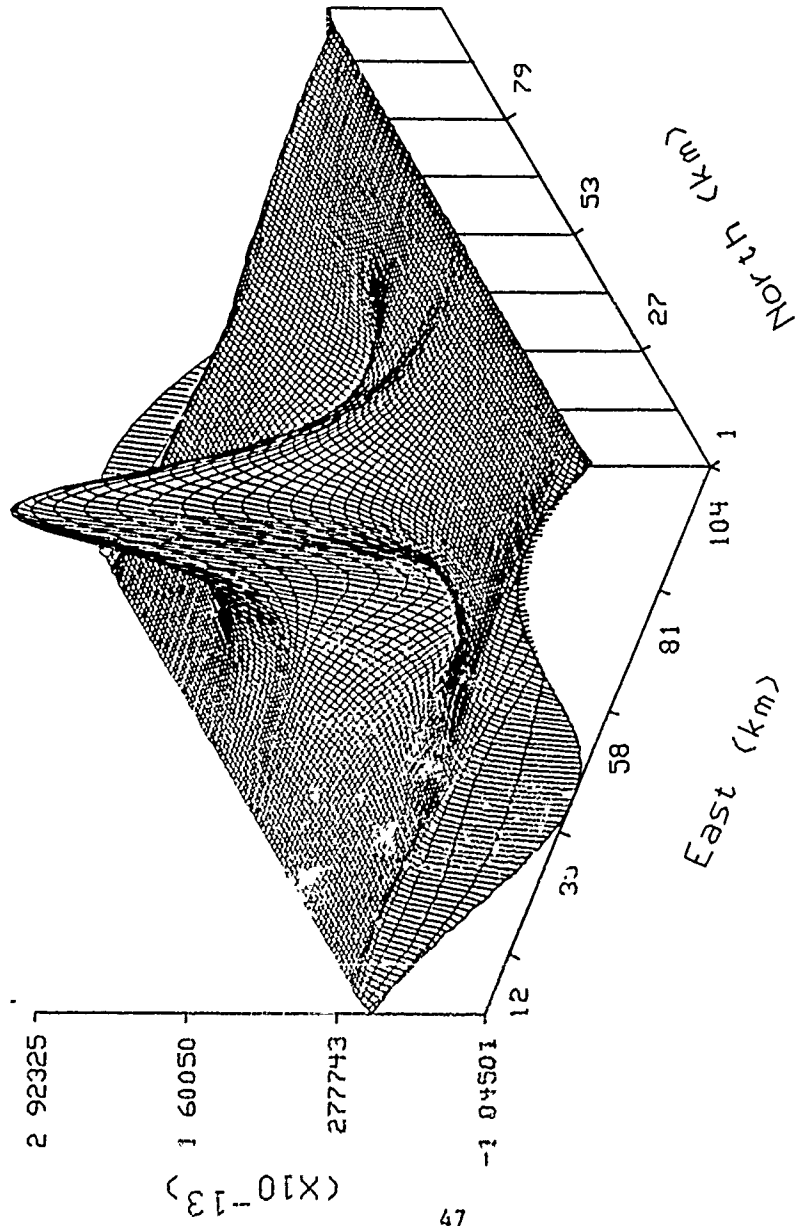
$\hat{T}_x$  (m/sec/sec)



Single Dipole, meas  $T_{xx}$  at  $h=2\text{km}$ , est  $h=0$

Figure 20:  $\hat{T}_z$  given  $T_{xx}$ , Single Dipole

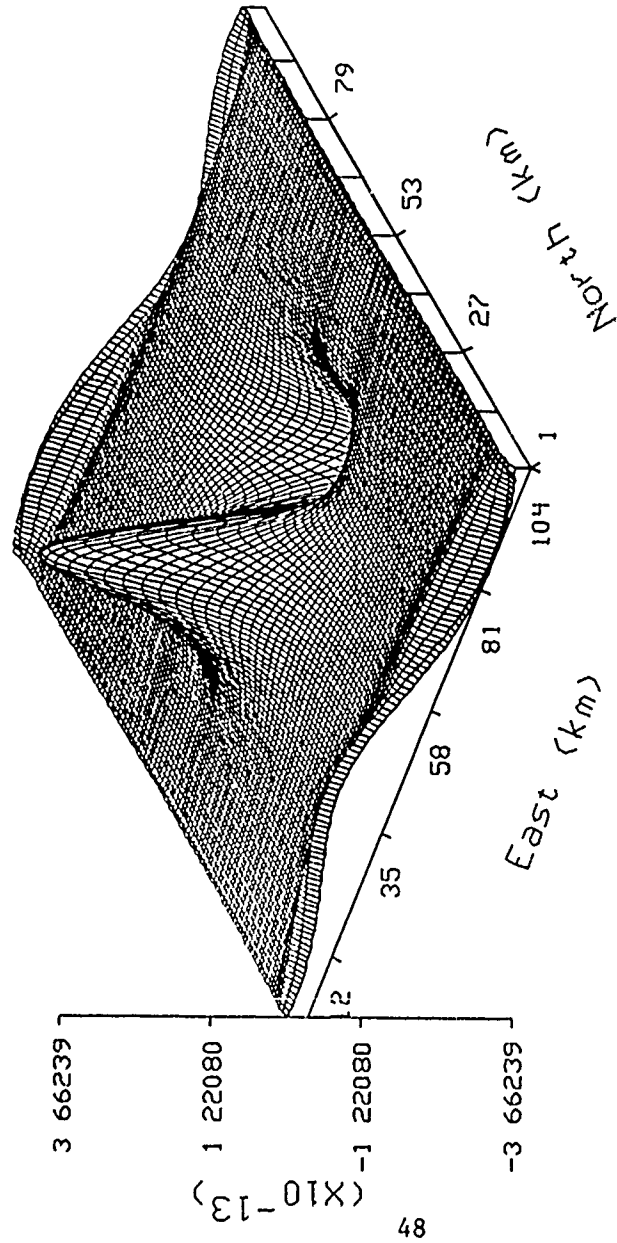
$\hat{T}_y$  (m/sec/sec)



Single Dipole, meas  $T_{xx}$  at  $h=2\text{km}$ , est  $h=0$

Figure21:  $\hat{T}_y$  given  $T_{xx}$ , Single Dipole

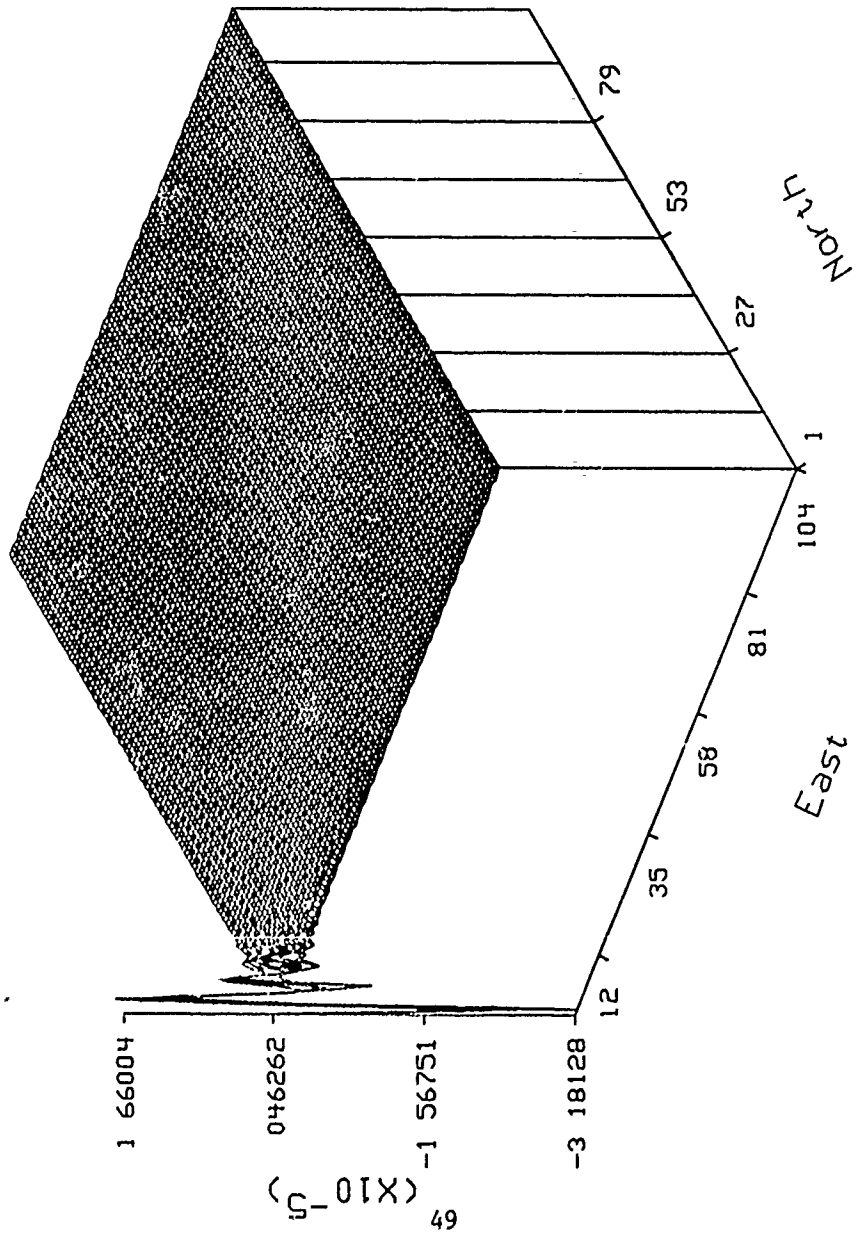
$\hat{T}_z$  (m/sec/sec)



Single Dipole, meas  $T_{xx}$  at  $h=2\text{km}$ , est  $h=0$

Figure22:  $\hat{T}_z$  given  $T_{xx}$ , Single Dipole

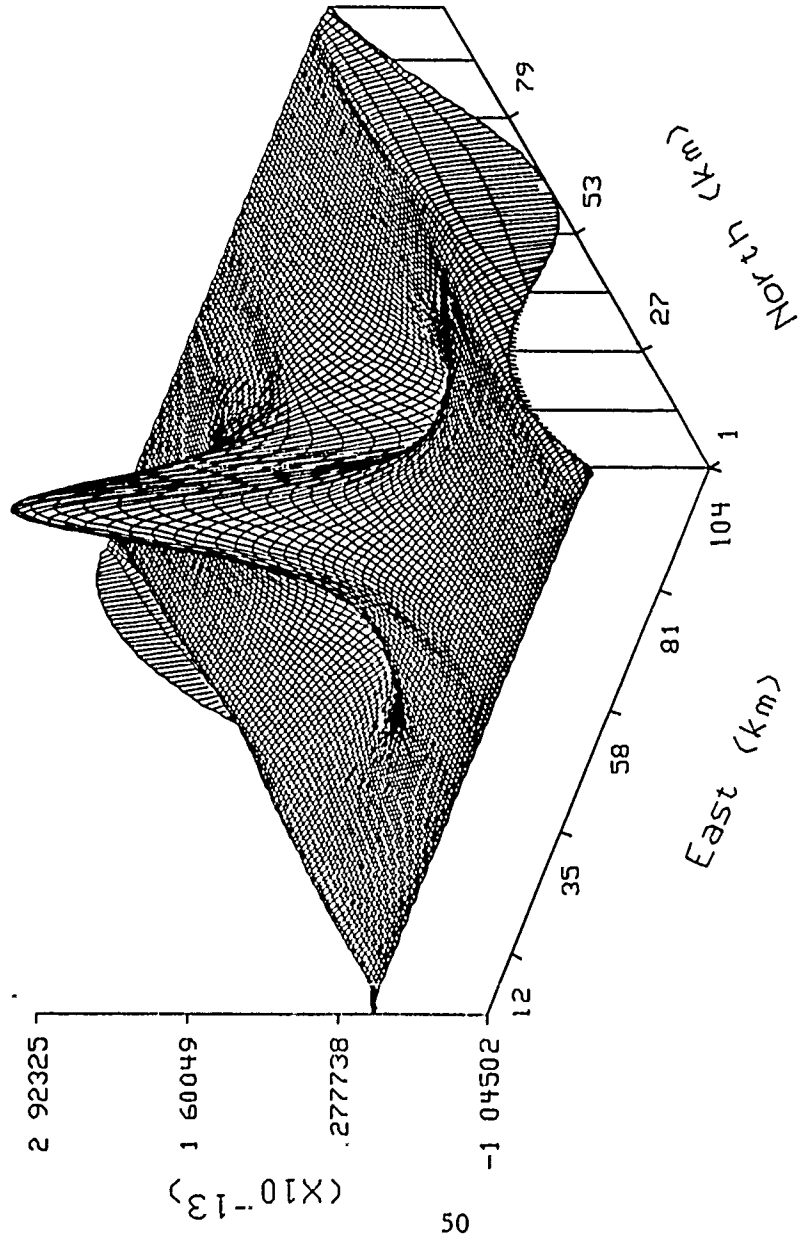
alpha hat



Single Dipole, meas  $T_{yy}$  at  $h=2\text{km}$

Figure23:  $\hat{\alpha}$  given  $T_{yy}$ , Single Dipole

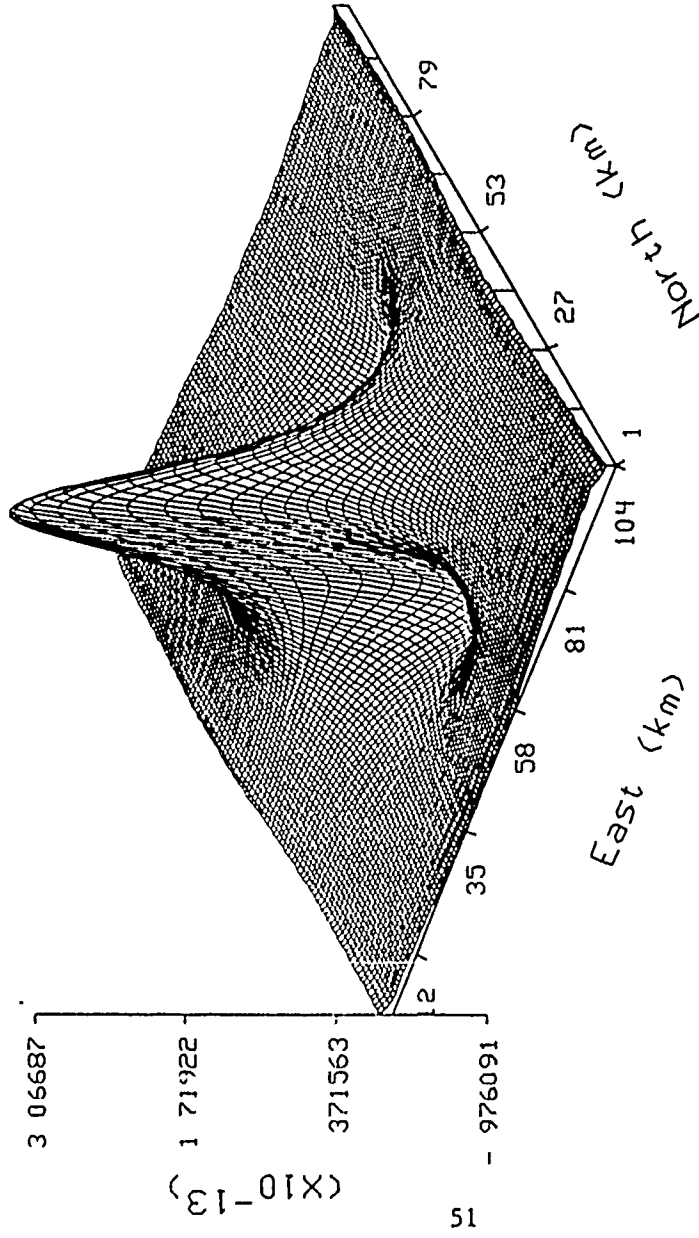
$\hat{T}_x$  (m/sec/sec)



Single Dipole, meas  $T_{yy}$  at  $h=2\text{km}$ , est  $h=0$

Figure24:  $\hat{T}_z$  given  $T_{yy}$ , Single Dipole

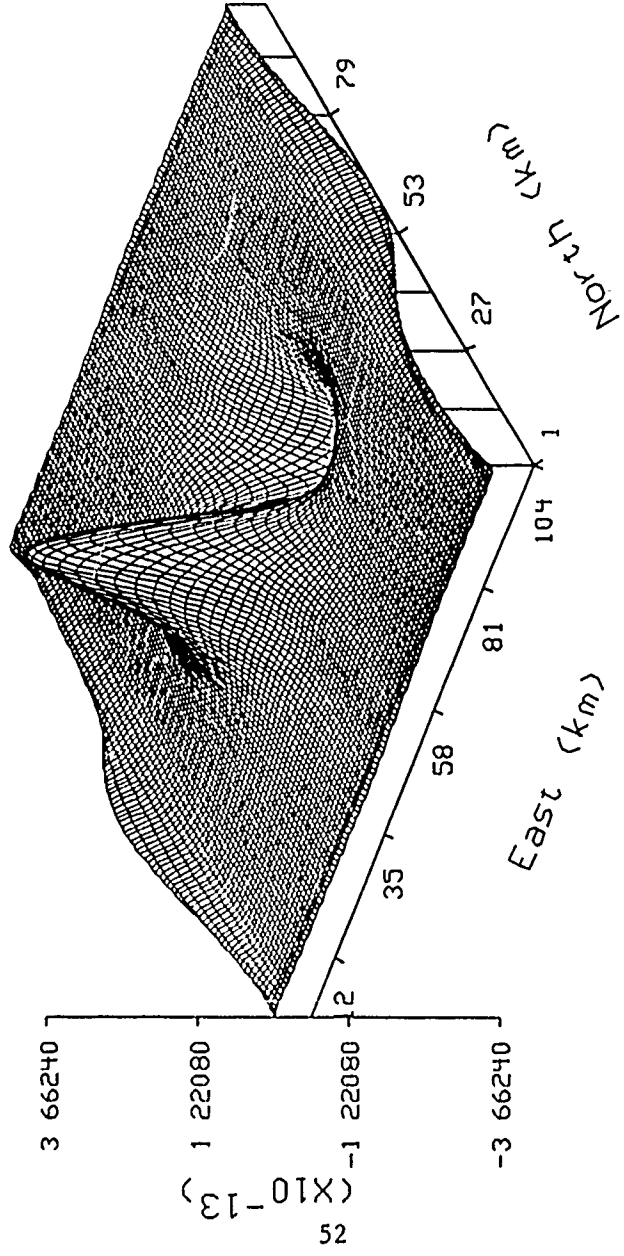
$\hat{T}_y$  (m/sec/sec)



Single Dipole. meas  $T_{yy}$  at  $h=2\text{km}$ , est  $h=0$

Figure 25:  $\hat{T}_y$  given  $T_{yy}$ , Single Dipole

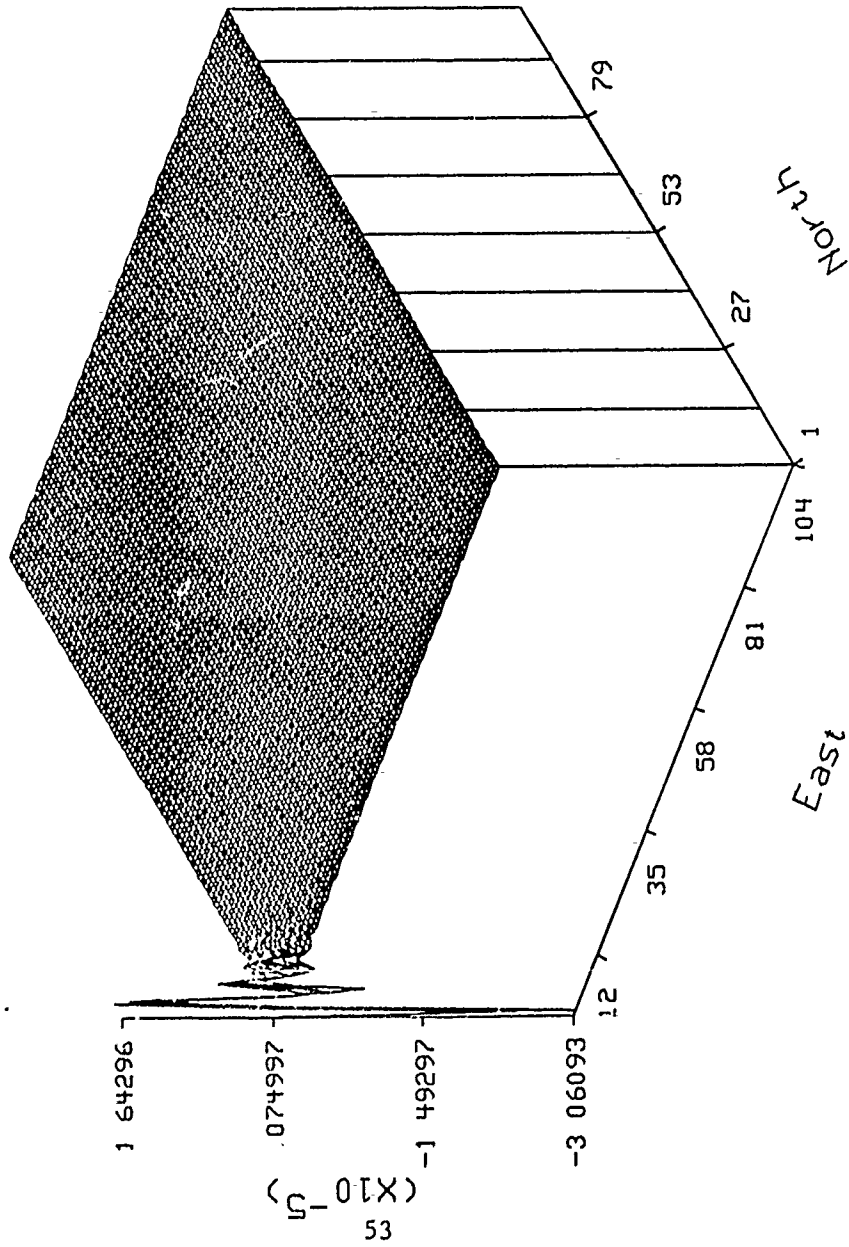
$\hat{T}_z$  (m/sec/sec)



Single Dipole, meas  $T_{yy}$  at  $h=2\text{km}$ , est  $h=0$

Figure26:  $\hat{T}_z$  given  $T_{yy}$ , Single Dipole

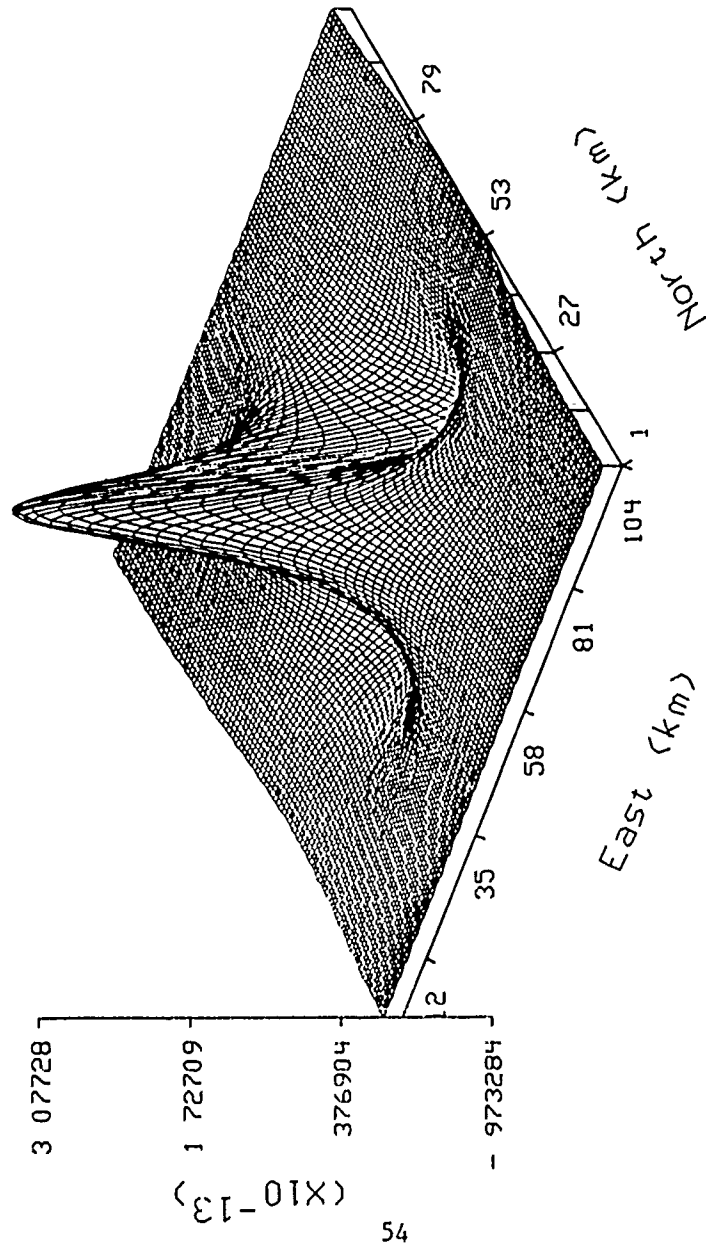
alpha hat



Single Dipole, meas  $T_{zz}$  at  $h=2$ km

Figure27:  $\hat{\alpha}$  given  $T_{zz}$ , Single Dipole

$\hat{T}_z$  (m/sec/sec)

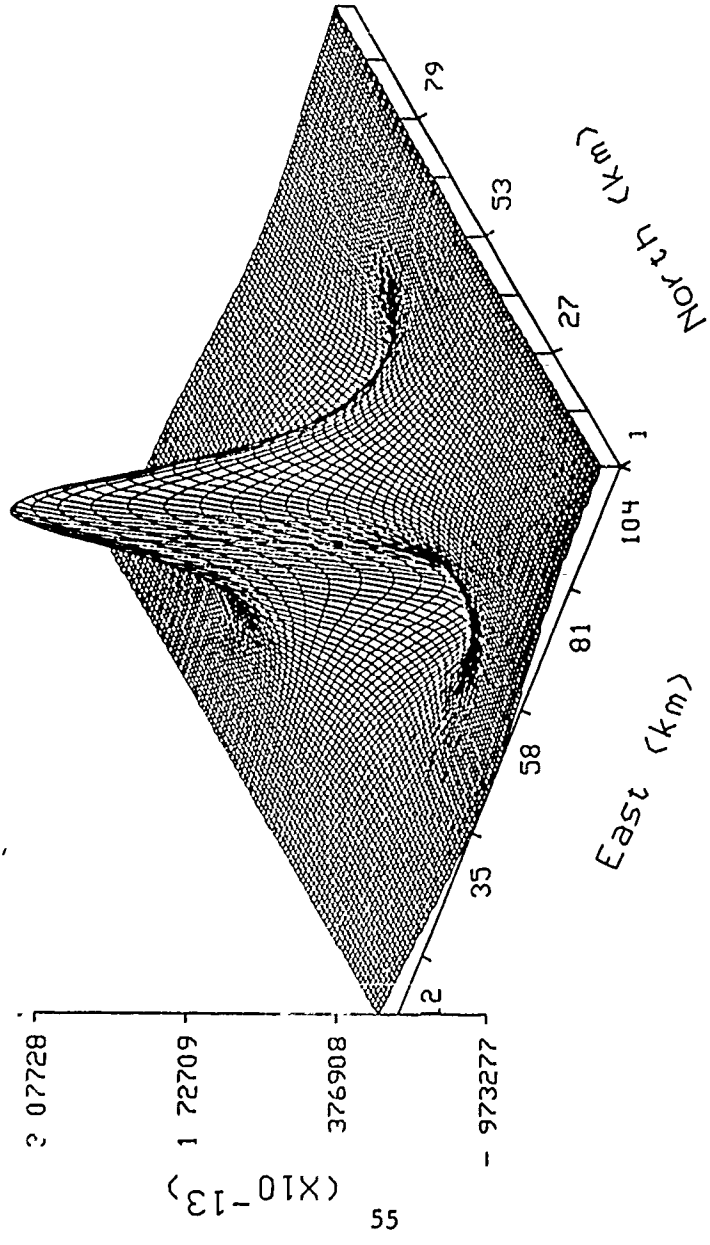


54

Single Dipole, meas  $T_{zz}$  at  $h=2\text{km}$ , est  $h=0$

Figure 28:  $\hat{T}_z$  given  $T_{zz}$ , Single Dipole

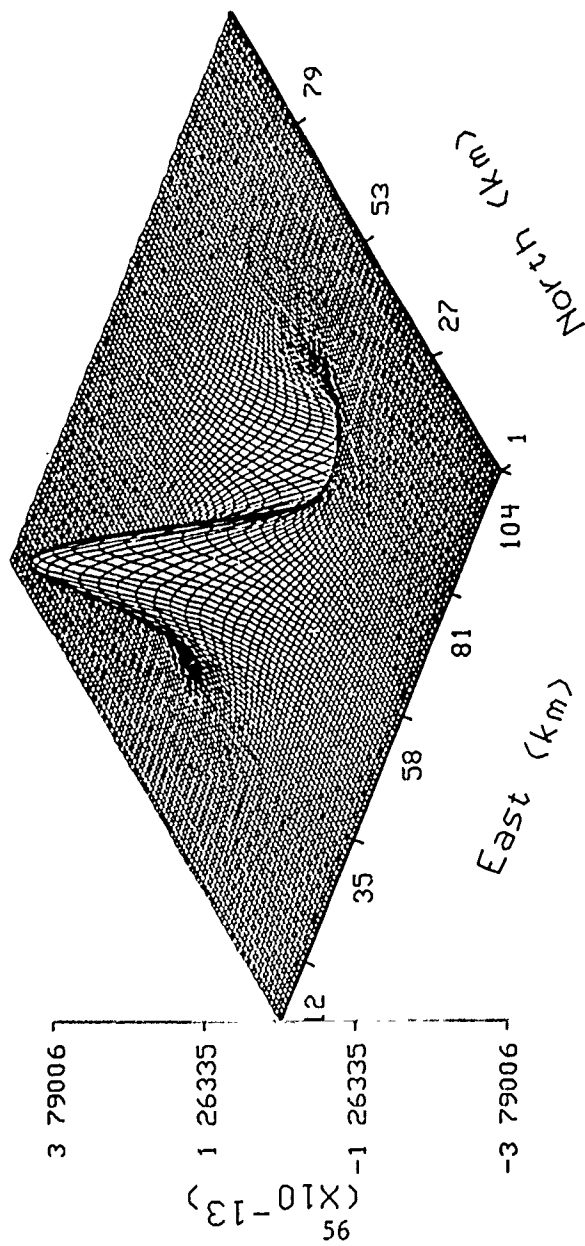
Ty hat (m/sec/sec)



Single Dipole, meas  $T_{zz}$  at  $h=2\text{km}$ , est  $h=0$

Figure 29:  $\hat{T}_y$  given  $T_{zz}$ , Single Dipole

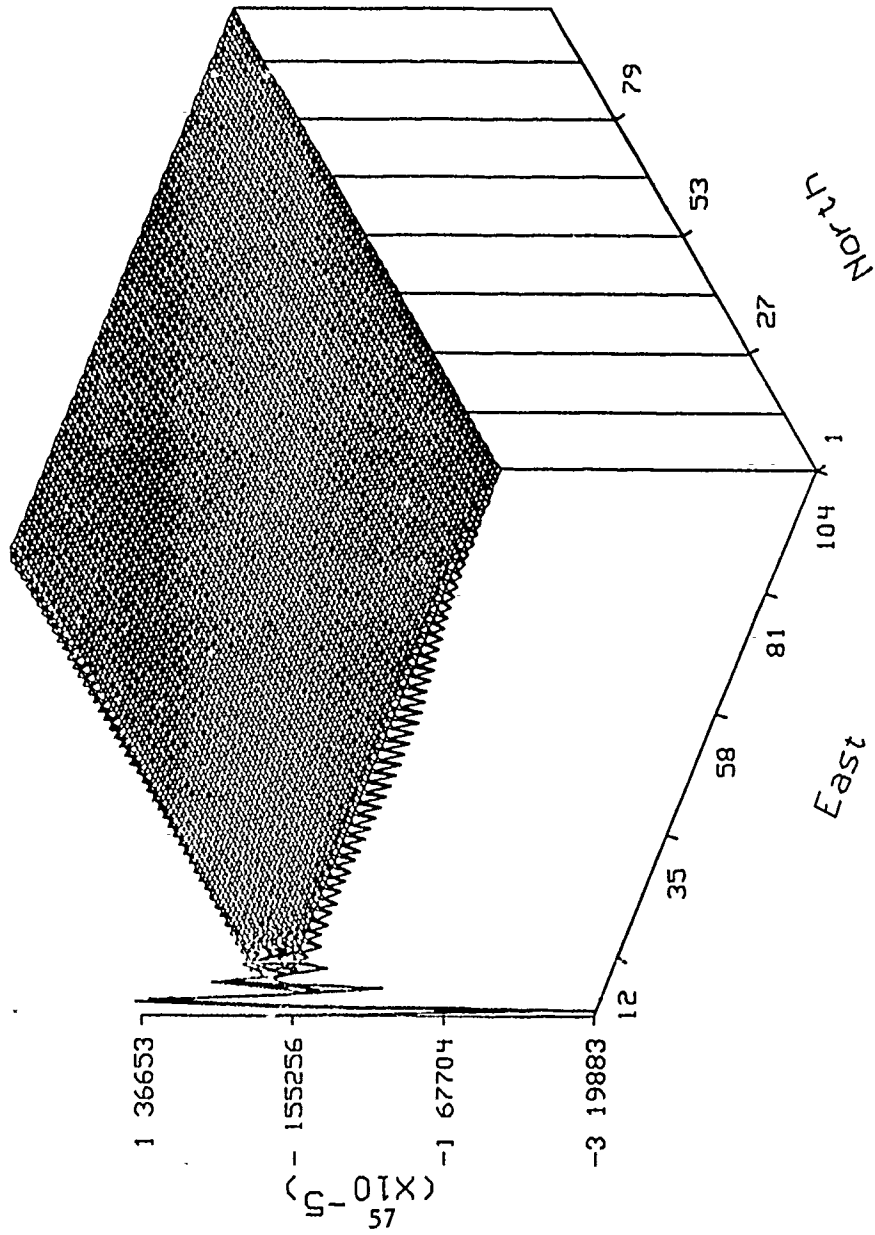
$\hat{T}_z$  (m/sec/sec)



Single Dipole, meas  $T_{zz}$  at  $h=2\text{km}$ , est  $h=0$

Figure30:  $\hat{T}_z$  given  $T_{zz}$ , Single Dipole

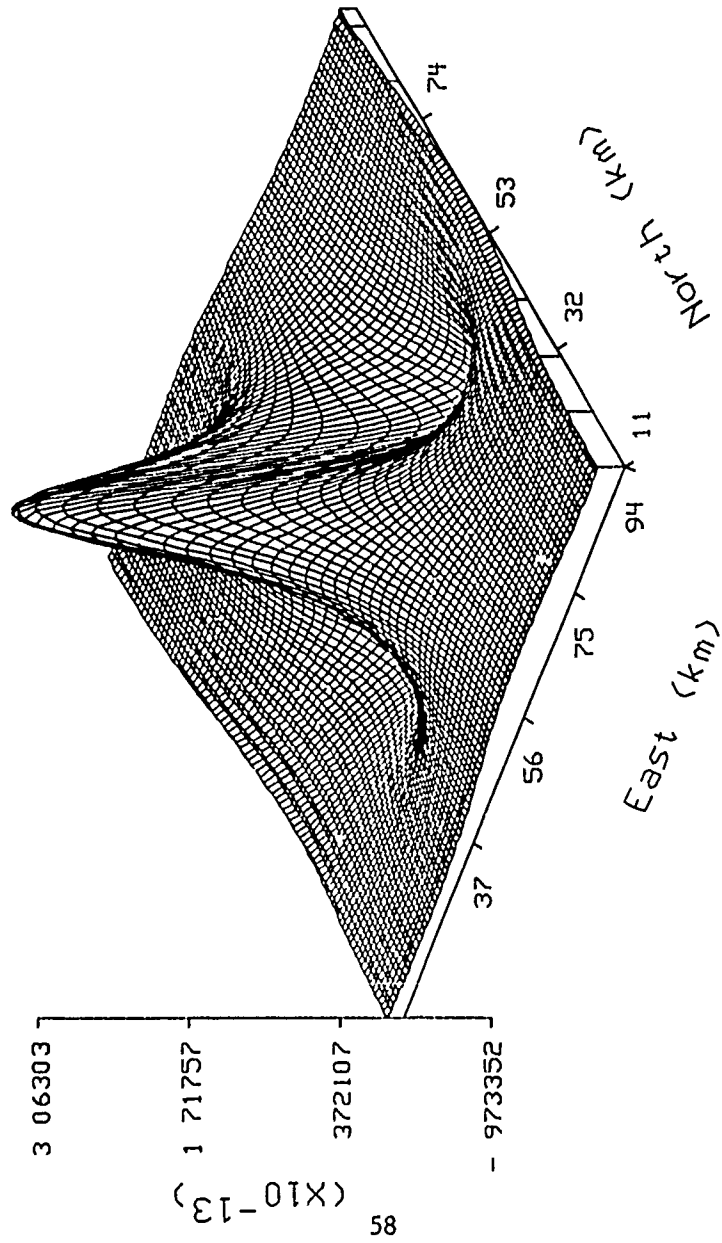
alpha hat



Single Dipole, meas  $T_{xy}$  at  $h=2\text{km}$

Figure31:  $\hat{\alpha}$  given  $T_{xy}$ , Single Dipole

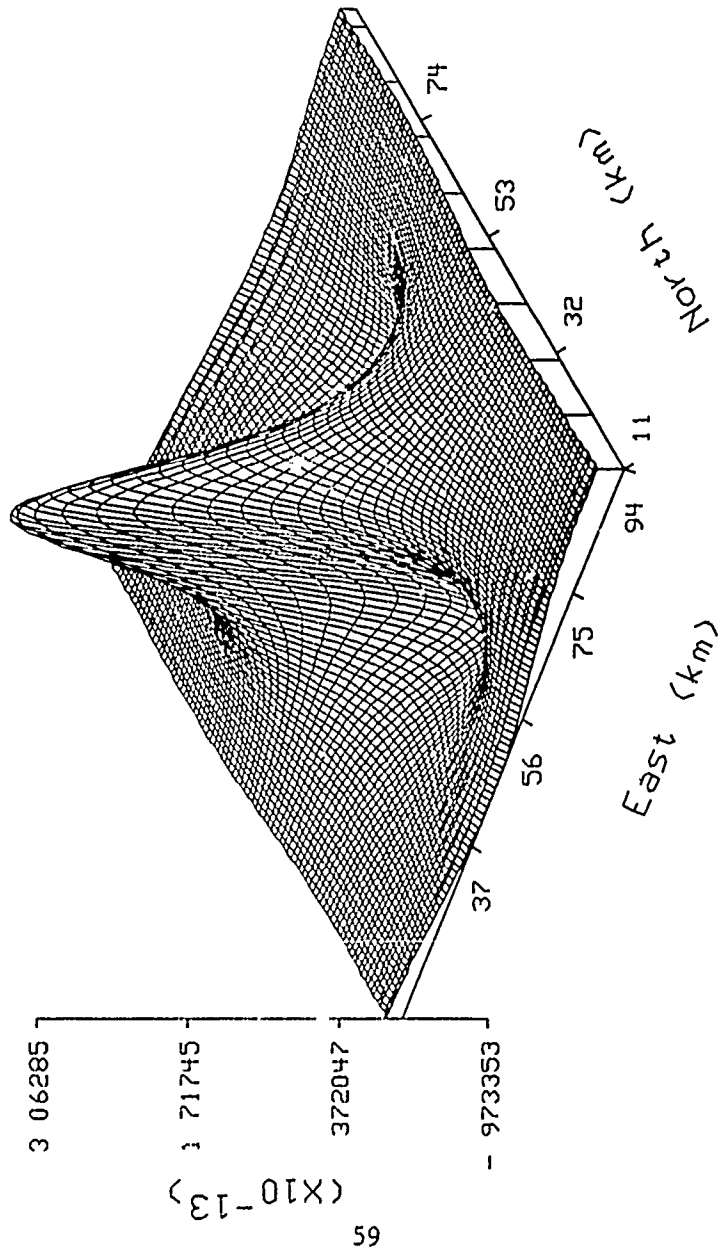
$\hat{T}_x$  (m/sec/sec)



Single Dipole, meas  $T_{xy}$  at  $h=2\text{km}$ , est  $h=0$

Figure 32:  $\hat{T}_x$  given  $T_{xy}$ , Single Dipole

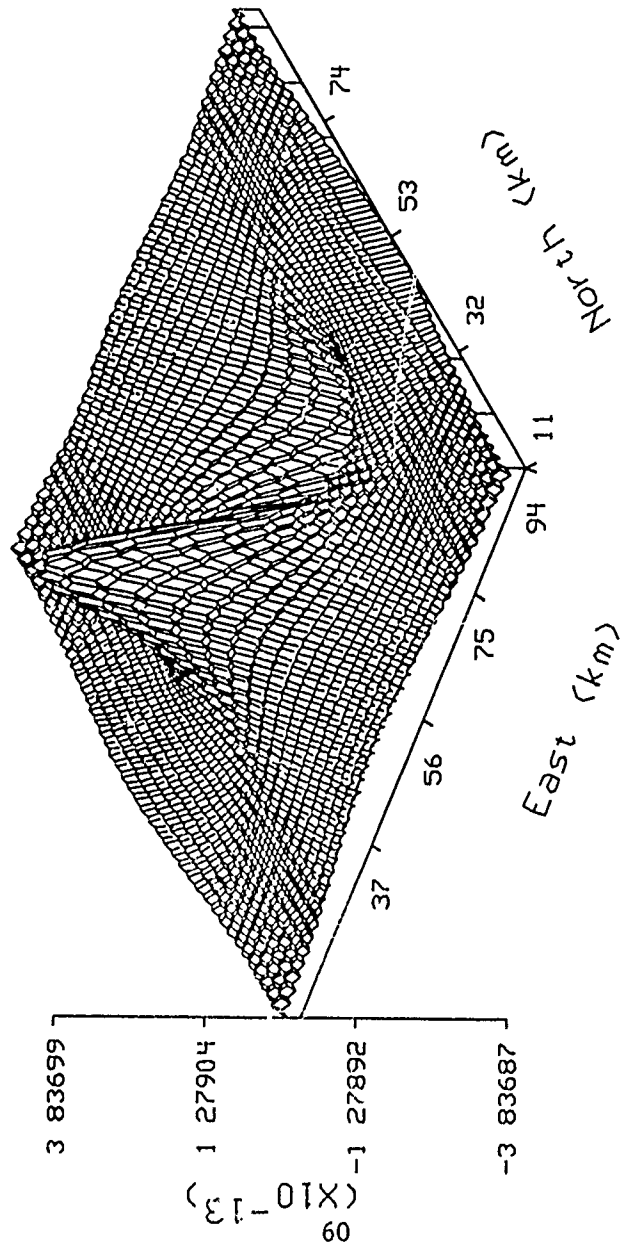
Ty hat (m/sec/sec)



Single Dipole, meas  $T_{xy}$  at  $h=2\text{km}$ , est  $h=0$

Figure 33:  $T_{xy}$  given  $T_{xy}$ , Single Dipole

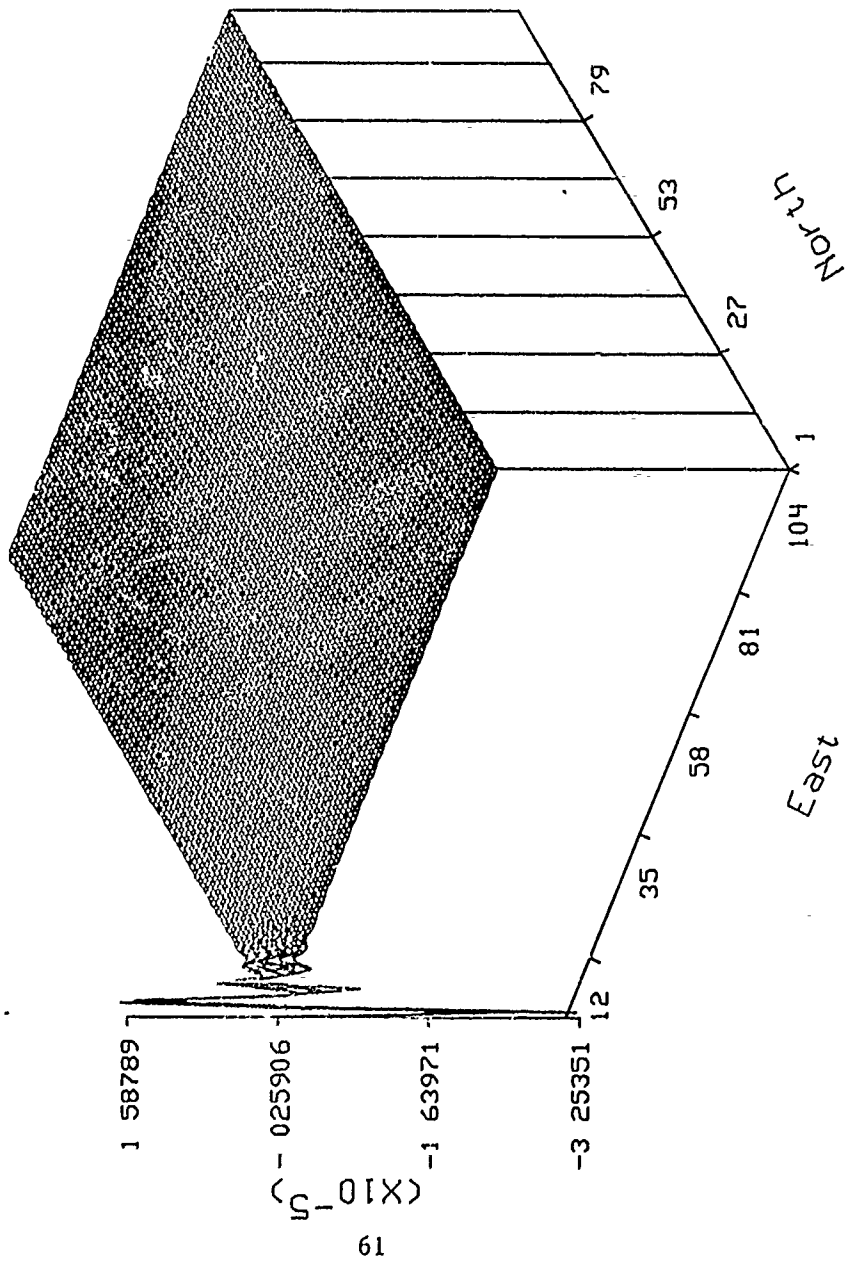
$\hat{T}_z$  (m/sec/sec)



Single Dipole, meas  $T_{xy}$  at  $h=2\text{km}$ , est  $h=0$

Figure34:  $\hat{T}_z$  given  $T_{xy}$ , Single Dipole

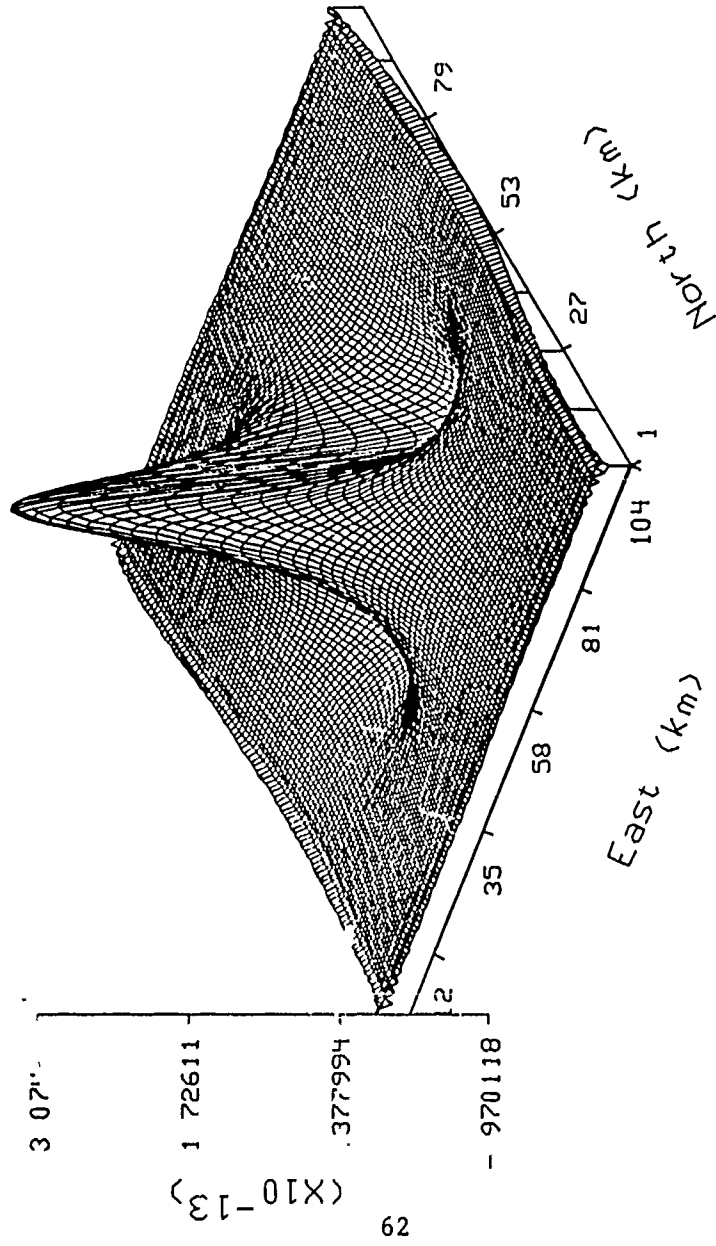
alpha hat



Single Dipole, meas  $T_{yz}$  at  $h=2\text{km}$

Figure35:  $\hat{\alpha}$  given  $T_{yz}$ ; Single Dipole

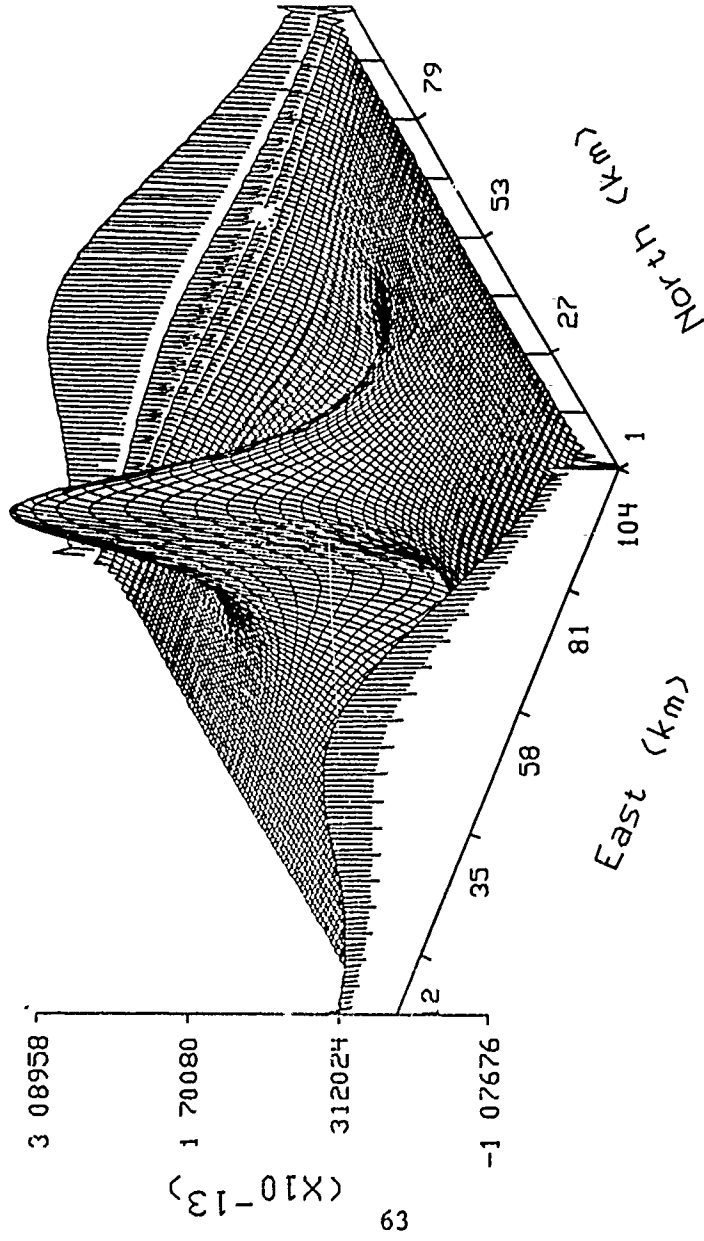
$\hat{T}_x$  (m/sec/sec)



Single Dipole, meas  $T_{yz}$  at  $h=2\text{km}$ , est  $h=0$

Figure 36:  $\hat{T}_x$  given  $T_{yz}$ , Single Dipole

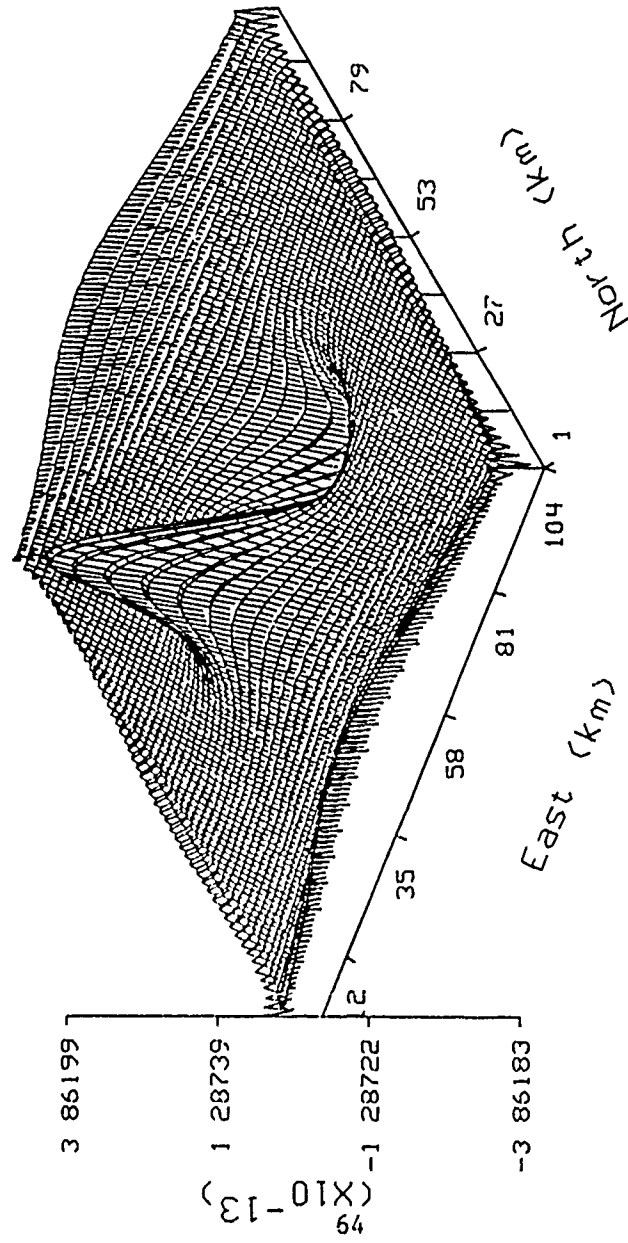
Ty hat (m/sec/sec)



Single Dipole, meas  $T_{yz}$  at  $h=2\text{km}$ , est  $h=0$

Figure37:  $\hat{T}_y$ , given  $T_{yz}$ , Single Dipole

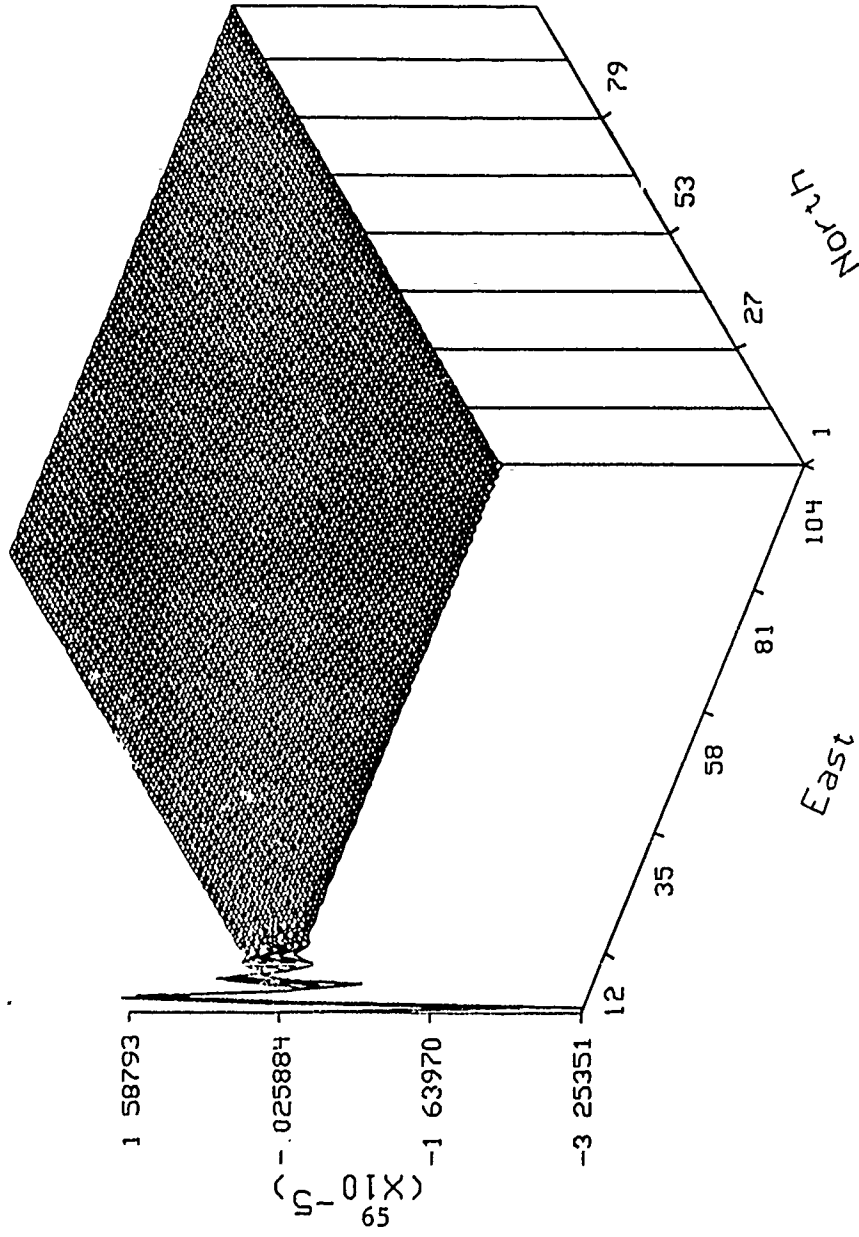
$\hat{T}_z$  (m/sec/sec)



Single Dipole, meas  $T_{17}$  at  $h=2$ km, est  $h=0$

Figure38:  $\hat{T}_z$  given  $T_{yz}$ , Single Dipole

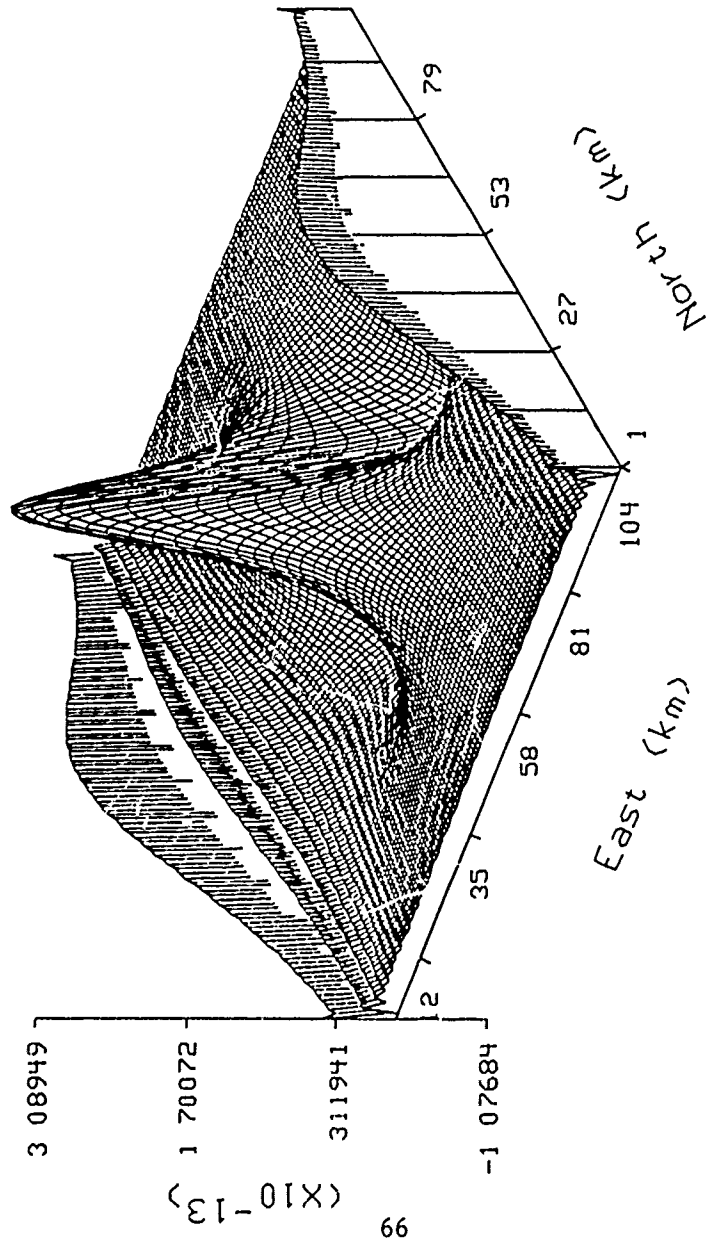
alpha hat



Single Dipole, meas  $T_{rz}$  at  $h=2\text{km}$

Figure39:  $\hat{\alpha}$  given  $T_{rz}$ , Single Dipole

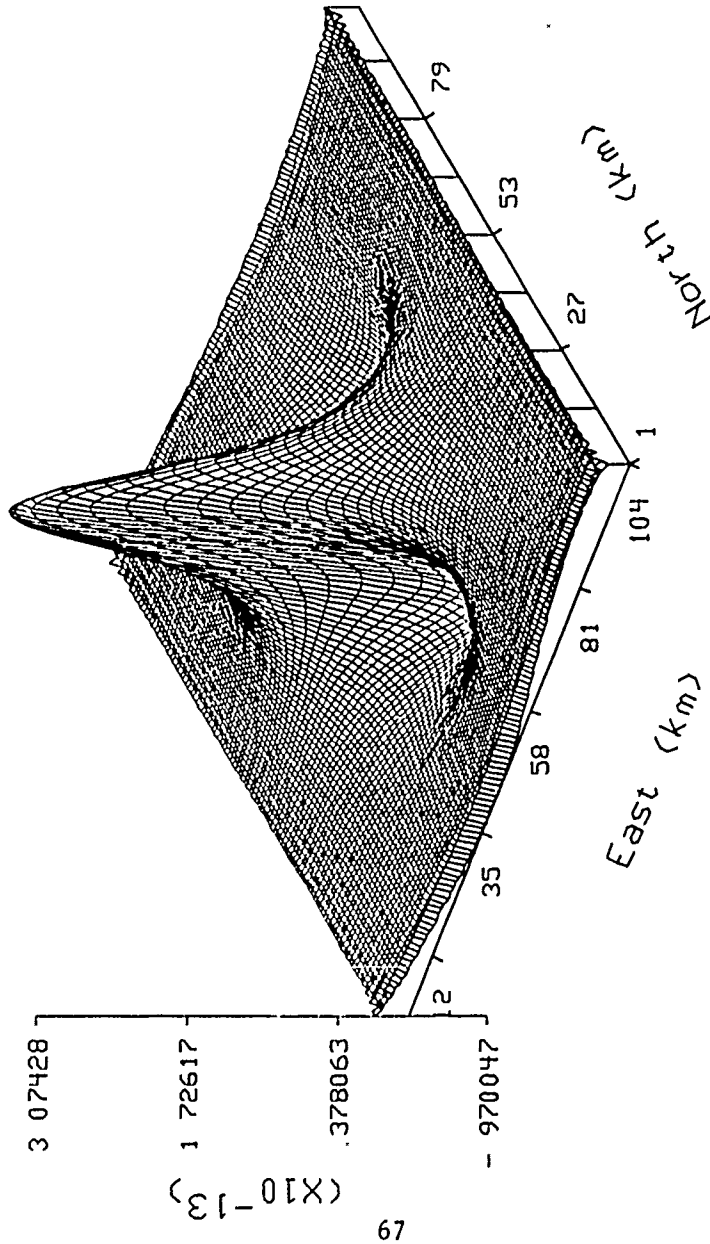
$\hat{T}_x$  (m/sec/sec)



Single Dipole, meas  $T_{xz}$  at  $h=2\text{km}$ , est  $h=0$

Figure 40:  $\hat{T}_x$  given  $T_{xz}$ , Single Dipole

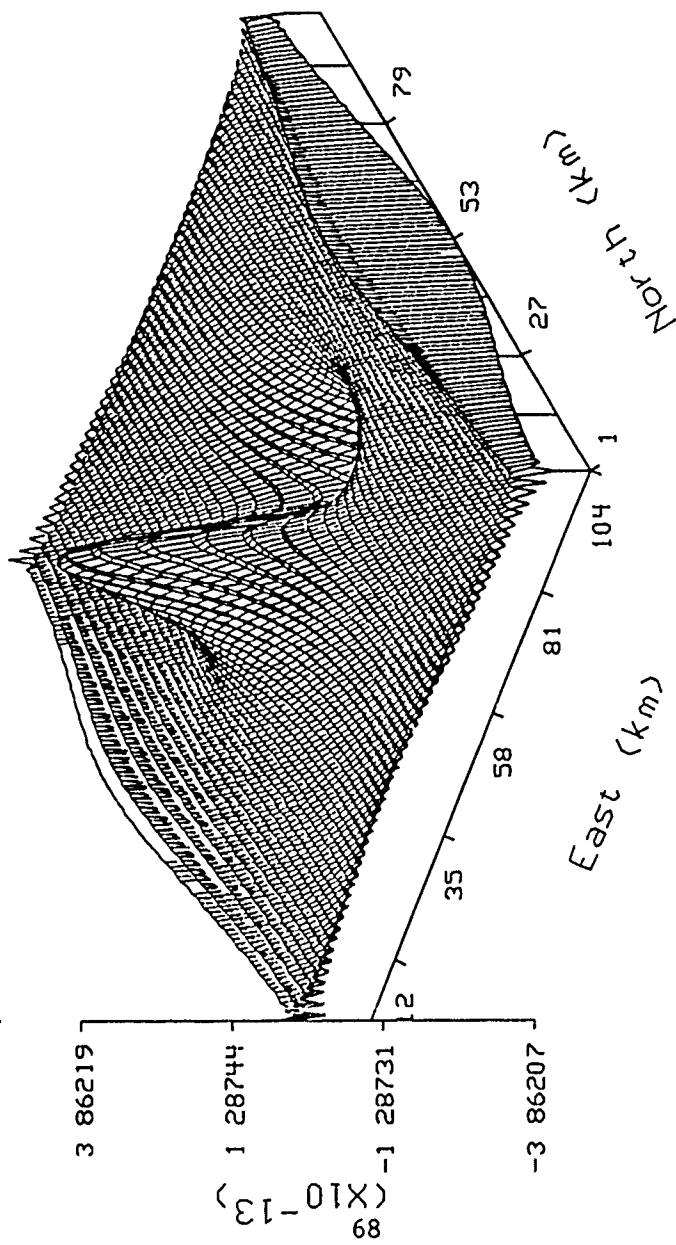
Ty hat (m/sec/sec)



Single Dipole, meas  $T_{xz}$  at  $h=2\text{km}$ , est  $h=0$

Figure41:  $\hat{T}_y$  given  $T_{xz}$ , Single Dipole

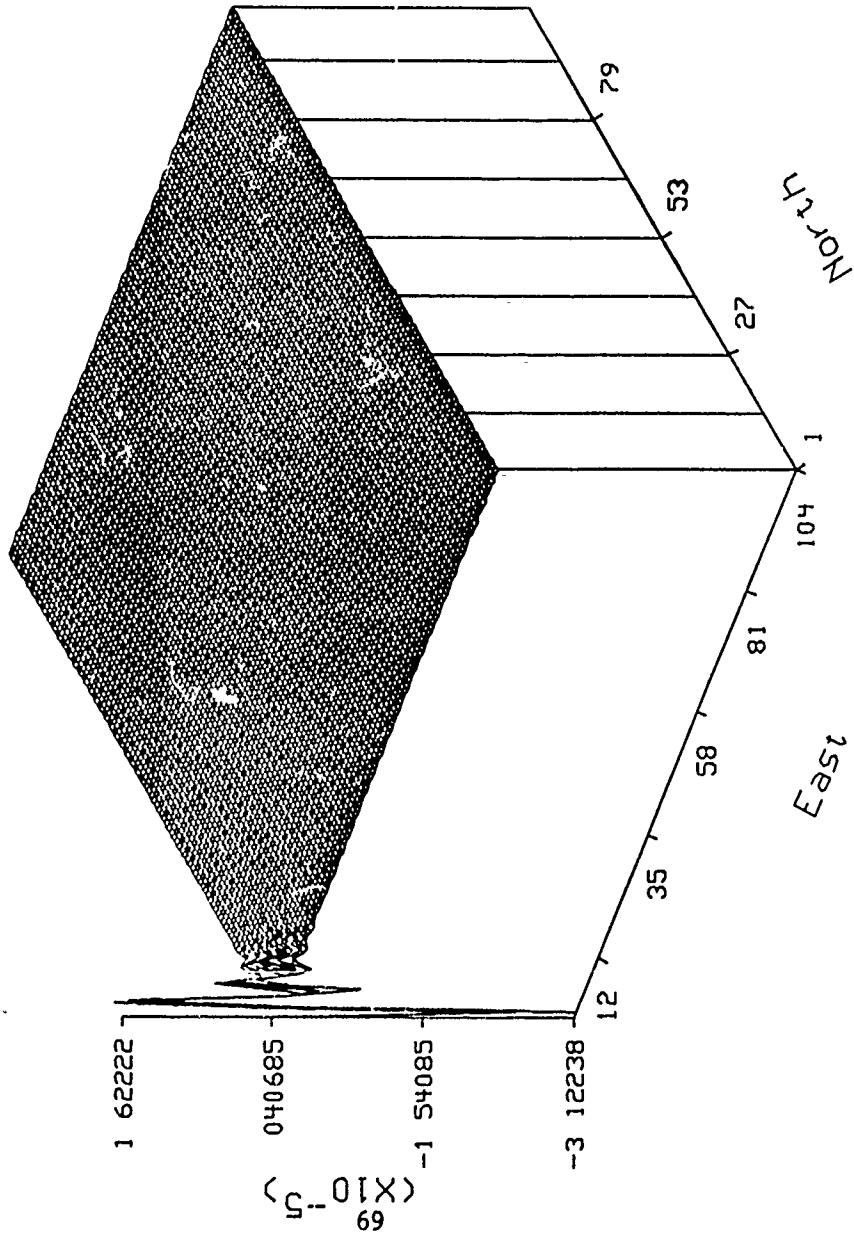
$\hat{T}_z$  (m/sec/sec)



Single Dipole, meas  $T_{xz}$  at  $h=2\text{km}$ , est  $h=0$

Figure 42:  $\hat{T}_z$  given  $T_{zz}$ , Single Dipole

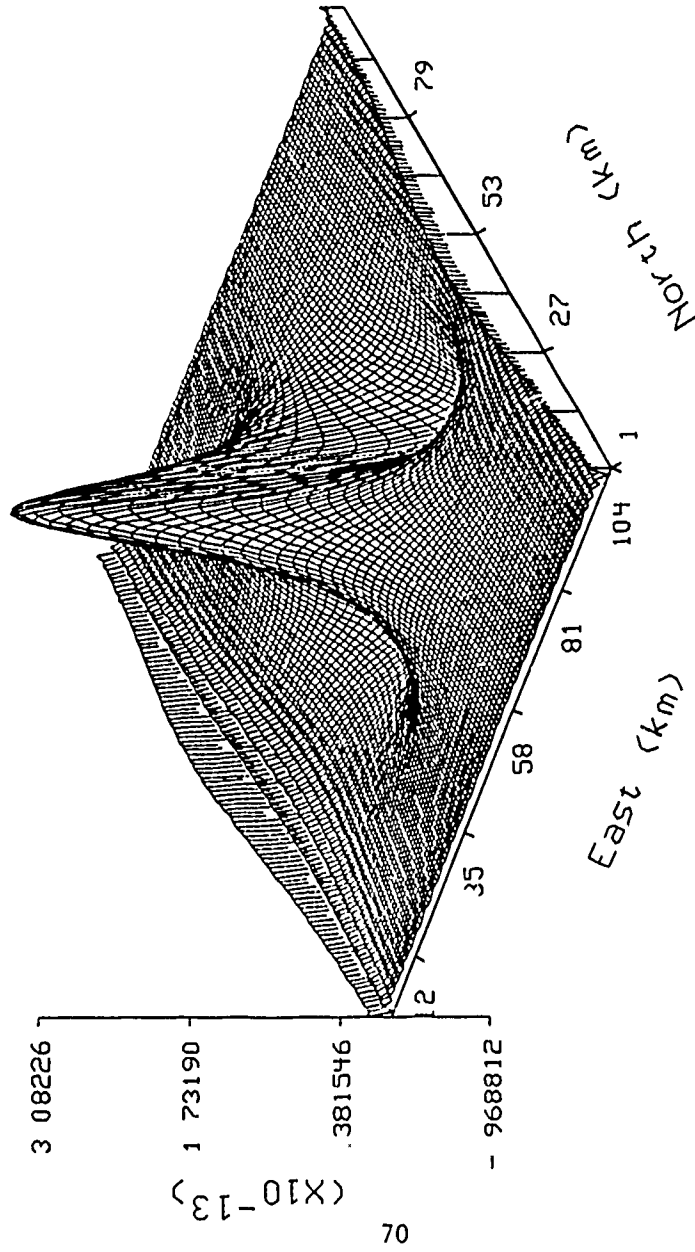
alpha hat



Single Dipole, meas full tensor at  $h=2\text{km}$

Figure43:  $\hat{\alpha}$  given full tensor gradient, Single Dipole

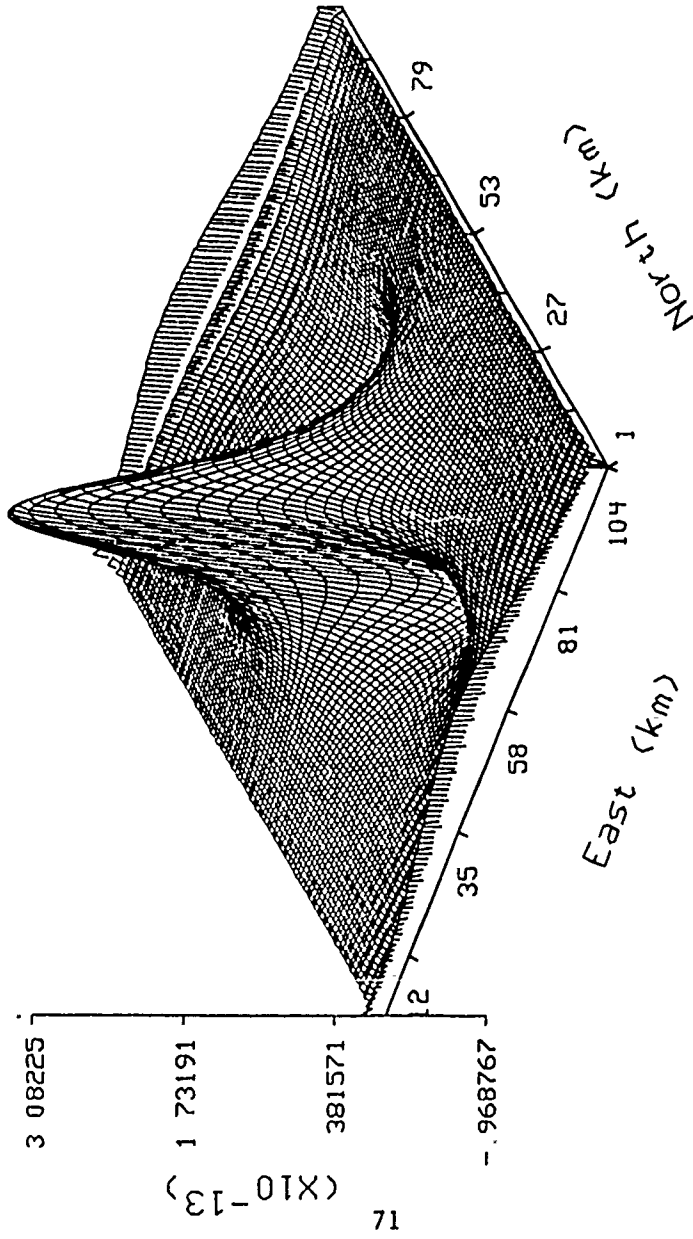
$\hat{T}_x$  (m/sec/sec)



Single Dipole, meas full tensor at  $h=2$ km, est  $h=0$

Figure44:  $\hat{T}_x$  given full tensor gradient, Single Dipole

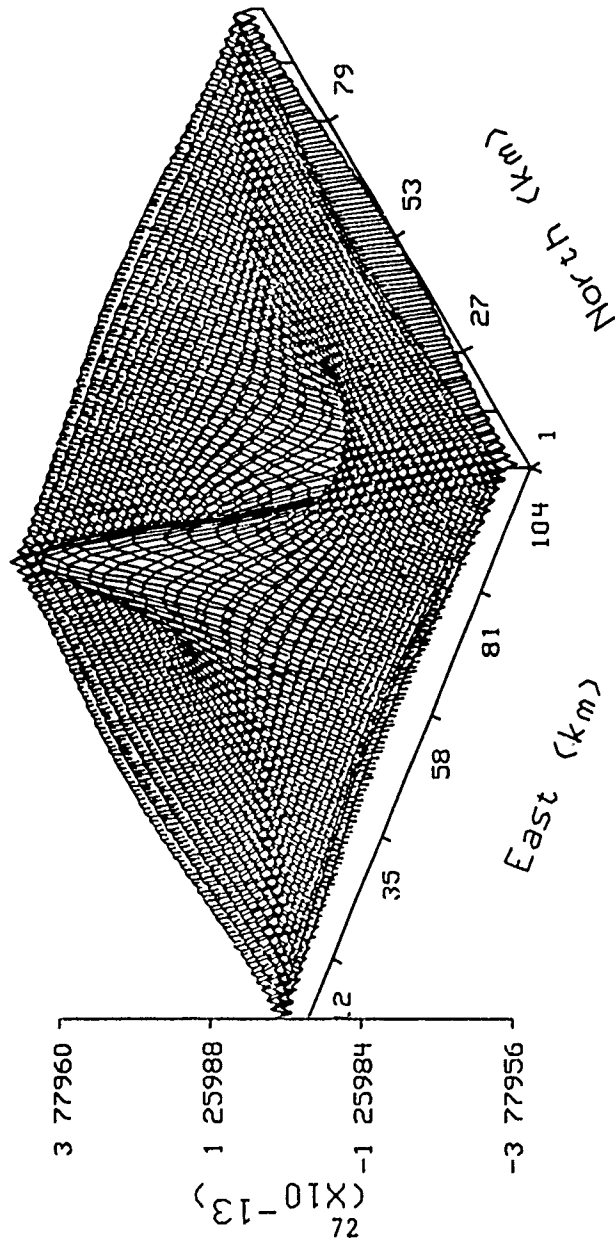
Ty hat (m/sec/sec)



Single Dipole, meas full tensor at h=2km, est h=0

Figure45:  $\hat{T}_y$  given full tensor gradient, Single Dipole

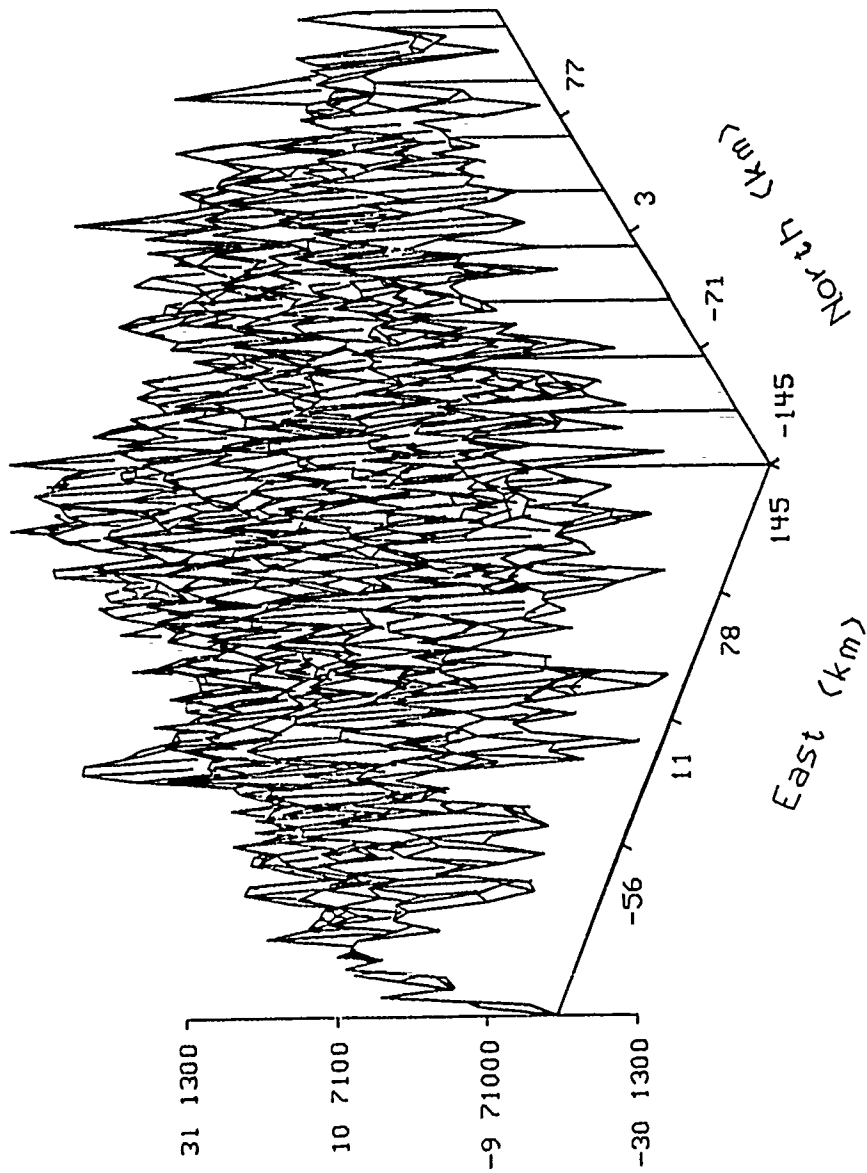
$\hat{T}_z$  (m/sec/sec)



Single Dipole, meas full tensor at  $h=2\text{km}$ , est  $h=0$

Figure46:  $\hat{T}_z$  given full tensor gradient, Single Dipole

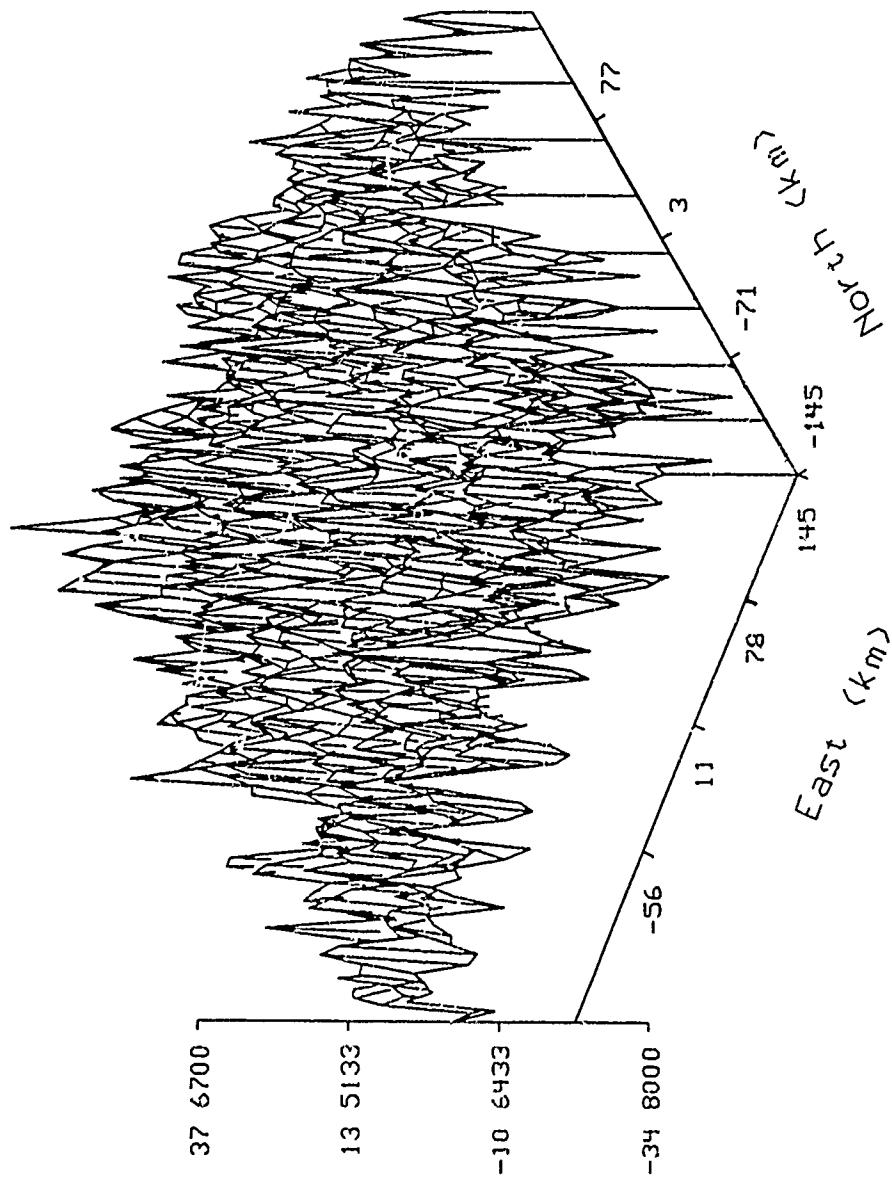
Txx (Eutvos)



Tape 1, file 1, meas at h=0.6km

Figure47: Measured  $T_{xx}$ , File 1

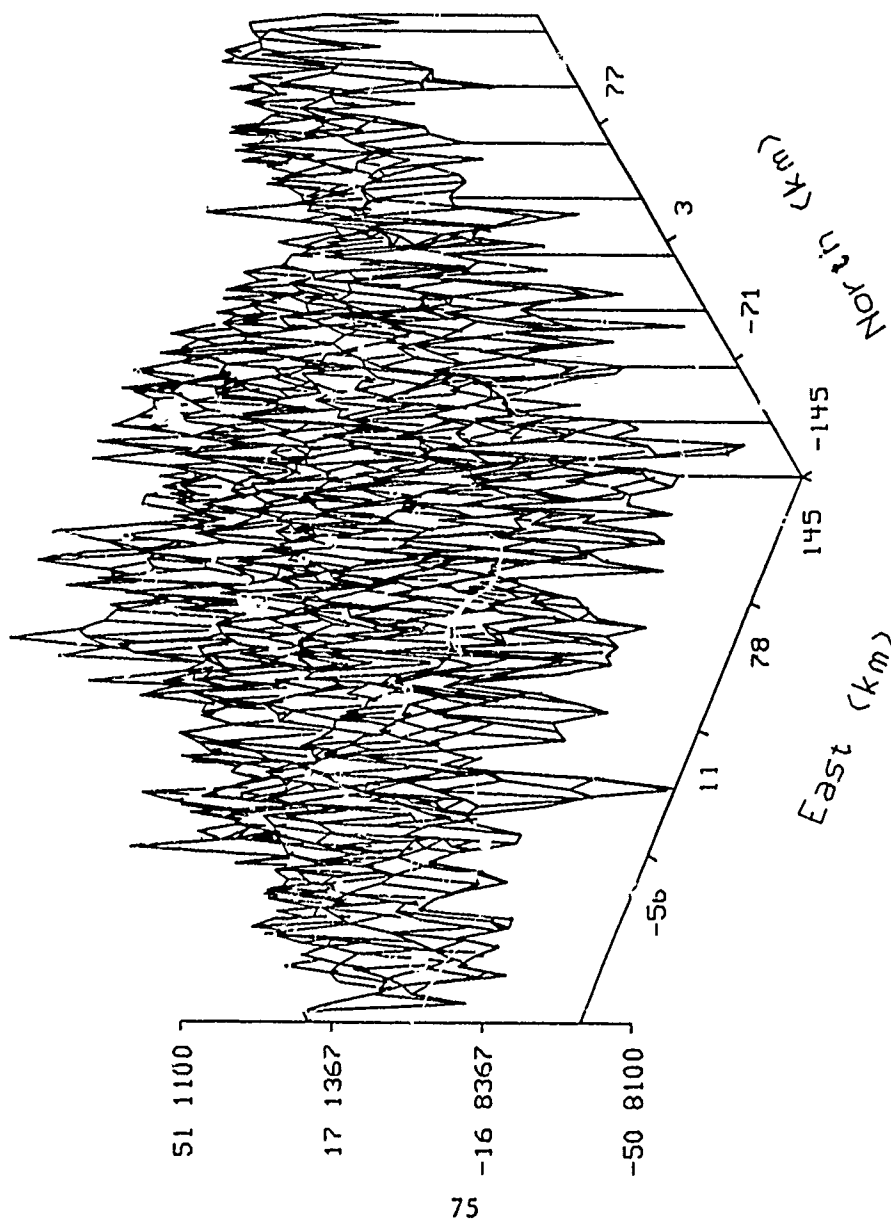
$T_{yy}$  (Eotvos)



Tape 1, file 1 meas at h=0 6km

Figure48: Measured  $T_{yy}$ , File 1

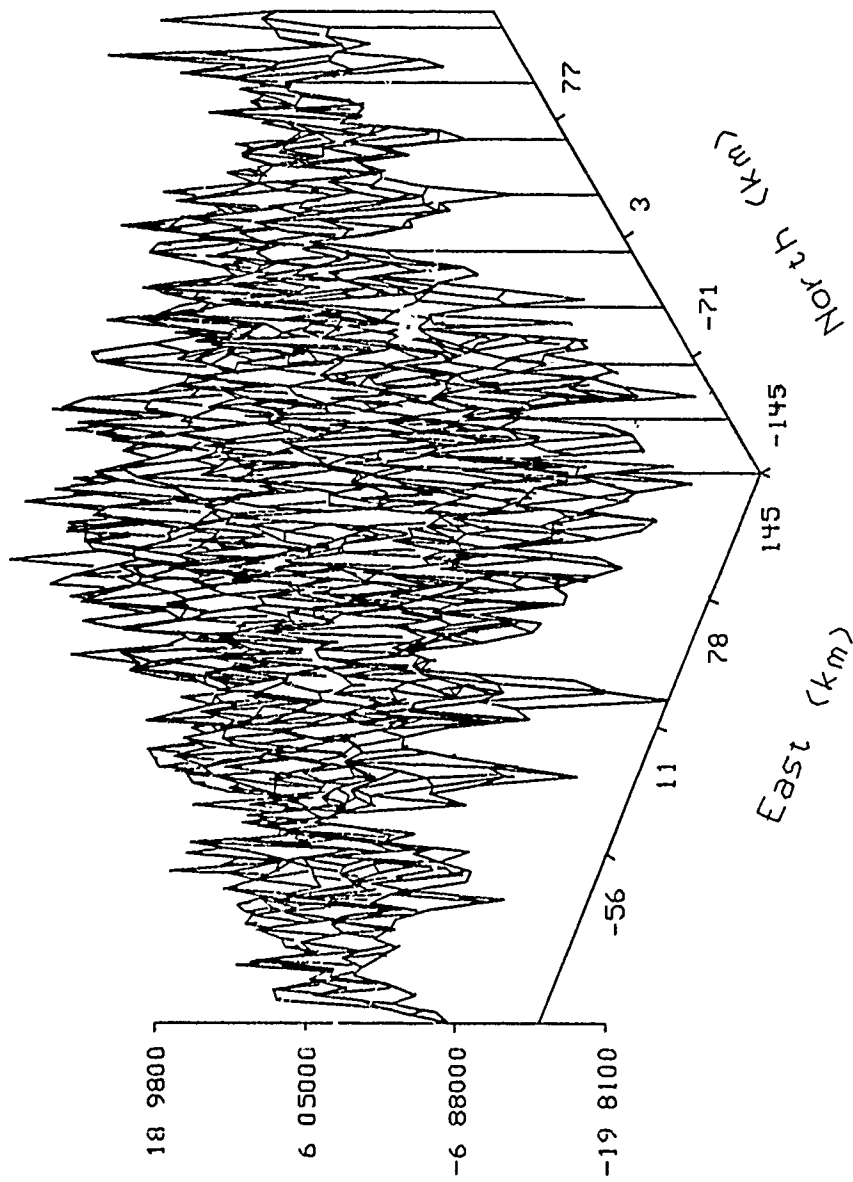
TZZ (Eotvos)



Tape 1, file 1, meas at h=0.6km

Figure49: Measured  $T_{zz}$ , File 1

$T_{xy}$  (Eotvos)

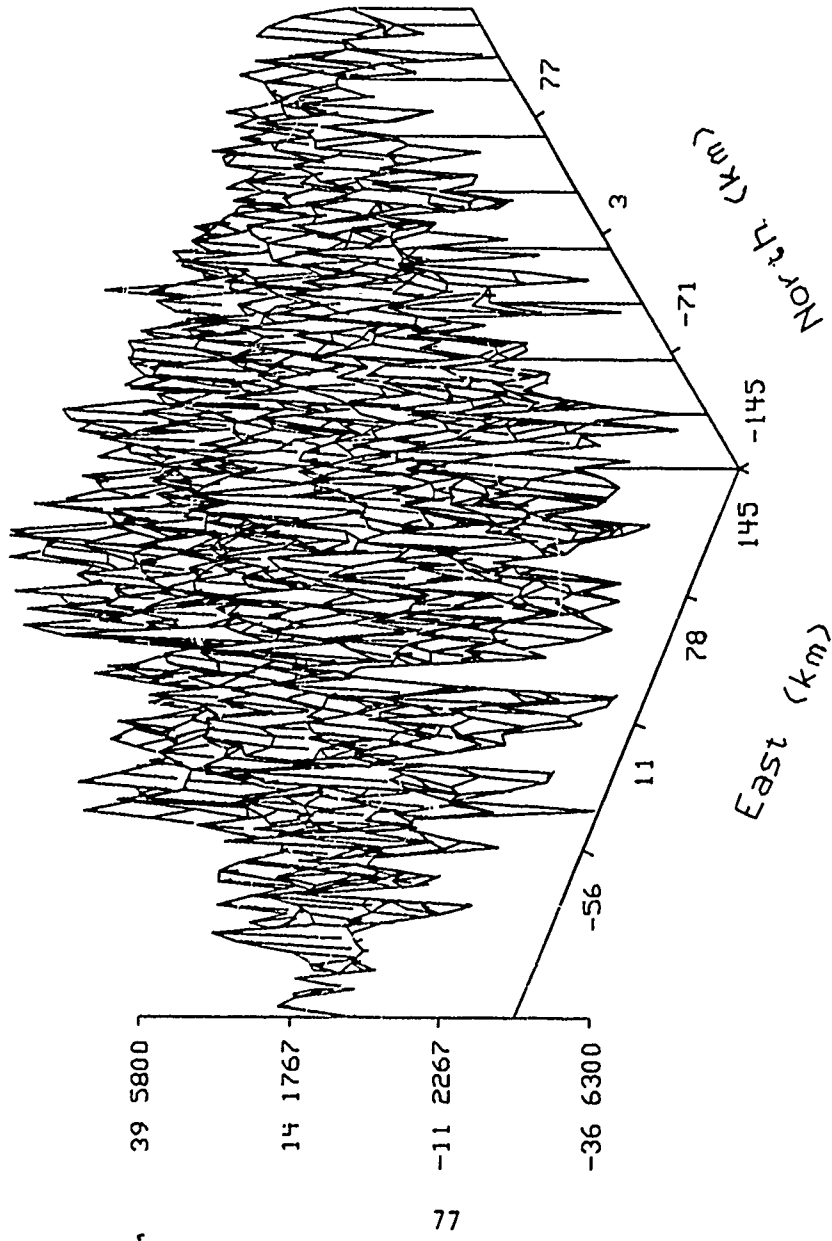


76

Tape 1, file 1, meas at h=0 6km

Figure50: Measured  $T_{xy}$ , File 1

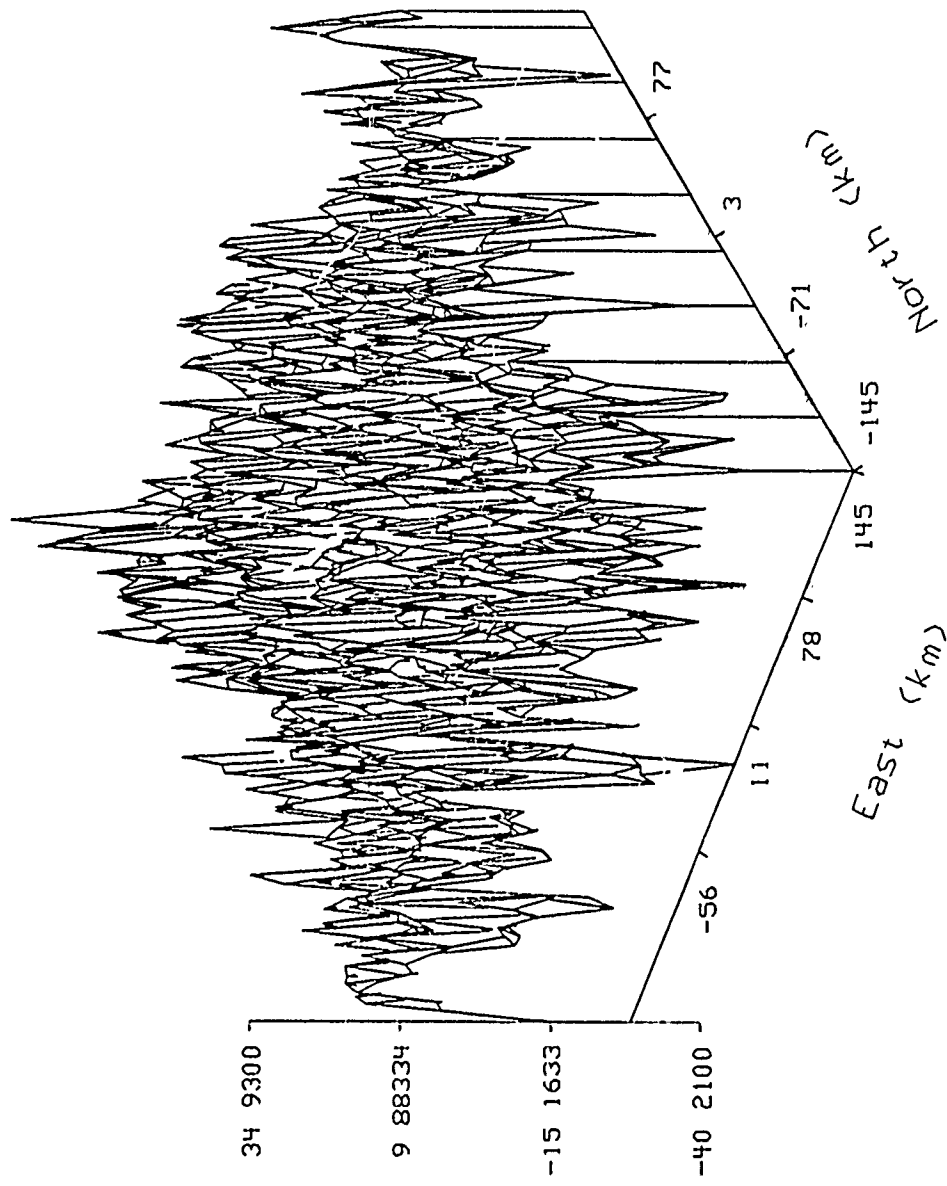
Tyz (Eotvos)



Tape 1, file 1, meas at h=0 6km

Figure51: Measured  $T_{yz}$ , File 1

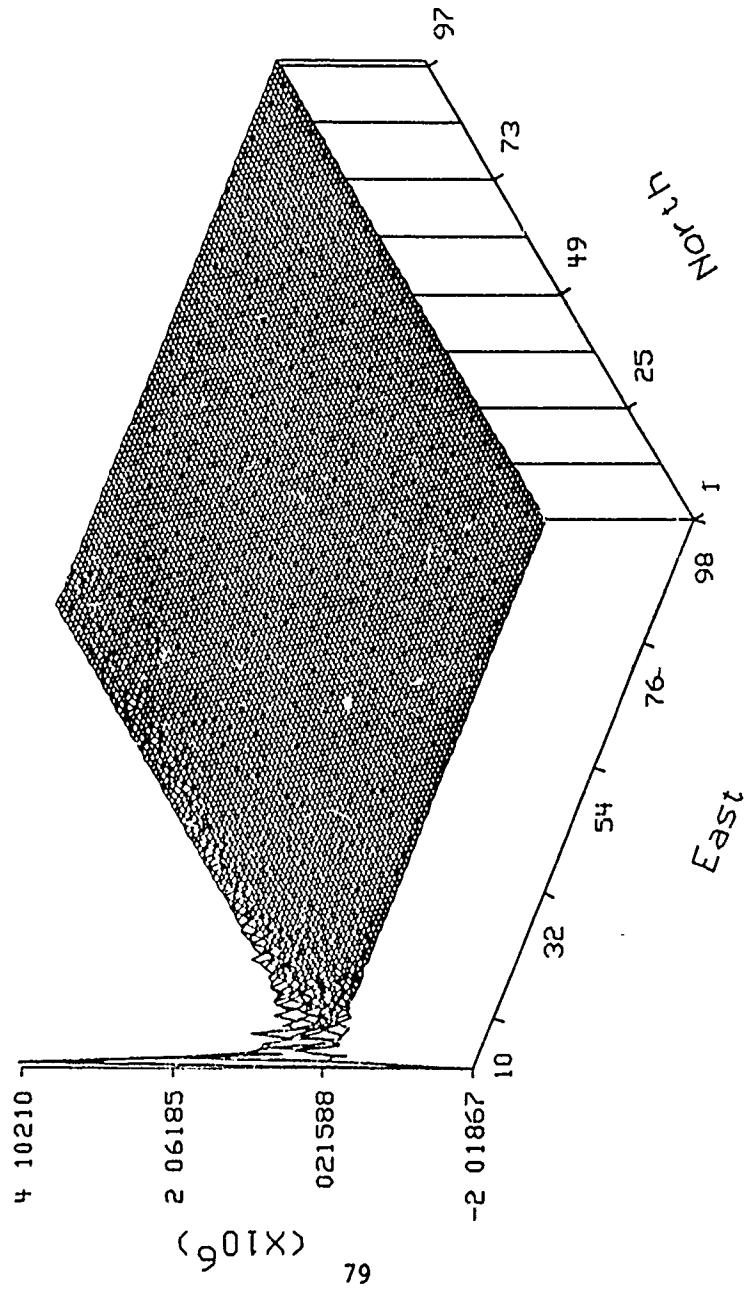
Txz (Eotvos)



Tape 1, file 1, meas at h=0 6km

Figure52: Measured  $T_{xz}$ , File 1

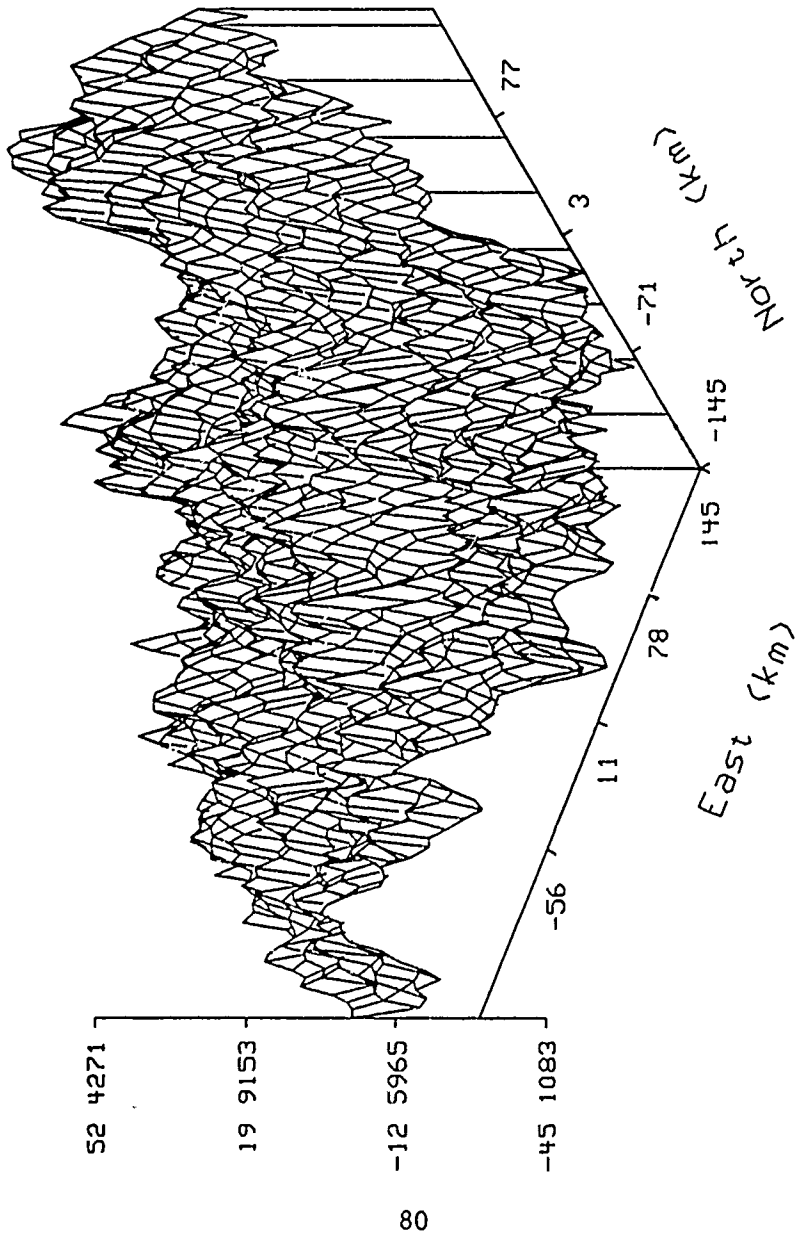
alpha hat



. Tape 1, file 1, meas Txx at h=0.6km

Figure53:  $\hat{\alpha}$  given  $T_{xx}$ ; File 1

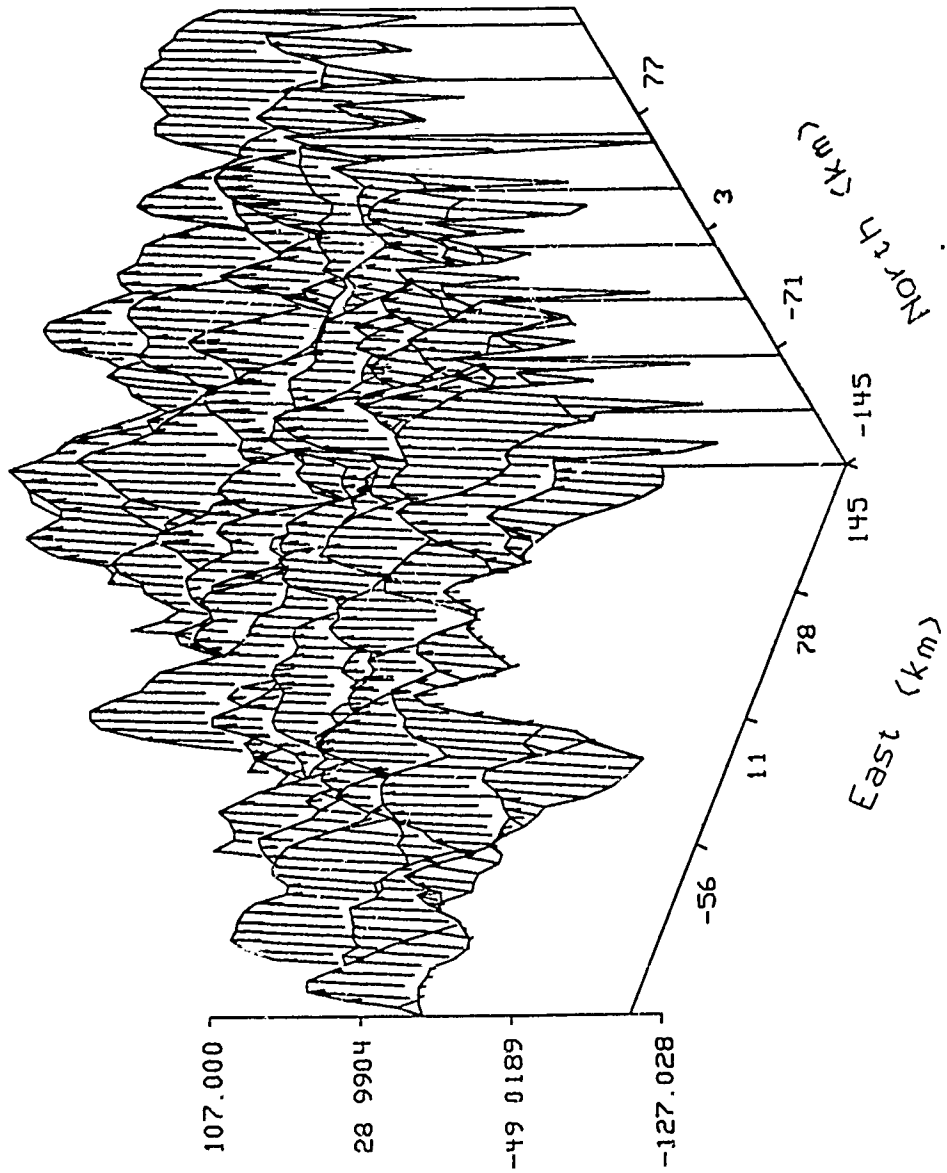
$\hat{T}_x$  (mgal)



Tape 1, file 1, meas  $T_{xx}$  at  $h=0$  6km, est  $h=0$

Figure 54:  $\hat{T}_x$  given  $T_{xx}$ , File 1

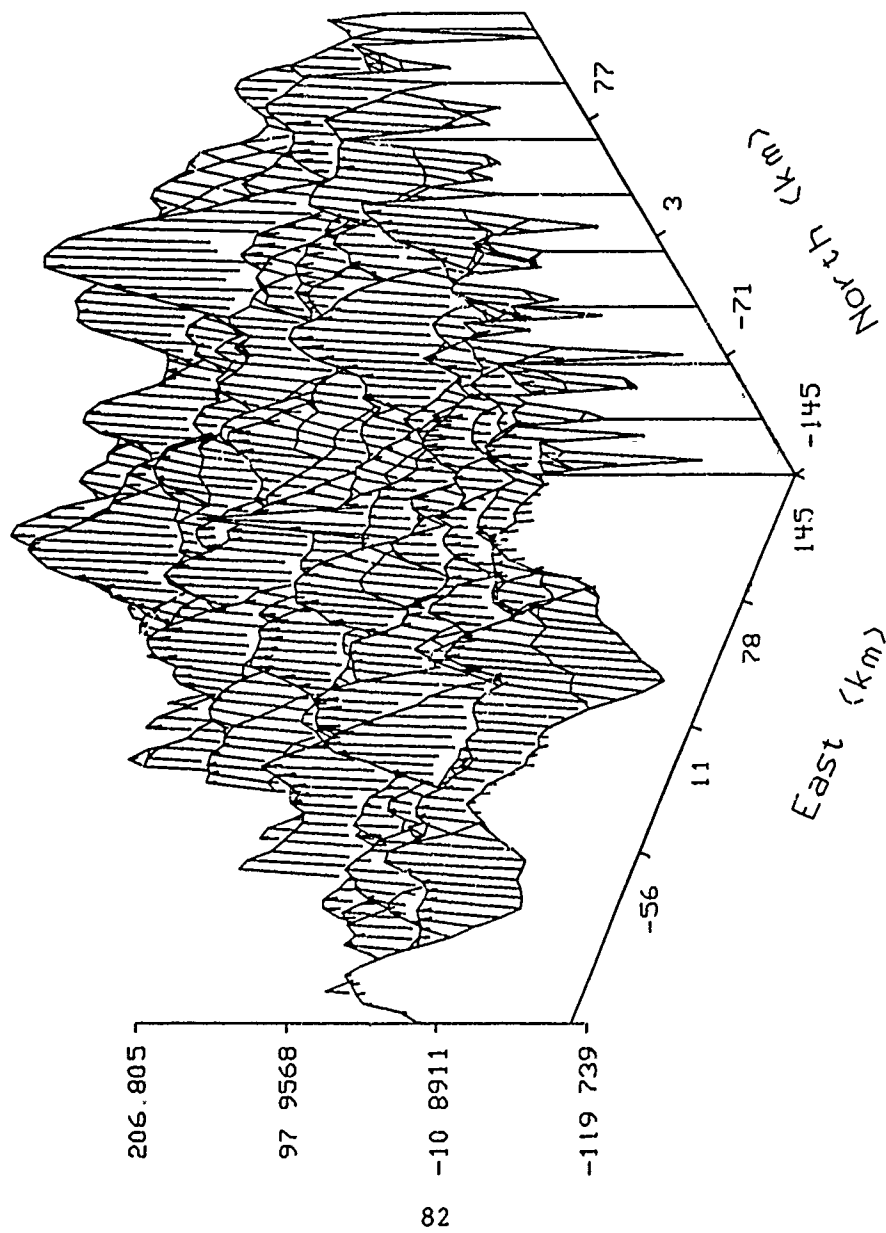
Ty hat (mgal)



Tape 1, file 1, meas Txx at h=0 6km, est h=0

Figure55:  $\hat{T}_y$  given  $T_{xx}$ , File 1

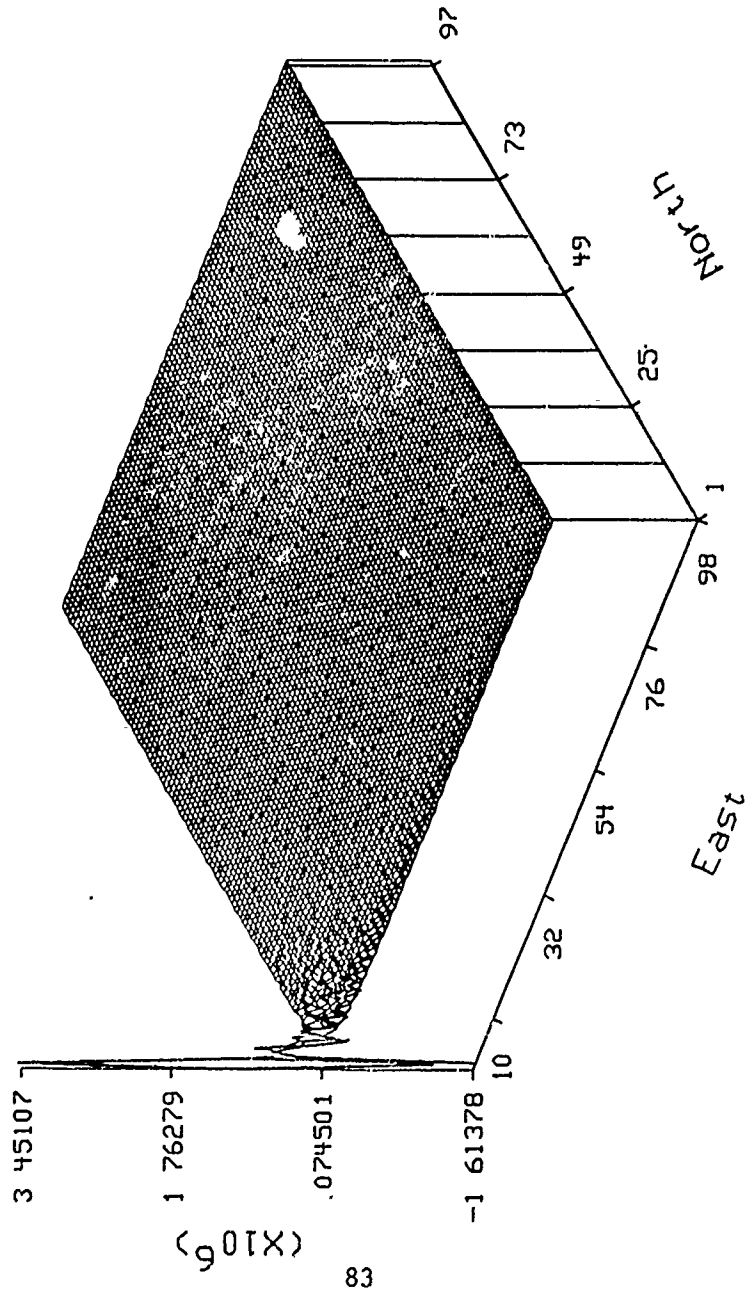
$\hat{T}_z$  (mgal)



Tape 1, file 1, meas  $T_{xx}$  at  $h=0$  6km, est  $h=0$

Figure 56:  $\hat{T}_z$  given  $T_{xx}$ , File 1

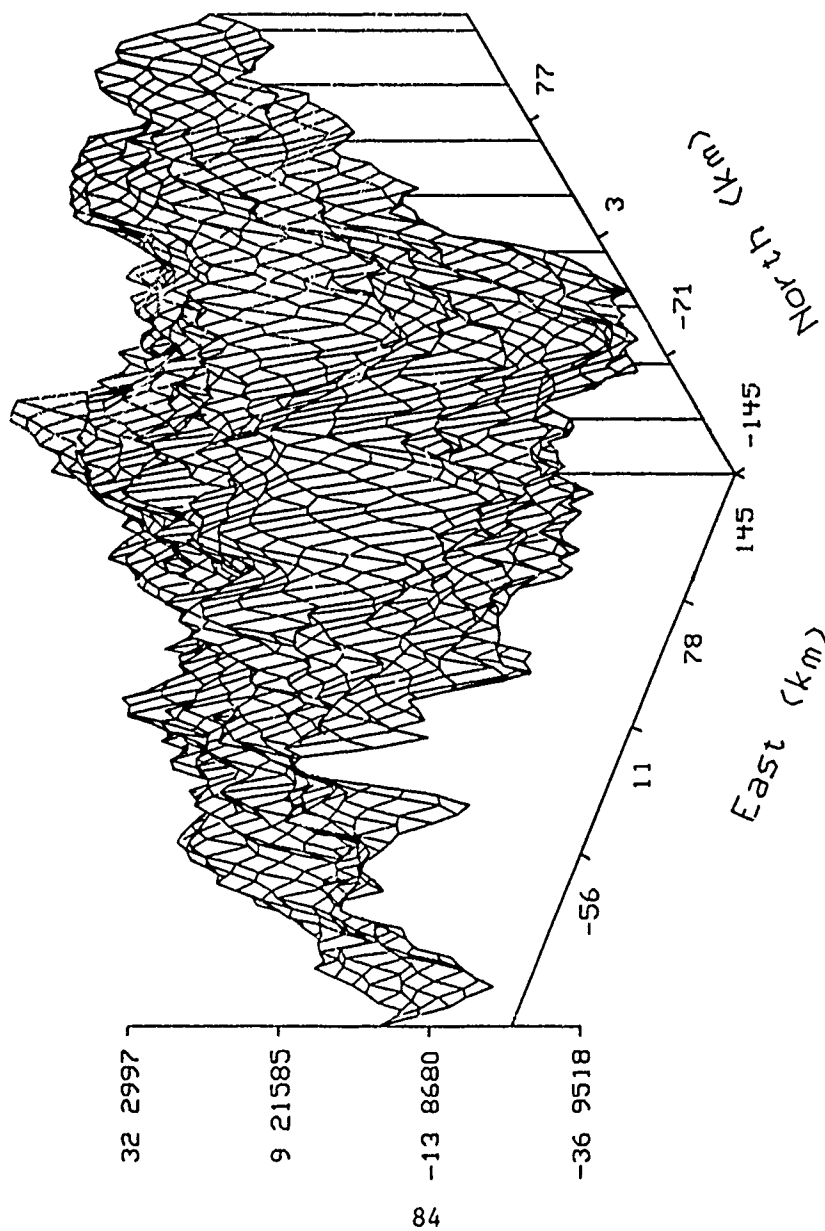
alpha hat



. Tape 1, file 1, meas  $T_{yy}$  at  $h=0.6\text{km}$

Figure57:  $\hat{\alpha}$  given  $T_{yy}$ , File 1

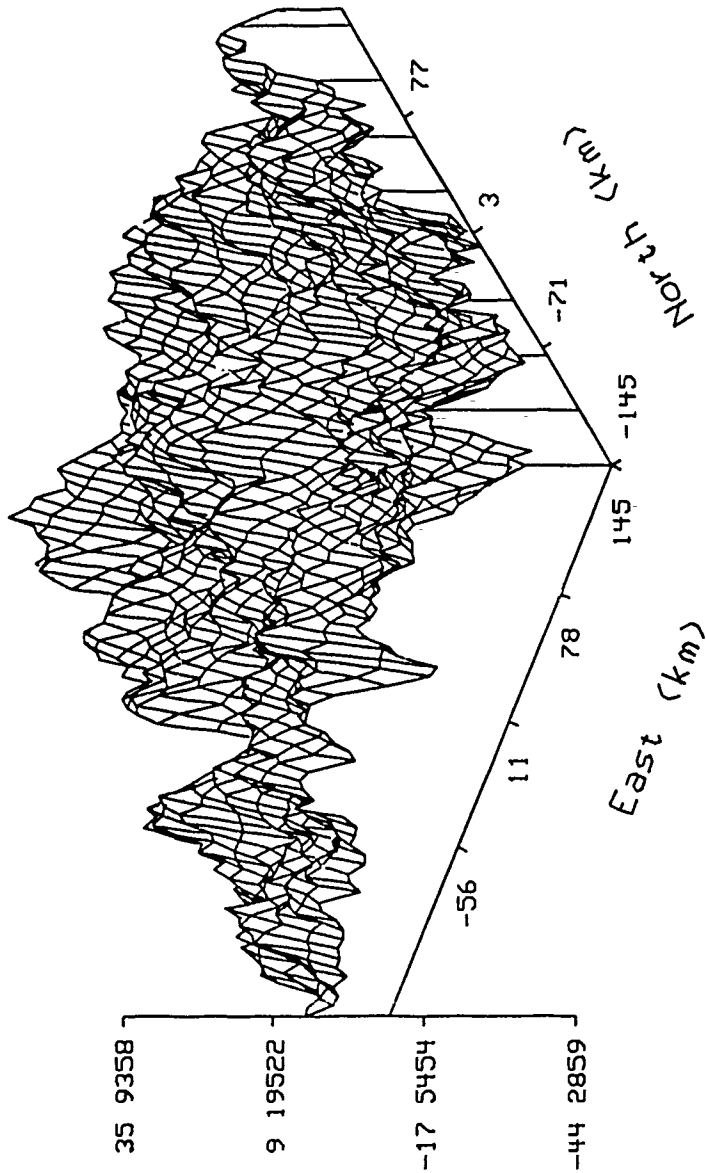
Tx hat (mgal)



Tape i, file 1, meas  $T_{yy}$  at  $h=0$  6km, est  $h=0$

Figure58:  $\hat{T}_z$  given  $T_{yy}$ , File 1

Ty hat (mgal)

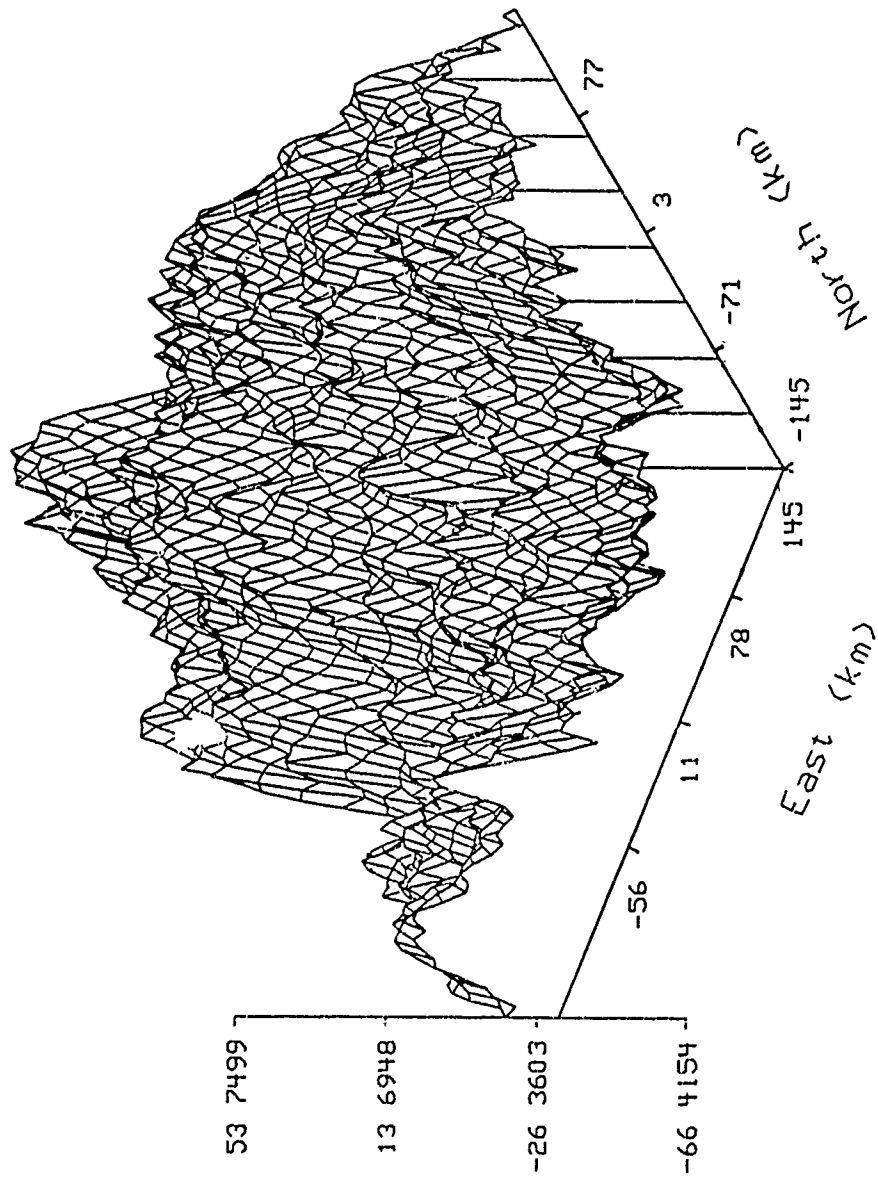


85

Tape 1, file 1, meas Tyy at h=0 6km, est h=0

Figure59:  $\hat{T}_y$  given  $T_{yy}$ , File 1

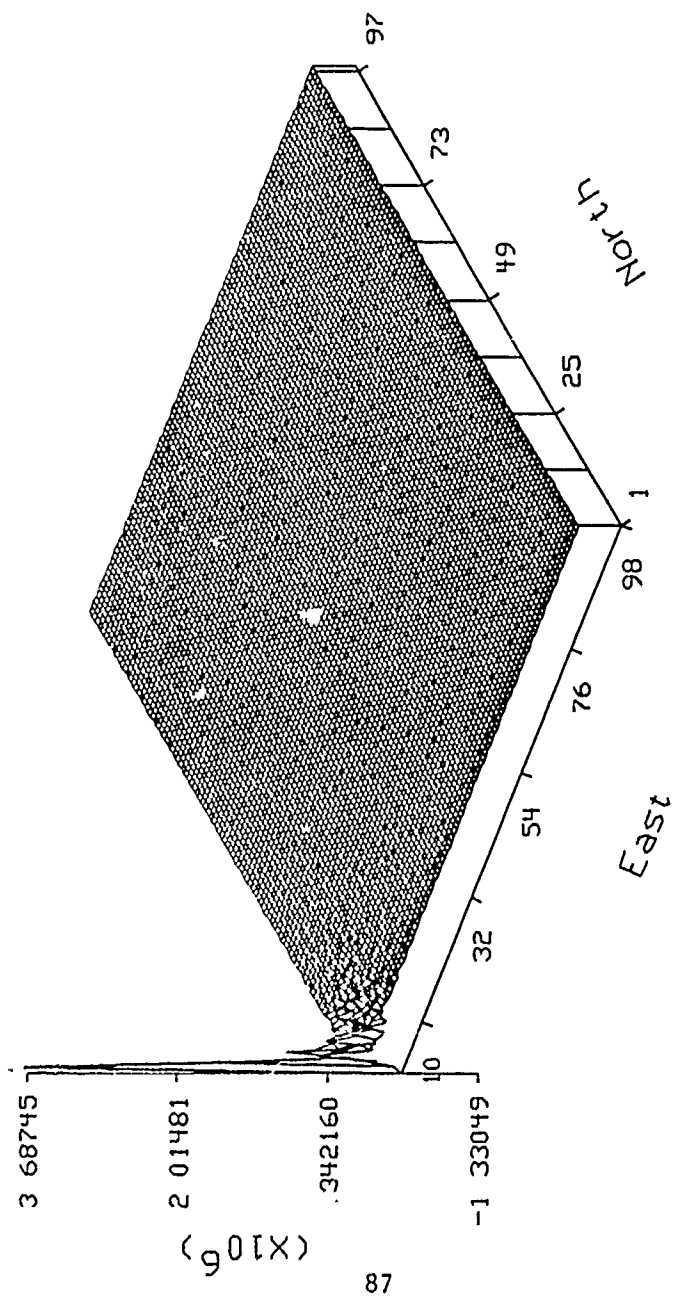
$\hat{T}_z$  (mgal)



Tape 1, file 1, meas  $T_{yy}$  at  $h=0$  6km, est  $h=0$

Figure 60:  $\hat{T}_z$  given  $T_{yy}$ , File 1

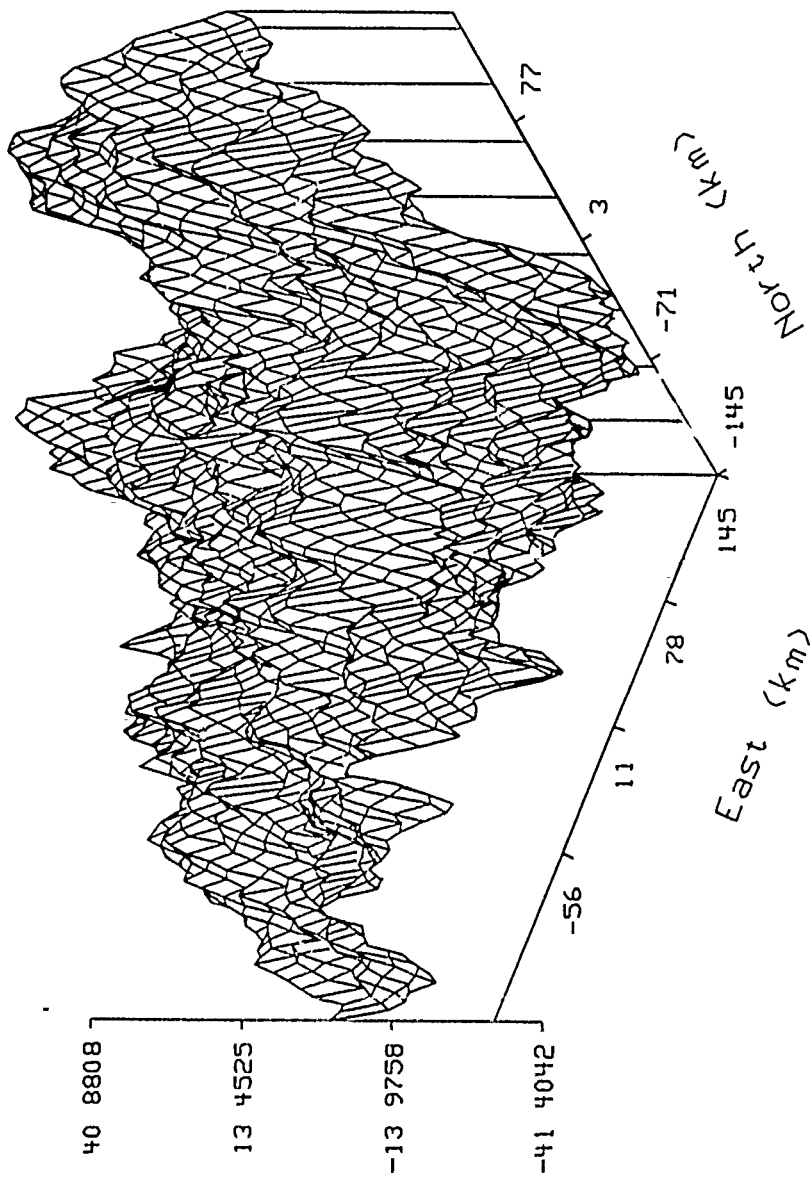
alpha hat



. Tape 1, file 1, meas Tzz at h=0.6km

Figure61:  $\hat{\alpha}$  given  $T_{zz}$ , File 1

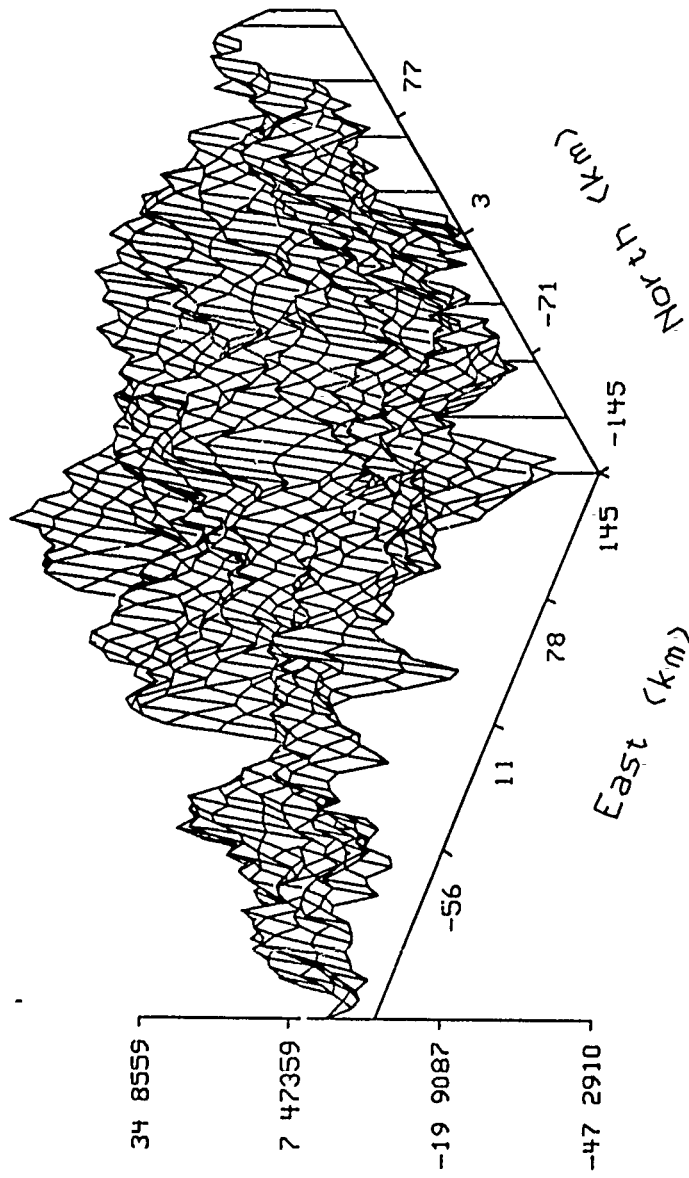
$\hat{T}_x$  (mgal)



Tape 1, file 1, meas  $T_{zz}$  at  $h=0$  6km, est  $h=0$

Figure62:  $\hat{T}_x$  given  $T_{zz}$ , File 1

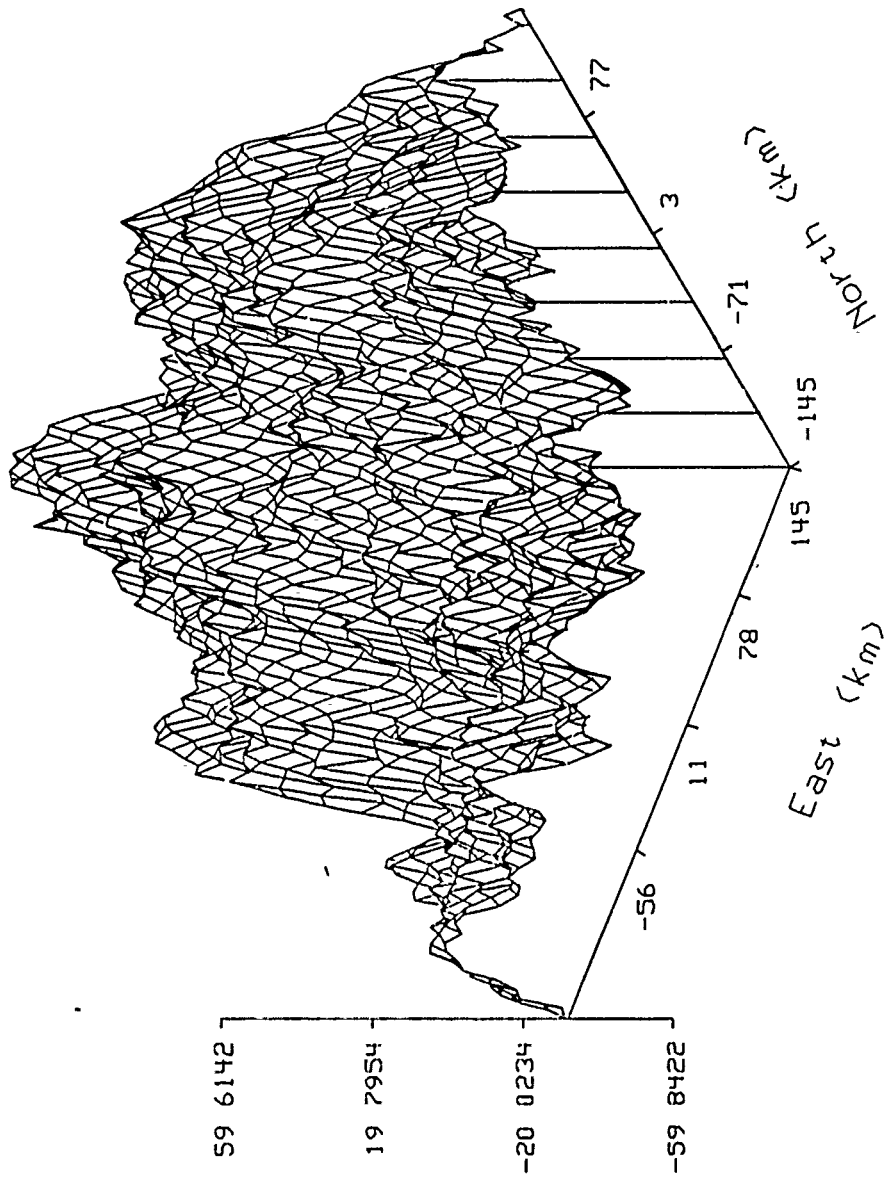
Ty hat (mgal)



Tape 1, file 1, meas Tzz at h=0 6km, est h=0

Figure63:  $\hat{T}_y$  given  $T_{zz}$ , File 1

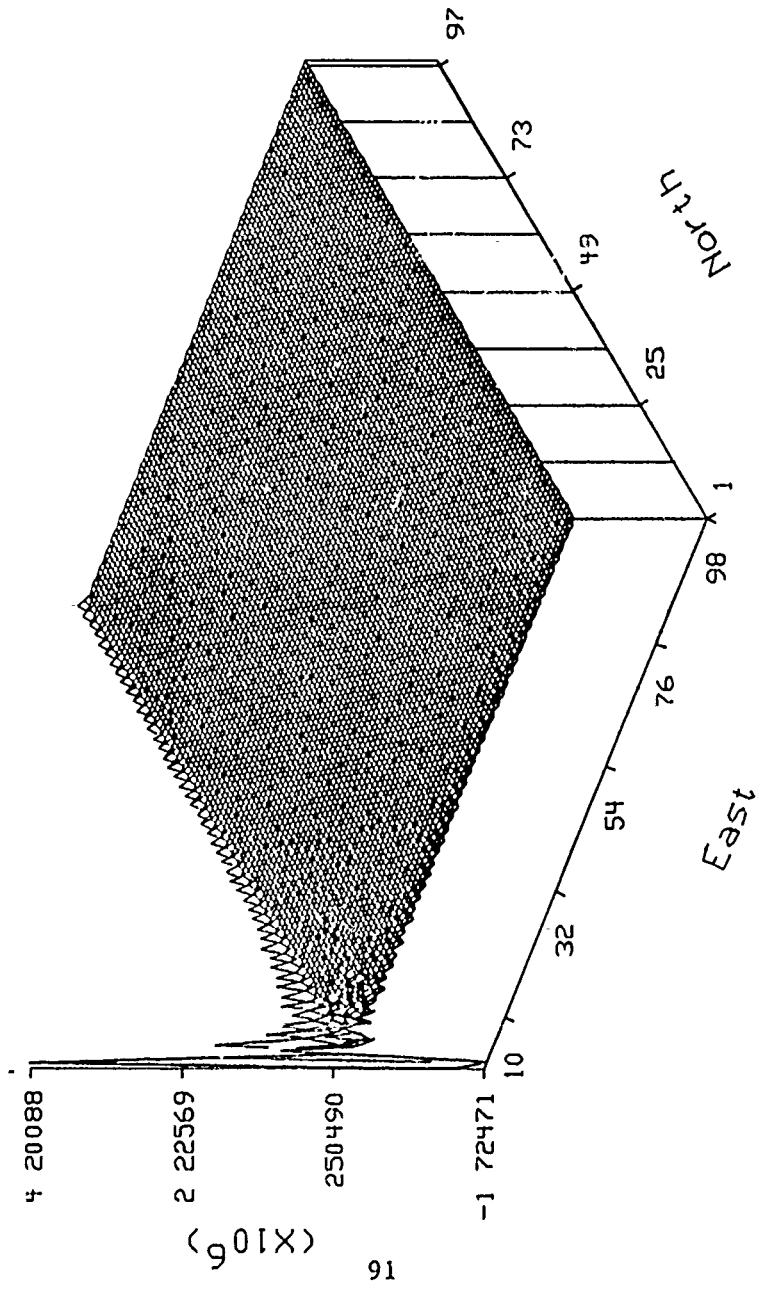
Tz hat (mgal)



Tape 1, file 1, meas Tzz at h=0 6km, est h=0

Figure64:  $T_z$  given  $T_{zz}$ , File 1

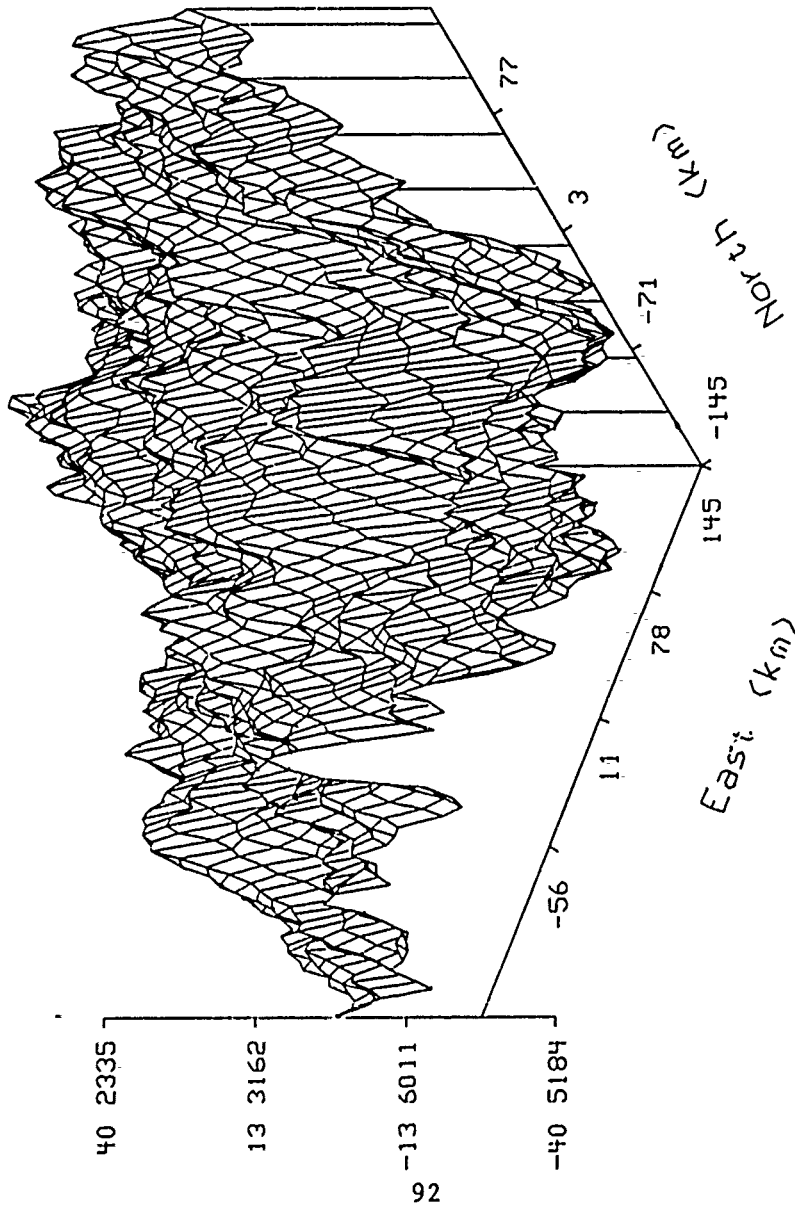
alpha hat



. Tape 1, file 1, meas Txy at h=0.6km

Figure65:  $\hat{\alpha}$  given  $T_{xy}$ , File 1

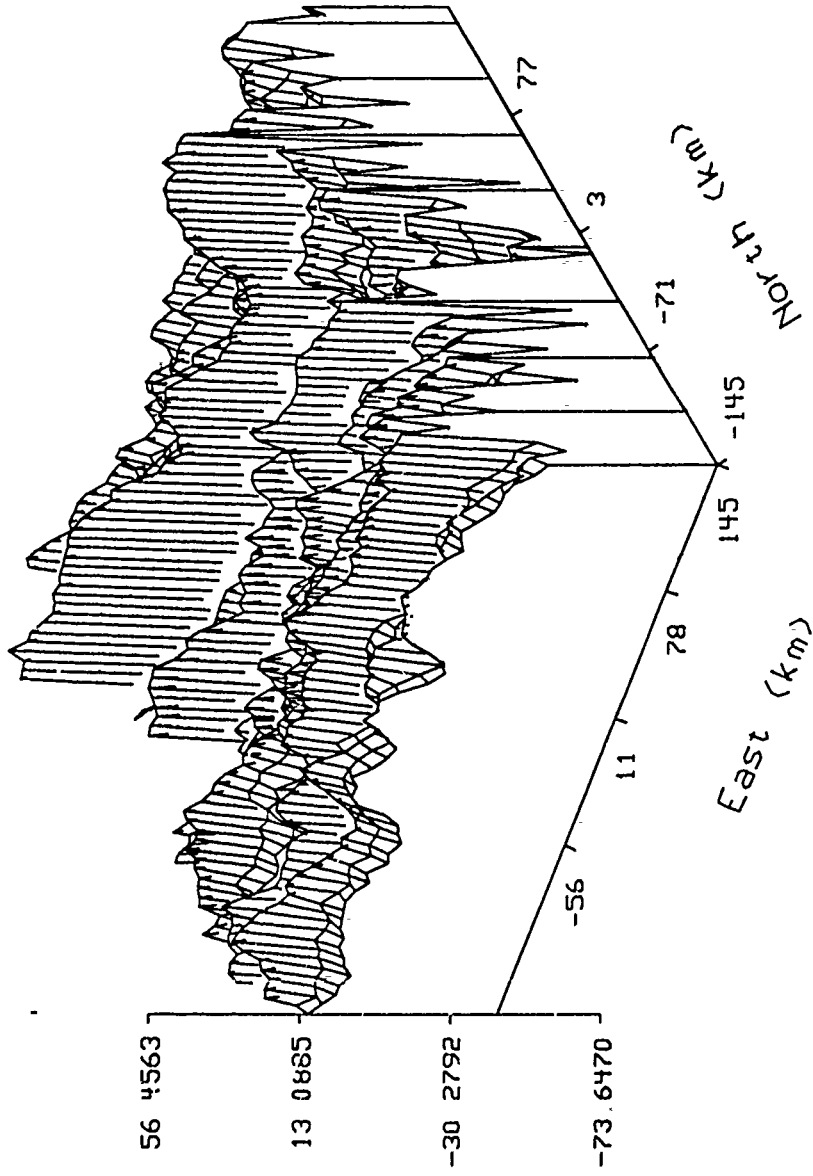
$\hat{T}_x$  (mgal)



Tape 1, file 1, meas  $T_{xy}$  at  $h=0$  6km, est  $h=0$

Figure66:  $\hat{T}_x$  given  $T_{xy}$ , File 1

Ty hat (mgal)

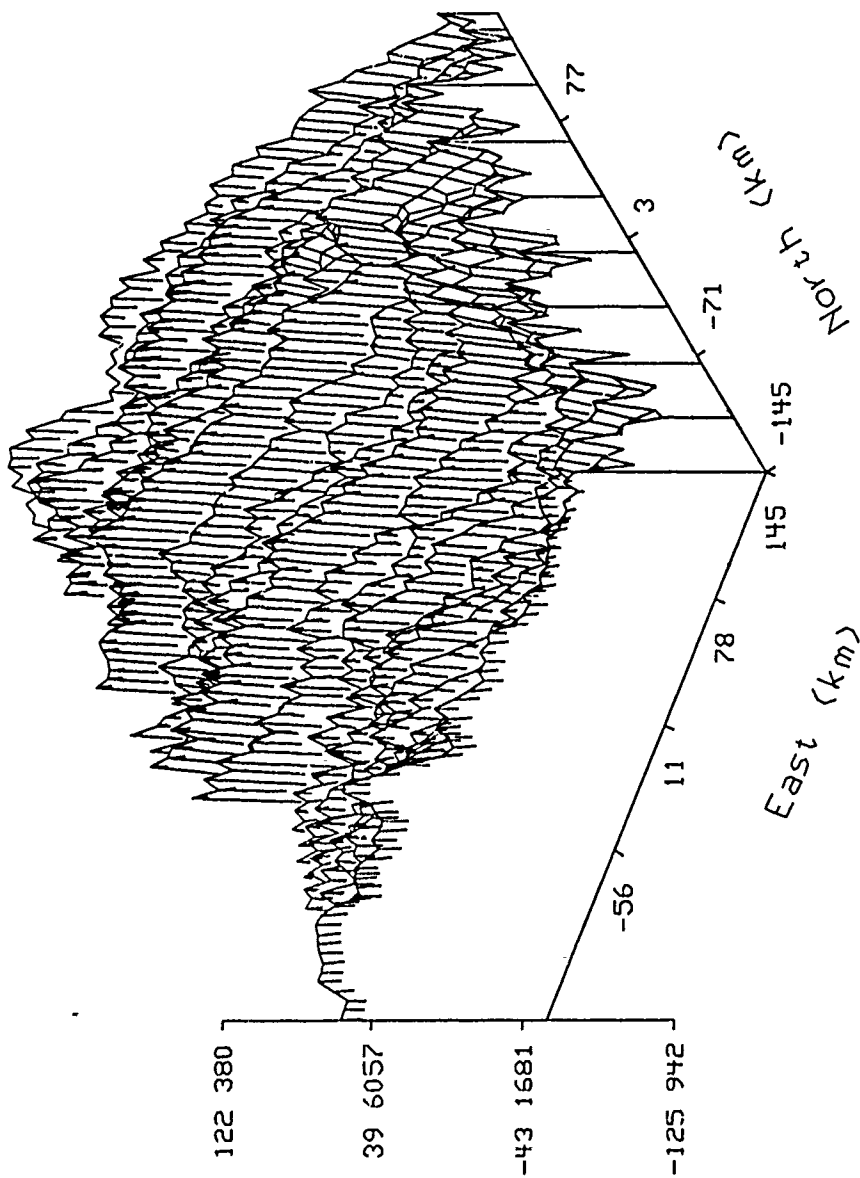


93

Tape 1., file 1, meas  $T_{xy}$  at  $h=0$  6km, est  $h=0$

Figure67:  $\hat{T}_y$  given  $T_{xy}$ , File 1

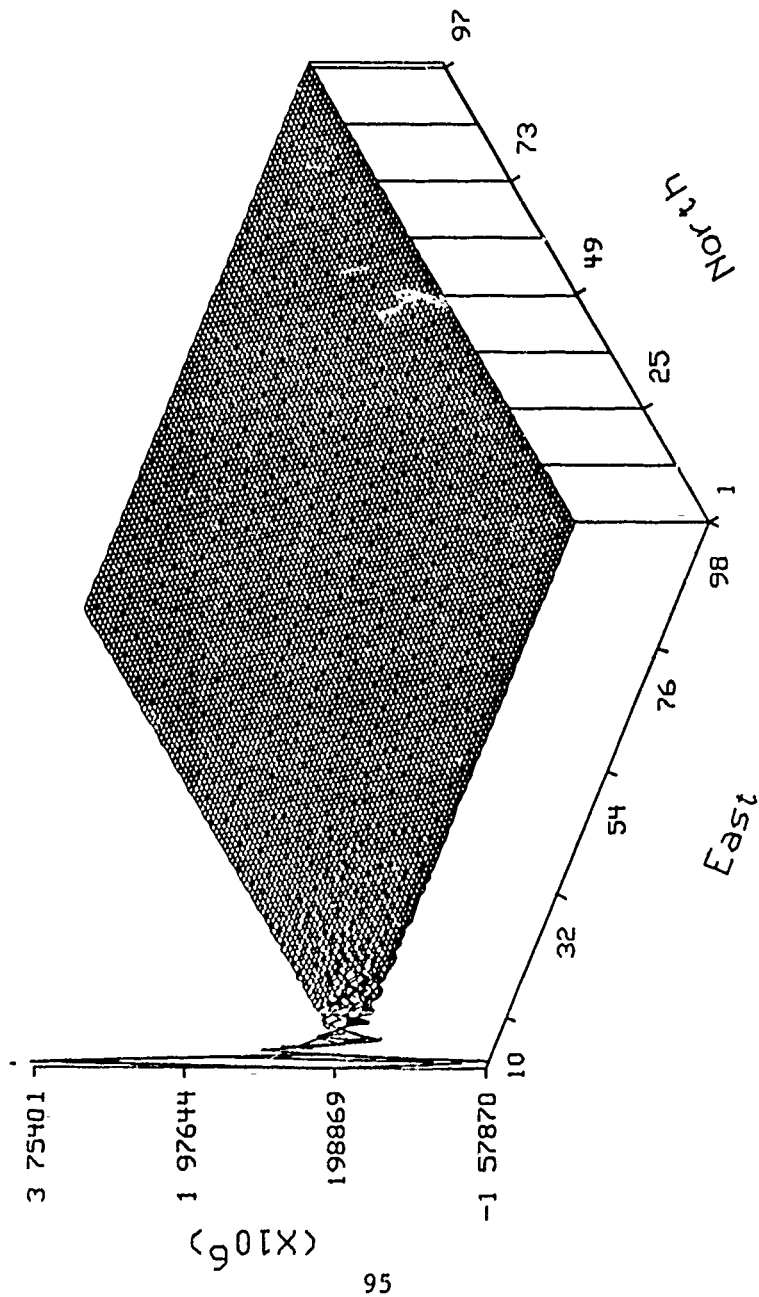
$\hat{T}_z$  (mgal)



Tape 1, file 1, meas  $T_{xy}$  at  $h=0$  6km, est  $h=0$

Figure68:  $\hat{T}_z$  given  $T_{xy}$ , File 1

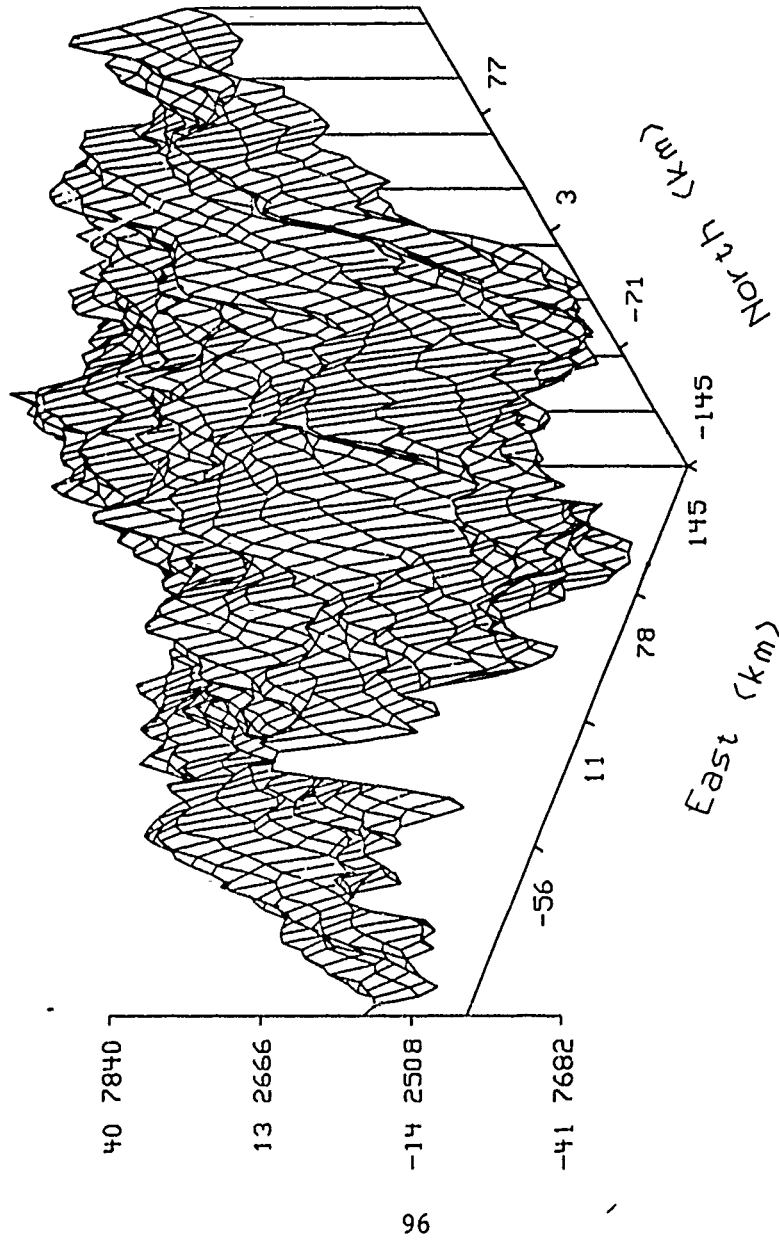
alpha hat



Tape 1, file 1, meas T<sub>yz</sub> at h=0.6km

Figure69:  $\hat{\alpha}$  given T<sub>yz</sub>, File 1

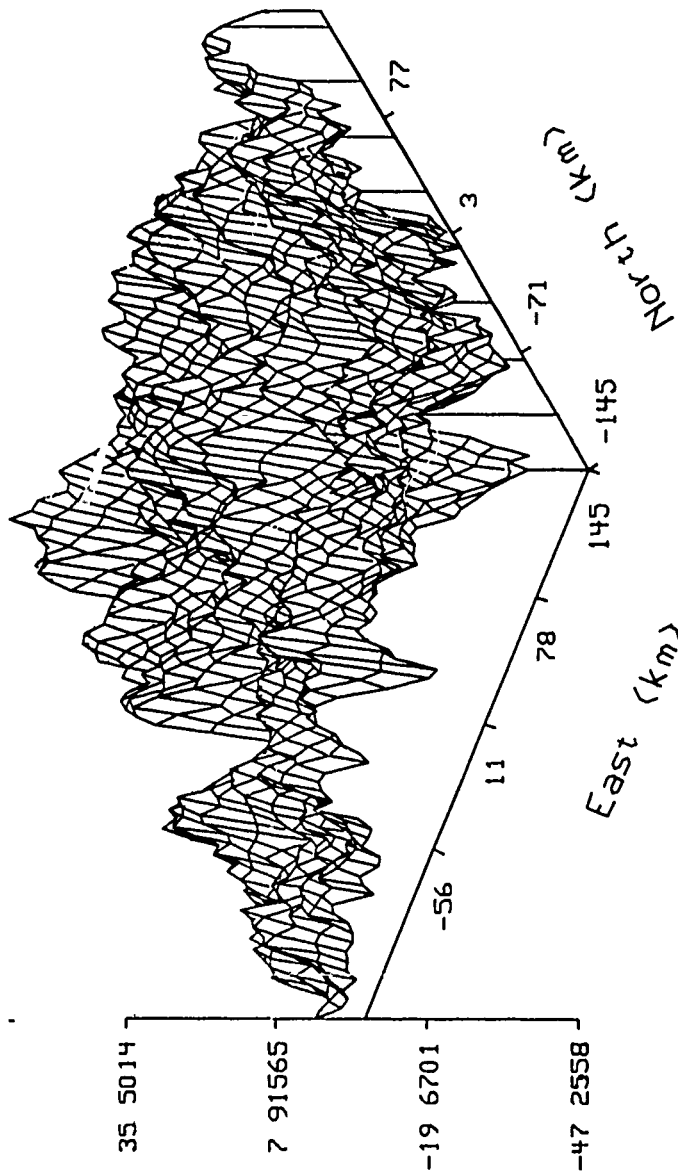
Tx hat (mgal)



Tape 1, file 1, meas Tyz at h=0 6km, est h=0

Figure70:  $\hat{T}_x$  given  $T_{yz}$ , File 1

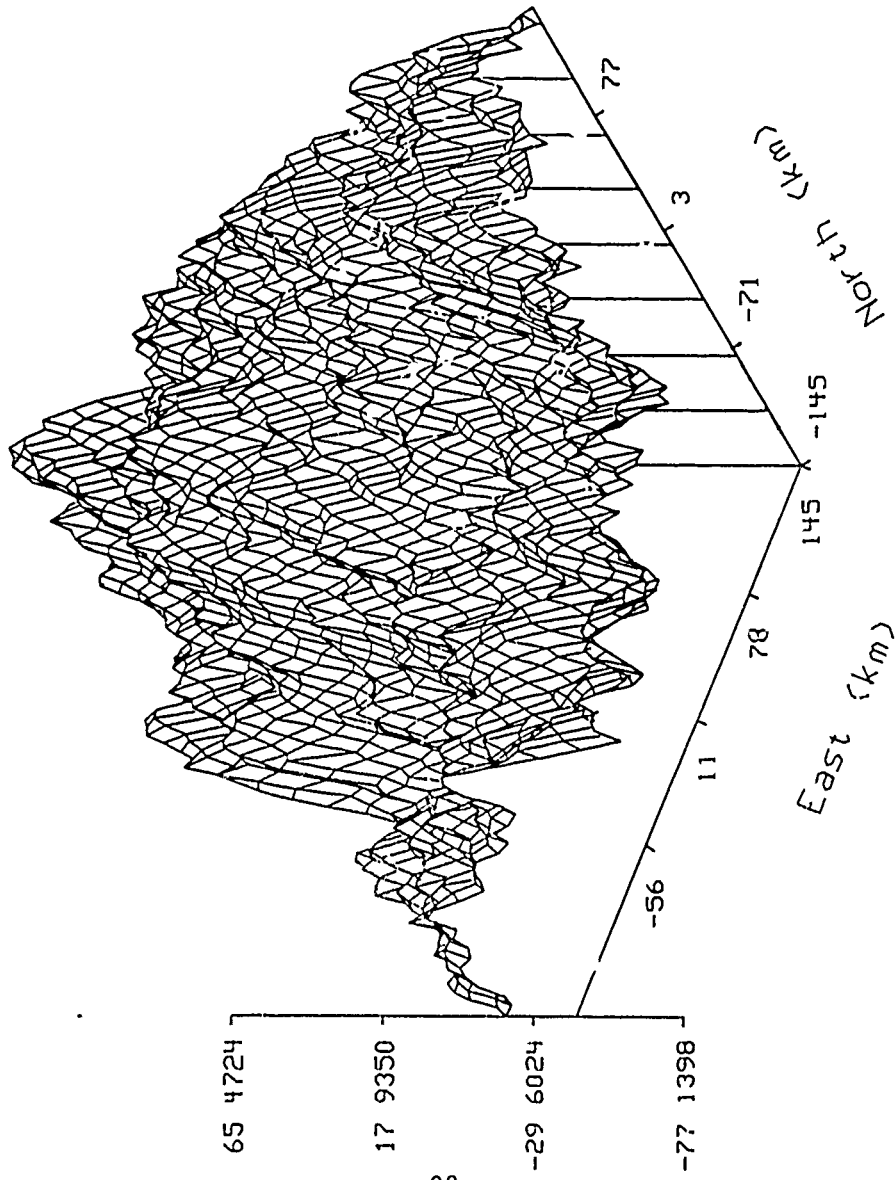
Ty hat (mgal)



Tape 1, file 1, meas Tyz at h=0 6km. est h=0

Figure 71:  $\hat{T}_y$  given  $T_{yz}$ , File 1

$\hat{T}_z$  (mgal)



Tape 1, file 1, meas  $T_{yz}$  at  $h=0$  6km, est  $h=0$

Figure 72:  $\hat{T}_z$  given  $T_{yz}$ , File 1

alpha hat

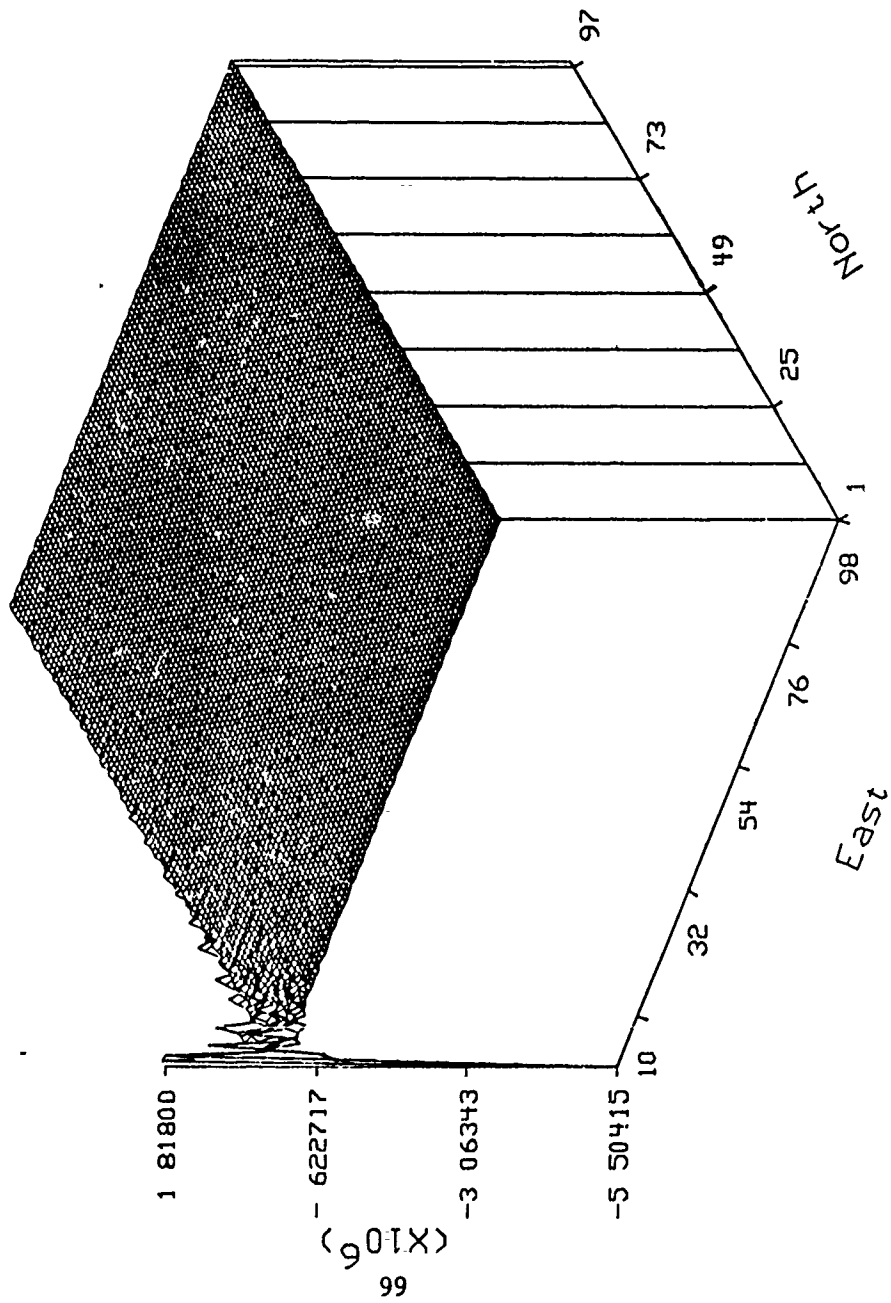
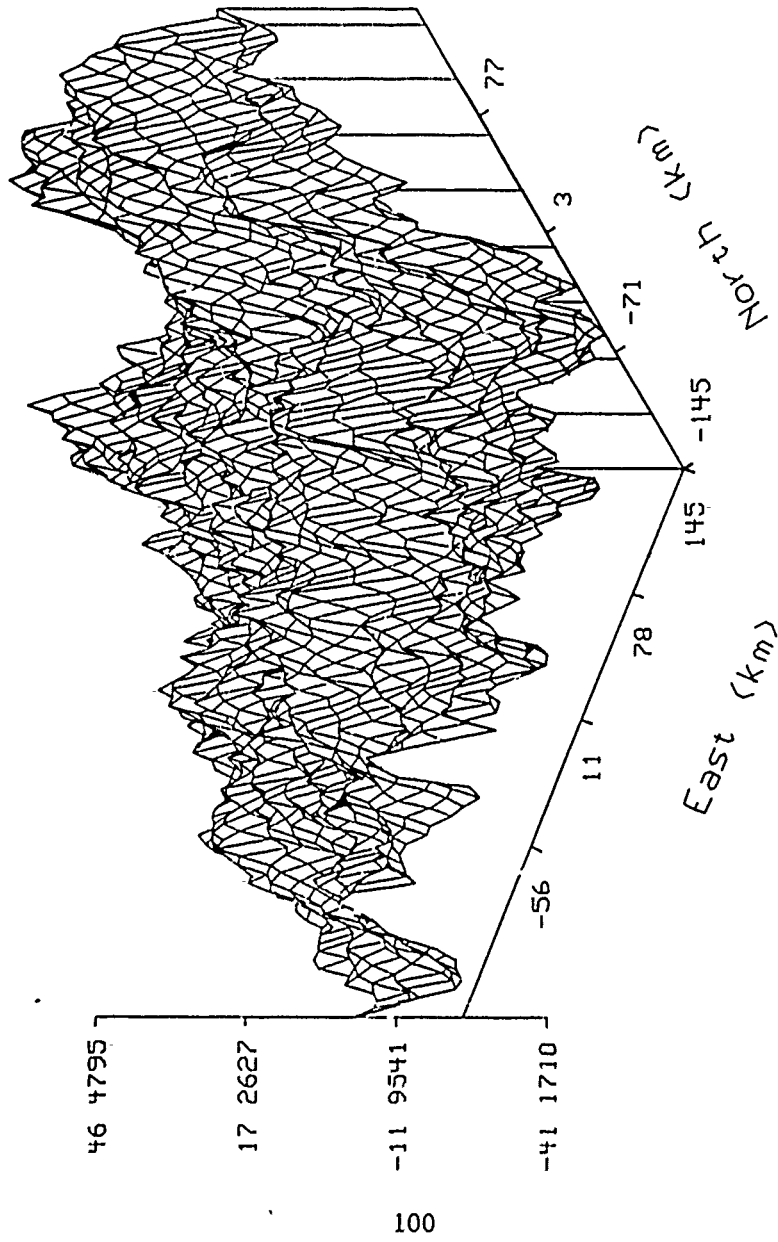


Figure 73:  $\hat{\alpha}$  given  $T_{xx}$ , File 1

File 1, Tape 1, meas  $T_{xx}$  at  $h=0.6\text{km}$

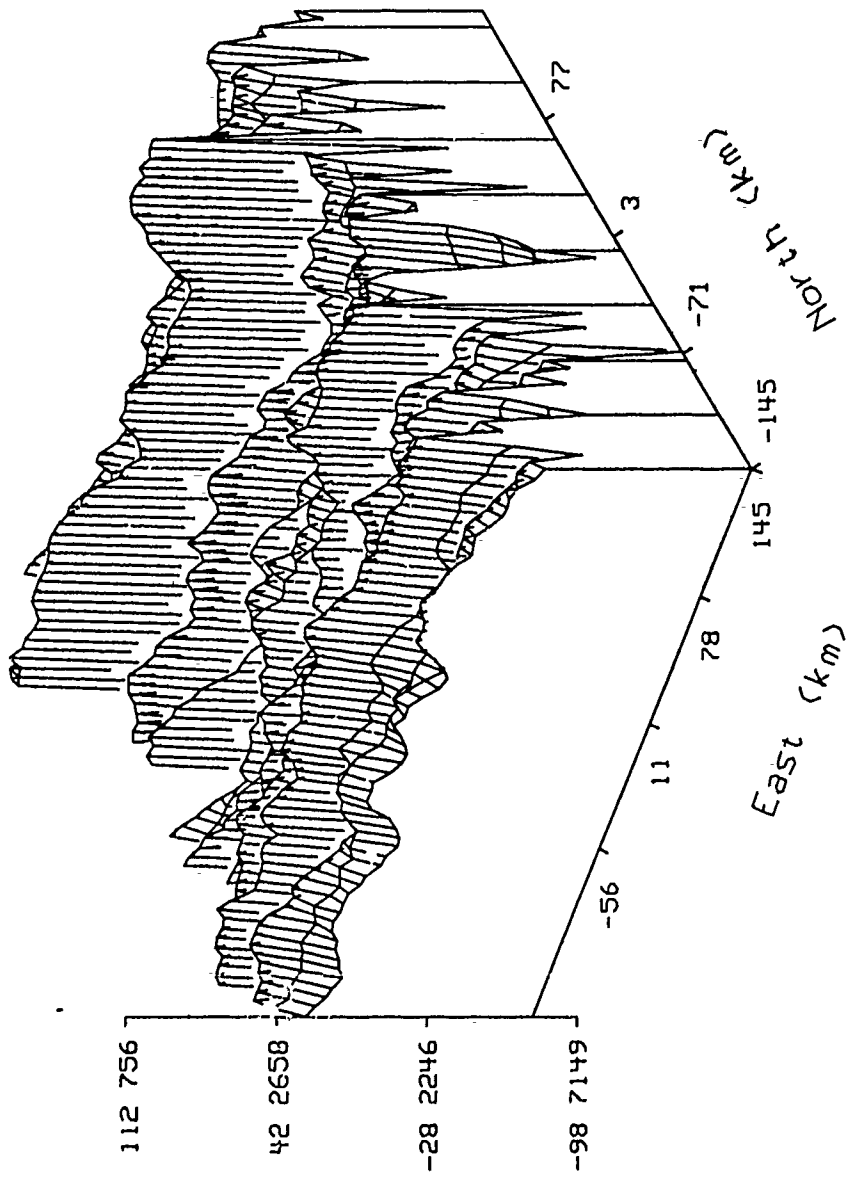
$\hat{T}_x$  (mgal)



Tape 1, file 1, meas  $T_{xz}$  at  $h=0$  6km, est  $h=0$

Figure74:  $\hat{T}_x$  given  $T_{zz}$ , File 1

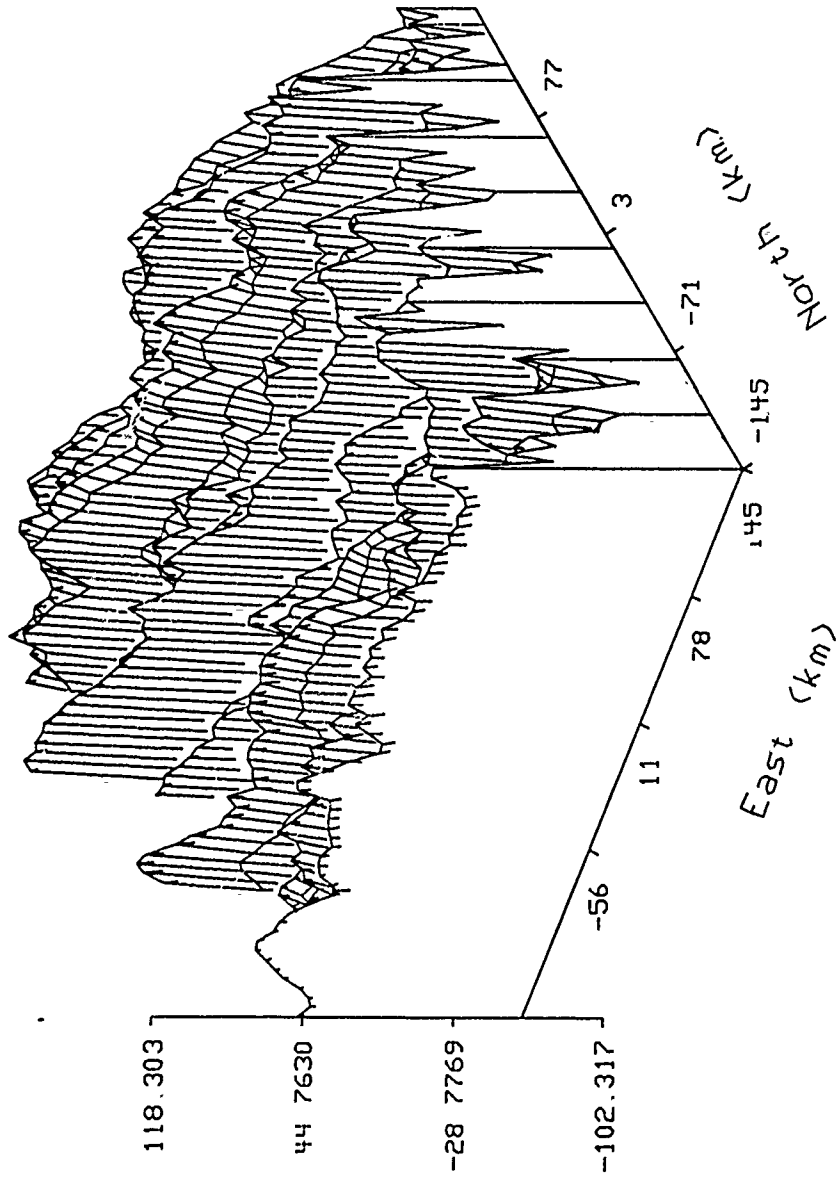
Ty hat (mgal)



Tape 1, file 1, meas  $T_{xz}$  at  $h=0$  6km, est  $h=0$

Figure75:  $\hat{T}_y$  given  $T_{zz}$ , File 1

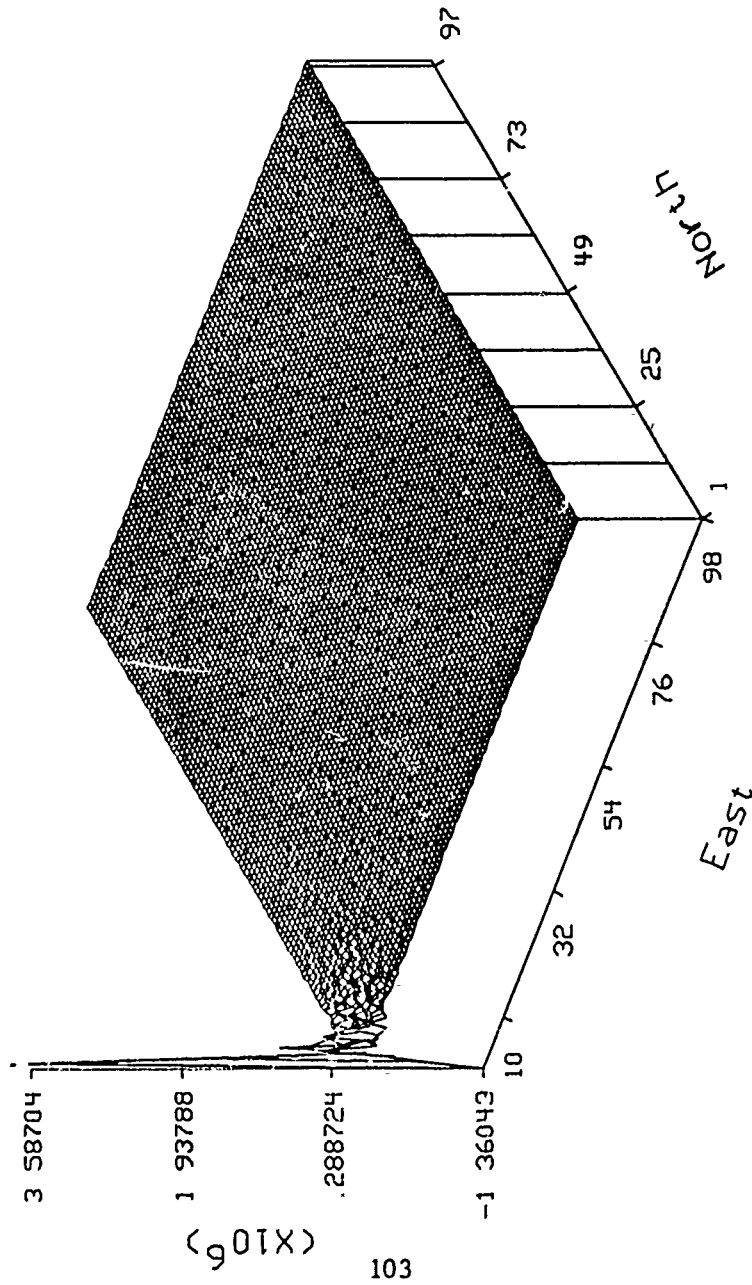
$\hat{T}_z$  (mgal)



Tape 1, file 1, meas  $T_xz$  at  $h=0$  6km, est  $h=0$

Figure76:  $\hat{T}_z$  given  $T_{xz}$ , File 1

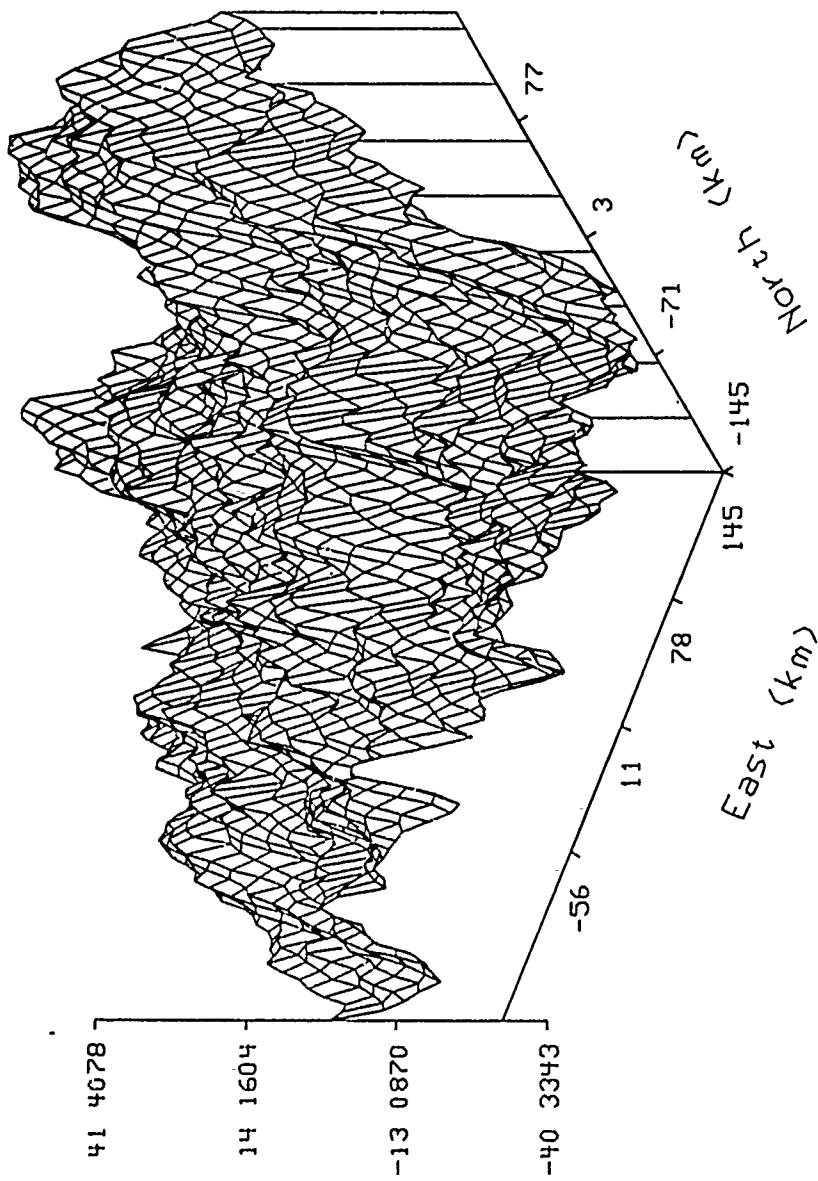
alpha hat



Tape 1, file 1, meas full tensor at h=0.6km

Figure77:  $\hat{\alpha}$  given full tensor gradient, File 1

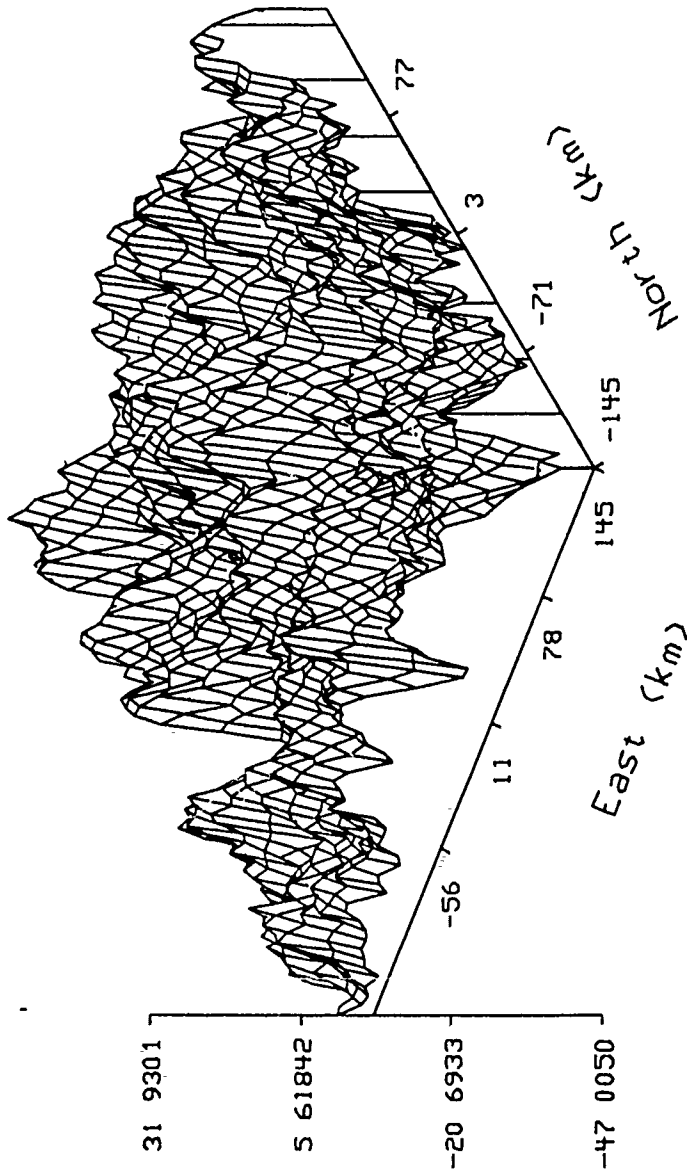
$\hat{T}_x$  (mgal)



Tape 1, file 1, meas full tensor at  $h=0$  6km, est  $h=0$

Figure78:  $\hat{T}_x$  given full tensor gradient, File 1

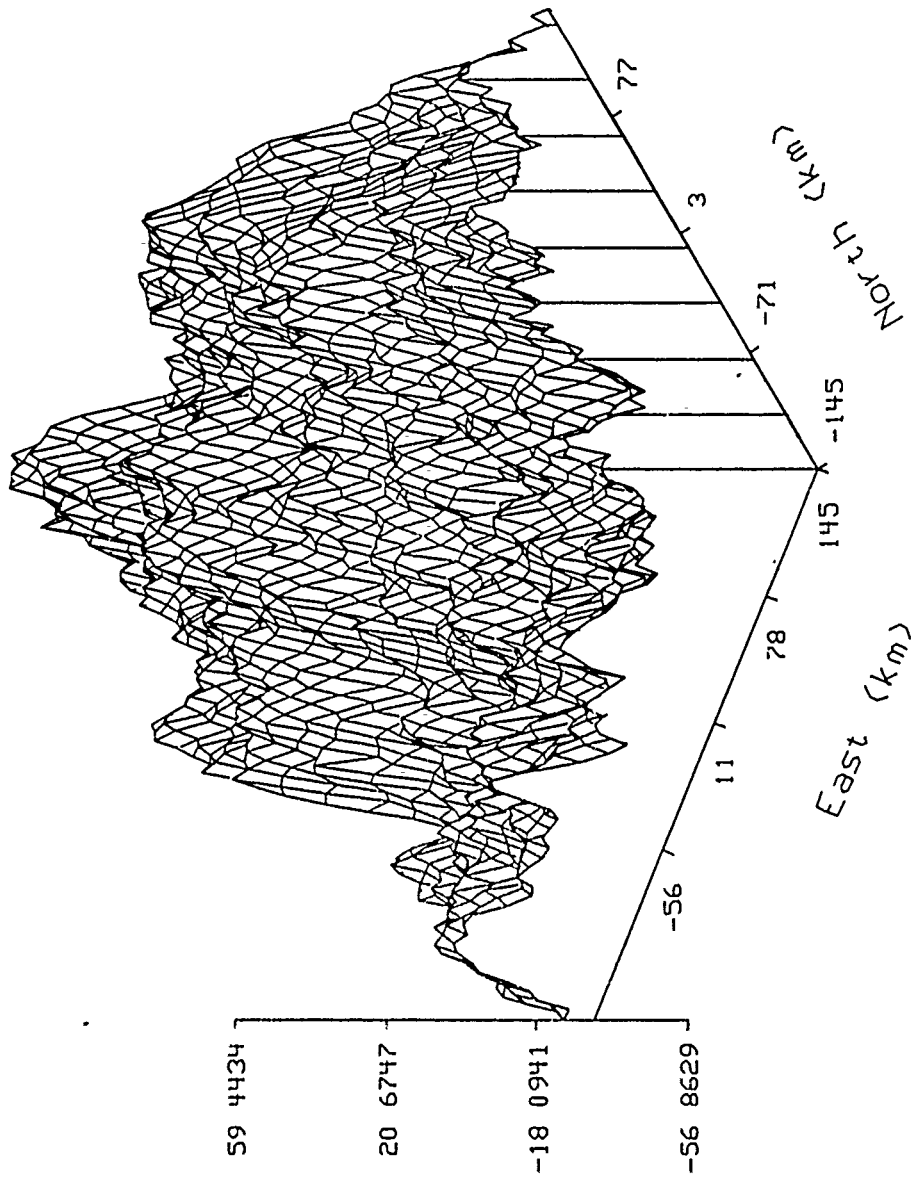
Ty hat (mgal)



Tape 1, file 1, meas full tensor at  $h=0.6\text{km}$ , est  $h=0$

Figure 79:  $\hat{T}_y$  given full tensor gradient, File 1

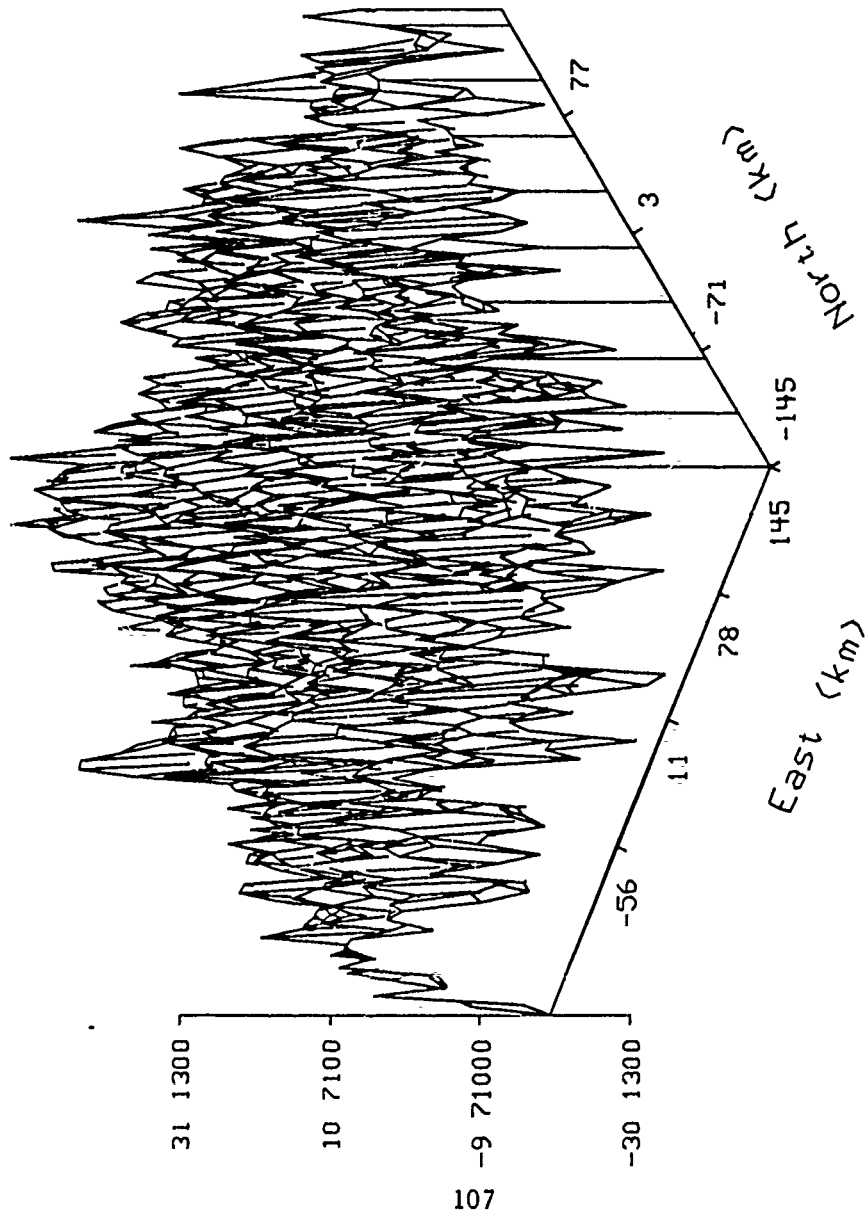
$\hat{T}_z$  (mgal)



Tape 1, file 1, meas full tensor at  $h=0$  6km, est  $h=0$

Figure80:  $\hat{T}_z$  given full tensor gradient, File 1

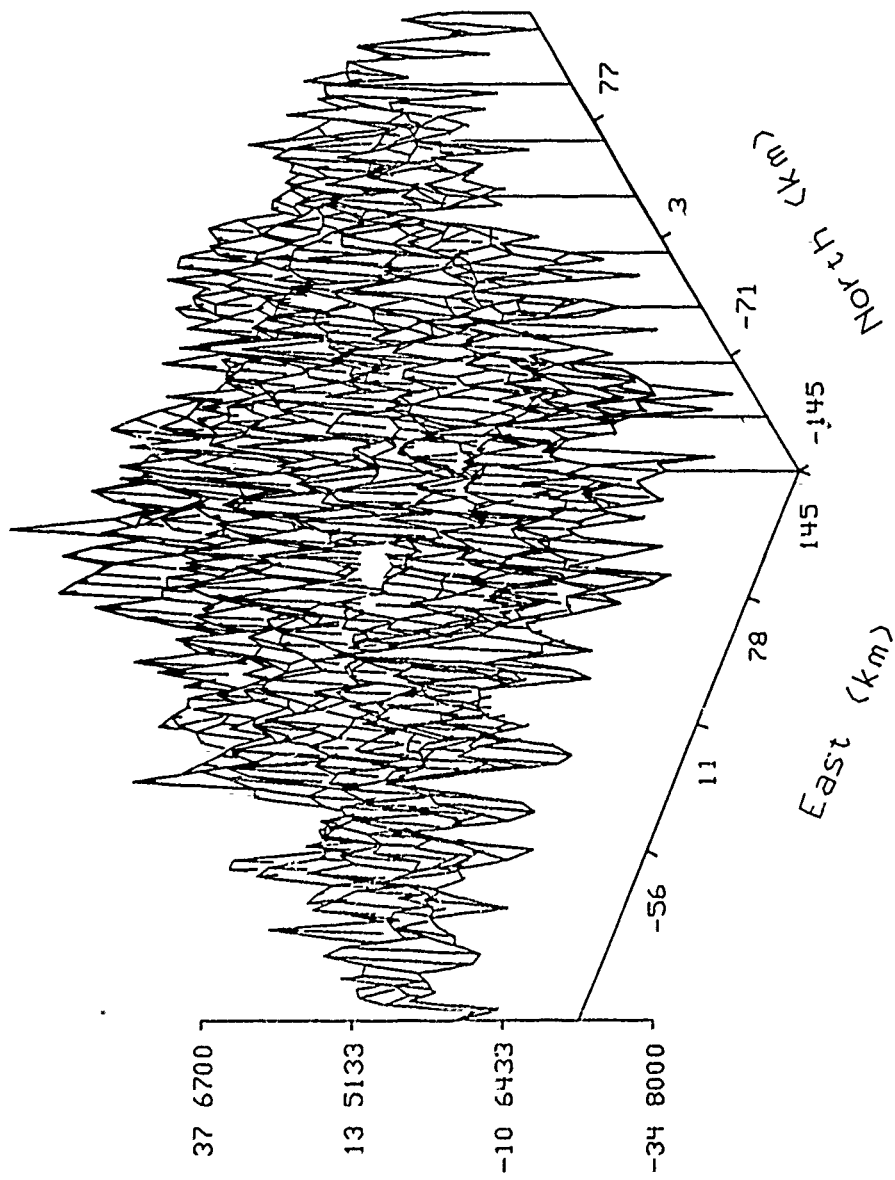
Txx (Eotvos)



. . . Tape 1, file 2, meas at h=0 6km

Figure81: Measured  $T_{xx}$ , File 2

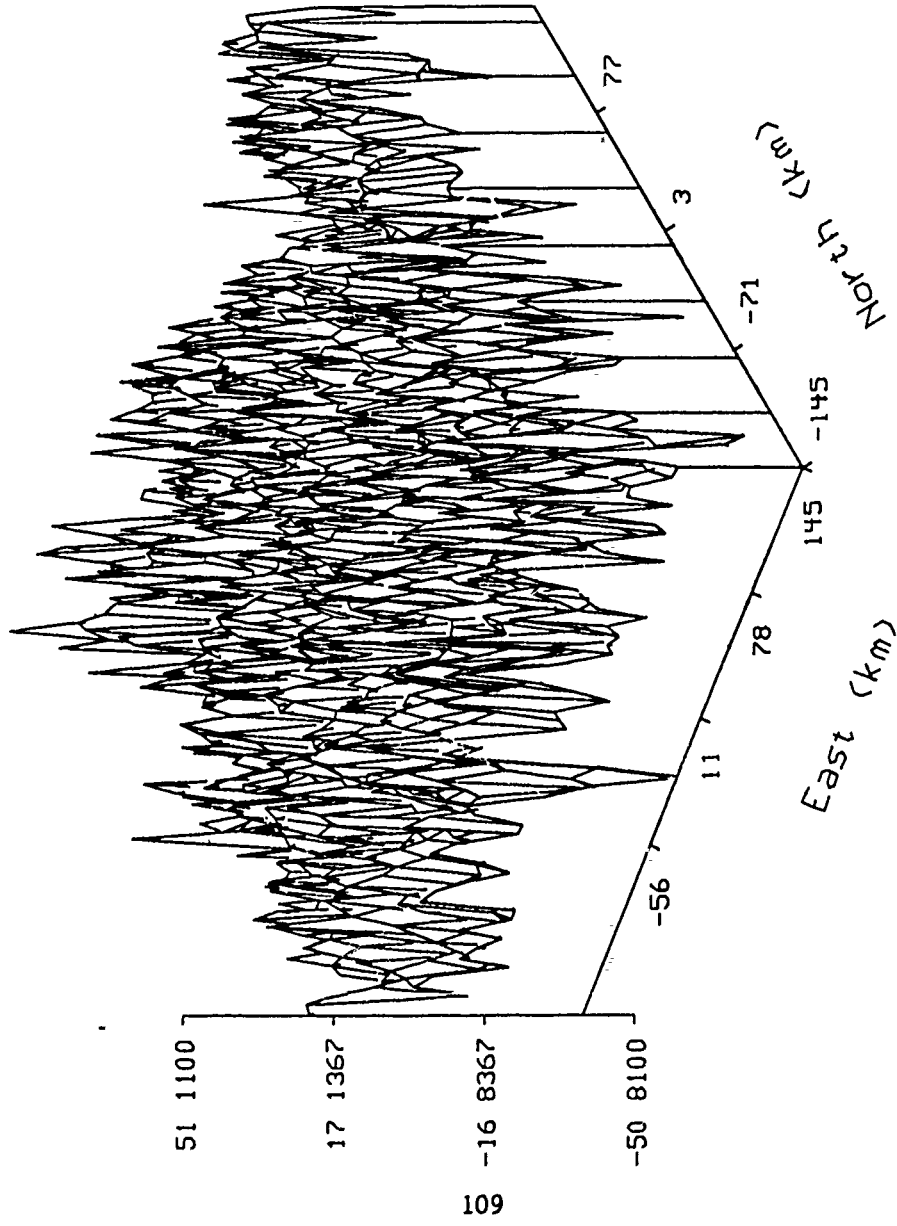
$T_{yy}$  (Eotvos)



.Tape 1, file 2, meas at h=0.6km

Figure82: Measured  $T_{yy}$ , File 2

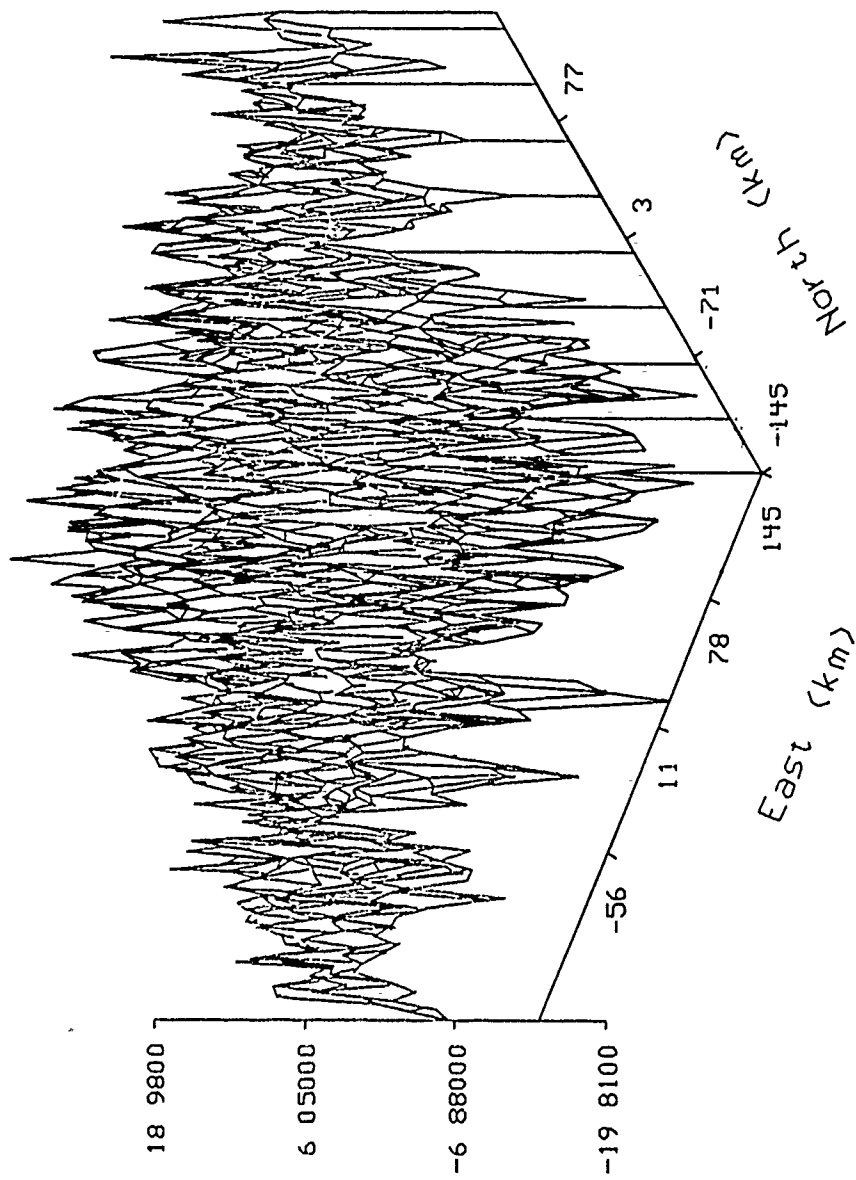
Tzz (Eotvos)



. . Tape 1, file 2, meas at h=0.6km

Figure83: Measured  $T_{zz}$ , File 2

Txy (Eotvos)

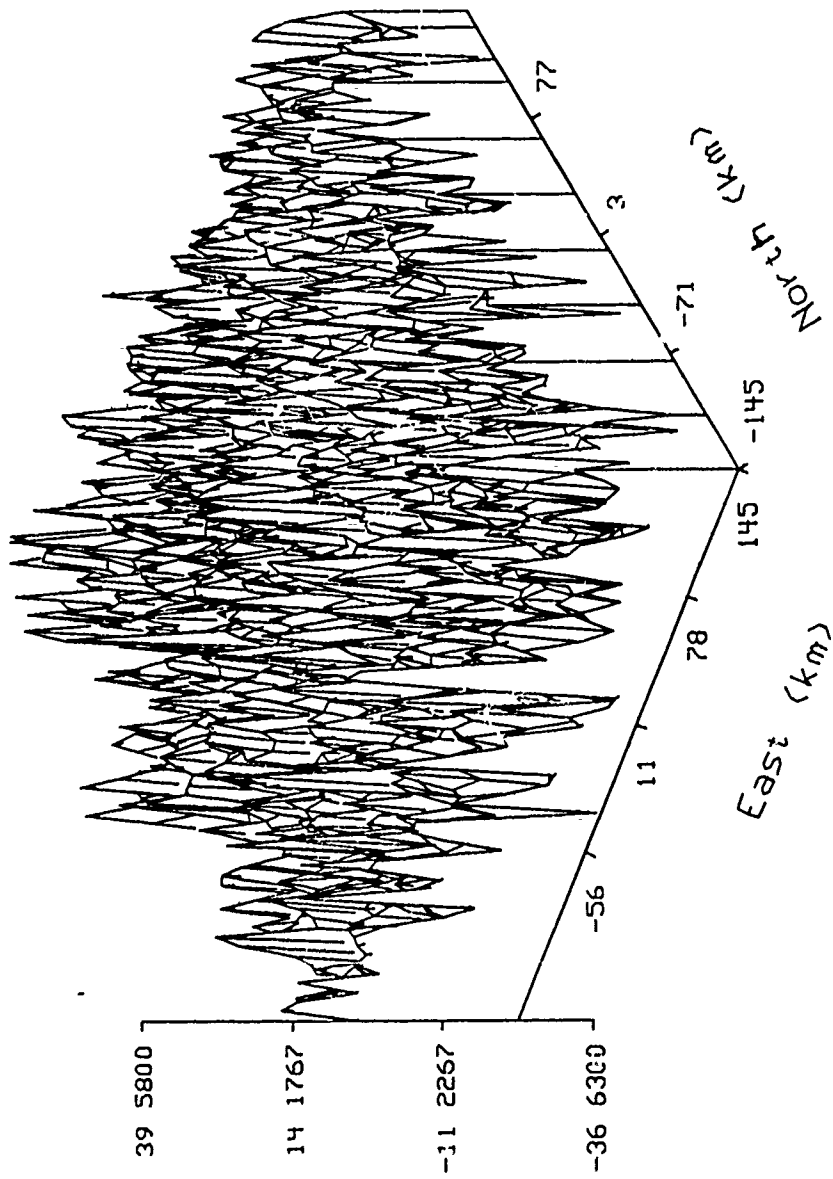


110

. . Tape 1, file 2, meas at h=0 6km

Figure84: Measured  $T_{xy}$ , File 2

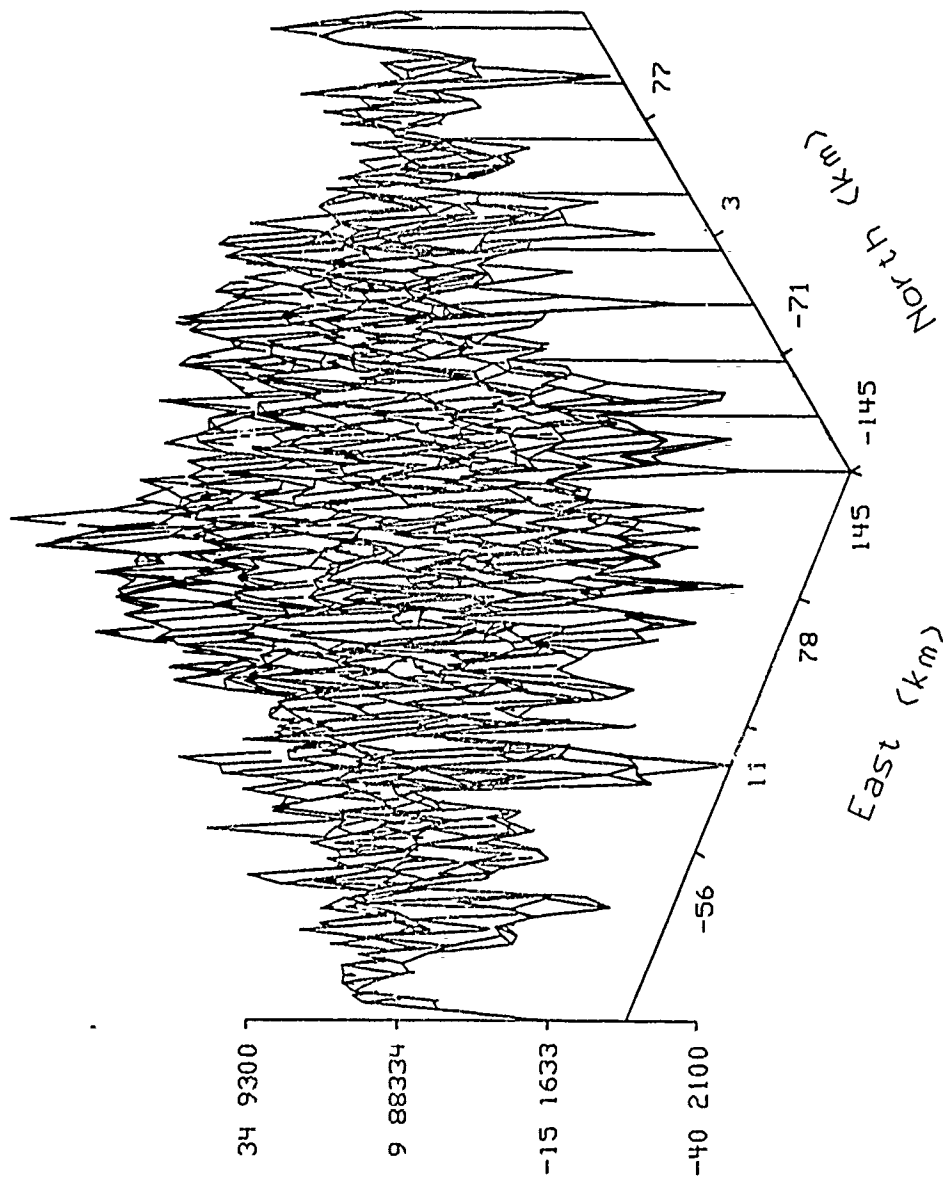
Tyz (Eotvos)



Tape 1, file 2, meas at h=0 6km

Figure85: Measured  $T_{yz}$ , File 2

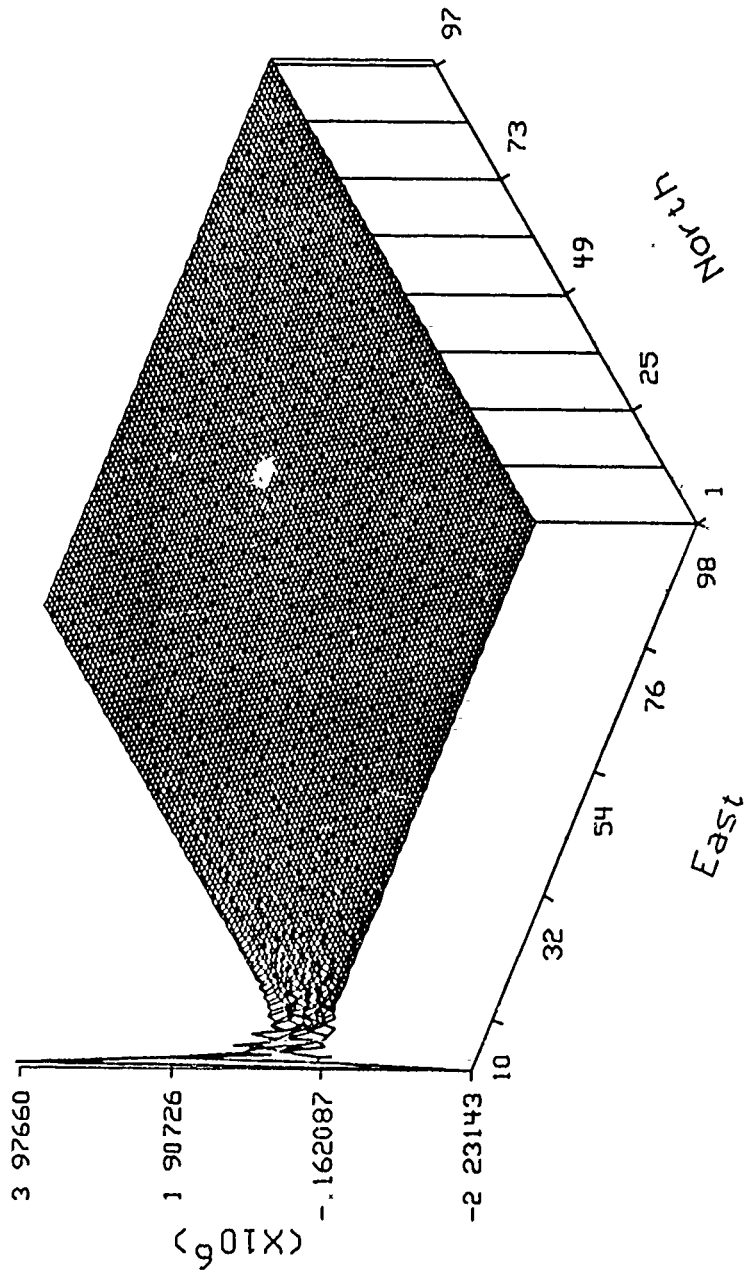
Txz (Eotvos)



. . . Tape 1, file 2, meas at h=0 6km

Figure 86: Measured  $T_{xz}$ , File 2

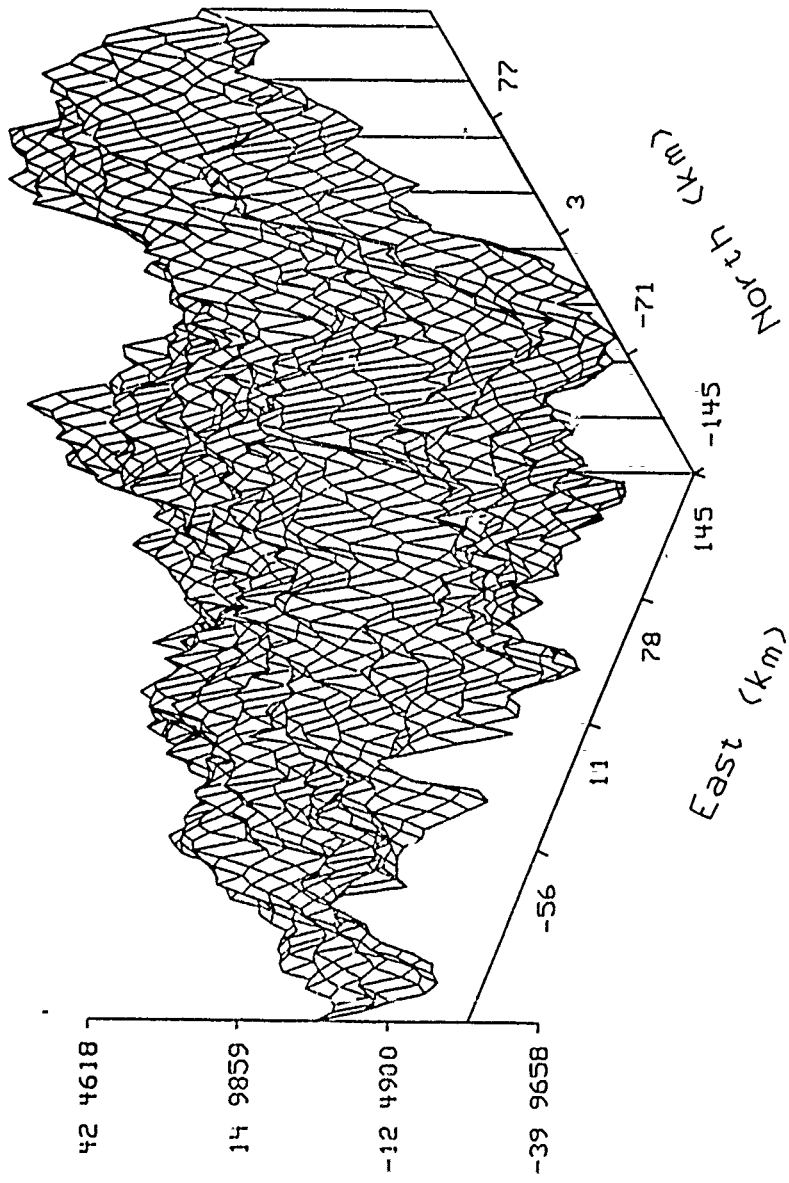
alpha hat



Tape 1, file 2, meas  $T_{xx}$  at  $h=0$  6km

Figure87:  $\hat{\alpha}$  given  $T_{xx}$ , File 2

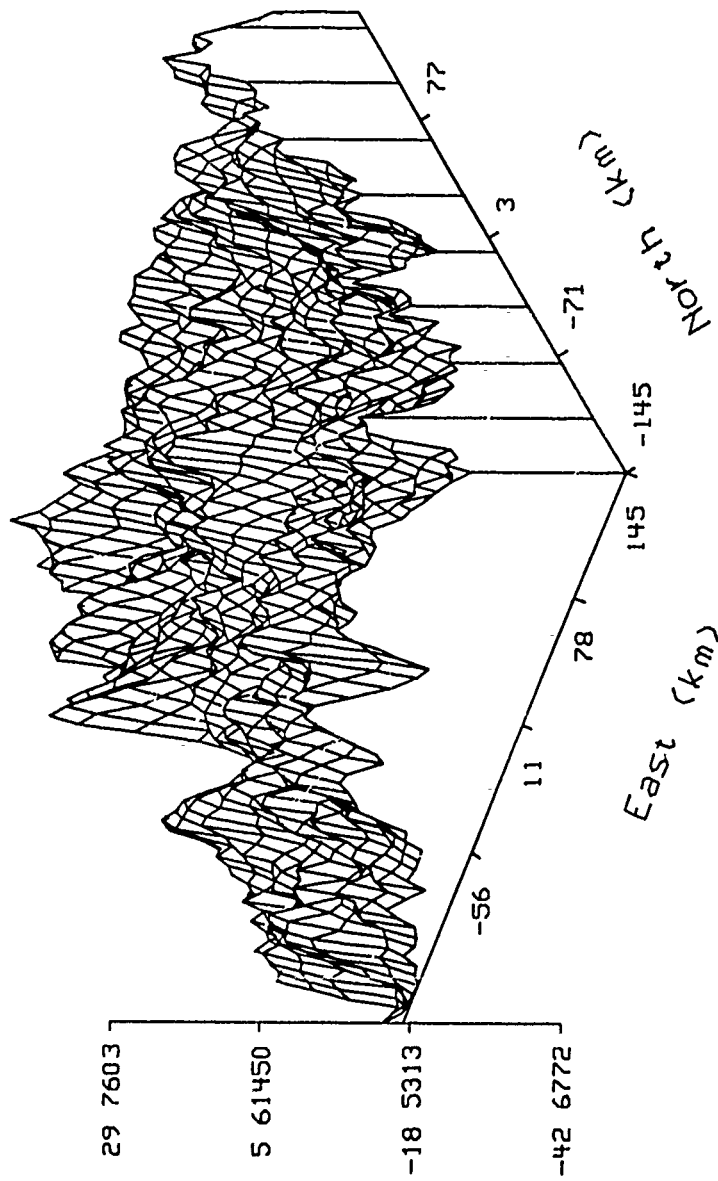
$\hat{T}_x$  (mgal)



Tape 1, file 2, meas  $T_{xx}$  at  $h=0$  km, est  $h=0$

Figure88:  $\hat{T}_z$  given  $T_{xx}$ , File 2

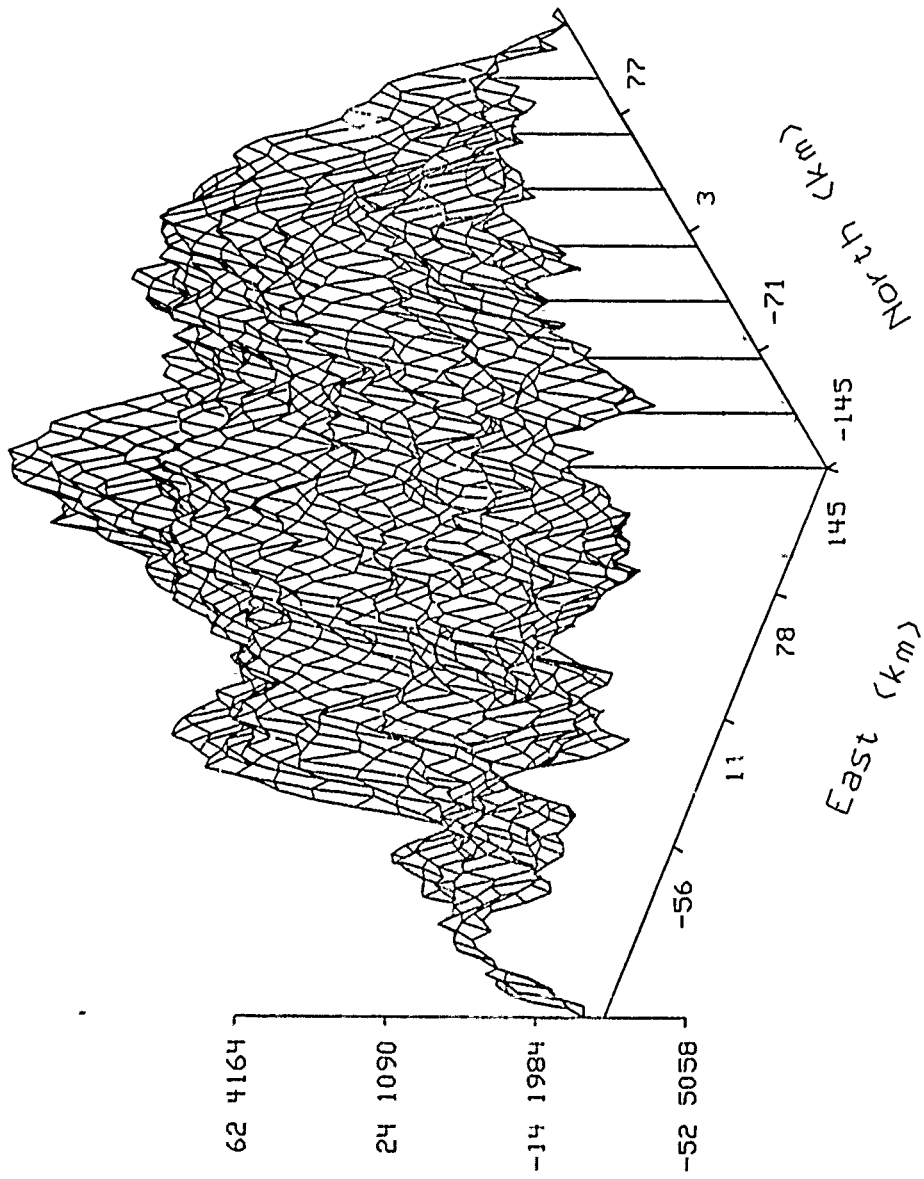
$\hat{T}_y$  (mgal)



Tape 1, file 2, meas  $T_{xx}$  at  $h=0$  6km, est  $h=0$

Figure89:  $\hat{T}_y$  given  $T_{xx}$ , File 2

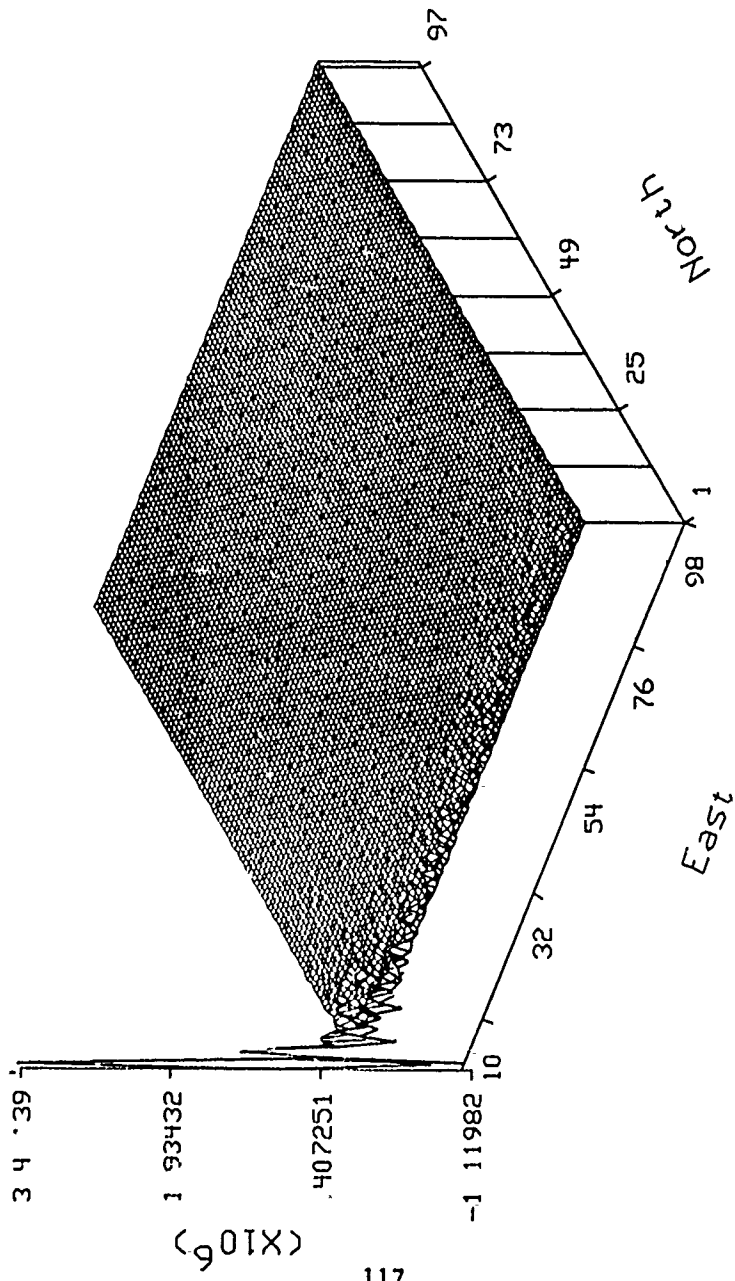
$\hat{T}_z$  (mgal)



Tape 1, file 2, meas  $T_{xx}$  at  $h=0$  6km, est  $h=0$

Figure90:  $\hat{T}_z$  given  $T_{xx}$ , File 2

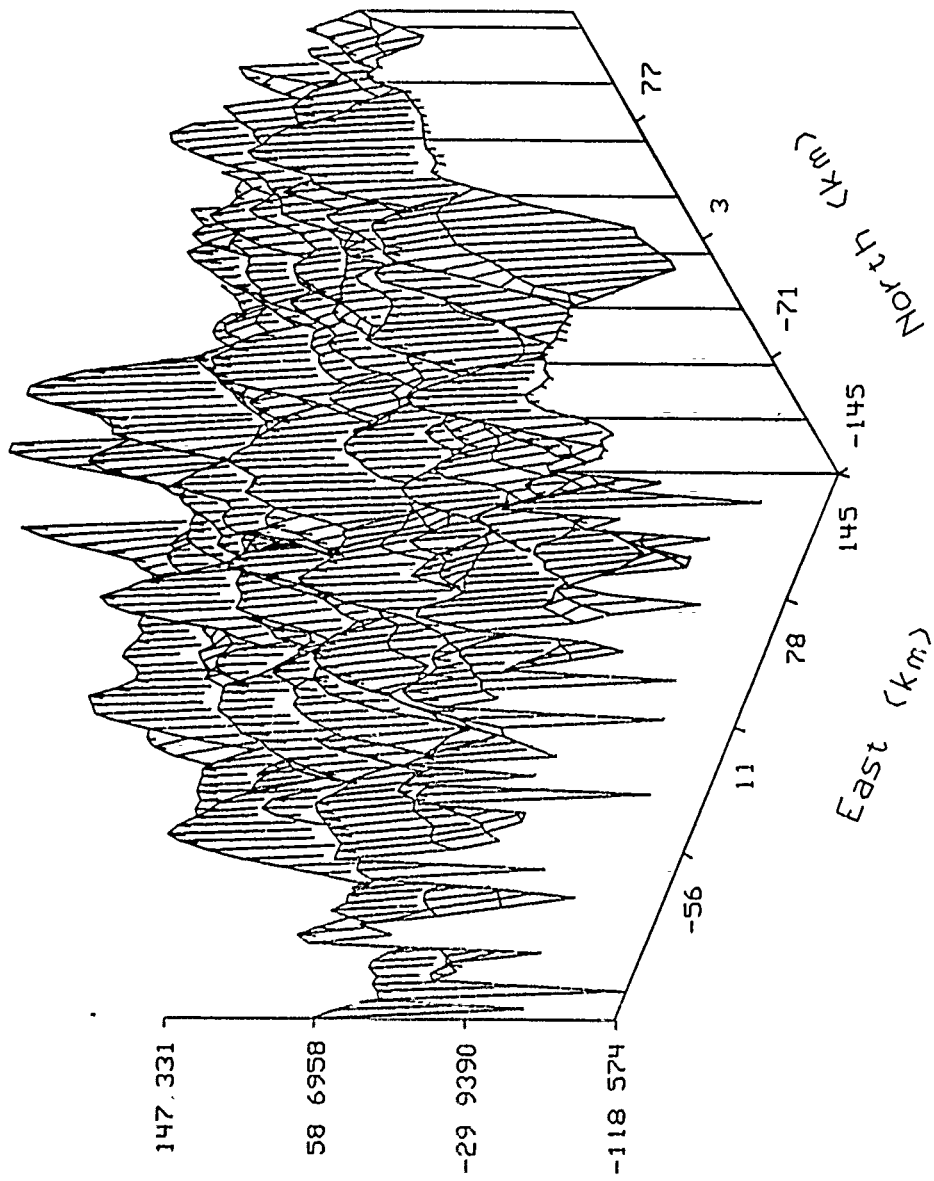
alpha hat



Tape 1, file 2, meas Tyy at h=0 6km

Figure91:  $\hat{\alpha}$  given  $T_{yy}$ , File 2

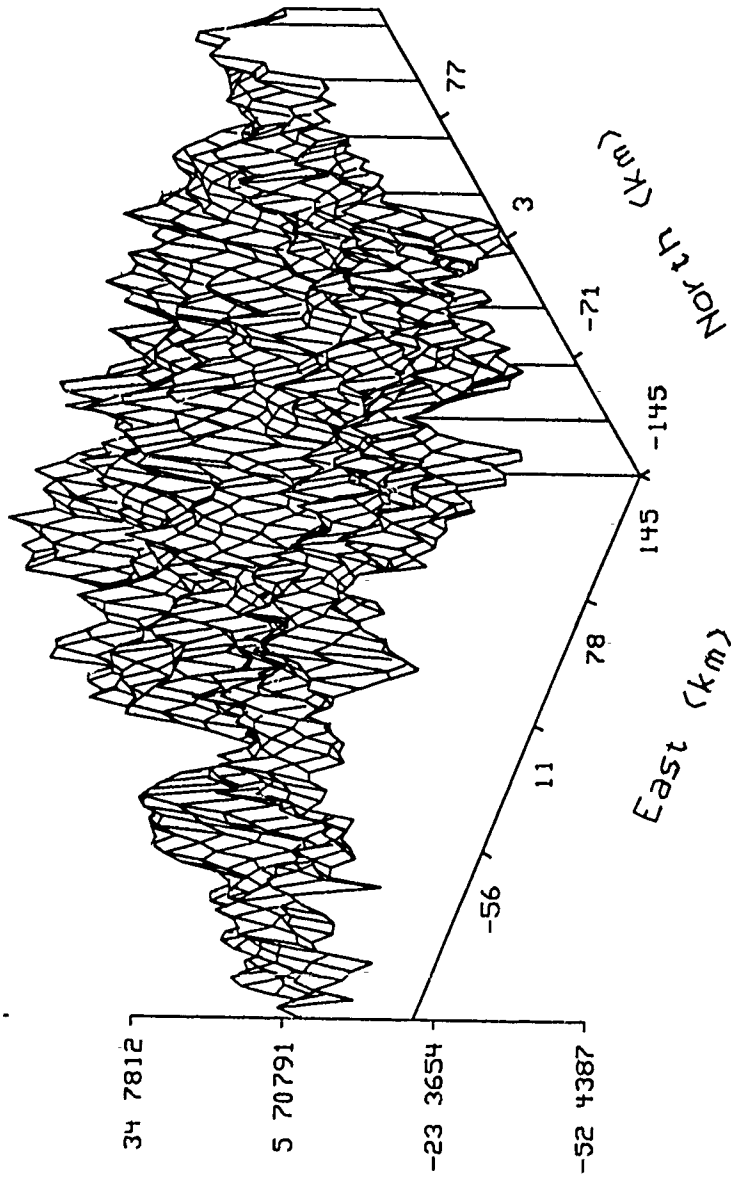
Tx hat (mgal)



Tape 1, file 2, meas Tuu at h=0 6km, est h=0

Figure92:  $\hat{T}_x$  given  $T_{yy}$ , File 2

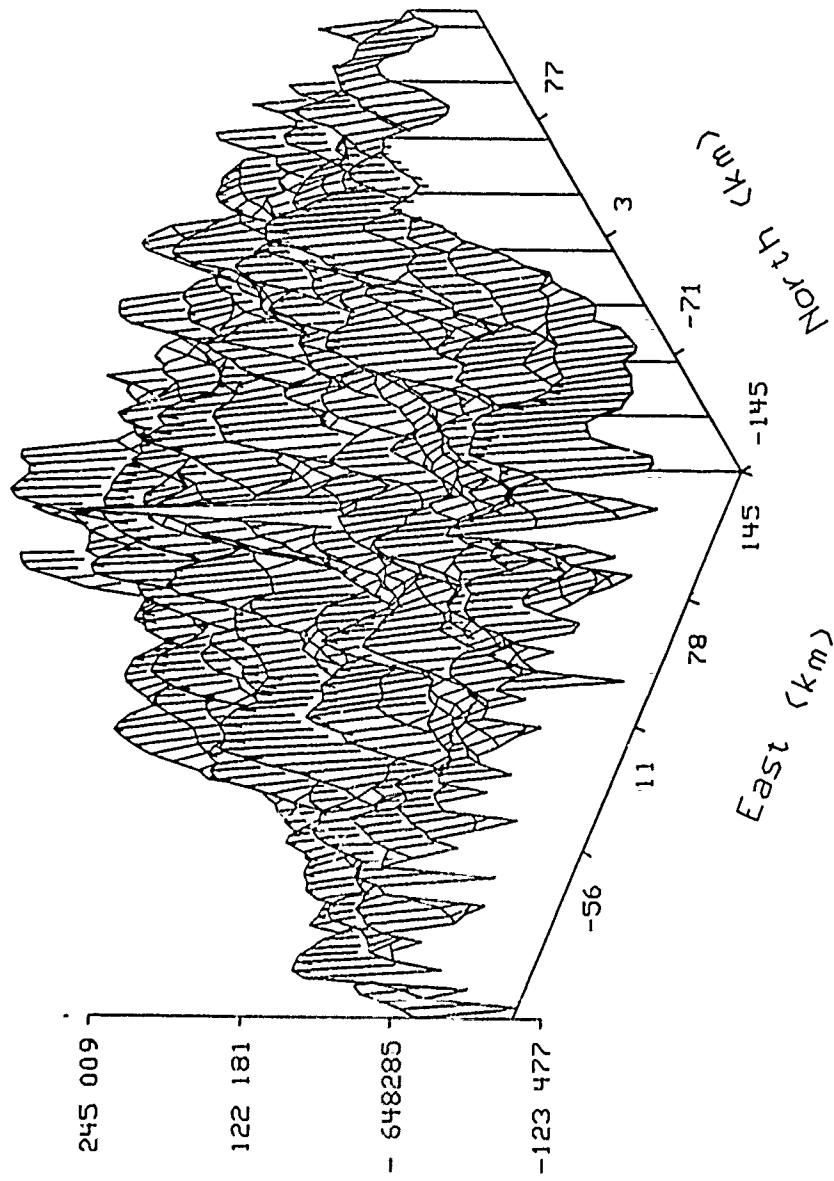
Ty hat (mgal)



Tape 1, file 2, meas Ty at h=0 6km, est h=0

Figure93:  $\hat{T}_y$  given  $T_w$ , File 2

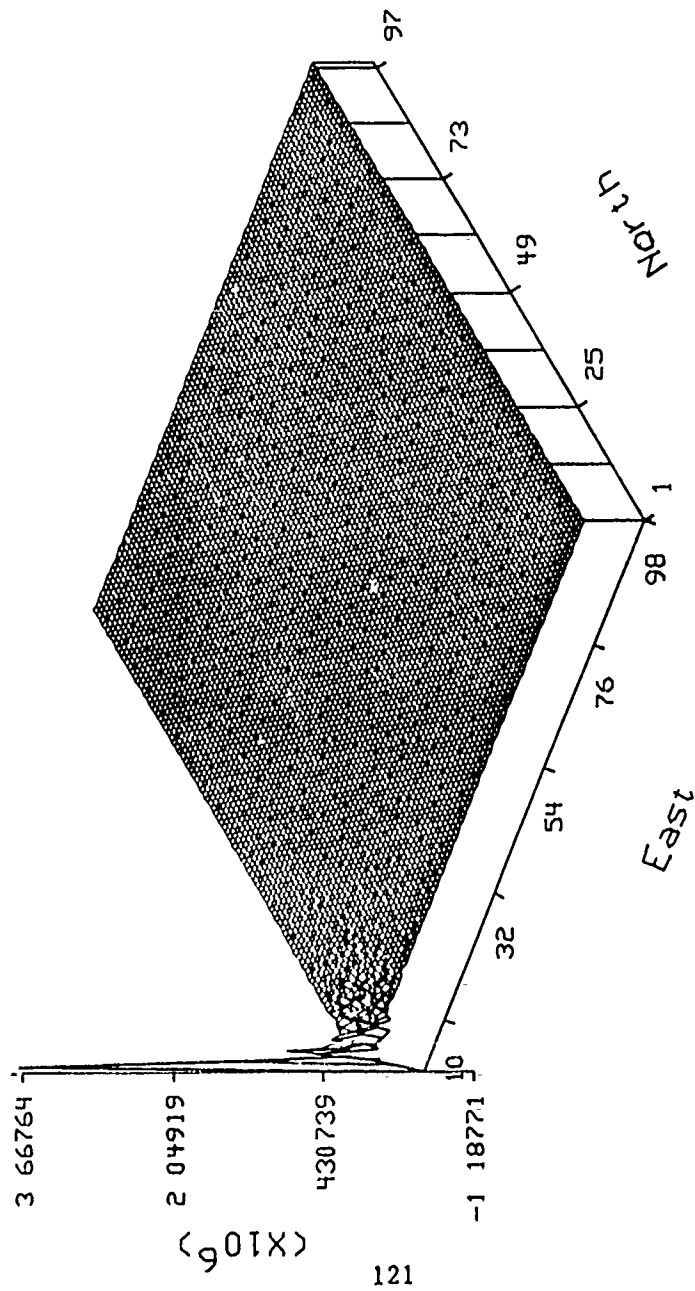
$\hat{T}_z$  (mgal)



Tape 1, file 2, meas  $T_{yy}$  at  $h=0$  6km, est  $h=0$

Figure94:  $\hat{T}_z$  given  $T_{yy}$ , File 2

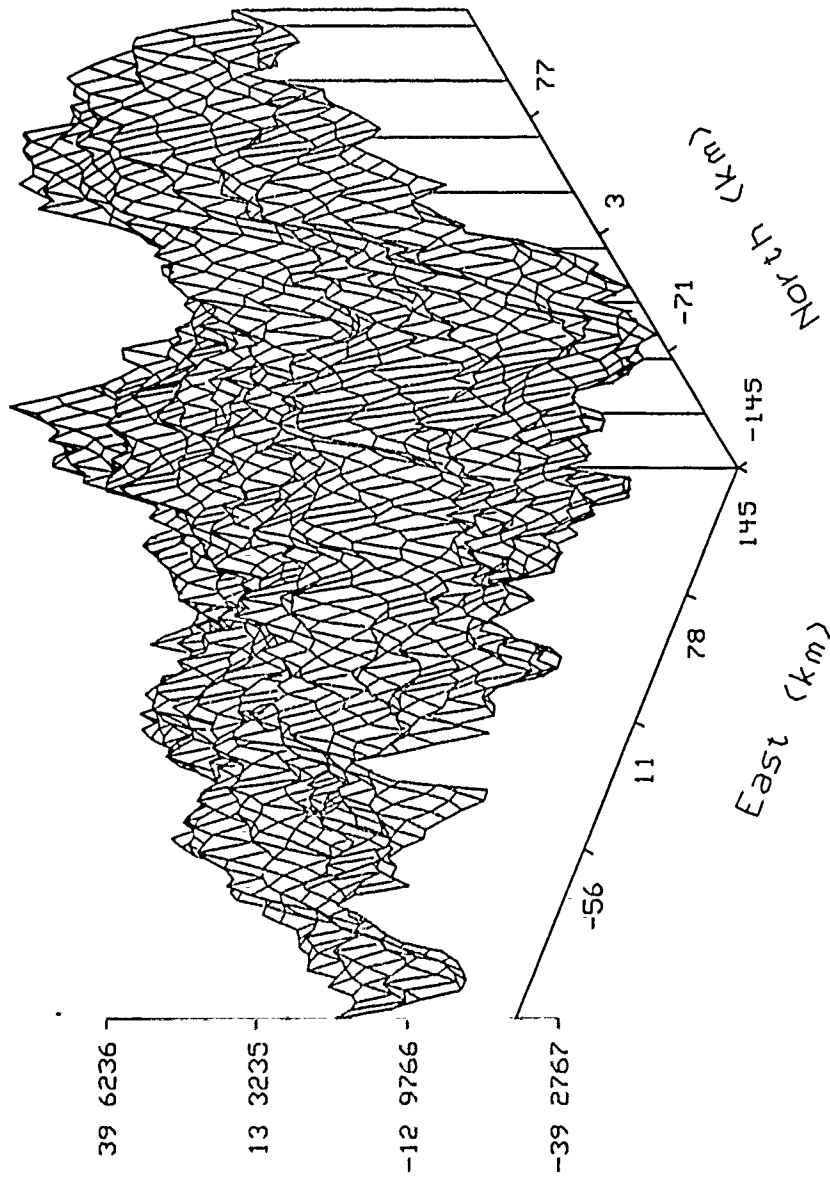
alpha hat



Tape 1, file 2, meas Tzz at h=0.6km

Figure95:  $\hat{\alpha}$  given  $T_{zz}$ , File 2

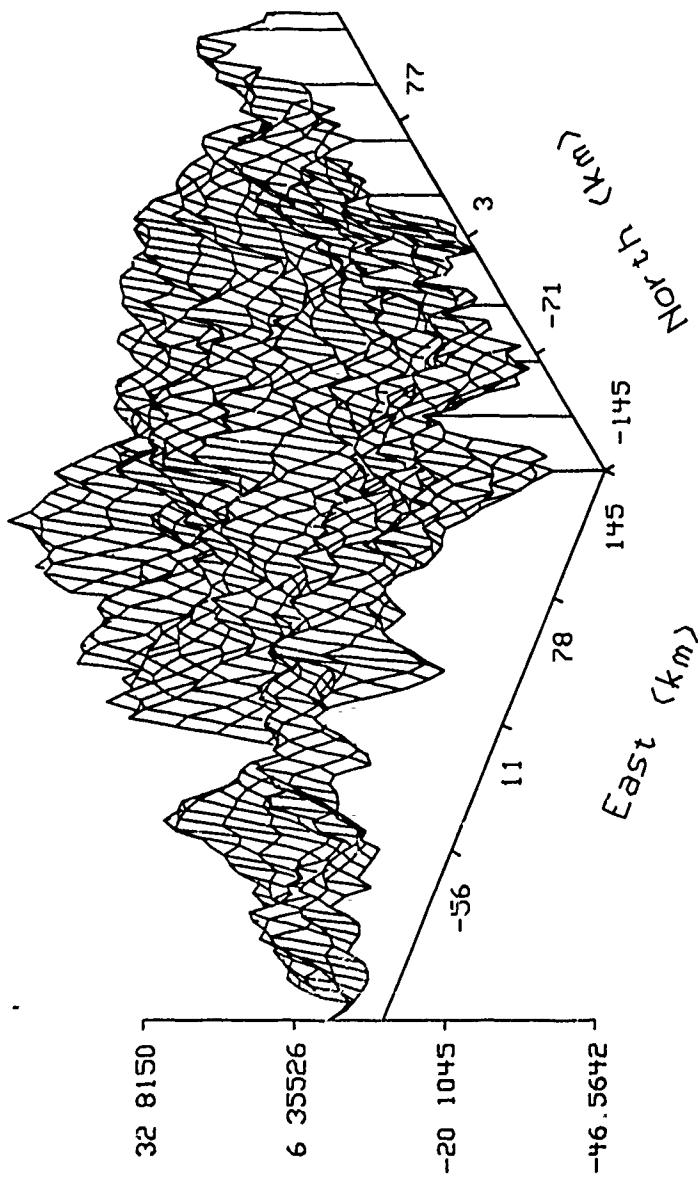
$\hat{T}_x$  (mgal)



Tape 1, file 2, meas  $T_{zz}$  at  $h=0$  6km, est  $h=0$

Figure96:  $\hat{T}_x$  given  $T_{zz}$ , File 2

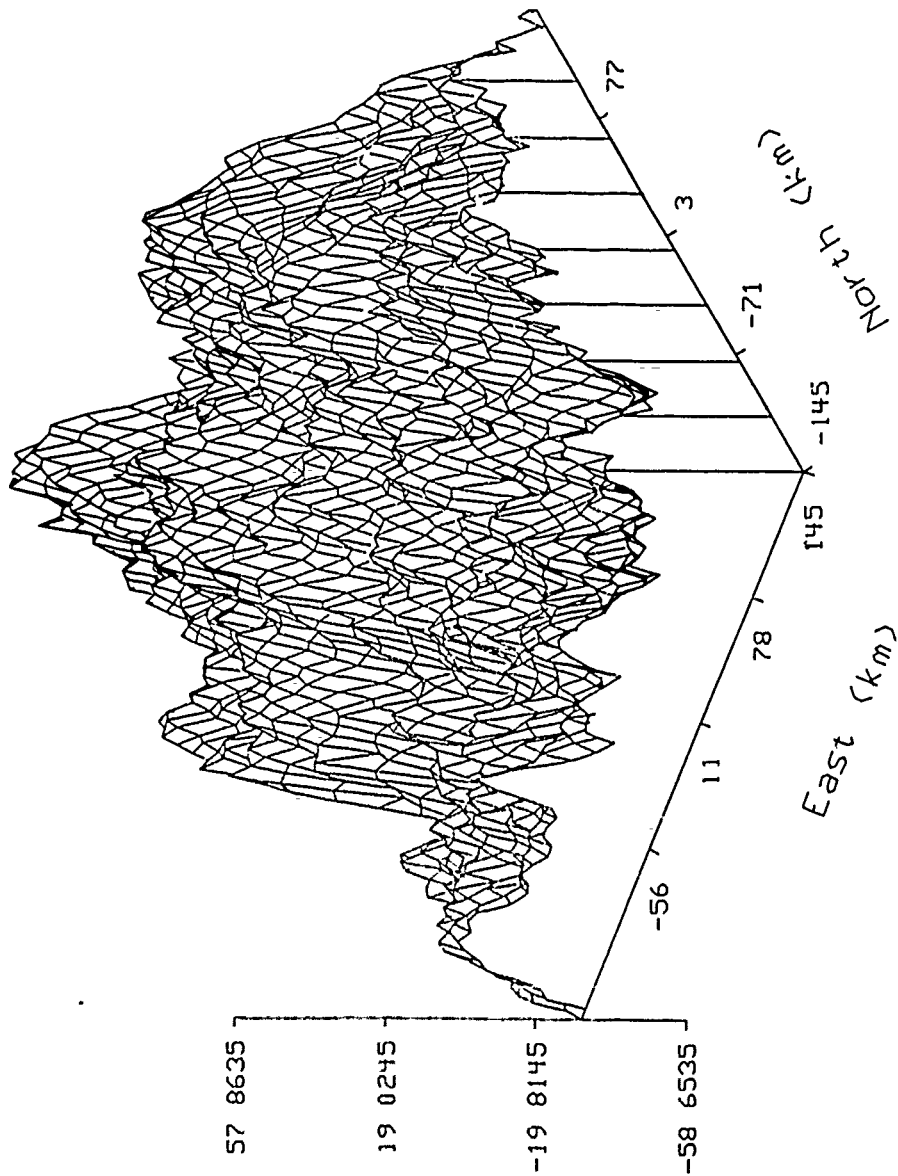
Ty hat (mgal)



Tape 1, file 2, meas Tzz at h=0 6km, est h=0

Figure97:  $\hat{T}_y$  given  $T_{zz}$ , File 2

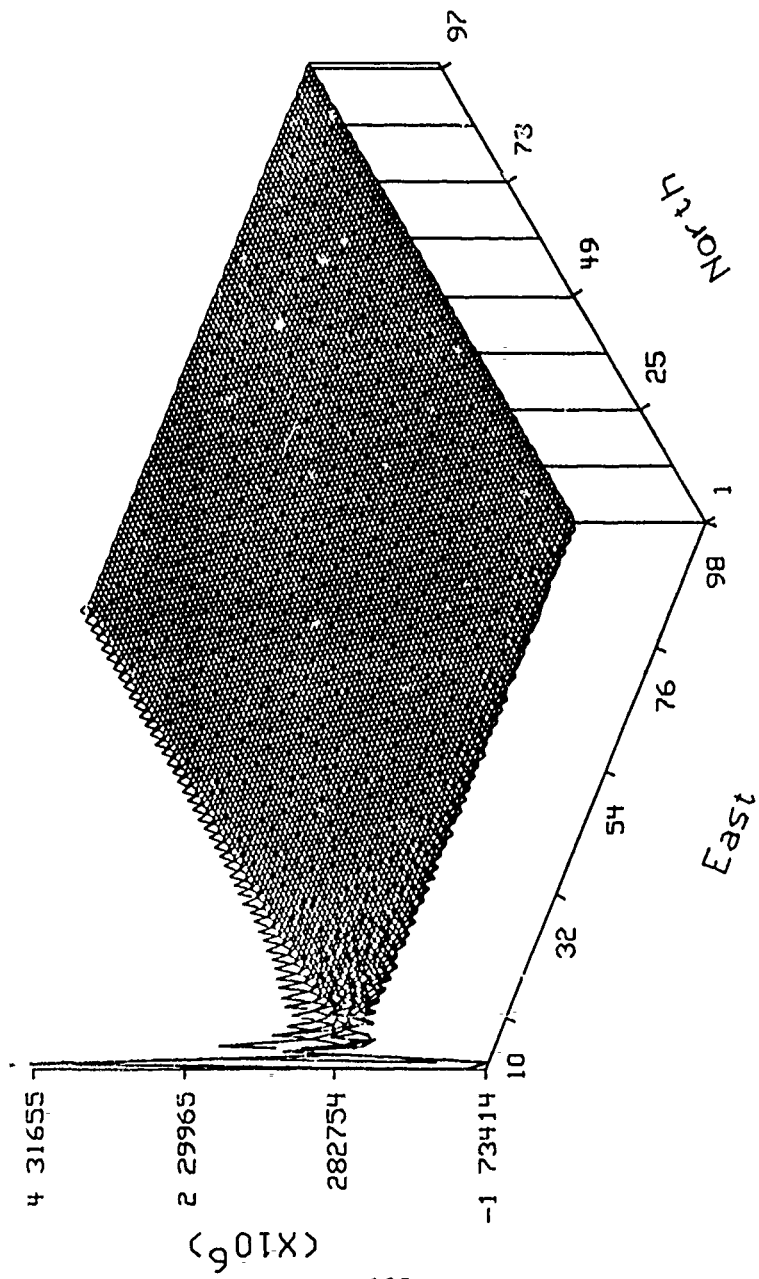
$\hat{T}_z$  (mgal)



Tape 1, file 2, meas  $T_{77}$  at  $h=0$  6km, est  $h=0$

Figure98:  $\hat{T}_z$  given  $T_{zz}$ , File 2

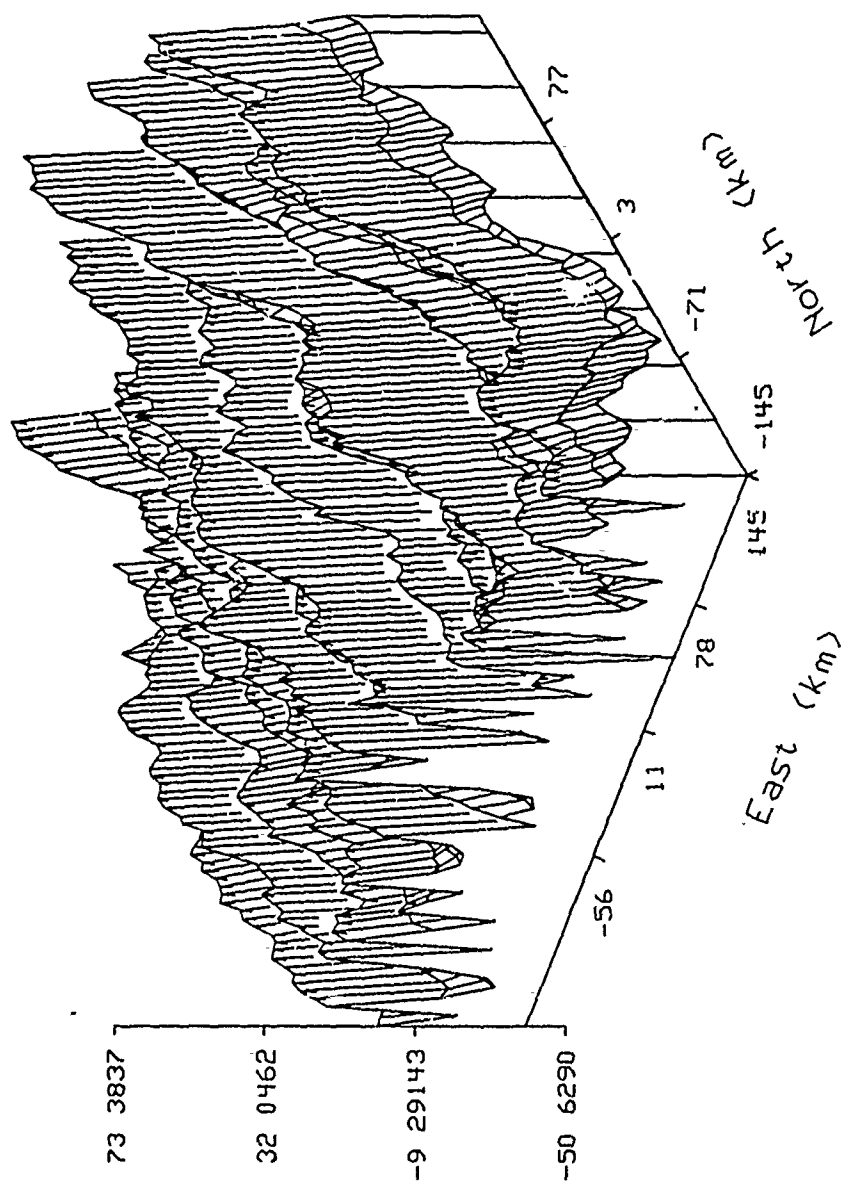
alpha hat



Tape 1, file 2, meas  $T_{xy}$  at  $h=0.6\text{km}$

Figure99:  $\hat{\alpha}$  given  $T_{xy}$ , File 2

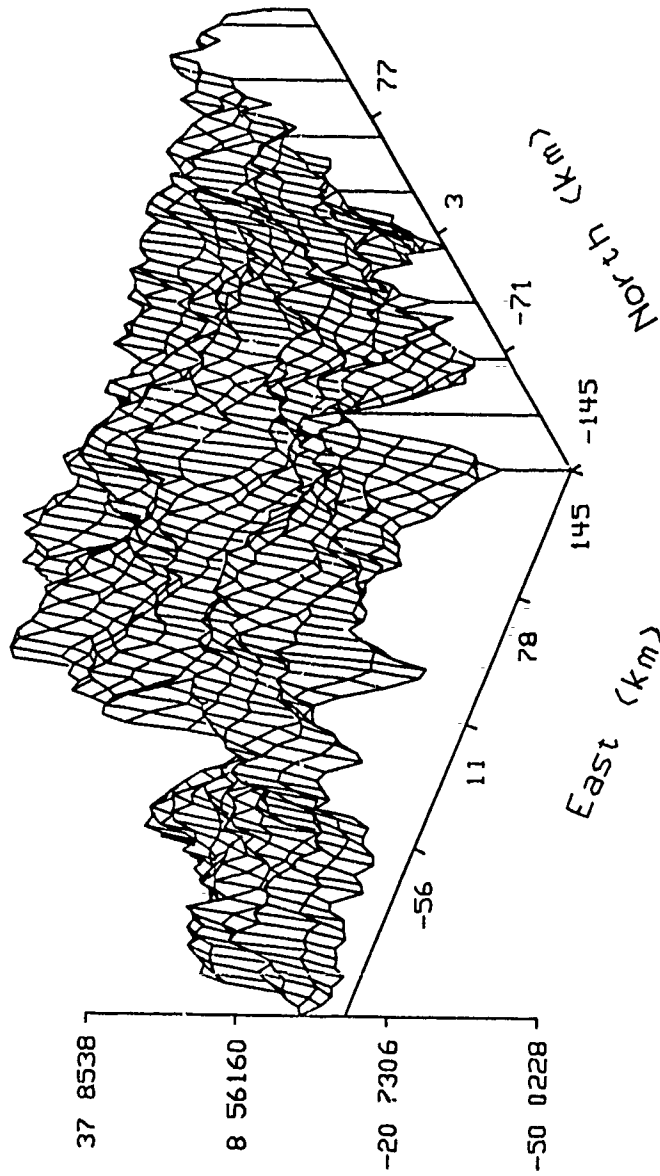
$\hat{T}_x$  (mgal)



Tape 1, file 2, meas  $T_{xy}$  at  $h=0$  6km, est  $h=0$

Figure100:  $\hat{T}_x$  given  $T_{xy}$ , File 2

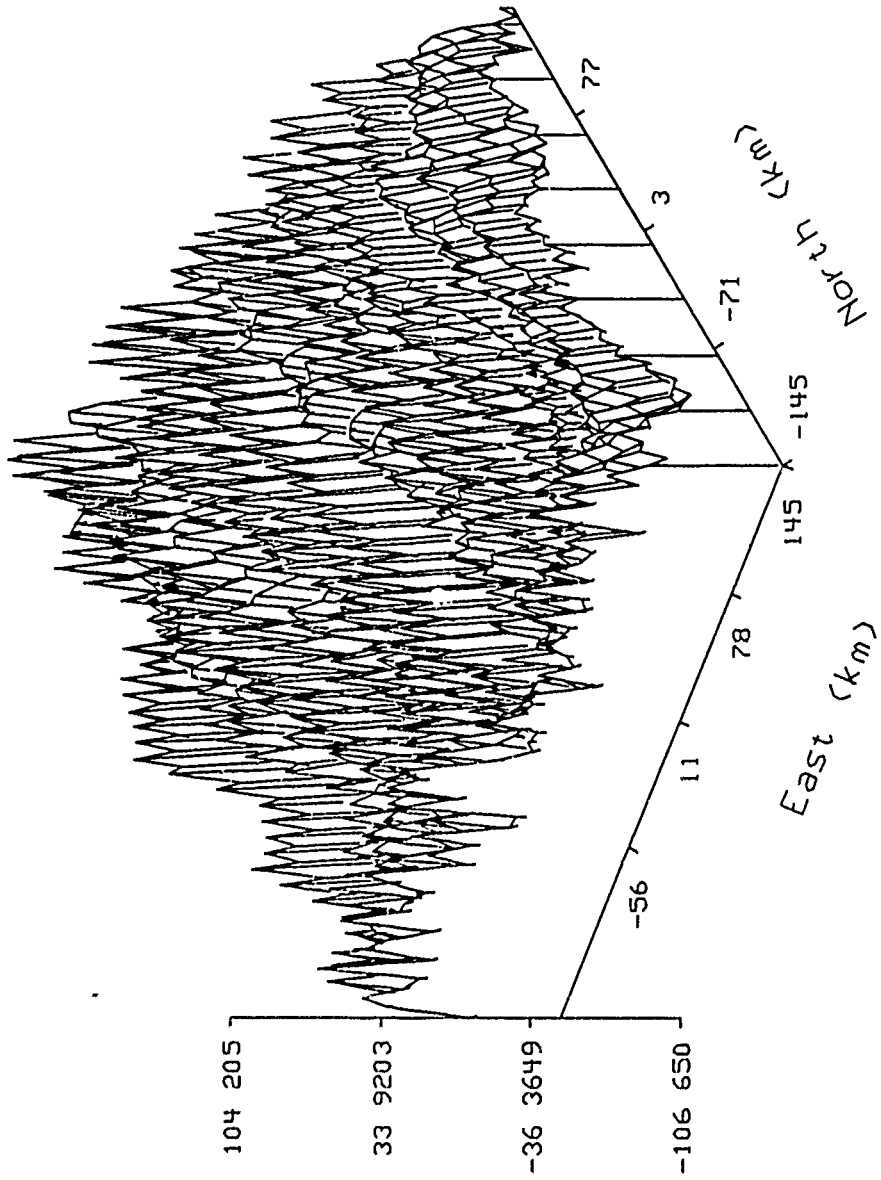
Ty hat (mgal)



Tape 1, file 2, meas  $T_{xy}$  at  $h=0$  6km, est  $h=0$

Figure101:  $\hat{T}_y$ , given  $T_{xy}$ , File 2

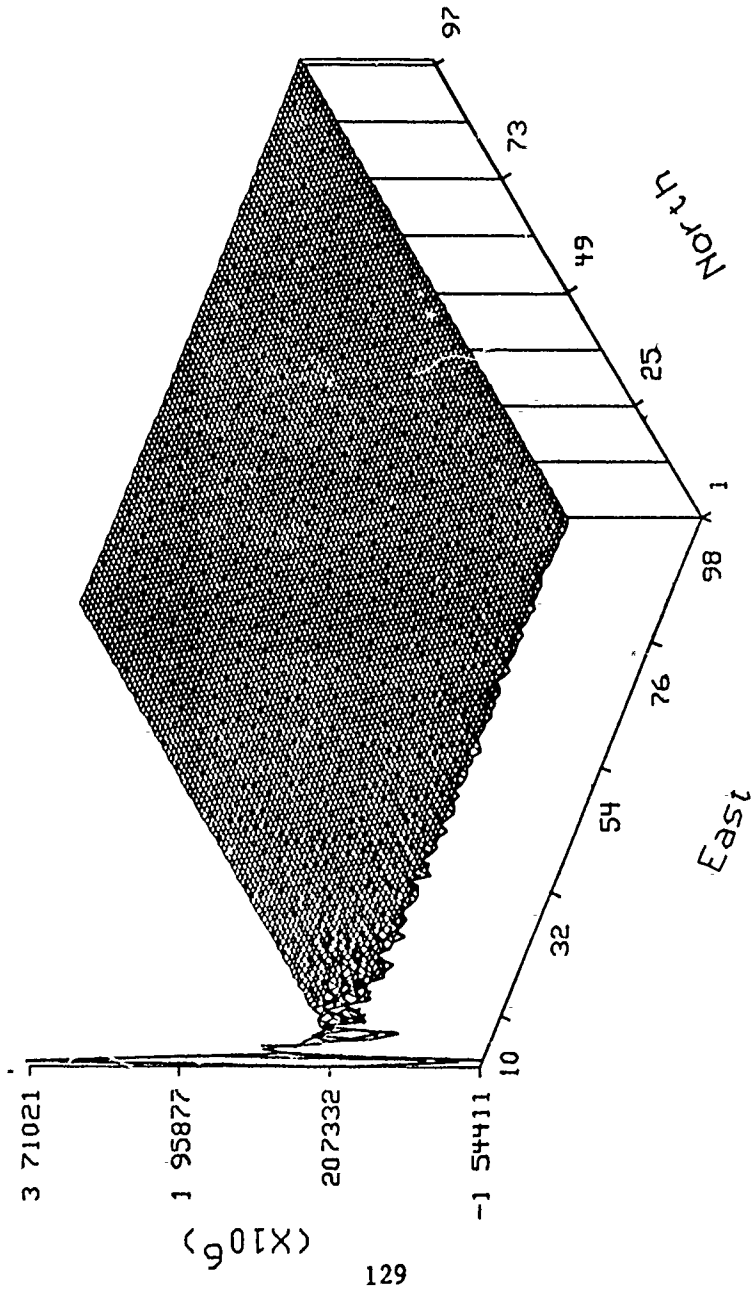
$\hat{T}_z$  (mgal)



Tape 1, file 2, meas  $T_{xy}$  at  $h=0$  6km, est  $h=0$

Figure102:  $\hat{T}_z$  given  $T_{xy}$ , File 2

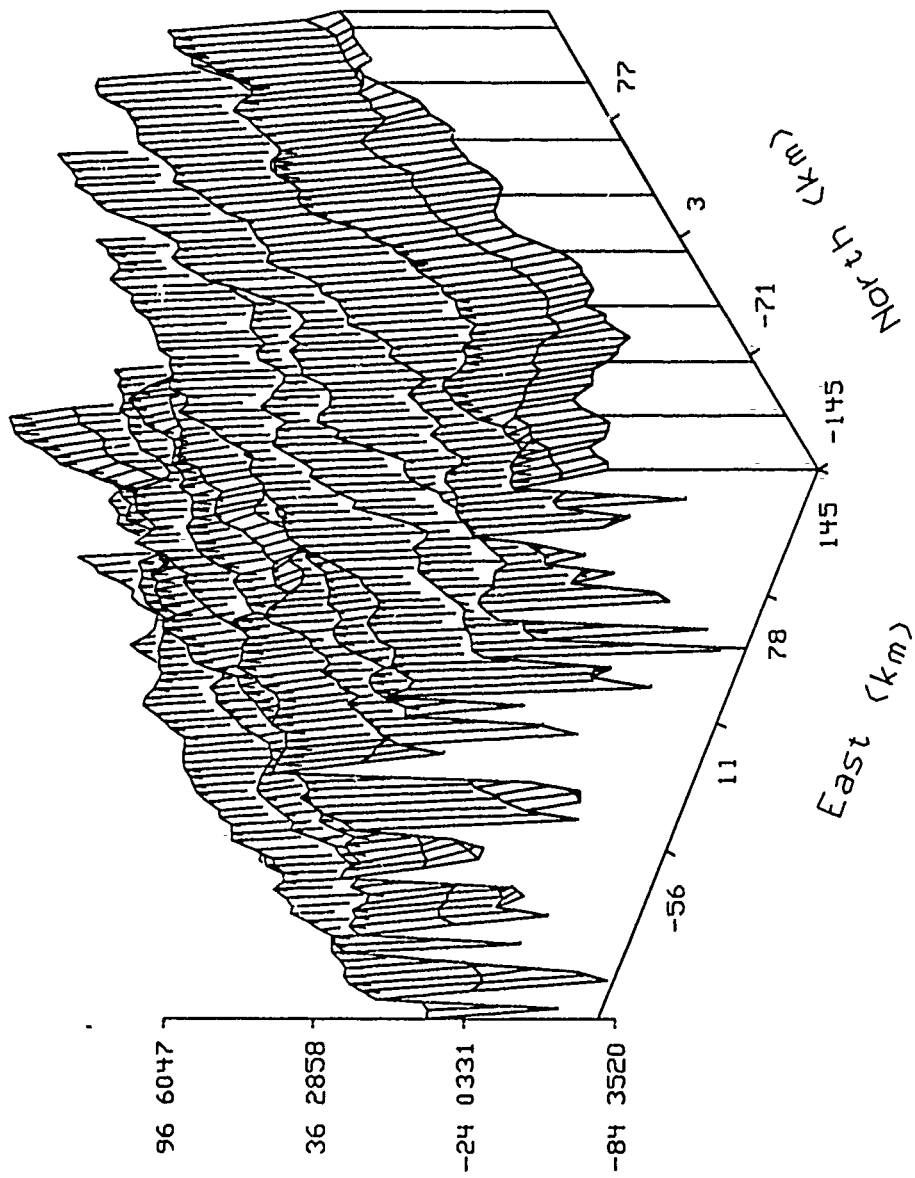
alpha hat



Tape 1, file 2, meas  $T_{yz}$  at  $h=0.6$  km

Figure103:  $\hat{\alpha}$  given  $T_{yz}$ , File 2

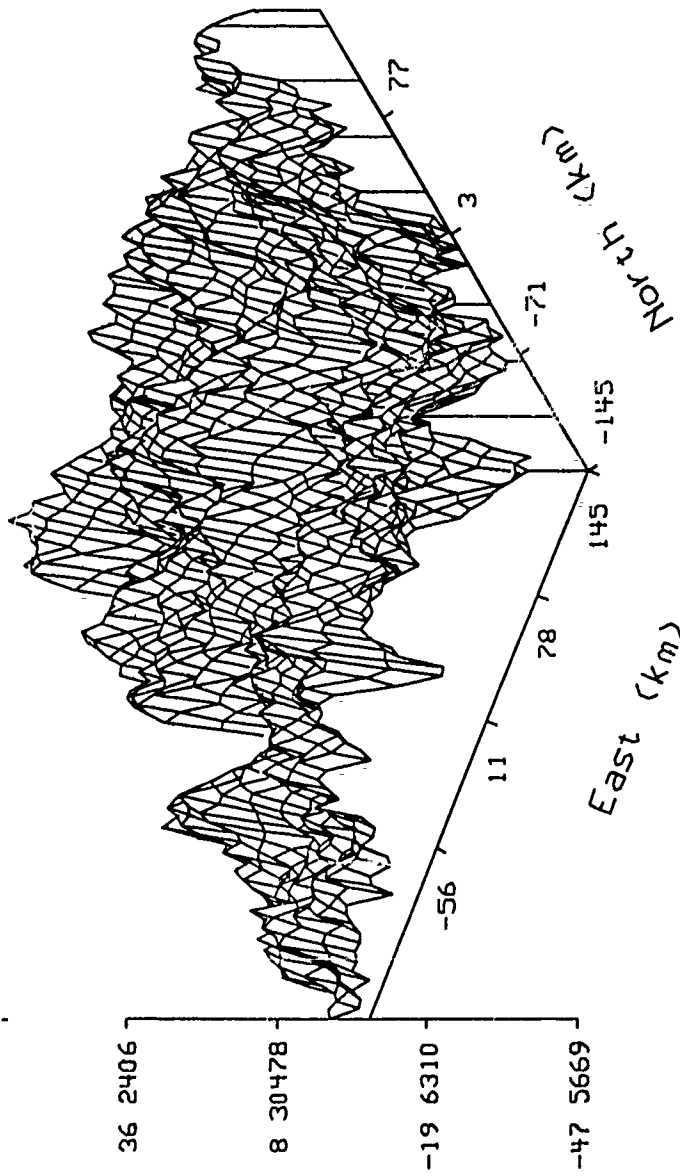
Tx hat (mgal)



Tape 1, file 2, meas Tyz at h=0 6km, est h=0

Figure104:  $\hat{T}_x$  given  $T_{yz}$ , File 2

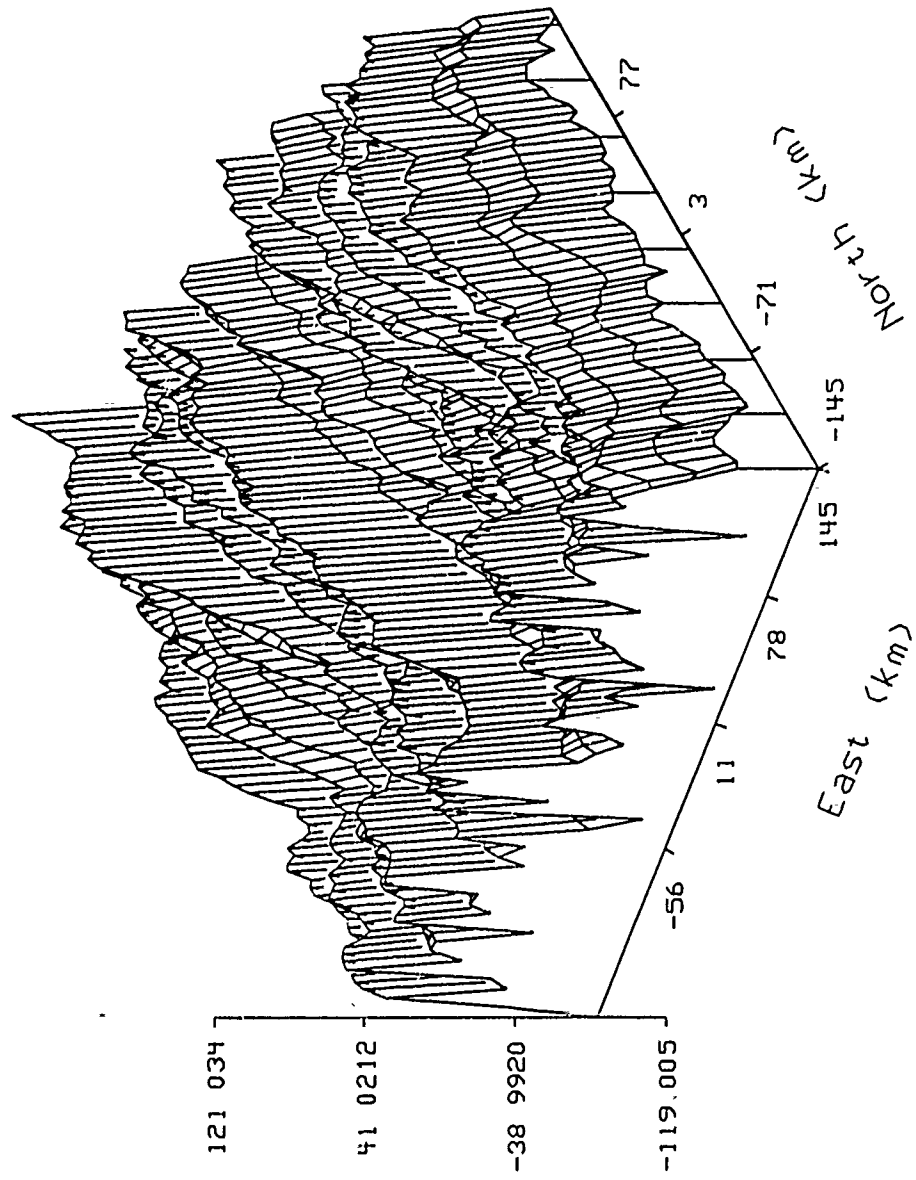
Ty hat (mgal)



Tape 1, file 2, meas Tuz at h=0 6km, est h=0

Figure105:  $\hat{T}_y$  given  $T_{yz}$ , File 2

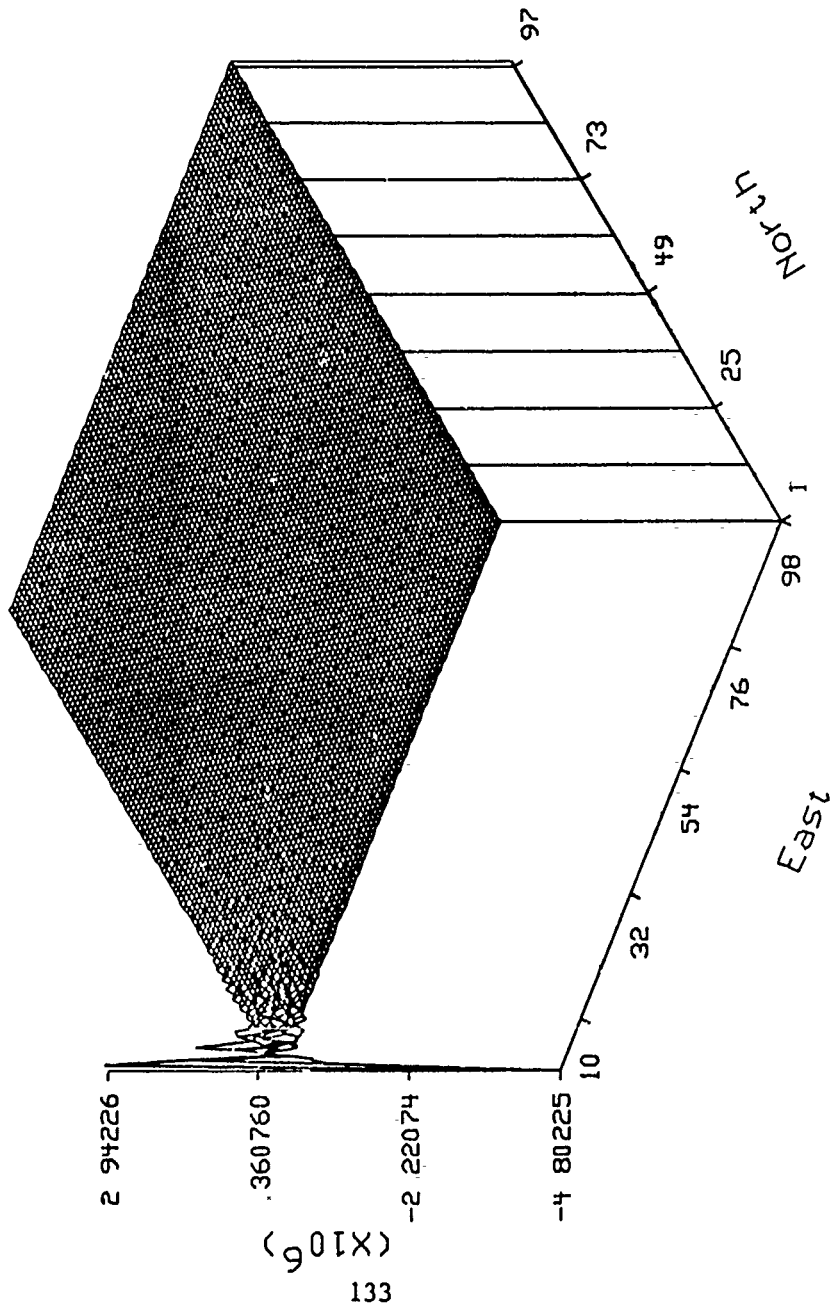
$\hat{T}_z$  (mgal)



Tape 1, file 2, meas  $T_{yz}$  at  $h=0$  6km, est  $h=0$

Figure106:  $\hat{T}_z$  given  $T_{yz}$ , File 2

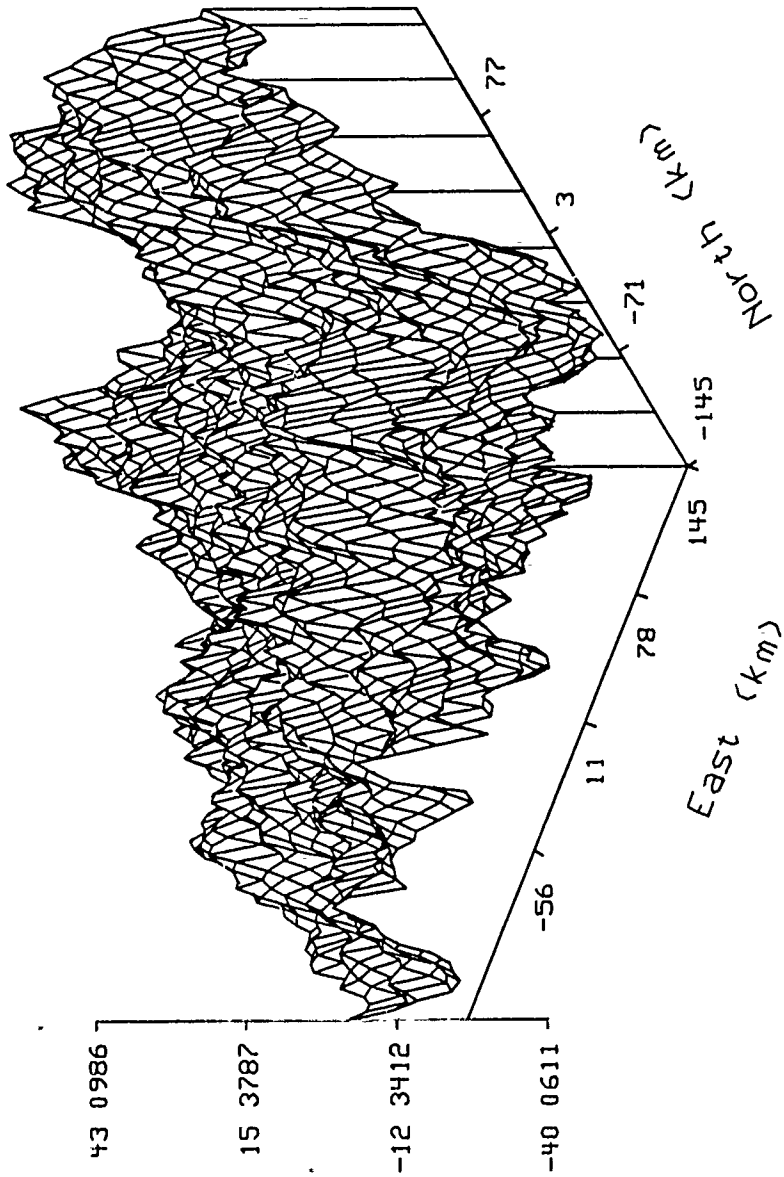
alpha hat



, Tape 1, file 2, meas Txz at h=0 km

Figure107:  $\hat{\alpha}$  given  $T_{zz}$ , File 2

Tx hat (mgal)

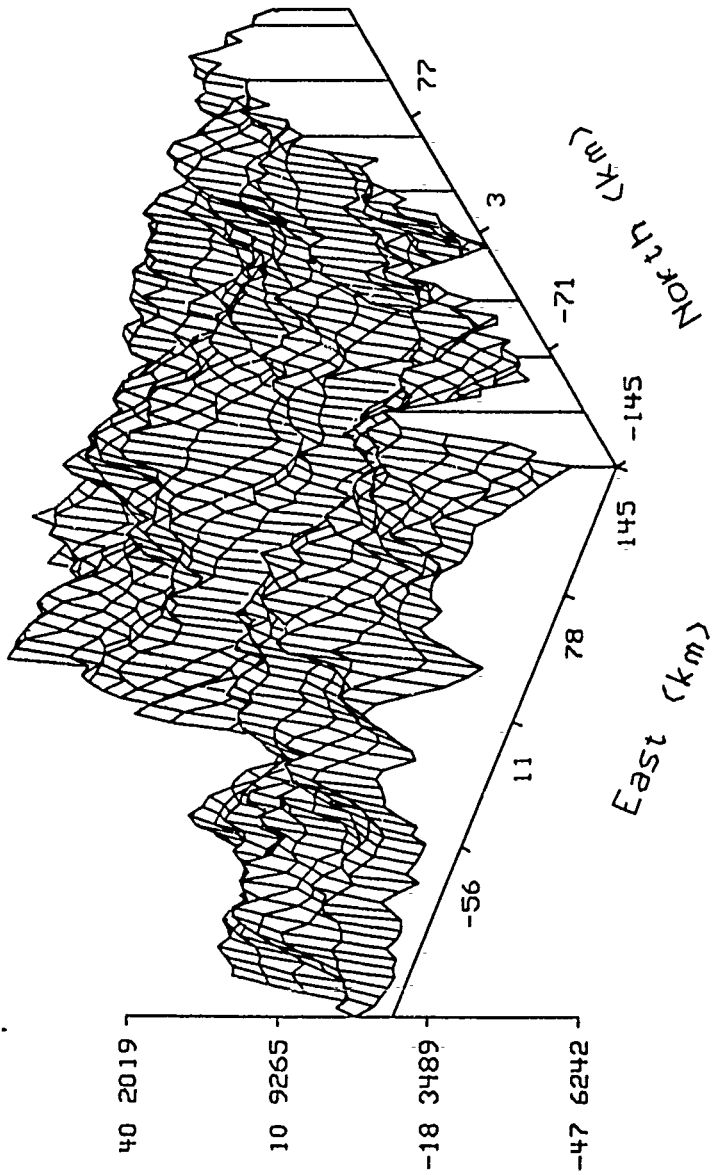


134

Tape 1, file 2, meas Txz at h=0 6km, est h=0

Figure108:  $\hat{T}_x$  given  $T_{xz}$ , File 2

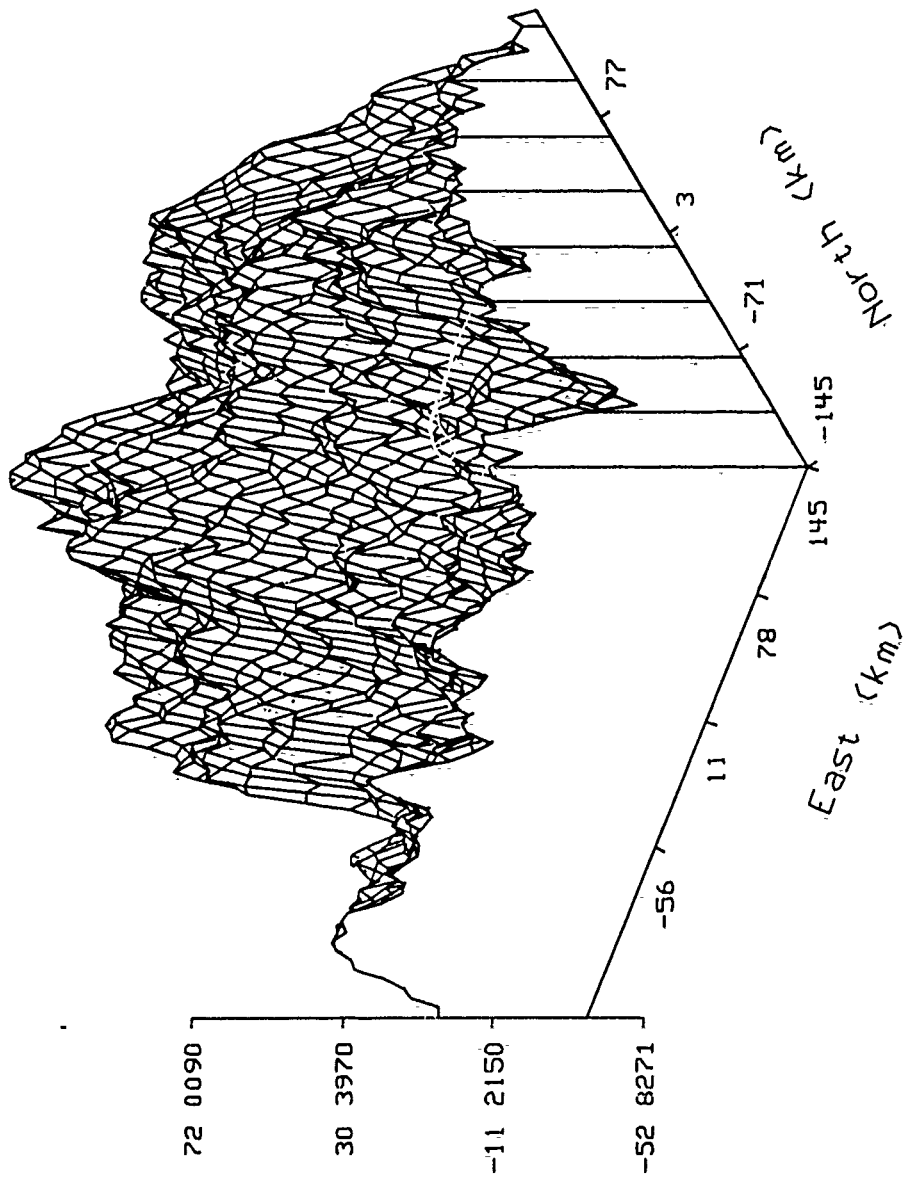
Ty hat (mgal)



Tape 1, file 2, meas  $T_{xz}$  at  $h=0$  6km, est  $h=0$

Figure109:  $\hat{T}_y$  given  $T_{zz}$ , File 2

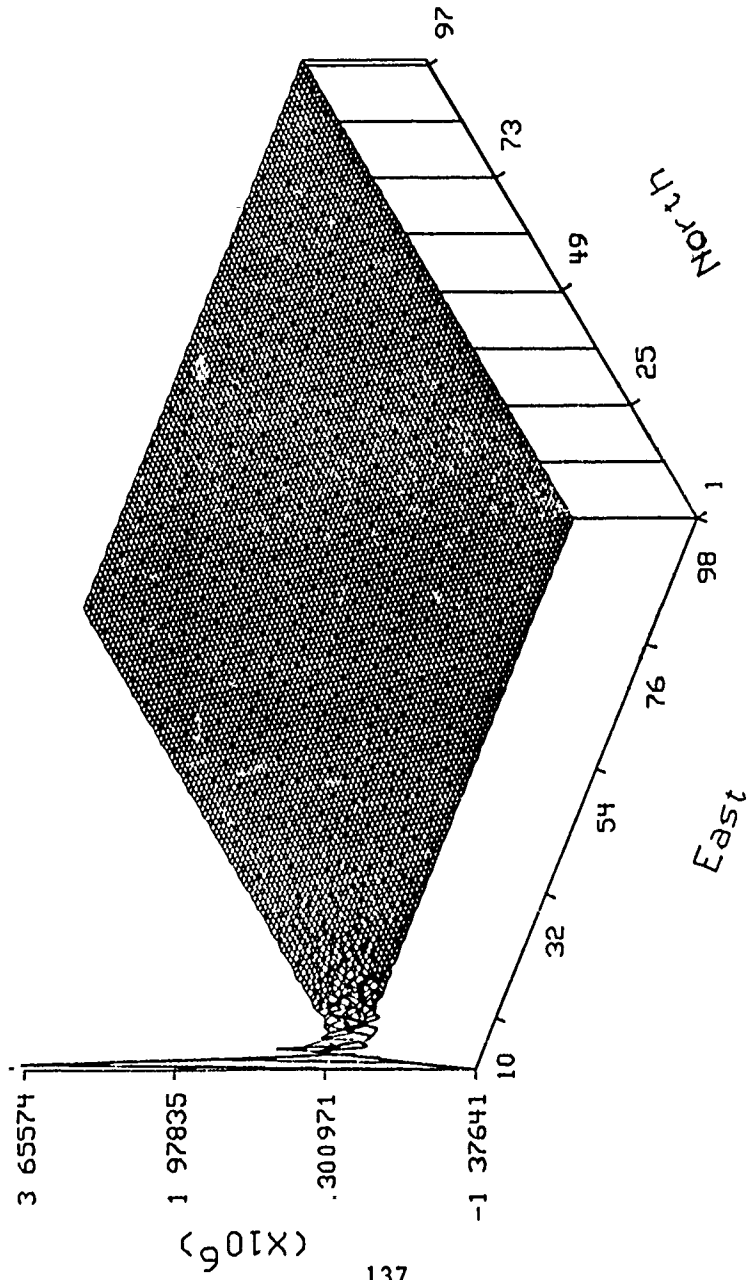
Tz hat (mgal)



Tape 1, file 2, meas Txz at h=0 6km, est h=0

Figure110:  $\hat{T}_z$  given  $T_{xz}$ , File 2

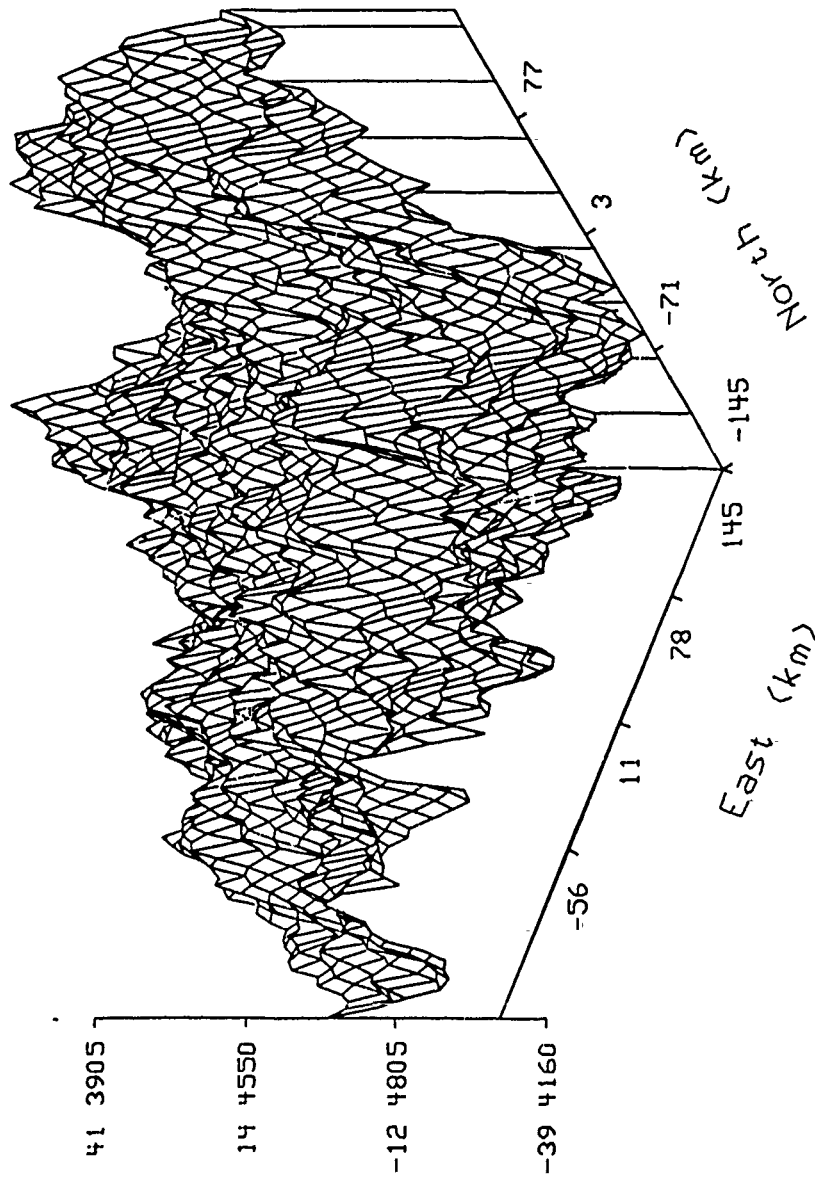
alpha hat



Tape 1, file 2, meas full tensor at  $h=0.6\text{km}$

Figure11:  $\hat{\alpha}$  given full tensor gradient, File 2

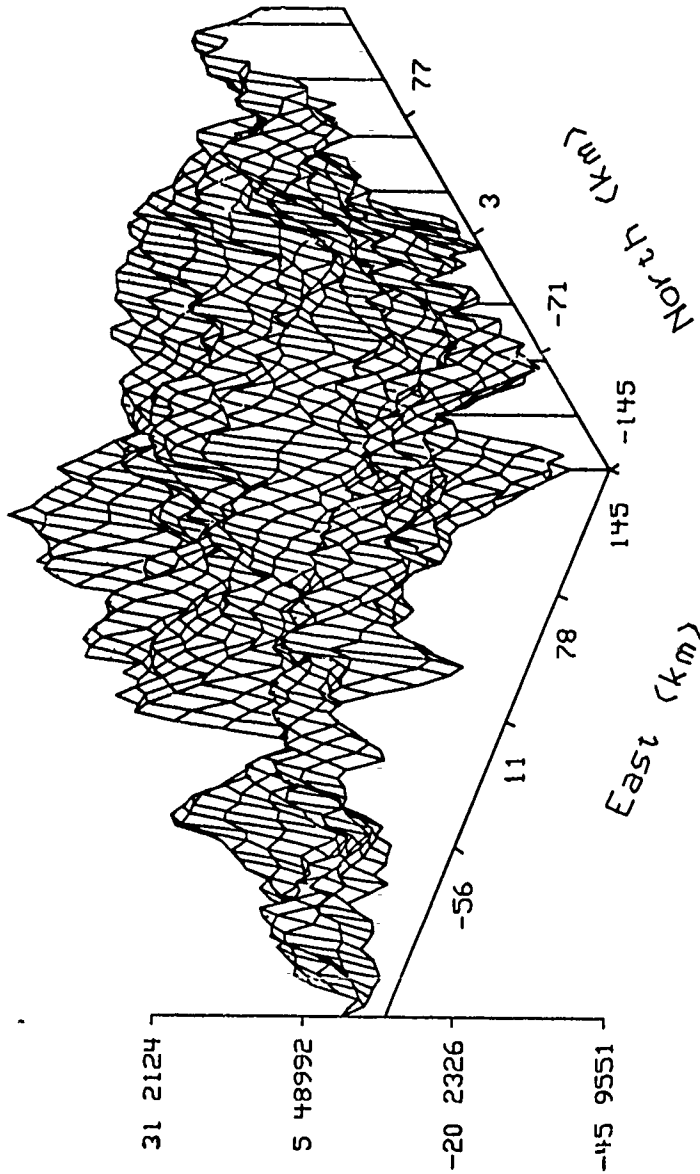
$\hat{T}_x$  (mgal)



Tape 1, file 2, meas full tensor at  $h=0.6\text{km}$ , est  $h=0$

Figure112:  $\hat{T}_x$  given full tensor gradient, File 2

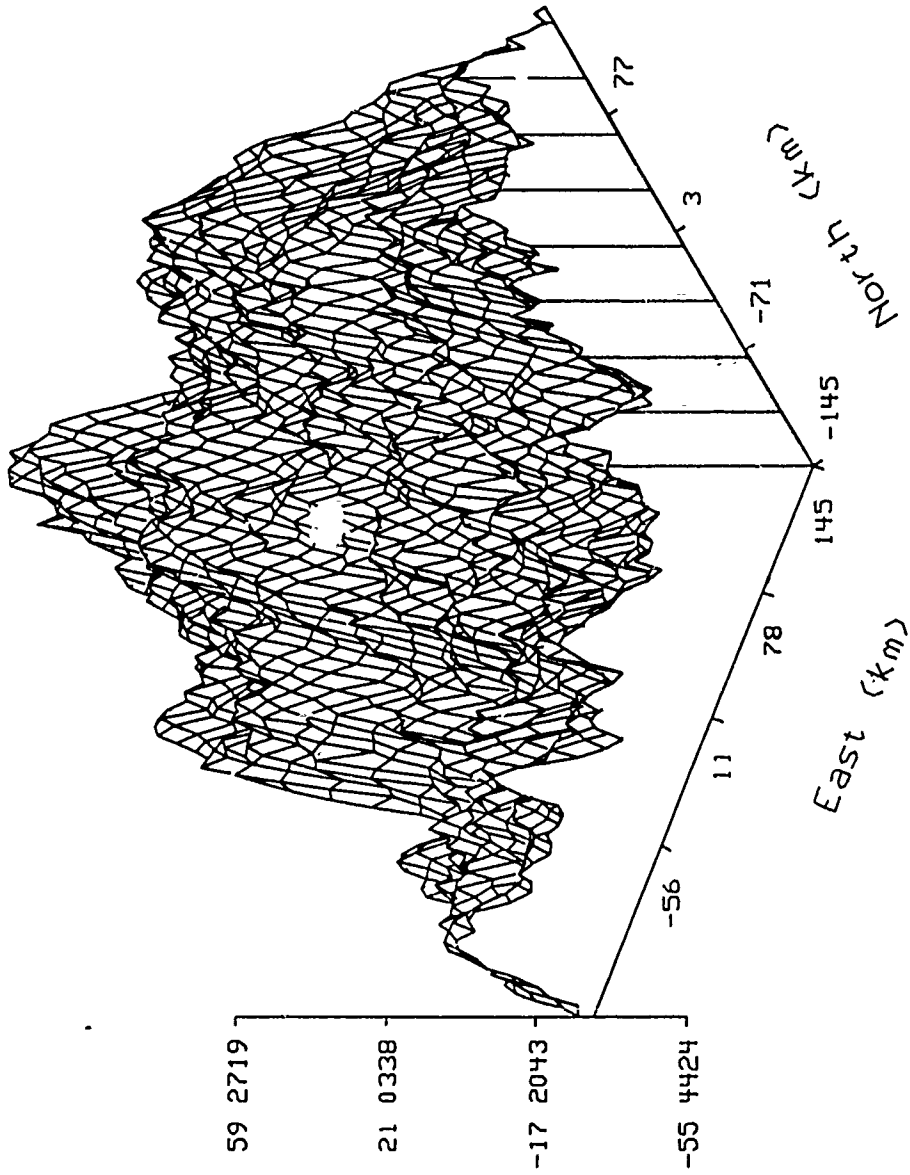
Ty hat (mgel)



Tape 1, file 2, meas full tensor at h=0 6km, est h=0

Figure113:  $\hat{T}_y$  given full tensor gradient, File 2

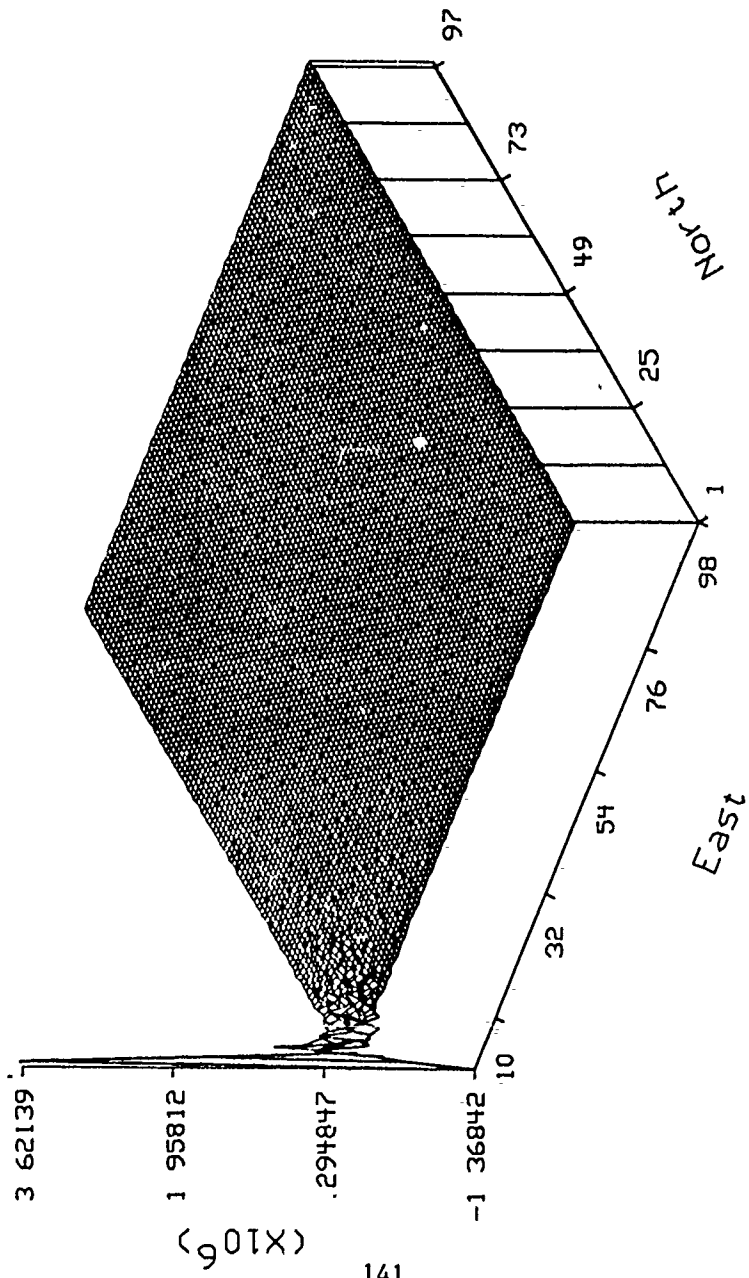
$\hat{T}_z$  (mgal)



Tape 1, file 2, meas full tensor at  $h=0.6$  km, est  $h=0$

Figure114:  $\hat{T}_z$  given full tensor gradient, File 2

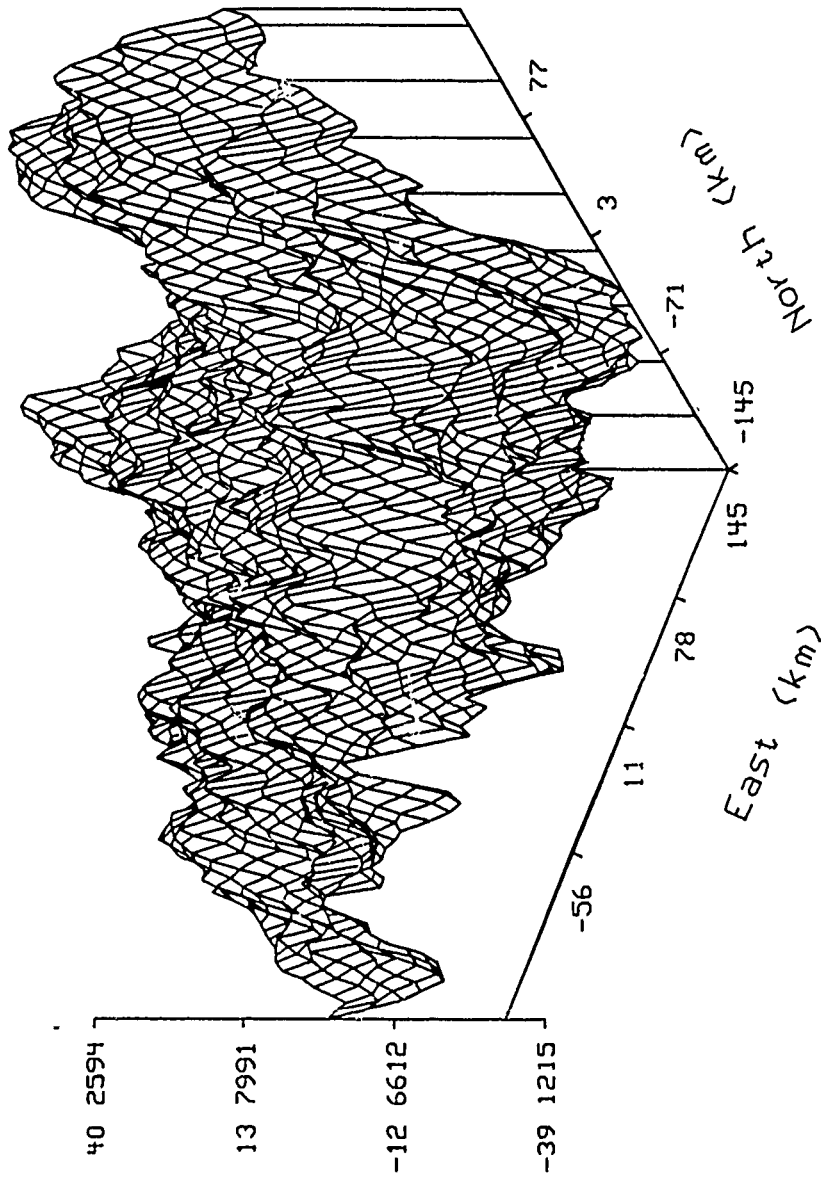
alpha hat



Tape, 1, files 1 & 2 combined, intersection method

Figure115:  $\hat{\alpha}$  given full tensor gradient, Files 1 & 2, intersection method

Tx hat (mgal)

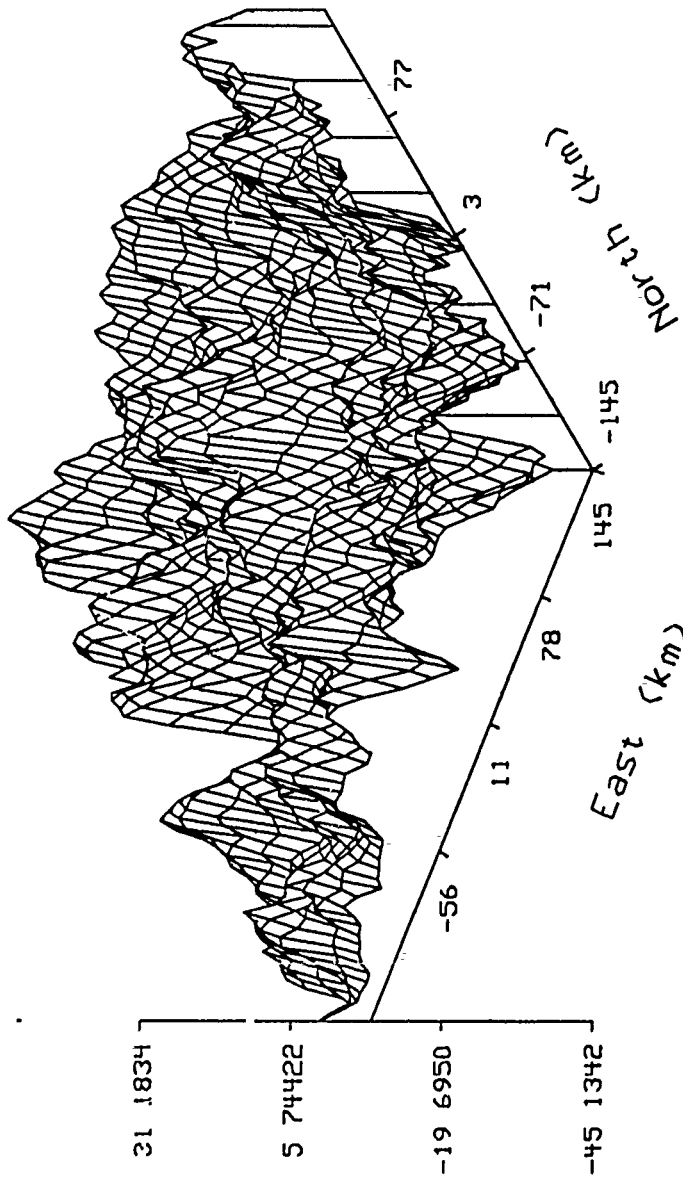


142

Tape, 1, files 1 & 2 combined, intersection method

Figure116:  $\hat{T}_z$  given full tensor gradient, Files 1 & 2, intersection method.

Ty hat (mgal)

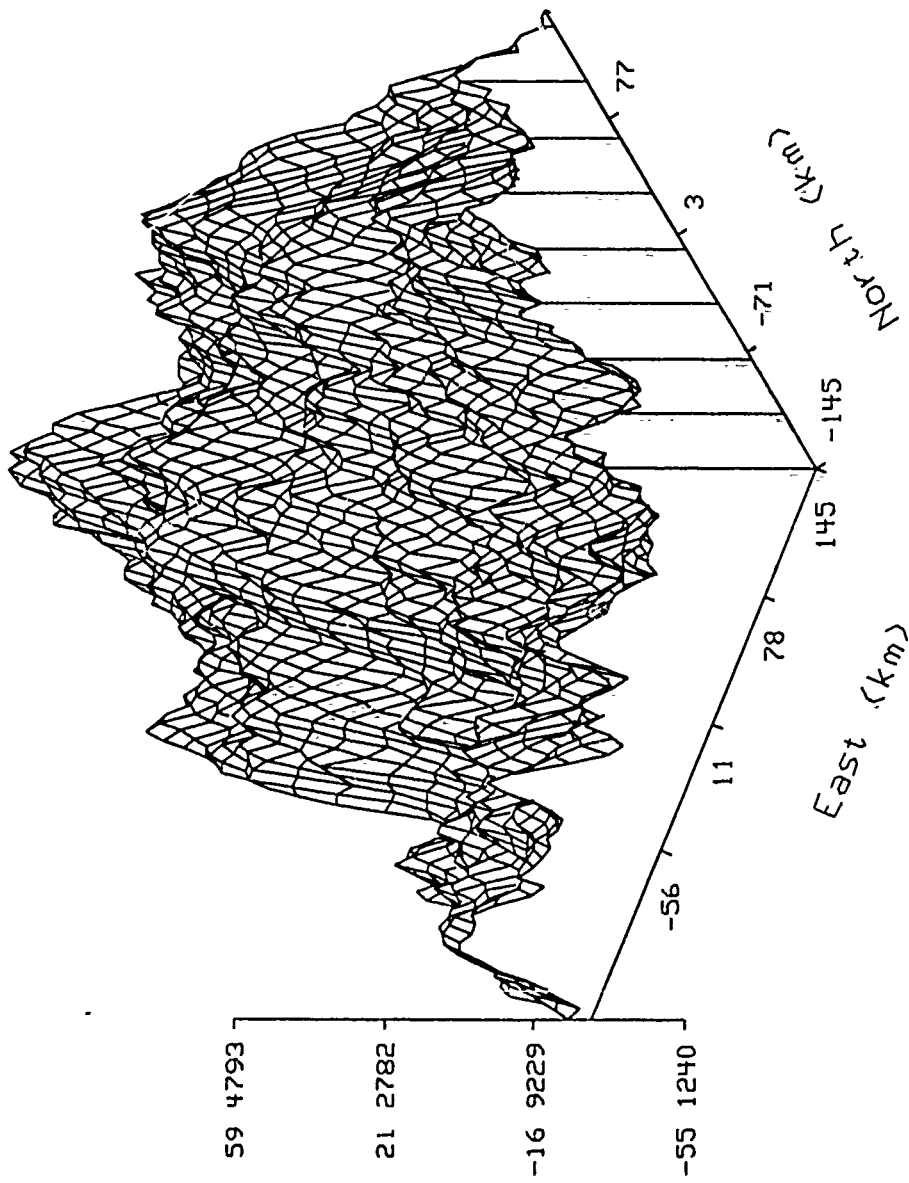


143

Tape 1, files 1 & 2 combined, intersection method

Figure117:  $\hat{T}$ , given full tensor gradient, Files 1 & 2, intersection method

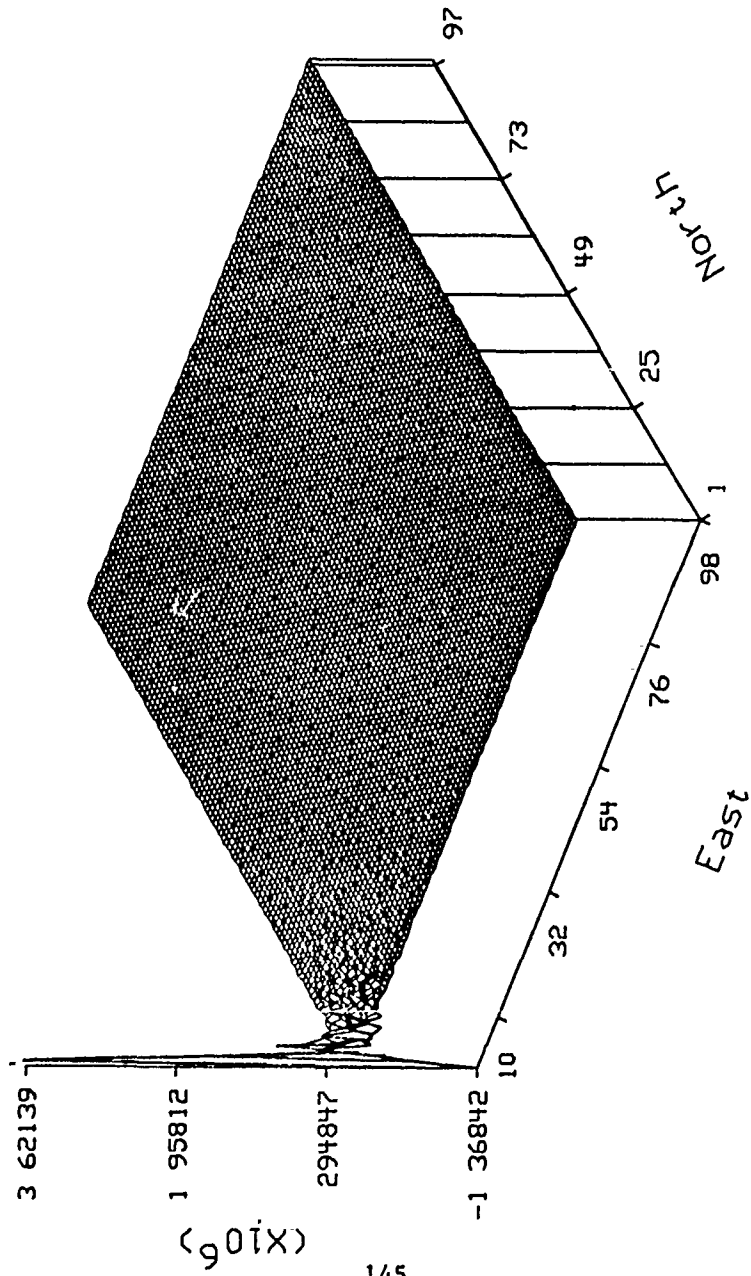
$\hat{T}_z$  (mgal)



Tape 1, files 1 & 2 combined, intersection method

Figure 118:  $\hat{T}_z$  given full tensor gradient, Files 1 & 2, intersection method

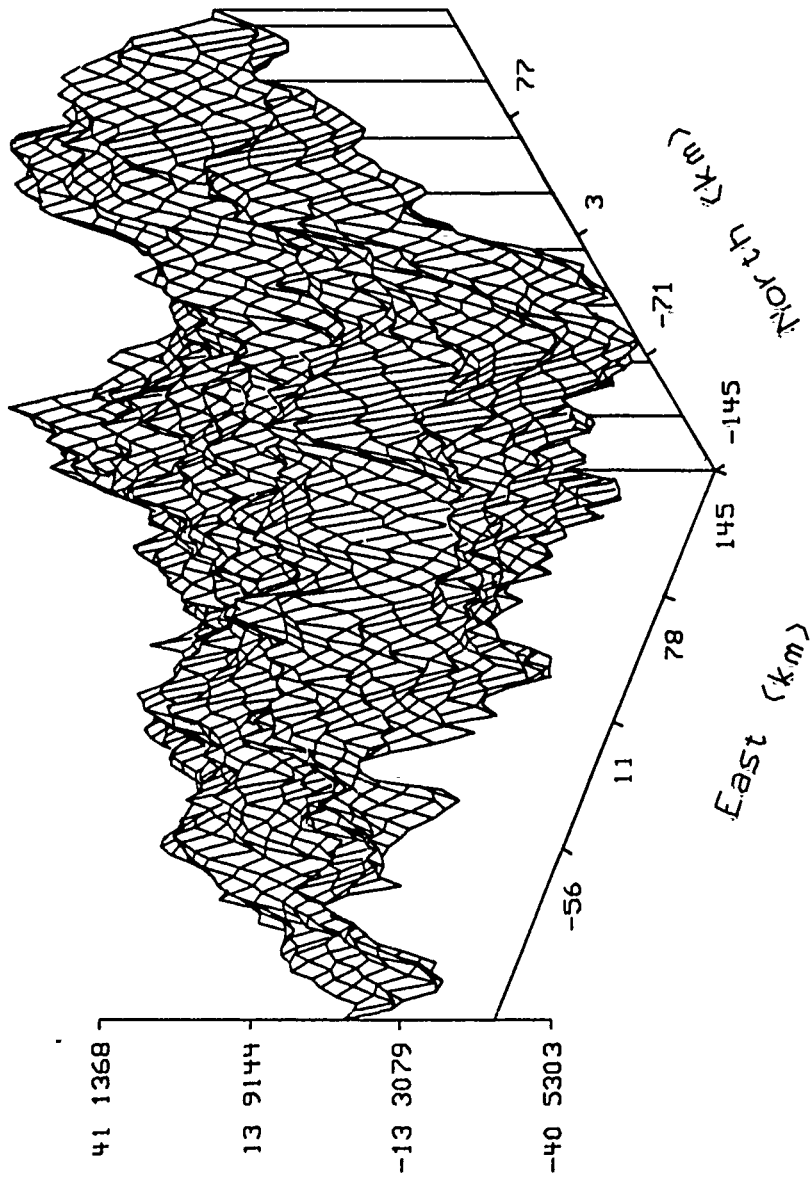
alpha hat



Tape 1, files 1 & 2 combined, union method

Figure119:  $\hat{\alpha}$  given full tensor gradient, Files 1 & 2, union method

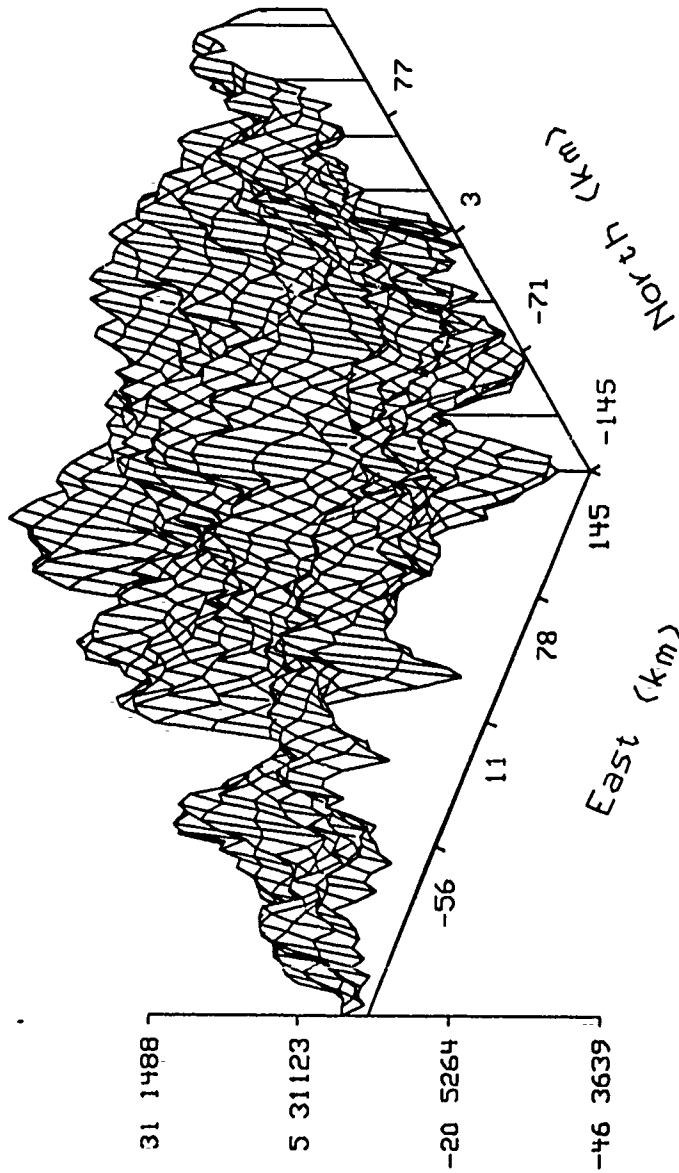
Tx hat (mgal)



Tape. 1, files 1 & 2 combined, union method

Figure120:  $\hat{T}_z$  given full tensor gradient, Files 1 & 2, union method

Ty hat (mgal)

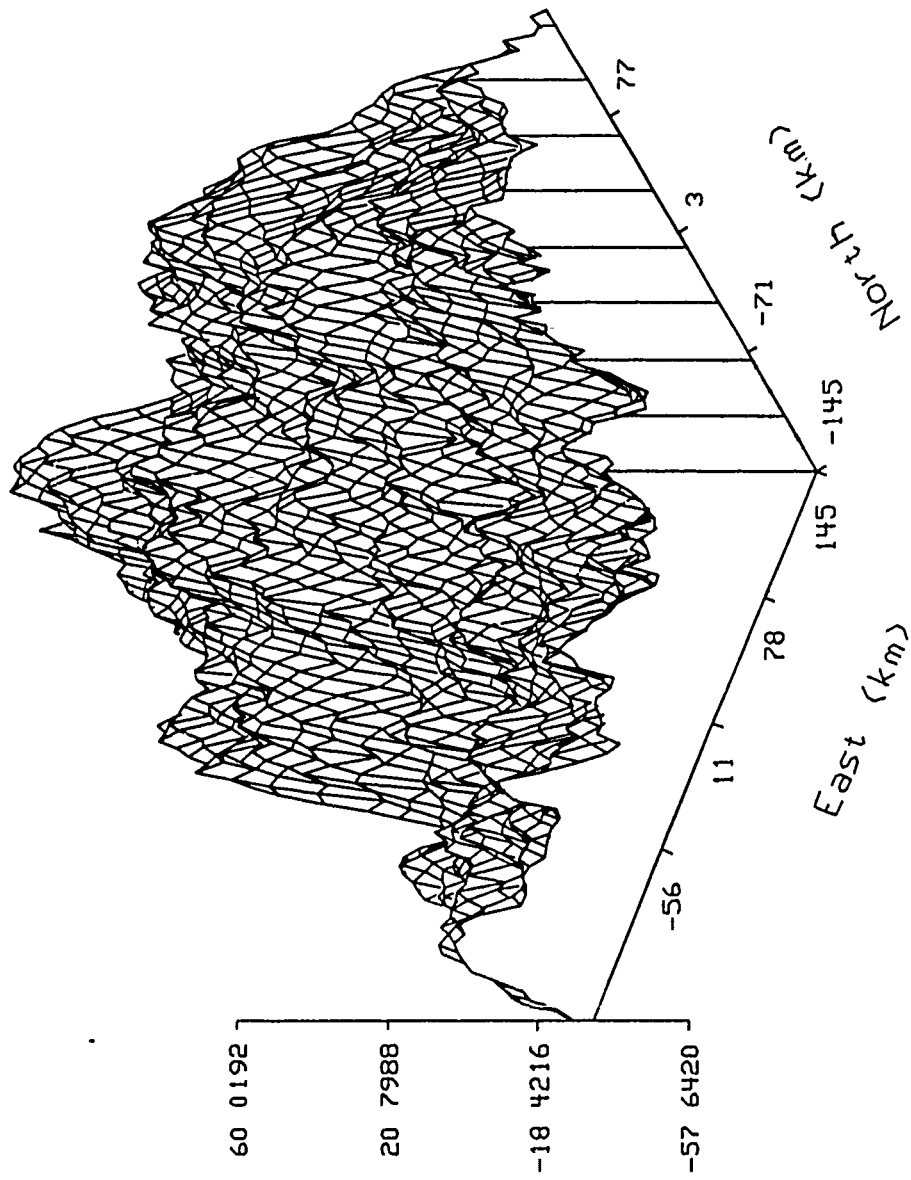


Tape .1, files 1 & 2 combined, union method

Figure121:  $\hat{T}_y$  given full tensor gradient, Files 1 & 2, union method

Tz hat (mgal)

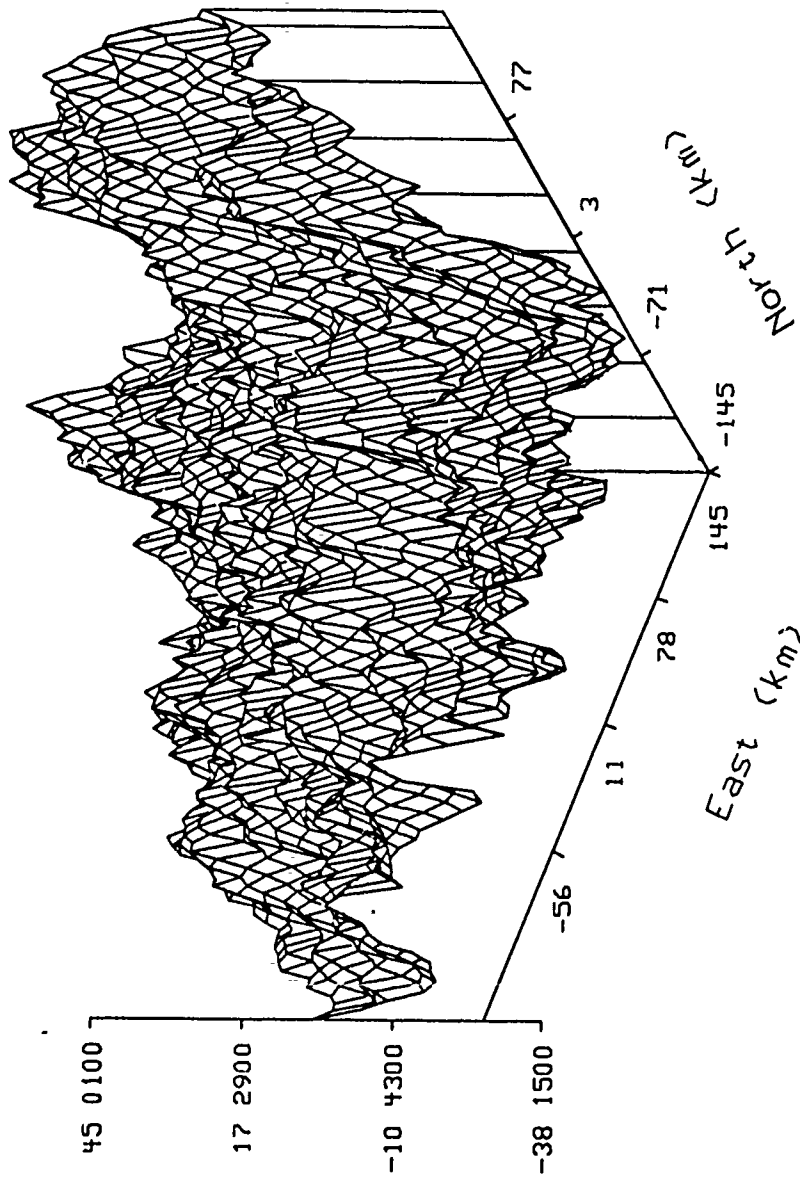
1964



Tape 1, files 1 & 2 combined, union method

Figure 122:  $\hat{T}_z$  given full tensor gradient, Files 1 & 2, union method

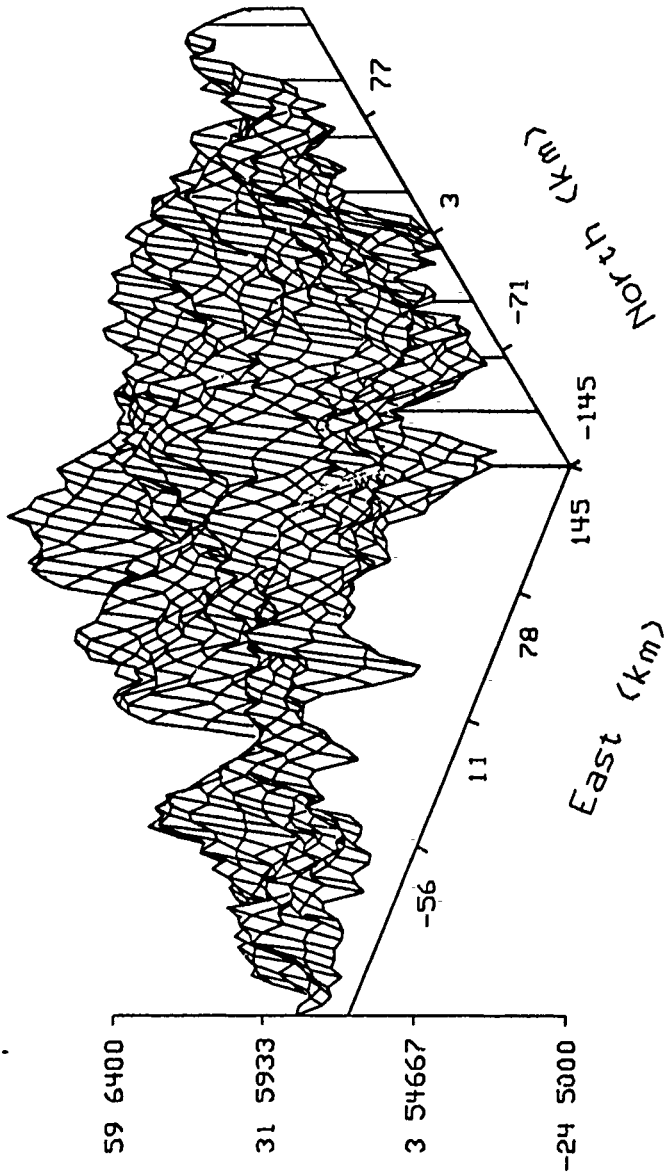
Tx (mgal)



Tape 1, file 3 (truth)

Figure123: Truth value of  $T_x$ , File 3

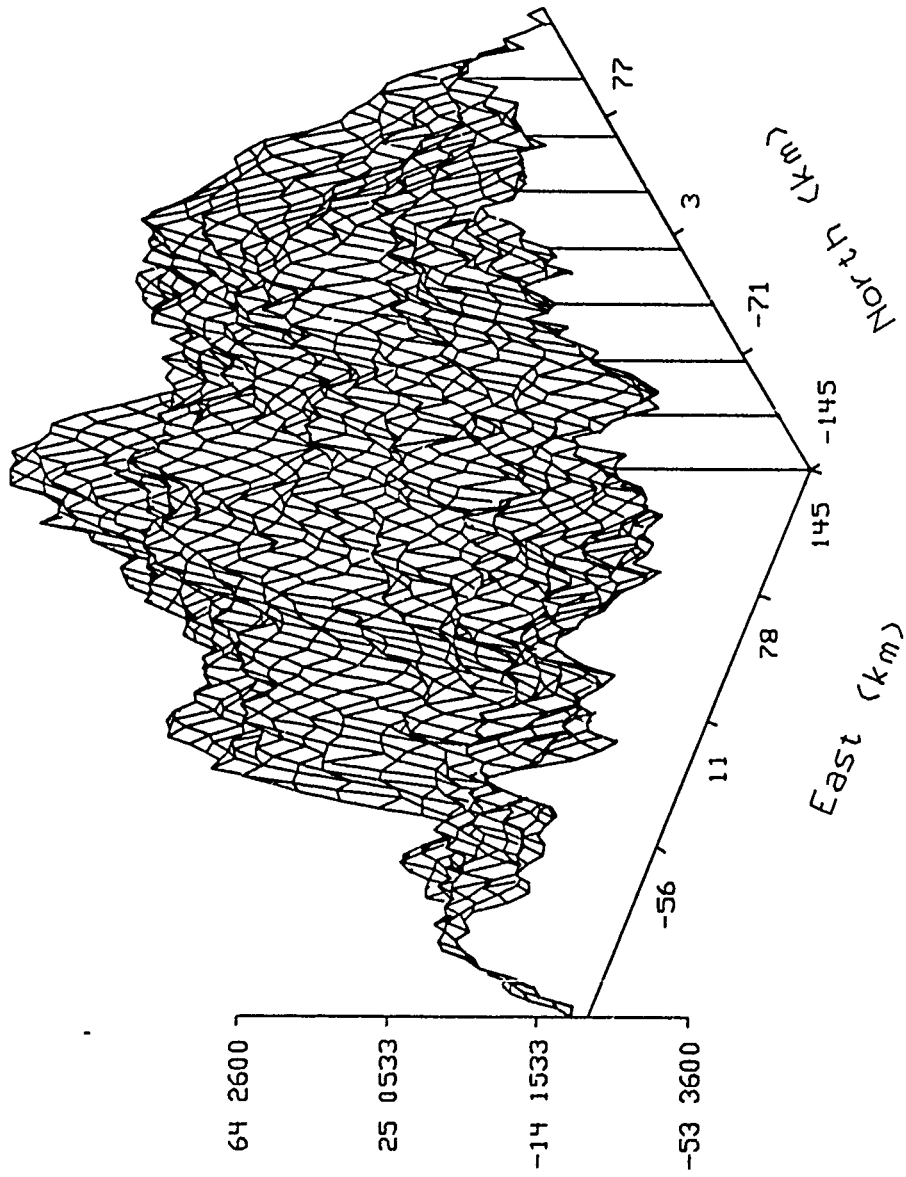
Ty (mgal)



Tape 1, file 3 (truth)

Figure124: Truth value of  $T_y$ , File 3

Tz (mgal)



Tape 1, file 3 (truth)

Figure125: Truth value of Tz, File 3